Carbon Nanotubes Deposited by Hot Wire Plasma CVD and water assisted CVD for Energetic and Environmental Applications

Shahzad Hussain

FEMAN Group, IN2UB Dept. Física Aplicada i Òptica,
Martí i Franquès, 1, 08028 Barcelona, Catalonia, Spain

Carbon Nanotubes Deposited by Hot Wire Plasma CVD and water assisted CVD for Energetic and Environmental Applications

A thesis submitted for the degree of Doctor of Philosophy

Presented by

Shahzad Hussain

PhD program: Nanoscience

Directors: Enric Bertran Serra and Roger Amade Rovira

Tutor: Enric Bertran Serra

Barcelona: July 2014

Dedicated to my loving Mother, my late Father,

Brothers and Sister.

The only Cure for ignorance is to ask.

La única cura para la ignorancia es preguntar.

Prophet Muhammad (PBUH)

This research work has been carried out in the lab of the FEMAN research group, Department of Applied Physics and Optics, Faculty of Physics, University of Barcelona Spain. During master thesis, for the program of official university master degree in Nanoscience and Nanotechnology author already acquired some basic knowledge about CNTs growth mechanism, sputtering, PECVD and characterization techniques. After the completion of master degree in July 2011,

The author was officially enrolled in the PhD program of Nanoscience, University of Barcelona in Sep 2011. The presented work has been supervised by Dr Enric Bertran and Dr Roger Amade in the framework of the projects, 2009SGR00185 of AGAUR of *Generalitat de Catalunya a*nd CTQ2009-14674-CO2-01 and MAT2010-20468 from MICINN of Spanish Government.

Acknowledgements

I would like to thank the research director Professor Dr Enric Bertran Serra for providing me the opportunity to learn the knowledge from him, to work in the laboratories and to obtain funding for the research work.

Special thanks to the co-director of my thesis, Dr. Roger Amade, who always has been there to provide scientific guidance, encouragement, help in writing research articles and fixing problems of reactors in the lab. Thank you again for the constructive discussions and being supportive at work, with positive and pleasant disposition all the time.

Also I would like to thank Dr. Eric Jover for guidance.

This work would not have been possible without the unconditional support of my parents, brothers and sister. Thanks to them for encouraging, supporting and loving me.

I like to thanks also my friends, José Raul and Melanie Warner, who always have had trust and faith on me to finish this doctoral thesis.

Also, special thanks to the colleagues in the FEMAN research group for all their collaboration and the department of applied physics.

Thanks again to Dr Enric Bertran for giving me this opportunity to work under your guidance and to learn from your research expertise. Thank you for your support and for being always available for discussions despite your busy schedules.

Shahzad Hussain

Outline of this thesis

Nanoscience and Nanotechnology have experienced a tremendous growth in few years. At this time, an increasingly large number of applications have been demonstrated. Specifically, carbon nanotubes are one of the nanomaterials with most promising new proposals for applications in mechanics and surface structures, energy and charge storage, environment, biomedicine, electrochemistry or photonics. Carbon nanotubes (CNTs) have unique characteristics that allow them to act as electrodes in charge storage devices, sensors and traps for pollutants, among others. The goal of the thesis was to synthesis the CNTs on different conductive and nonconductive substrates and to study their possible role in various applications such as energy and environment.

On the one hand, for applications that require a certain amount of energy in pulse form, the traditional capacitors used in electronic circuits are not suitable because they cannot store enough energy in the volume and weight available. However, given the characteristics of CNTs that have a narrow size distribution, large specific surface area, low resistivity and high stability, CNTs have been regarded as suitable material for electrodes in supercapacitors.

On the other hand, the development of new systems, based in CNTs, which could overcome some of the current limitations in the capture of emerging pollutants in fluids, such as, nanometric particles–being, moreover, difficult to detect and organic pollutants at very low concentrations, is an additional objective of the present project.

This project focuses on the optimization of CNTs obtained by the same technology Hot Wire Plasma Chemical Vapor Deposition (HWCVD)) and water assisted-Chemical Vapor Deposition (WACVD) for specific applications in two of the main fields mentioned above: Energy and Environment.

Chapter 1- Introduction

This chapter provides a brief introduction of Nanoscience and Nanotechnology, carbon and about its allotropes. Carbon nanotubes history, properties and applications are explained. Moreover, this chapter

also deals with an introduction about supercapacitors, type of capacitance, and about their applications.

Chapter 2- Experimental techniques and setup

In this chapter, the introduction of plasma, sputtering, CVD and plasma enhanced chemical vapor deposition (PECVD) have been described. Growth mechanisms of CNTs by chemical vapor deposition (CVD) are explained. Different properties and applications are as well discussed. In the next part, details about the reactor used to perform the experiments for the deposition of thin films and CNTs have been written.

Chapter 3- Characterization techniques

This chapter is related to the basics and work principles of different characterization techniques. The characterization of thin films and CNTs involves various optical, spectroscopic and X-ray techniques.

Chapter 4- Growth of vertically-aligned multiwall carbon nanotubes (VAMWCNTs) by Hot Wire-PECVD and water plasma functionalization

In this chapter growth parameters and results of CNTs grown by hot-wire PECVD have been shown in details. In particular the different morphologies like multi-walled CNTs (MWCNTs) and vertically aligned CNTs (VACNTs) have been focused. Water plasma functionalization process of CNTs parameter has been optimized by Box-Wilson experiment design. Results of untreated and water plasma treated CNTs characterized by different microscopic, spectroscopic and X-ray techniques have been shown. The influence of oxygen functional groups after water plasma treatment for supercapacitor applications has been studied.

Chapter 5- Water plasma functionalized MWCNTs /MnO_2 composites for supercapacitor applications

In this chapter preparation of MWCNTs/MnO_2 composite electrode by anodic deposition of MnO_2 on the untreated and water plasma functionalized have been demonstrated. Composite electrodes MWCNTs/MnO_2 were characterized by field emission scanning electron microscopy (FESEM), Raman shift spectroscopy and X-ray photoelectron spectroscopy (XPS). The electrochemical properties of the

MWCNTs/MnO_2 for supercapacitor applications were investigated by cyclic voltammetry (CV), charge/discharge and electrochemical impedance spectroscopy (EIS). The influence of the voltage window on the change in the structure morphology of MnO_2 has been studied as well.

Chapter 6- Nitrogen plasma functionalization of VA MWCNTs for supercapacitor applications

This chapter provides a detailed study about nitrogen plasma functionalization of VAMWCNTs. FESEM, high resolution transmission electron microscopy (HRTEM), Raman and XPS techniques were performed to examine the change in morphology, structure and chemical state of the CNTs after the functionalization. The importance of various nitrogen based functional groups on the surface of CNTs has been explained in details.

Chapter 7- Study of CNTs structural evolution during water assisted growth and transfer methodology for electrochemical applications

This chapter is devoted to the water assisted CVD growth of CNTs. The influence of the growth time on the evolution of MWCNTs to single-walled CNTs (SWCNTs) has been described. FESEM, HRTEM, Raman, XPS and X-ray diffraction (XRD) were used to analyze the CNTs. Method to transfer of grown nanotubes on a conductive substrate exhibited. Electrochemical properties of transferred CNTs were studied by CV, EIS and charge/discharge measurements**.**

Chapter 8- Growth of CNTs on conductive substrates (carbon paper and copper)

This chapter discusses the growth of CNTs on the conductive substrate by (water assisted CVD (WA-CVD) and radiofrequency excited PECVD (RF-PECVD). The importance of pretreatment by hydrogen plasma of copper substrate and various intermediate layers between buffer layer (alumina) and copper substrate have been demonstrated. SEM, HRTEM and Raman were used for morphological and structural characterization respectively. Electrochemical properties of CNTs grown on copper were analyzed by using $LiClO_4$ as an electrolyte for supercapacitor applications.

Chapter 9- Growth and functionalization of VACNTS on quartz filter for environmental applications

This is the last chapter of the results. This chapter discloses the successful growth and functionalization of CNTs on quartz filter. SEM, HRTEM and Raman techniques were used to analyze the samples. Adsorption/desorption properties of chlorinated compounds through CNTs/Quartz filter (CNTsQF) were investigated by quadrupolar mass spectroscopy (QMS).

Contents

PART III- EXPERIMENTAL RESULTS

9.5. References - 269

PART IV- CONCLUSIONS 272

Appendix: List of deposited CNTs - 277

Publications: - - - - - - - - - - - - - - - - - - -

List of Figures

Figure 1.1: Technology and fundamental sciences meet on the nanoscale [3]. - - -

Figure 1.12: The CNTs (n, m) that are metallic and semiconducting, respectively denoted by open and solid circles on the map of chiral vectors (n, m) [16]. - 41

Figure 1.13: Forecast (2011-2016) for global CNTs market [35].- - - - - -46

Figure 1.14: Global CNTs market by industry [35]. - - - - - - - - - - - - - - -47

Figure 1.15: Trends in CNT research and commercialization. (A) Journal publications and issued worldwide patents per year, (B to E) Selected CNT related products: composite bicycle frame, antifouling coatings, printed electronics and electrostatic discharge shielding [36]. - - - - - - - - - - - - - 48

Figure 1.16: The process of production of CNT wire [36]. - - - - - - - - - -50

Figure 1.17: Sketch of Ragone plot for various energy storage and conversion devices. The indicated areas are rough guide lines [45]. - - - - 52

Figure 1.18: Taxonomy of supercapacitors [46]. - - - - - - - - - - - - - - - - - 53

Figure 2: Photograph of Ar plasma. - 59

Figure 2.1: Experimental set-up of an arc discharge apparatus [10]. - - - 73

Figure 2.2: Schematic drawing of a laser ablation apparatus [10]. - - - - -74

Figure 2.3: Schematic diagram of thermal CVD apparatus [10]. - - - - - - 75

Figure 2.4: Schematic diagram of a vapor phase growth apparatus [10]. - 77

Figure 2.5: (a) The classical VLS mechanism during SWCNT growth by metallic catalyst. (b) The supposed VS mechanism during SWCNT growth from SiO_2 nanoparticles as nucleation centers [17]. - - - - - - - - - - - - - - -78

Figure 2.6: Melting temperature of selected metals as a function of particle diameter [22]. -83

Figure 2.7: TEM image sequence showing a growing CNF in 3:1 NH_3:C_2H_2 at 1.3 mbar and 480 °C. The video was recorded at 30 frames/s, and the time of the respective stills is indicated. Drawings (lower row) indicate schematically the Ni catalyst deformation and C-Ni interface [31]. - 84

Figure 2.8: In-situ TEM image sequence showing a SWCNT nucleation and growth, and corresponding growth scheme [31]. - - - - - - - - - - - - - - 84

Figure 2.9: Schematic of growth model of bamboo-shaped CNTs in presence of nitrogen and hence CN at different plasma composition, depending on it occurs via surface diffusion (SD) and/or bulk diffusion (BD) of carbon species through catalyst particles [35]. - - - - - - - - - - - - -87

Figure 2.10: Typical defects in a SWCNT [38]. - - - - - - - - - - - - - - - - - - 89

Figure 2.11: Functionalization possibilities for SWNTs: A) defect-group functionalization, B) covalent sidewall functionalization, C) noncovalent exohedral functionalization with surfactants, D) noncovalent exohedral functionalization with polymers, and E) endohedral functionalization with, for example, C_{60} [38]. -89

Figure 2.12: Schematic figure of PEDRO. Several techniques can be used: PECVD, magnetron sputtering, RIE, and IBE. - - - - - - - - - - - - - - - - - - - 92

Figure 2.13: Plasma enhanced chemical vapour deposition (PECVD) reactor. -94

Figure 2.14: General representation of the structure of the double-layer [51]. -97

Figure 2.15: cyclic voltammogram. - 100

Figure 3.1: Resolving power of unaided eye versus light and electron microscopy [2]. - 109

Figure 3.2: Geometry of SEM [4]. - 113

Figure 3.3: Layout of optical components in basic TEM [9]. - - - - - - - 116

Figure 3.4: Vibrational and electronic energy-level diagram of a molecule showing the processes of IR absorption, Raman and Rayleigh scattering and fluorescence emission [10]. -119

Figure 3.5: Raman spectra from different types of sp^2 nanocarbons [12]. - 121

Figure 3.6: Schematic representation of the XPS process [14]. - - - - - - 123

Figure 3.7: Bragg´s law of diffraction. - 126

Figure 3.8: Characteristic line for hydrogen. - - - - - - - - - - - - - - - - - - - 129

Figure 3.9: Schematic figure of QMS [23]. - 131

Figure 3.10: The full electromagnetic spectrum [24]. - - - - - - - - - - - - - 132

Figure 4: Water plasma photographs (a) 75 W, 135 Pa, (b) 140 W, 135 Pa. - 137

Figure 4.1: HRTEM images of PECVD grown MWCNTs. - 140-141

Figure 4.2: Box-Wilson experimental design samples distribution for two main parameters (RF power and water pressure). - - - - - - - - - - - - - - - - -143

Figure 4.3: (a) OES spectra with low and high RF power at constant water pressure, (b) OES spectra at low and high water pressure at constant RF. - 145

Figure 4.4: FE-SEM images of MWCNTs before and after water plasma treatments; (a) untreated MWCNTs, (b) water plasma treated CNTs (75 W, 135 Pa) (c, d) water plasma treated at extreme conditions (140 W, 135 Pa). - 147

Figure 4.5: HRTEM images of (a, b) untreated samples of CNTs, (c, d) water plasma treated CNTs (75 W, 135 Pa), (e, f) water plasma treated CNTs (140 W,135 Pa). - 148

Figure 4.6: Raman spectra of untreated (a) and H_2O plasma treated CNTs under different conditions (b: 10 W, 1.35 mbar, c: 75 W, 1.35 mbar, d: 121 W, 0.5 mbar, e: 121 W, 2.2 mbar, f: 140 W, 1.35 mbar). - - - - - - - - - - -149

Figure 4.7: Influence of plasma power on the relative carbon and oxygen content of the samples. The solid lines are drawn to guide the eyes. - - - 152

Figure 4.8: (a) XPS spectra of untreated MWCNTs and (b) H_2O plasma treated MWCNTs at 140 W and 135 Pa. - 153

Figure 4.9: Percentage area of different carbon-carbon and carbon-oxygen bonds as a function of plasma power at a constant pressure of 50 Pa, obtained from the polynomial model (1).- 155

Figure 4.10: Showing the increase in hydrophilicity of the MWCNTs by the H_2O plasma treatment. Contact angle (a) Untreated sample (b) H_2O plasma treated with power 29 W and water pressure 50 Pa, (c) H_2O plasma treated with power 75W and water pressure135 Pa and (d) H_2O plasma treated with power 75W and water pressure 260 Pa. - - - - - - - - - - - - - -157

Figure 4.11: a) Interaction between power and pressure for decreasing the contact angle. (b) Pareto diagram of standardized effects of the different parameters A (RF power) and B (water pressure) on the H_2O treated CNTs. - 157-158

Figure 4.12: (a) CV of water plasma treated MWCNTs at a plasma power of 29 W and a water pressure 220 Pa applying different scan rates (10, 20, 30, 40, 50, 100 and 150 mVs^{-1}) and peak current versus square root of the scan rate (inset graph). (b) Comparison between the cyclic voltammograms of untreated and water plasma treated CNTs at a scan rate of 50 mVs^{-1}.- 159

Figure 4.13: cyclic voltammograms at different scan rates (10, 20, 30, 40, 50, 100 and 150 mVs^{-1}), (a) Untreated CNTs, (b) H_2O treated CNTs. - 160

Figure 5: Image of MnO_2 nanoflowers deposited on CNTs. - - - - - - - - 167

Figure 5.1: Box-Wilson experimental design samples distribution for two main parameters (RF power and water pressure). - - - - - - - - - - - - - - - - -170

Figure 5.2: Schematic diagram of the electrolytic cell for deposition of manganese oxide [16]. - 171

Figure 5.3: SEM images of untreated CNTs (a) and wpCNTs (b). Inset graphs show top view of the CNTs mat. -172

Figure 5.4: SEM images of wpCNTs/MnO_2 before electrochemical cycling (a), wpCNTs/MnO_2 after electrochemical cycling (0-1V) (b), and wpCNTs/MnO_2 after electrochemical cycling (0.1–0.8 V) (c). Inset graphs show top view of the CNTs mat. -173

Figure 5.5: Raman spectra of (A) wpCNTs/MnO_2 (75W, 135 Pa) before cycling, (B) wpCNTs/MnO_2 (75W, 135 Pa) after 2000 cycles (between 0-1V), and (C) wpCNTs/MnO_2 (75W, 135 Pa) after 2000 cycles (between 0.1–0.8 V). Inset figure shows Raman spectra of (D) untreated CNTs and (E) wpCNTs (75W, 135 Pa). - 175

Figure 5.6: XPS spectra of (a) Mn 2p and (b) O1s, (A) wpCNTs/MnO_2 (75W, 135 Pa) before cycling (B) wpCNTs/MnO_2 (75W, 135 Pa) after 2000 cycles (between 0-1V), and (C) wpCNTs/MnO_2 (75W, 135 Pa) after 2000 cycles (between 0.1–0.8 V). -176

Figure 5.7: (a) Cyclic voltammograms obtained at a scan rate of $10mVs^{-1}$ for untreated MWCNTs/MnO_2 and wpCNTs/MnO_2 under different plasma conditions ((a): untreated, (b): 75W, 135 Pa, (c): 140 W, 135 Pa, (d): 10 W, 135 Pa). (b) Cyclic voltammograms of nanocomposite wpCNTs/MnO_2 (10 W, 135 Pa) at different scan rates, 10, 20, 30, 40, 50, 100, and 150 mVs^{-1}. - 179

Figure 5.8: 3-dimensional graph of the specific capacitance of water plasma-treated CNTs/MnO_2 electrodes with respect to rf-power and water pressure. -180

Figure 5.9: Nyquist plot of untreated and different wpCNTs/MnO_2 samples. Asterisks correspond to a frequency of 9.32 Hz. - - - - - - - - - - -181

Figure 5.10: (a) Charge/discharge curves at different current densities from1.75, 0.70, 0.52, and 0.35 $mAcm^{-2}$, as indicated by the arrow, for wpCNTs/MnO_2 (75 W, 135 Pa). (b) Galvanostatic charge/discharge cyclic stability in the 0.1–0.8 V potential. - 182

Figure 5.11: (a) Charge/discharge curves obtained at different current densities from 0.1, 0.2, 0.3, 0.4 mAcm^{-2}, as indicated by the arrow for wpCNTs/MnO$_2$ (10 W, 135 Pa) and (b) charge/discharge cyclic stability between 0 and 1 V for untreated and water plasma treated CNTs/MnO$_2$ electrodes. -184

Figure 6: Nitrogen plasma photographs at (a) 29 W, 50 Pa (b) 75 W, 10 Pa. -189

Figure 6.1: Box-Wilson experimental design samples distribution for two main parameters (RF power and nitrogen pressure). - - - - - - - - - - - - - -191

Figure 6.2: FE-SEM images of (a) untreated CNTs, (b) nitrogen plasma treated. HRTEM images of (c) nitrogen-plasma treated CNTs at 75 W plasma power, 260 Pa nitrogen pressure and (d) nitrogen-plasma treated CNTs at 10 W plasma power, 135 Pa nitrogen pressure. - - - - - - - - - - 192

Figure 6.3: Relative contents of nitrogen and oxygen at a constant plasma power of 75 W against nitrogen pressure obtained from the polynomial model (see (6.1)). -193

Figure 6.4: (a, c) High resolution deconvoluted C1s and N1s spectra, respectively, of untreated MWCNTs. (b, d) high resolution deconvoluted C1s and N1s spectra, respectively, of nitrogen-plasma treated MWCNTs. Red and blue curves correspond to experimental data and obtained fitting, respectively. - 194

Figure 6.5: Nitrogen concentrations at a constant power of 75 W against nitrogen pressure, obtained from the polynomial model (see (6.1)). - 197

Figure 6.6: (a) Raman spectra of several samples obtained at different conditions of nitrogen plasma treatment. (b) Variation in the wavenumber of D and G peaks with respect to the disorder, (c) Structural disorder with respect to the nitrogen concentration. The solid lines are drawn to guide the eyes. -198

Figure 6.7: (a) CV of nitrogen plasma treated MWCNTs at a plasma power of 29 W and a nitrogen pressure 50 Pa applying different scan rates (10, 20, 30, 40, 50, 100 and 150 mVs^{-1}) and peak current versus square root of the scan rate (inset graph). (b) Comparison between the cyclic voltammograms of untreated and nitrogen plasma treated CNTs at a scan rate of 50 mVs^{-1}. - 200

Figure 6.8: (a) Comparison of the cyclic voltammograms obtained at a scan rate of 10 mVs^{-1} for untreated MWCNTs, NPCNTS, and NPCNTs/MnO_2. (c) Cyclic voltammograms of nanocomposite NPCNTs/MnO_2 at different scan rates; 10, 20, 30, 40, 50, 100 and 150 mVs^{-1}. - 203

Figure 7: Image and photograph of ultralong CNTs. - - - - - - - - - - - - - - 210

Figure 7.1: Transfer procedure of WA-CNTs from Si wafer to the sided adhesive conductive Aluminum tape and preparation of the transferred CNTs for the plasma treatment. - 215

Figure 7.2: SEM images of different thickness catalyst layers annealed at different temperatures. - 217

Figure 7.3: SEM images of samples A (a, b), B (c, d) and C (e, f). Side (a, c, d) and top (b, d, e) views. -218

Figure 7.4: TEM images of sample A (a) and C (b). Arrow signs indicate amorphous carbon and structural defects for sample A and C, respectively. - 219

Figure 7.5: Raman spectra of samples A, B and C in three different frequency regions. Graphs in the middle column show the peaks obtained from the fitting process. -221

Figure 7.6: Comparison of various Raman properties. - - - - - - - - - - - - -222

Figure 7.7: XPS survey scan of samples A, B and C. Inset shows high resolution spectra of C1s. - 223

Figure 7.8: XRD spectra of samples A, B and C. - - - - - - - - - - - - - - - - 225

Figure 7.9: SEM images of transferred CNTs on the adhesive tape and EDS spectra of untreated and water plasma treated CNTs. - - - - - - - - - 226

Figure 7.10: Raman spectra of transferred CNTs on Al tape and water plasma treated CNTs/Al. -227

Figure 7.11: CV comparison of untreated CNTs/Al and wp-treated CNTs/Al, (b) CVs of wp CNTs/Al at various scan rates 10, 20, 30, 40, 50, 100, 150 mVs^{-1}, (c) specific capacitance comparison of untreated and water plasma treated CNTs/Al at different scan rates.- - - - - - - - - - - - - - 228-229

Figure 7.12: (a) Galvanostatic charge discharges cyclic stability in the 0.0-0.9 V potential range, (b) Nyquist plot of untreated and water plasma treated CNTs/Al. - 230

Figure 8: Images of water assisted grown CNTs on carbon paper. - 236

Figure 8.1: (a) Sample A, (b) sample (B), (c) sample (d) (see table 8.1). - 240

Figure 8.2: Optical emission spectroscopy of hydrogen plasma reduction of copper at different times. (a) 1 min, (b) 3 min, (c) 5 min, (d) 9 min and (e) 10 min. - 243

Figure 8.3: SEM images of samples (A, B, C, D and nitrogen plasma treated sample D (E)) - 244

Figure 8.4: Raman spectra of sample D before and after nitrogen plasma treatment. - 246

Figure 8.5: (a) comparison of specific capacitance, (b) cyclic voltammograms at 10, 50, 100 and 150 mVs^{-1}. - - - - - - - - - - - - - - - - - - 247

Figure 8.6: Nyquist plot for untreated and nitrogen plasma treated CNTs. - 249

Figure 8.7: Galvanostatic charge/discharge curves (a) untreated CNTs, (b) nitrogen plasma treated CNTs. - 250

Figure 8.8: Charge/discharge cyclic stability. - - - - - - - - - - - - - - - - - -252

Figure 9.1: Experimental set-up to measure adsorption of VOCs. A) filter holder, B) flow valve, C) manual valve, D) flask containing VOC, E) pneumatic valve, F) RGA input. -260

Figure 9.2: SEM images of CNTs grown on quartz filter (a) at 700ºC for 15 min and (b) at 730ºC for 30 min. (c) WP-treated CNTsQF at 10 W plasma power and 135 Pa pressure. -260

Figure 9.3: HRTEM image of untreated CNTs on quartz filter. - - - - - -263

Figure 9.4: Raman spectra of untreated CNTsQF and WP-CNTsQF. - 264

Figure 9.5: Comparative desorption study. Desorption process of (a) trichloroethylene, (b) chloroform and (c) 1,2-dichlorobenzene. Squares: QF, triangles: CNTsQF and circles: WPCNTsQF. - - - - - - - - - - - - - - -266

List of Tables

PART I - INTRODUCTION

Chapter 1
Introduction

Chapter 1: Introduction

1.1. Nanoscience and Nanotechnology

Nanoscience is the study of phenomena and manipulation of materials at atomic, molecular and macromolecular scales, where properties differ significantly from those at a larger scale. Nanotechnologies are the design, characterization, production and application of structures, devices and systems by controlling shape and size at nanometer scale.

The recent development of nanoscience and nanotechnology has opened up novel fundamental and applied frontiers in materials science and engineering. The concept of nanotechnology was first introduced by Nobel laureate Richard Feynman in December 29, 1959, at the annual meeting of the American Physical Society at the California Institute of Technology (Caltech). In his classic lecture entitled: "There is a plenty room at the bottom", Feynman stated, "The principles of physics, as far as I can see, do not speak against the possibility of maneuvering things atom by atom". Later, NoRio Taniguchi from the Tokyo Science University first defined the nanotechnology as: (1) the creation of useful materials, devices, and systems through the control matter at the nanometer (10^{-9} m) length scale and (2) the exploitation of novel properties and phenomena developed at that scale. The main breakthrough in nanotechnology occurred in 1981 when Binnig and Rohrer at IBM Zurich invented the scanning tunneling microscope (STM) the first instrument to generate real space images of surfaces with atomic resolution [1].

Small structure can be manufactured by possibly using one of these two ways (1) bottom up approach and (2) top down approach. In the first approach individual atoms and/or molecules can be precisely placed where they are needed by scanning probe microscopy (e.g. AFM, STM, optical tweezers) or self-assembling. The second approach macro-scale systems are converted into nanoscale ones by a series of sequential reduction operations to remove the unwanted portions away from the object that is wanted. The smallest features that can be created by the "top down" approach depend on the tools used and the system operator's experience and skills.

At the nanoscale dimensions the properties of the materials change such as energy due to quantum effects. As the size decreases, the ratio of the surface atoms increases. These high energy surface atoms are very

reactive. Due to the high surface-to-volume ratio associated with nanometer-sized materials, therefore, a tremendous improvement in chemical properties is also achievable through a reduction in size. A nanomaterial is an object that has at least one dimension in nanometer scale (approximately 1 to 100 nm) [2]. Nanoscience and nanotechnology is the meeting ground where today's industrial needs converge with fundamental sciences involving the mesoscale between atomistic and phenomenological theories. Nanoscience research, starting from physics, chemistry and biology, is expected to lead to a better understanding of nature. Technologies that could benefit from the nanoscale are manifold. They are situated in electronics, biotechnology, pharmaceuticals, and energy related disciplines (figure 1.1).

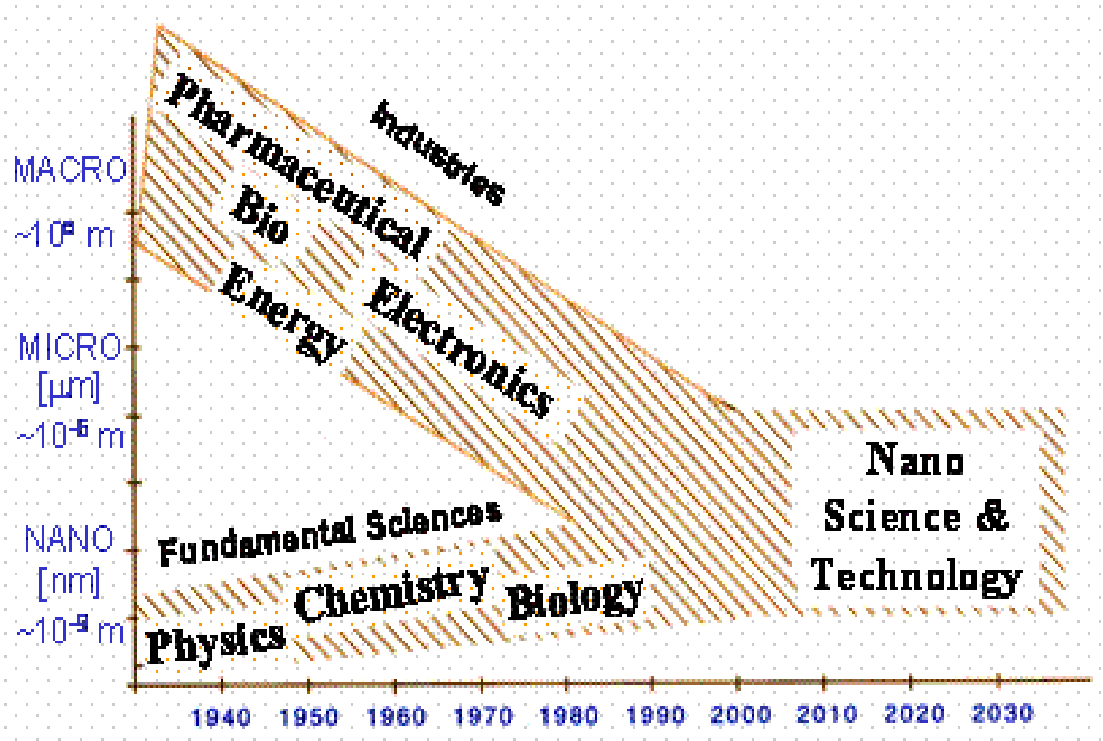

Figure 1.1: Technology and fundamental sciences meet on the nanoscale [3].

1.2. Carbon

Carbon is the sixth element of the periodic table. Carbon based materials, clusters and molecules are unique in many ways. One distinction

relates to the many possible configurations of the electronic states of a carbon atom, which is known as the hybridization of atomic orbitals. Each carbon atom has six electrons which occupy $1s^2$, $2s^2$, and $2p^2$ atomic orbitals, making carbon the first element in Group IV. The $1s^2$ orbital contains two strongly bound electrons, and they are called core electrons. Four electrons occupy the $2s^2$ $2p^2$ orbitals, and these more weakly bound electrons are called valence electrons. In the crystalline phase the valence electrons give rise to 2s, 2px, 2py, and 2pz orbitals which are important in forming covalent bonds in carbon materials. Since the energy difference between upper 2p energy levels and the lower 2s level in carbon is small compared with the binding energy of the chemical bonds, the electron wave functions for these four electrons can readily mix with each other, thereby changing the occupation of the 2s and three 2p atomic orbitals so as to enhance the binding energy of the C atom with its neighboring atoms. This mixing of 2s and 2p atomic orbitals is called hybridization, whereas the mixing of a single 2s electron with n =1, 2, 3 electrons is called sp^n hybridization.

In carbon, three possible hybridizations occur: *sp*, sp^2, and sp^3; other group IV elements such as Si, Ge exhibit primarily sp^3 hybridization. Carbon differs from Si and Ge insofar as carbon does not have inner atomic orbitals except for the spherical 1s orbitals, and the absence of nearby inner orbitals facilitates hybridization involving only valence s and p orbitals from carbon [4]. (Figure 1.2) shows schematic image of *sp*, sp^2 and sp^3 hybridization.

The sp^3 hybridization corresponds to the well-known tetrahedral configuration in which carbon binds to 4 neighbors giving rise to three-dimensional interconnectivity of carbon atoms that is found in diamond. The sp^2 bonding in which carbon atoms bind to 3 neighbor's also known as trigonal hybridization gives planer structures found in graphite and graphene. Diagonal or sp^1 hybridization that gives linear molecules in which carbon binds to only 2 neighbors is found in polyyne chains.

Carbon exists in three forms: graphite, amorphous carbon and diamond. Depending on how the carbon atoms are arranged, their properties vary. For example, the most common form of carbon, graphite, is soft, black, and stable. In graphite, the carbon atoms are located at the corners of regular and fused hexagons arranged in parallel layers and its density is 2.26 g/cm^3. However, diamond is hard and transparent due to its regular repetitive

pattern where each carbon atom is bound to four other carbon atoms and its density of 3.51 g/cm^3 is greater than that of graphite. They are constituted by carbon atoms bonded by sp^2, sp^3 and combinations of both hybridizations. There exists another configuration of carbon: the polymer-like form. It is found when carbon is diluted with hydrogen, and it presents low hardness, high transparency and electrically it behaves as an electric insulator.

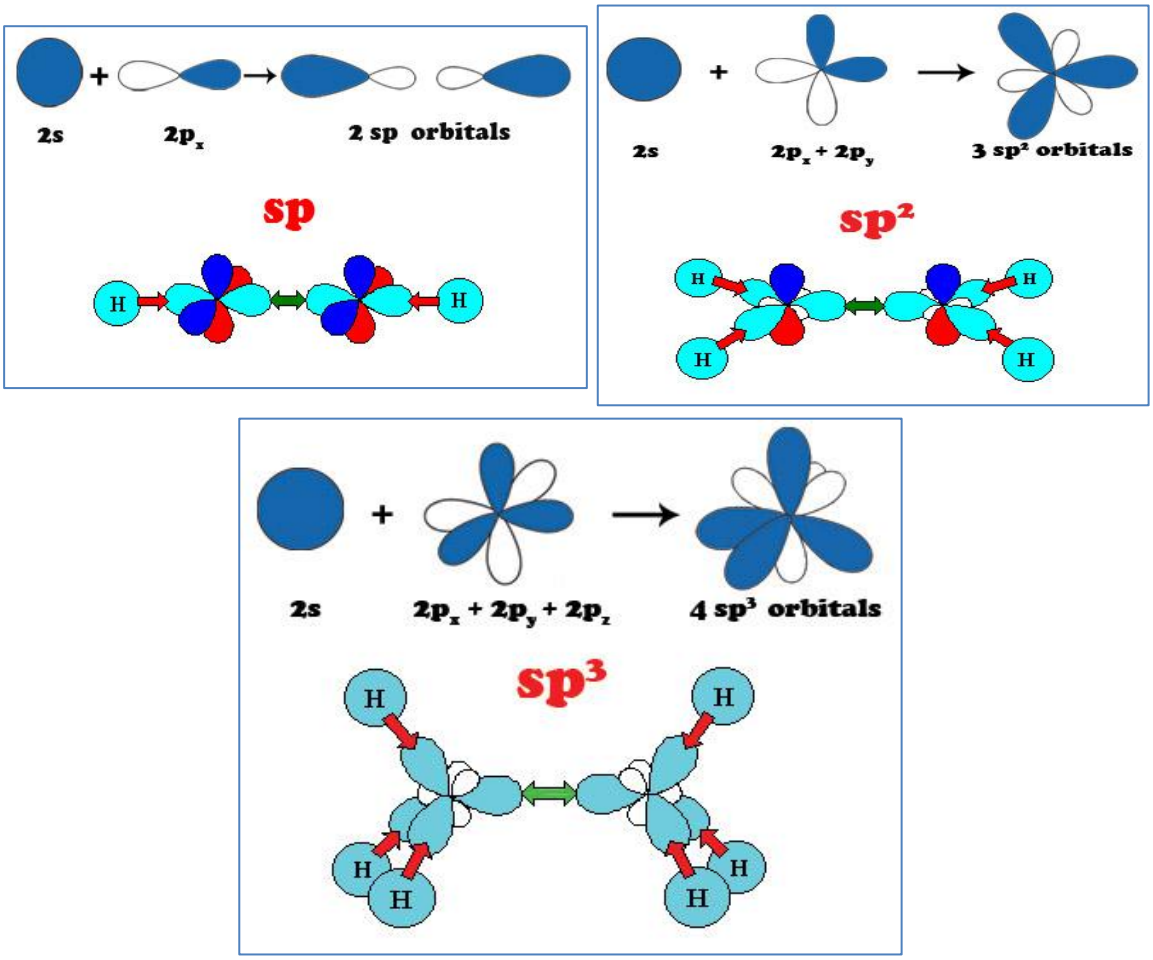

Figure 1.2: Schematic hybridization of carbon [47].

The commonest crystalline forms of carbon are cubic diamond and hexagonal graphite. To these must be added carbynes and Fullerenes, both of which are crystalline carbon forms. Fullerenes are sometimes referred to as the third allotrope of carbon. However, since fullerenes were discovered more recently than carbynes, they are chronologically the fourth crystalline allotrope of carbon [5]. Consequently, carbynes have not been as extensively characterized as other forms of carbon. The structures and

chemical bonding of these crystalline forms of carbon are reviewed in this section.

1.3. Diamond

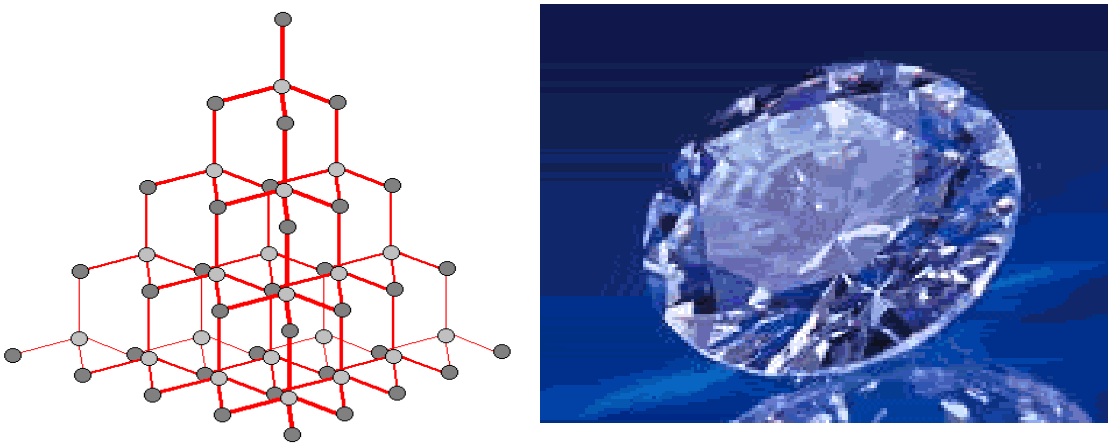

Figure 1.3: Schematic image of diamond lattice and image of diamond.

Diamonds are probably the most well-known allotrope of carbon. The carbon atoms are arranged in a diamond lattice, which is a variation of the face-centered cubic crystal structure. It has superlative physical qualities, most of which originate from the strong covalent bonding between its atoms. Each carbon atom in a diamond is covalently bonded to four other carbons in a tetrahedron (figure 1.3). These tetrahedrons together form a three-dimensional network of six-membered carbon rings in the chair conformation, allowing for zero bond-angle strain. The C-C bond sp^3 is 0.154 nm long, which is a bit longer and weaker than that in graphite sp^2, and its crystallographic structure consists of two superimposed face-centered cubic (f.c.c.) lattices shifted by one-quarter of the cube diagonal. This stable network of covalent bonds and hexagonal rings is the reason that diamond is so incredibly strong. As a result, diamond exhibits the highest hardness and thermal conductivity of any bulk material. In addition, its rigid lattice prevents contamination by many elements. The surface of diamond is lipophilic and hydrophobic, which means it cannot be wet by water but can be by oil. Diamonds do not generally react with any chemical reagents, including strong acids and bases. Uses of diamond include in cutting, drilling, and grinding; in jewelry; and in the semi-conductor industry. Natural and synthetic diamonds contain various impurities.

Nitrogen and boron are found as substitutional impurity atoms in the crystal lattice.

1.4. Graphite

Graphite has a layered, planar structure (figure 1.4). In each layer, the carbon atoms are arranged in a hexagonal lattice with separation of 0.142 nm, and the distance between planes is 0.34 nm. The basis of the crystal structure of graphite is the graphene plane or carbon layer plane, i.e., an extended hexagonal array of carbon atom with sp^2 σ bonding and delocalized π bonding. The commonest crystal form of graphite is hexagonal and consists of a stack of layer planes in the stacking sequence ABABAB (figure 1.4). The graphene layers often do not stack perfectly forming the perfect graphite crystal structure with perfect Bernal 'ABAB' layer stacking. Instead, stacking faults are often formed (meaning departures from the ABAB stacking order). These stacking faults give rise to a small increase in the interlayer distance from the value 0.3354 in 3D graphite until a value of about 0.3440 nm is reached, at which interplanar distance, the stacking of the individual carbon layers become uncorrelated with essentially no site bonding between the carbon atoms in the two layers. The resulting structure of these uncorrelated 2D graphene layers is called *turbostratic graphite [6]*. The large interlayer spacing suggests that the contribution to interlayer bonding from π bond overlap is negligible. The usual assumption has been that interlayer potentials are of the van der der Waals type. The two known forms of graphite, *alpha* (hexagonal) and *beta* (rhombohedral), have very similar physical properties (except that the graphene layers stack slightly differently). The hexagonal graphite may be either flat or buckled. The alpha form can be converted to the beta form through mechanical treatment, and the beta form reverts to the alpha form when it is heated above 1300 °C. Graphite can conduct electricity due to the vast electron delocalization within the carbon layers; as the electrons are free to move, electricity moves through the plane of the layers. Graphite also has self-lubricating and dry lubricating properties. Graphite has applications in prosthetic blood-containing materials and heat-resistant materials as it can resist temperatures up to 3000 °C.

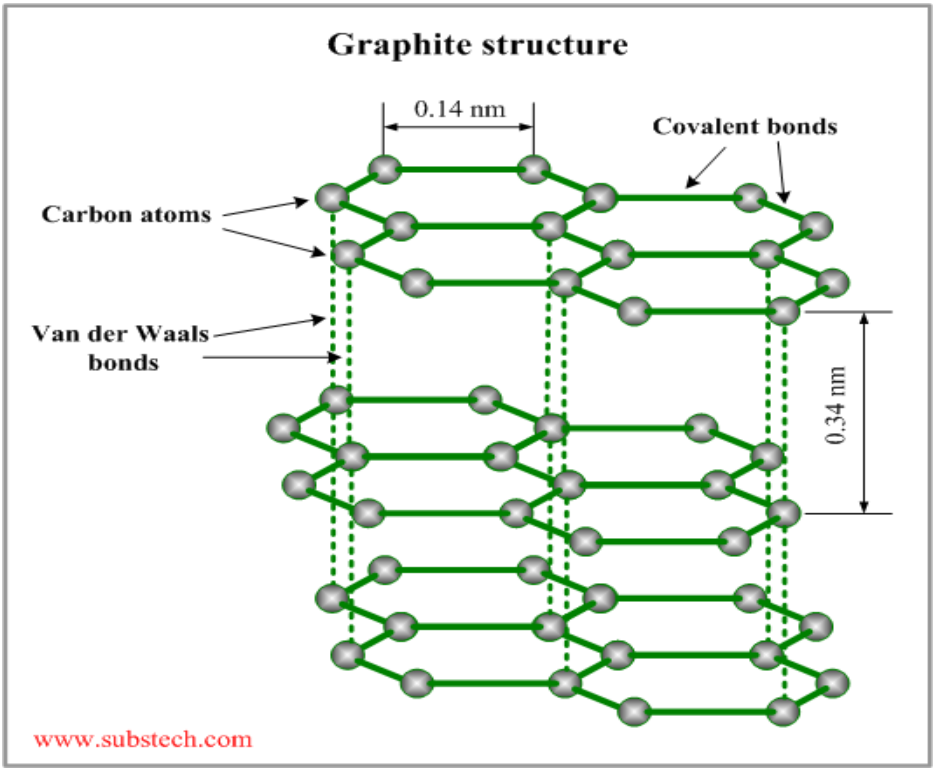

Figure 1.4: Crystalline structure of graphite.

The most commonly used high-quality graphitic material today is *Highly Oriented Pyrolytic Graphite* (HOPG), which is prepared by the pyrolysis of hydrocarbons at temperatures of above 2000 °C and the resulting pyrolytic carbon is subsequently heat treated to higher temperatures to improve its crystalline order. Single layer of graphite is called graphene. This material displays extraordinary electrical, thermal, and physical properties. It is an allotrope of carbon whose structure is a single planar sheet of sp^2 bonded carbon atoms that are densely packed in a honeycomb crystal lattice. The carbon-carbon bond length in graphene is ~0.142 nm, and these sheets stack to form graphite with an interplanar spacing of 0.34 nm. Graphene is the basic structural element of other carbon allotropes such as graphite, charcoal, carbon nanotubes, and fullerenes. Graphene is a semi-metal or zero-gap semiconductor, allowing it to display high electron mobility at room temperature. Graphene is an exciting new class of material whose unique properties make it the subject of ongoing research in many laboratories [5].

1.5. Amorphous carbon

Amorphous carbon refers to carbon that does not have a crystalline structure. Even though amorphous carbon can be manufactured, there still exist some microscopic crystals of graphite-like or diamond-like carbon. The properties of amorphous carbon depend on the ratio of sp^2 to sp^3 hybridized bonds present in the material. Graphite consists purely of sp^2 hybridized bonds, whereas diamond consists purely of sp^3 hybridized bonds. Materials that are high in sp^3 hybridized bonds are referred to as tetrahedral amorphous carbon (owing to the tetrahedral shape formed by sp^3 hybridized bonds) or as diamond-like carbon (owing to the similarity of many of its physical properties to those of diamond).

1.6. Fullerenes

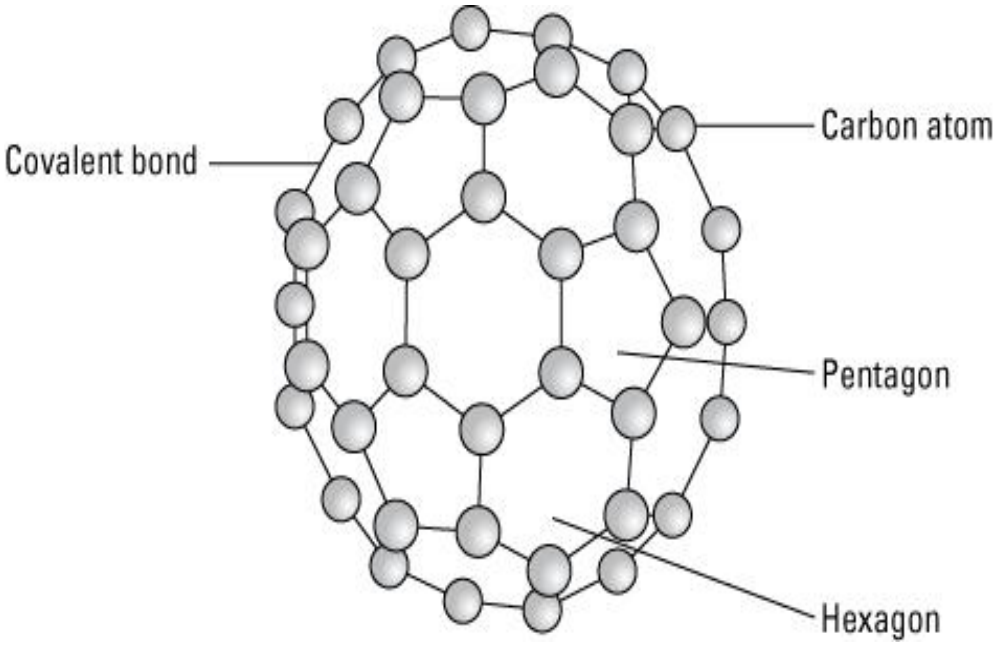

Figure 1.5: Fullerene molecule

Fullerene is unique in the larger family of carbon-based materials as interrelated prototypes for zero-dimensional quantum dots. The fullerene molecule is the fundamental building block of the crystalline phase, and through doping and chemical reactions, forms the basis of a large family of materials, many having especially interesting properties. Likewise, carbon nanotubes, which are capped at each end by half of a fullerene, have

aroused great interest in the research community because of their exotic electrical and mechanical properties. The C_{60}, molecule, Buckminsterfullerene, was discovered in the mass spectrum of laser-ablated graphite in 1985 and crystals of C_{60} were first isolated from soot formed from graphite arc electrodes in 1990. Although these events are relatively recent, the C_{60} molecule has become one of the most widely-recognized molecular structures in science and in 1996 the co-discoverers Curl, Kroto and Smalley were awarded the Nobel Prize for chemistry.

The C_{60} molecule contains 12 pentagons and 20 hexagons (figure 1.5). In the C_{60} molecule each carbon atom is bonded to three others by two longer bonds (length 0.145 nm) and one shorter bond (bond length 0.14 nm). These are conventionally referred to in the Fullerene literature as two C-C single bonds and one C=C. double bond. The double bonds lie between two hexagons and are therefore known as 6:6 bonds whereas the single bonds link a hexagon to a pentagon and are known as 6:5 bonds. It follows that there is bonding anisotropy in the C_{60} molecule since bonds around a pentagon are all single bonds and bonds around a hexagon are alternately single bonds and double bonds. It appears therefore that the bonding in C_{60} is mainly sp^2 with delocalized π electrons, but with some sp^3 character resulting from curvature of the C-C bonds [5].

1.7. The phase and transition diagram of carbon

Elucidation of the phase relationships between the different forms of carbon is a difficult field of study because of the very high temperatures and pressures that must be applied. However, the subject is one of great technical importance because of the need to understand methods for transforming graphite and disordered forms of carbon into diamond. The diagram has been shown in (figure 1.6) [7].

1.8. Carbon nanotubes (CNTs)

The ability to generate fullerenes in gram quantities in the laboratory, using a relatively simple apparatus, gave rise to intense research activity on these molecules and caused a renaissance in the study of carbon. Iijima observed, in 1991, that nanotubules of graphite were deposited on the negative electrode during the direct current arcing of graphite for the preparation of fullerenes. These nanotubes are concentric graphitic cylinders closed at either end due to the presence of five-membered rings

[8]. Nanotubes can be multi-walled with a central tubule of nanometric diameter surrounded by graphitic layers separated by ~ 0.34 nm. Unlike in multiwalled nanotubes (MWNTs), in single-walled nanotubes (SWNTs), there is only the tubule and no graphitic layers. CNTs possess significantly different properties compared with diamond and graphite. CNTs are low dimensional nanomaterials having critical size about 10000 times thinner than human hair. The typical diameter of nanotubes ranges from about 1 to 100 nm. A conceptual diagram is shown in (figure 1.7).

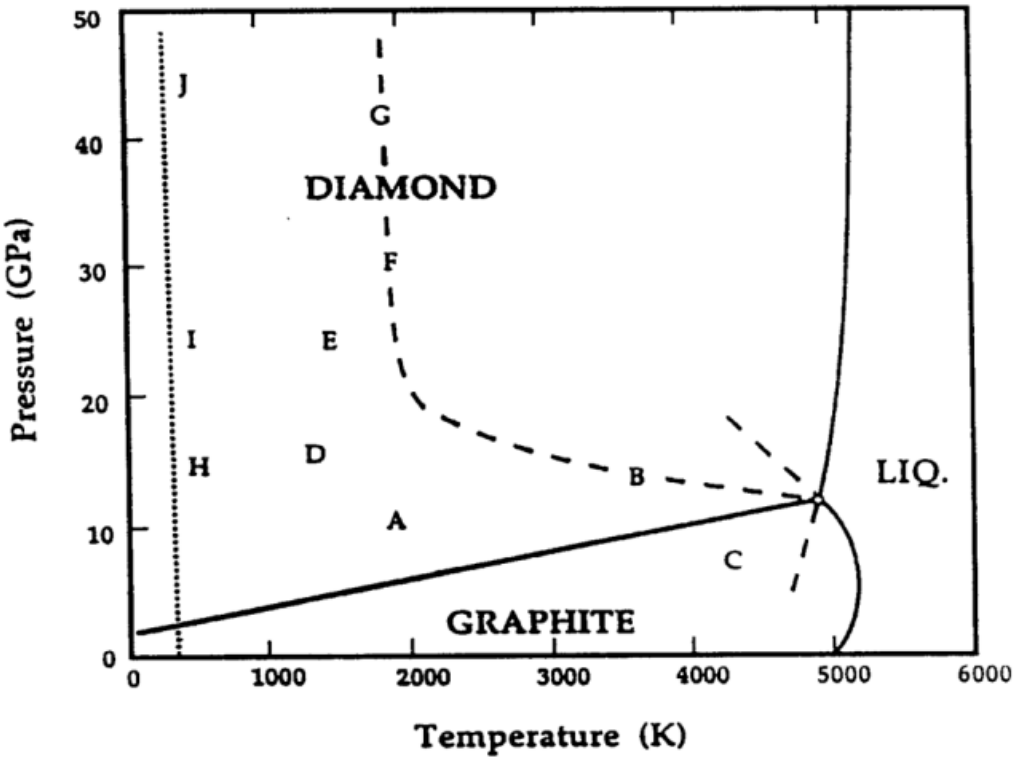

Figure 1.6: A version of the phase diagram of carbon. *Solid lines* represent equilibrium phase boundaries. A: commercial synthesis of diamond from graphite by catalysis; B: rapid solid phase graphite to diamond synthesis; C: fast transformation of diamond to graphite; D: hexagonal graphite to hexagonal diamond synthesis; E: shock compression graphite to hexagonal diamond synthesis; F: shock compression graphite to cubic-type diamond synthesis; B, F,G: graphite or hexagonal diamond to cubic diamond synthesis; H, I, J: compressed graphite acquires diamond-like properties, but reverts to graphite upon release of pressure [7].

1.8.1. History of Carbon nanotubes

Natural deposits of CNTs may well exist in some as yet undiscovered locations. However, these locations have not been found. Historically (late 1800s), carbon fibers have synthesis and used as filaments in the incandescent light bulb were replaced by tungsten by 1910. With the development of the electron microscopy in the 1930s, scientists have a new technique, extremely useful to study the structure of materials at a very fine scale. In 1952, Russian scientists reported intriguing transmission electron microscope (TEM) images of filamental carbon structures synthesized from iron-catalyzed decomposition of carbon monoxide at temperatures in the range of 400-700 °C. They recognized the catalytic properties of iron in facilitating the growth of tubular carbon, and also discussed the initial formation of iron carbide at the base of the tubes followed by the subsequent growth of carbon filaments, a theory which is widely accepted today. A year later British material researchers also announced similar filamental formation in the presence of iron. In 1955, Hoffer et al. stated carbon filaments could be synthesized as well by using either cobalt or nickel [10].

A major breakthrough occurred in 1985 with the experimental discovery of a zero-dimensional (relatively speaking, compared with larger forms of carbon) allotrope of carbon named C60 (buckyball). This discovery renewed focus on low-dimensional crystalline allotropes of carbon, and speculation about the possibility of SWCNTs. In 1991 accidentally Ijima noticed elongated hollow structures in carbon soot which were MWCNTs, including double-wall nanotubes (figure 1.8) [11].

This extends the run of accidental discoveries related to low-dimensional carbon allotropes. The observation immediately had a high impact, in part due to the broad dissemination that comes with a widely circulating journal. The actual experimental discovery of nanotubes with single walls occurred in 1993 in back to back articles by two separate groups [8, 12]. After 1991, considerable attention of scientists to carbon nanotubes (CNTs) caused remarkable increase of publication around carbon nanotube related subjects of interests (figure 1.9).

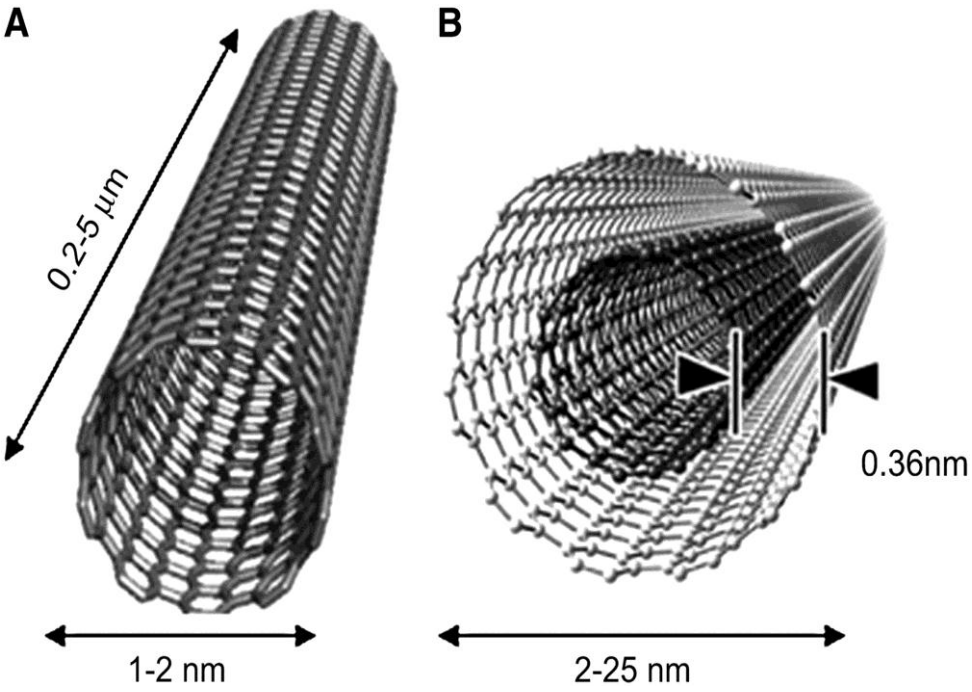

Figure 1.7: Conceptual diagram of single-walled carbon nanotube (SWCNT) (A) and multiwall carbon nanotube (MWCNT) [9].

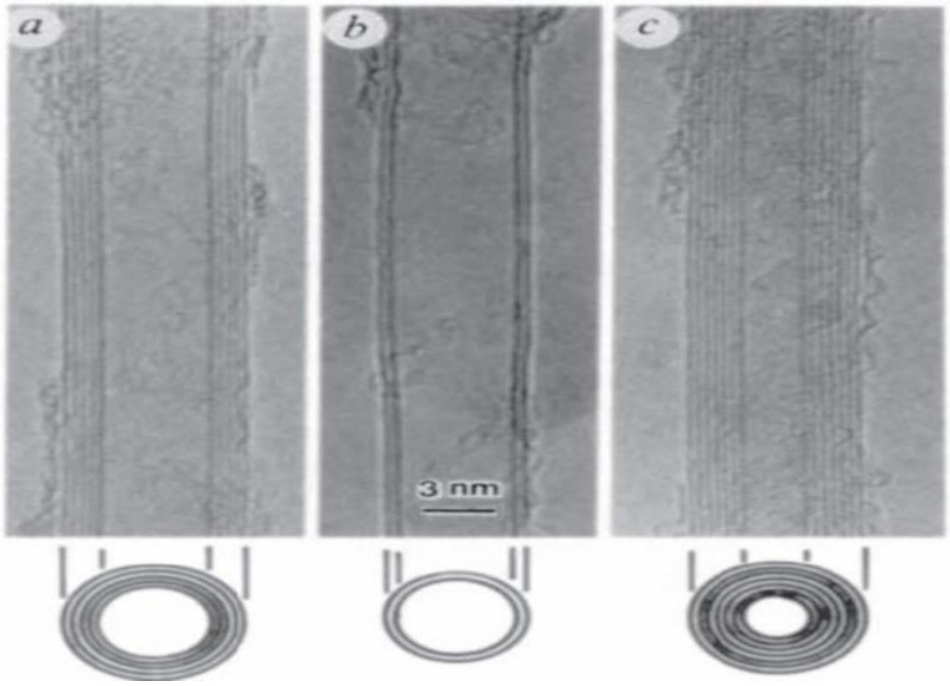

Figure 1.8: TEM micrographs of carbon nanotubes [11].

Increasing the number of publications from 77 in 1995 to 5619 in 2010 and total number of 37112 publications until the end of 2010, all shows that there are some interesting points in carbon nanotubes which led to this enormous attention of researchers [13]. The minimum diameter of a stable freestanding SWNT is limited by curvature-induced strain to ~0.4 nm.

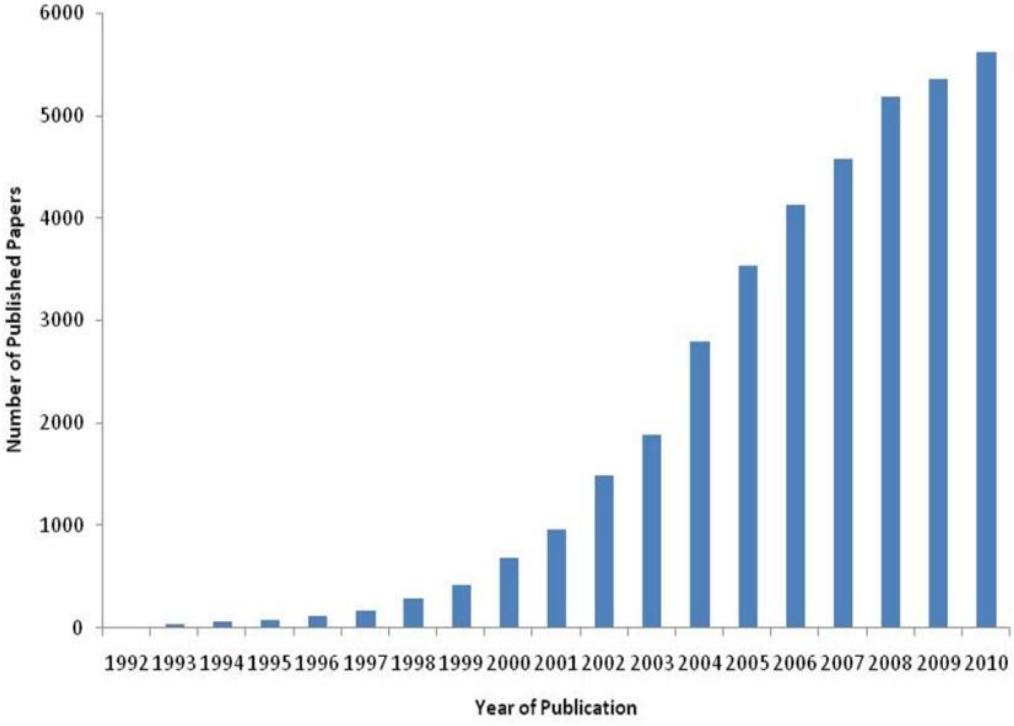

Figure 1.9: The annual number of published papers on carbon nanotubes since their discovery until the end of 2010 [13].

CNTs possess significantly different properties compared with diamond and graphite. At the rate Moore's Law is progressing, by 2019 it will result in transistor just a few atoms in width. This means that the strategy of ever finer photolithography will have run its course; we have already seen a progression from a micron, to sub-micron to 45 nm scale. Carbon nanotubes, whose walls are just 1 atom thick, with diameters of only 1 to 2 nm, seem to be one of the perfect candidates to take us right to the end of Moore's Law curve. We possibly cannot go beyond that. So, certainly, carbon nanotubes have a promising future [14].

1.8.2. Definition of CNT

A single-wall carbon nanotube can be described as a graphene sheet rolled into a cylindrical shape so that the structure has one-dimensional axial symmetry, and in general exhibits a spiral conformation, called chirality.

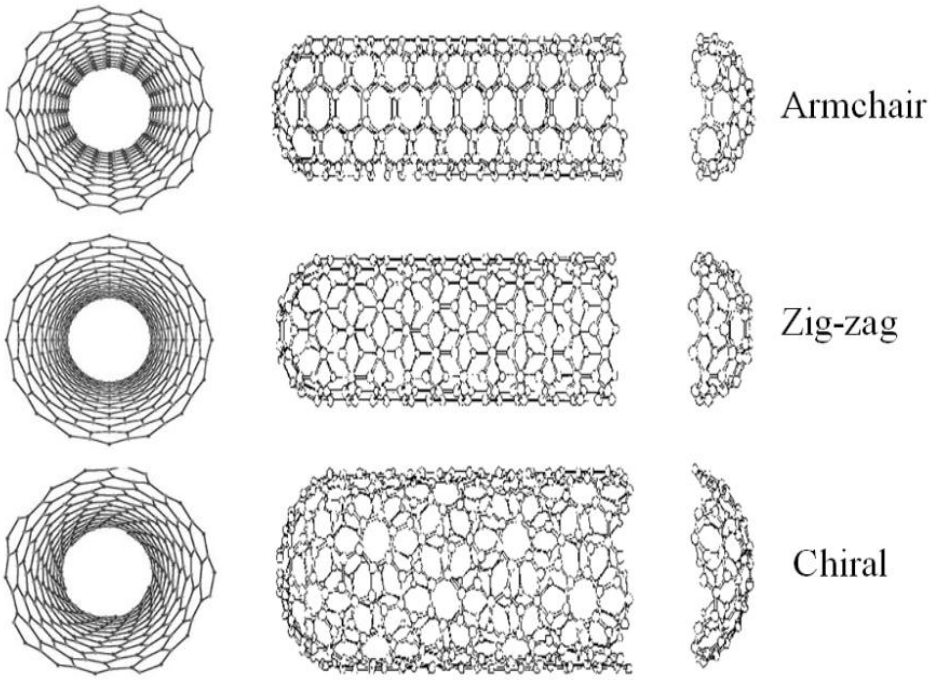

Figure 1.10: Classification of carbon nanotubes: (a) armchair, (b) zigzag, and (c) chiral nanotubes.

CNT is the orientation of six-membered carbon rings (hexagon) in a honeycomb lattice relative to the axis of the nanotube. The terminations of the nanotubes often called caps or end caps consist of a hemisphere of a fullerene. Each cap contains six pentagons and an appropriate number and placement of hexagons that are selected and fit perfectly to the long cylindrical section. Multi Walled Nanotubes (MWNT) can be considered as a collection of concentric SWNTs with different diameters. The length and diameter of these structures differ a lot from those of SWNTs and, of course, their properties are also very different.

The primary symmetry classification of a CNT is as either being achiral (armchair and zigzag) or chiral shown in (figure 1.10).

1.8.3. Chiral vector: C_h

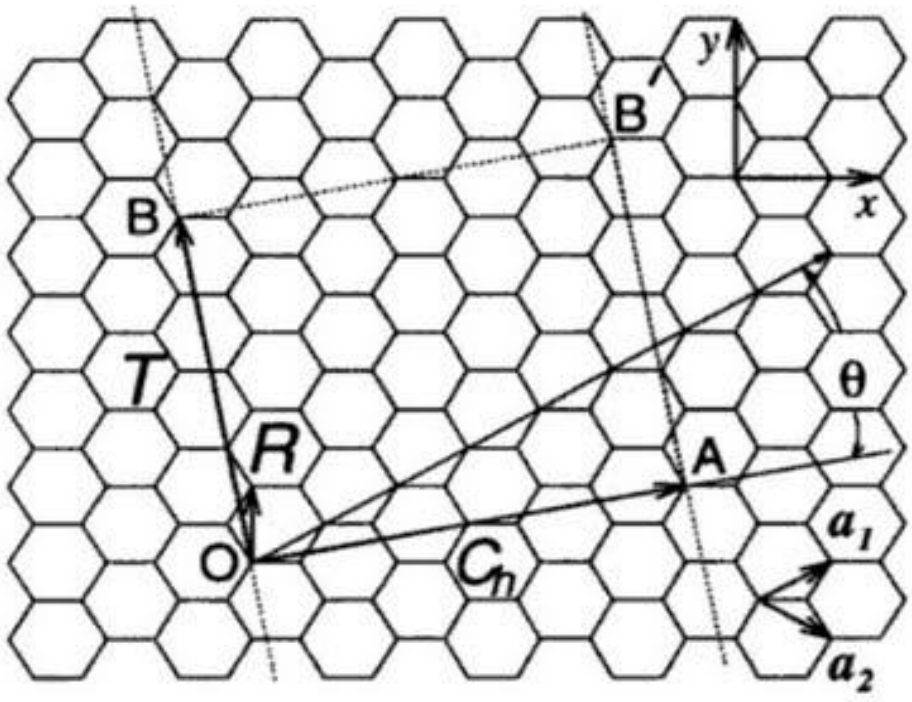

Figure 1.11: The unrolled honeycomb lattice of a nanotube. When we connect sites of O and A, and B and B´, a nanotube can be constructed. The rectangle OAB´B defines the unit cell for the nanotube [16].

The unrolled honeycomb lattice of the nanotube is shown in (figure 1.11). The structure of a single-wall CNT is specified by the vector ($\overrightarrow{OA}$ in (Figure1.11)) which corresponds to a section of the nanotube perpendicular to the nanotube axis. $\overrightarrow{OB}$ indicates the direction of the nanotube axis, and the direction $\overrightarrow{OA}$ corresponds to the transversal direction or equator. By considering the crystallographically equivalent sites O, A, A, B, and B´, and by rolling the honeycomb sheet so that points O and A coincide (and points B and B´ coincide), a paper model of a CNT can be constructed. The vector $\overrightarrow{OA}$ and $\overrightarrow{OB}$ define the chiral vector C_h and translational vector T of a carbon nanotubes, respectively.

The chiral vector C_h can be expressed by the real space unit vectors a_1 and a_2 of the hexagonal lattice as defined

$$\vec{a}_1 = \left(\frac{\sqrt{3}}{2}a, \frac{a}{2}\right), \quad \vec{a}_2 = \left(\frac{\sqrt{3}}{2}a, -\frac{a}{2}\right)$$

Where a_1 and a_2 are not orthogonal to each other and that the inner product between a_1 and a_2 yield. $a_1.a_1 = a_2.a_2,\ a_2.a^2 = \frac{a^2}{2}$

Where $a = |\vec{a}_1| = |\vec{a}_2| = 1.42 \times \sqrt{3} = 2.46\text{Å}$ is the lattice constant of two dimensional graphite.

$C_h = na_1 + ma_2 \equiv (n, m)$, (n, m are integers, $0 \leq |m| \leq n$)

An armchair nanotube corresponds to the case of $n = m$, that is $C_h = (n, n)$ and a zigzag nanotube corresponds to the case of $m = 0$ or of $C_h = (n, 0)$. All other (n, m) chiral vectors correspond to the chiral nanotubes. Because of the hexagonal symmetry of the honeycomb lattice, we need to consider only $0 < |m| < n)$ in $C_h = (n, m)$ for chiral nanotubes.

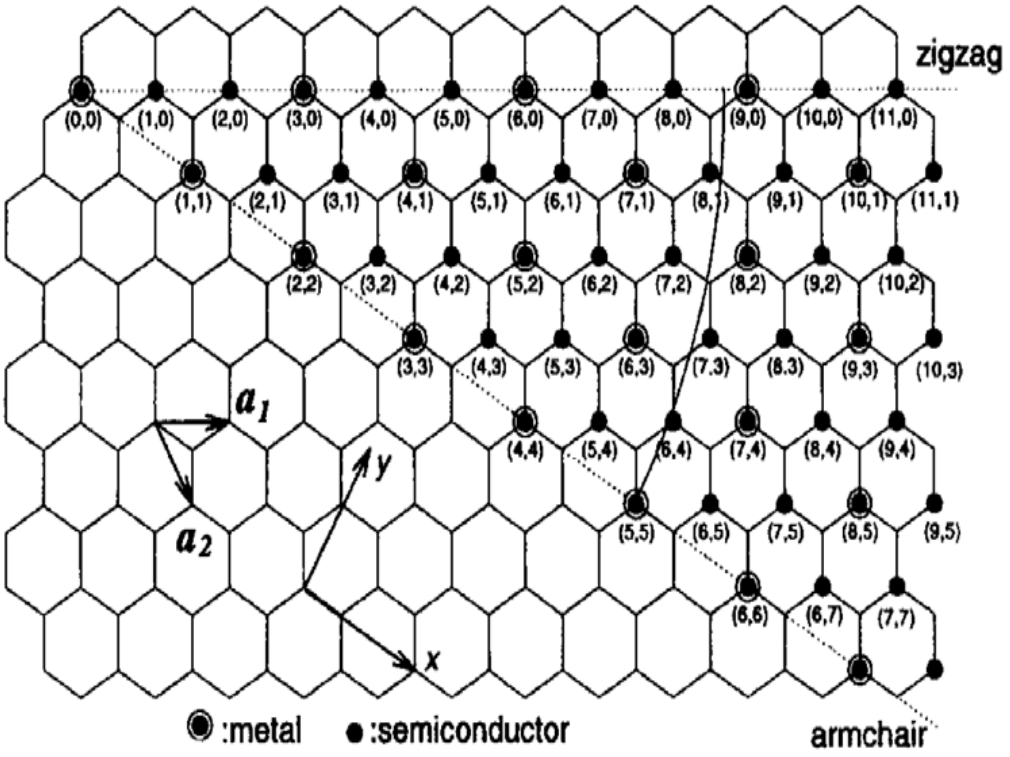

Figure 1.12: *The unrolled honeycomb lattice of a nanotube. When we connect sites of O and A, and B and B´, a nanotube can be constructed. The rectangle OAB´B defines the unit cell for the nanotube[16].*

The diameter of the CNT, d_t, is given by L/π, in which L is the circumferential length of CNT.

$d_t = L/\pi\ , L = |C_h| = \sqrt{C_h.C_h} = a\sqrt{n^2 + m^2 + nm}$

The chiral angle θ is defined as the angle between the vectors Ch and a_1, with values of θ in the range $0 \leq |\theta| \leq 30^0$, because of the hexagonal symmetry of the honeycomb lattice. The chiral angle θ is defined by taking the inner product of Ch and a_1, to yield an expression for cosθ:

$$cos\theta = \frac{C_h . a_1}{|C_h||a_1|} = \frac{2n+m}{2\sqrt{n^2+m^2+nm}}$$

Zigzag and armchair nanotubes corresponds to θ=0° and θ=30°, respectively.

The translation vector T is defined to be the unit vector of a 1D carbon nanotube. The vector T is parallel to the nanotube axis and is normal to the chiral vector C_h in the unrolled honeycomb lattice. As shown in the figure T is normal to C_h and extends from the origin to the first lattice point B in the honeycomb lattice. It is common to represent T in terms of integers (t_1, t_2) as shown in table length of T is $\frac{\sqrt{3}L}{d_R}$ and d_R is either equal to highest common divisor of (n, m) denoted by d, or to 3d, depending on whether n-m=3dr, r being an integer. Corresponding to selected and represented (n, m) pairs list in (table 1.1) for various parameters [15].
(Figure 1.12) shows carbon nanotubes are those are metallic and semiconducting, denoted by open and solid circles, respectively. It follows that approximately one third of carbon nanotubes are metallic and other two third are semiconducting [16].

Table1.1: Parameters of CNTs [15]

Symbole	Name	Formula	Value
A	length of unit vector	$a = \sqrt{3}a_{C-C} = 2.49Å$	$a_{C-C} = 1.44Å$
a_1, a_2	unit vector	$\left(\frac{\sqrt{3}}{2}, \frac{1}{2}\right)a, \left(\frac{\sqrt{3}}{2}, -\frac{1}{2}\right)a$	x, y coordinate
Ch	chiral vector	$C_h = na_1 + ma_2 \equiv (n, m),$	$(0 \leq \|m\| \leq n)$
L	length of *Ch*	$L = \|C_h\| = a\sqrt{n^2+m^2+nm}$	
Dt	diameter	$d_t = L/\pi$	

Θ	chiral angle	$Sin\theta = \frac{\sqrt{3}m}{2\sqrt{n^2+m^2+nm}}$ $cos\theta = \frac{2n+m}{2\sqrt{n^2+m^2+nm}}$ $tan\theta = \frac{\sqrt{3}m}{2n+m}$	$0 \leq \lvert\theta\rvert \leq \frac{\pi}{6}$
T	translation vector	$T = t_1 a_2 + t_2 a_2 \equiv (t_1, t_2)$ $t_1 = \frac{2m+n}{d_R}$, $t_2 = -\frac{2n+m}{d_R}$	
T	length of T	$T = \lvert T\rvert = \frac{\sqrt{3}L}{d_R}$	
N	Number of hexagons in the nanotube unit cell	$N = \frac{2(n^2+m^2nm)}{d_R}$	

1.8.4. Properties of carbon nanotubes

Carbon nanotubes have gained in interest as nanoscale materials due to their remarkable physical properties such as their very high Young's modulus, their ultimate strength and their high electric and thermal conductivity. However, directly measuring the properties of these nanoparticles is very difficult by conventional methods. Therefore, several properties have been first evaluated using by theoretical studies. The covalent bond sp^2 in the CNTs is one of the strongest bonds therefore; a fiber formed by these axially oriented covalent bonds would be an extremely strong material. The mechanical parameter most commonly used to characterize a CNT is by measuring its Young's modulus. Theoretical investigations have led to estimated Young's modulus of CNTs in the range of 1 TPa [17]. Different experimental methods have been developed to measure the elastic properties of individual nanotubes. One method allows the determination of the CNT stiffness by the observation of the amplitude of their intrinsic thermal vibrations in a transmission

electronic microscope (TEM). Average Young's modulus values of 1.8 TPa and 1.25 TPa were obtained for MWNTs and SWNTs, respectively [18, 19]. Quantum mechanics calculations predict that defect-free single-walled carbon nanotubes possess Young's modulus values of 1 TPa, tensile strengths of 100 GPa, and multiwalled carbon nanotubes with a mean fracture strength >100 GPa [20]. For illustration, a tensile strength of 200 GPa for MWNT corresponds to the ability to endure a weight of 20 tons on a cable with a cross-section of 1 mm^2. Carbon nanotubes thus represent the strongest and stiffest materials in terms of tensile strength and elastic modulus. The above mechanical properties of CNTs refer to axial properties of the nanotube. Simple geometrical considerations suggest that CNTs should be much softer in the radial direction than along the tube axis. Indeed, TEM observations of radial elasticity show that even van der Waals forces can deform two adjacent nanotubes [21]. Nanoindentation experiments with AFM indicated Young's modulus of the order of several GPa in the radial Axis [22]. In spite of these excellent mechanical properties, carbon nanotubes possess also a remarkable flexibility. Besides their experimental observations, the bending of nanotubes at large angles is completely reversible up to 100° despite the formation of complex kink shapes [23].

Carbon nanotubes are expected to be very good thermal conductors along the tube, but good insulators laterally to the tube axis. It was demonstrated that thermal conductivity of CNTs is determined primarily by phonons [24]. Experimental thermal conductivity measured on individual MWNTs reaches 3300 W/(m.K), which is about twice as high as diamond [25]. Moreover, CNTs are thermally stable up to 2800°C in vacuum and up to 700°C under air [26]. Other important physical properties of CNTs are their electronic properties, which are dependent on the molecular structure (chirality) of CNTs [27].

The determination of electronic properties of MWNTs is a complicated task as the carbon sheets in the MWNTs can have different electronic character and chirality. However, Bachtold *et al*. demonstrated that current flows only through the outer-shell of MWNTs based on measurements of the Aharonove-Bohm oscillation. In studies of MWNTs with outer shell side-bonded to metal electrodes, it was also concluded that the electrical transport is dominated by outer-shell conduction [28, 29]. In 2005 H J Li *et al.* showed a multichannel quasiballistic conducting

behavior occurring in the MWCNTs with large diameter, which can be attributed to the participation of multiple walls in electrical transport and the large diameter of the MWCNTs [30]. The diameter being in the nanometer range gives rise to quantum effects in carbon nanotubes. In fact, the unique electrical properties of nanotubes arise from the confinement of the electrons in tubes, which allows motion only along the tube axis. The scattering processes are therefore reduced in the tube and metallic CNTs can carry enormous current densities up to 10^9A/cm² without being destroyed [31]. This density is about 2-3 orders of magnitude higher than the current density of metals such as copper. A high electrical conductivity value of 10^3 S/cm is often measured by both two- and four-probe processes on individual SWNTs and MWNTs [32, 33].

The chemical reactivity of a CNT is, compared with a graphene sheet, enhanced as a direct result of the curvature of the CNT surface. Carbon nanotube reactivity is directly related to the pi-orbital mismatch caused by an increased curvature. Therefore, a distinction must be made between the sidewall and the end caps of a nanotube. For the same reason, a smaller nanotube
diameter results in increased reactivity. Covalent chemical modification of either sidewalls or end caps has shown to be possible. For example, the solubility of CNTs in different solvents can be controlled this way. Though, direct investigation of chemical modifications on nanotube behavior is difficult as the crude nanotube samples are still not pure enough [34].

1.8.5. Applications

Carbon nanotubes (CNTs) have recently emerged as one of the most important classes of nanomaterials having enormous potential to spark off the next industrial revolution. The unique and extraordinary properties of the CNTs, such as, extremely high electrical and thermal conductivities, very small diameters (less than 100 nm), large aspect ratios (length/diameter ratios, greater than 1000), outstanding mechanical properties, a tip-surface area near the theoretical limit (the smaller area of the tip-surface, the more concentrated electric field, and the largest enhancement factor of the electric field) and an excellent price-performance ratio, make it an ideal candidate for electronic devices, chemical/electrochemical and biosensors, electron field emitters, lithium-ion batteries, white light sources, hydrogen storage cells, cathode ray tubes

(CRTs), electrostatic discharge (ESD) and electrical-shielding applications [35]. It is possible to make transistors based on carbon nanotubes that operate at room temperature and can function as a digital switch using a single electron. Worldwide commercial interest in carbon nanotubes (CNTs) is reflected in a production capacity that presently exceeds several thousand tons per year.

The global CNTs market is highly consolidated and oligopolistic in nature, dominated by a few large suppliers/producers operating in multiple industry segments. The global CNTs industry turned over around $668.3 million in 2010, with multi-walled carbon nanotubes (MWCNTs) production value of approximately $631.5 million and single-walled carbon nanotubes (SWCNTs) production value of around $36.8 million, and is forecast to grow to $1.1 billion by 2016 at a Compound Annual Growth Rate (CAGR) of 10.5% (figure 1.13). Used across a wide range of industries including plastics and composites, electrical and electronics, and energy as well as a range of industrial sectors, CNTs have become an

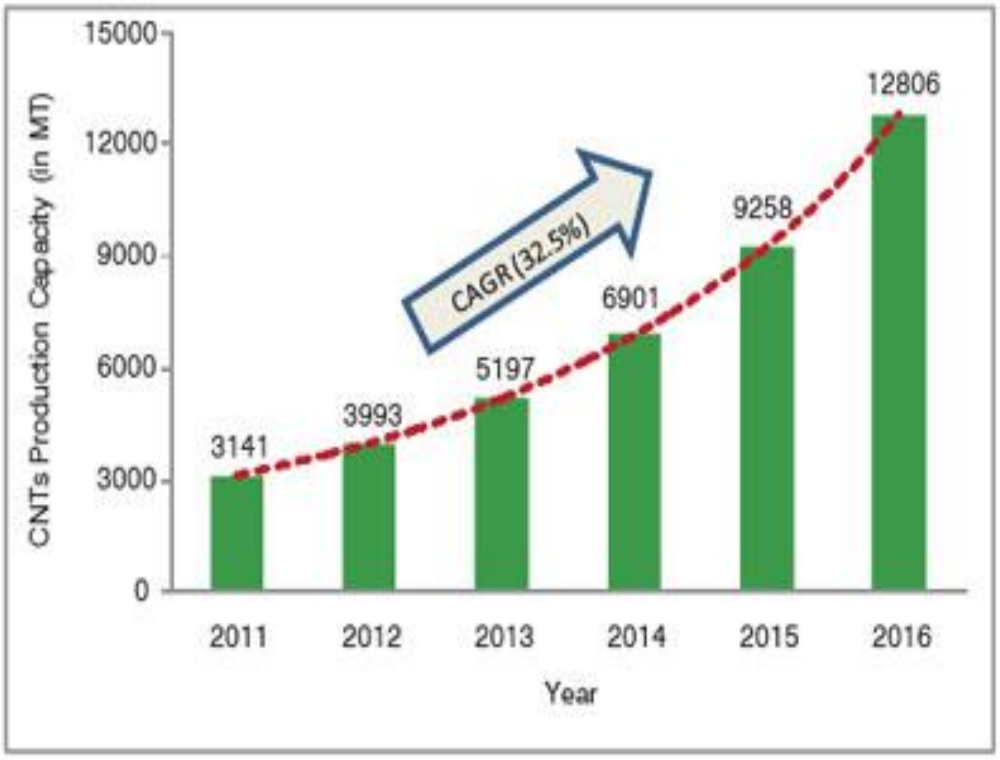

Figure 1.13: Forecast (2011-2016) for global CNTs market [35].

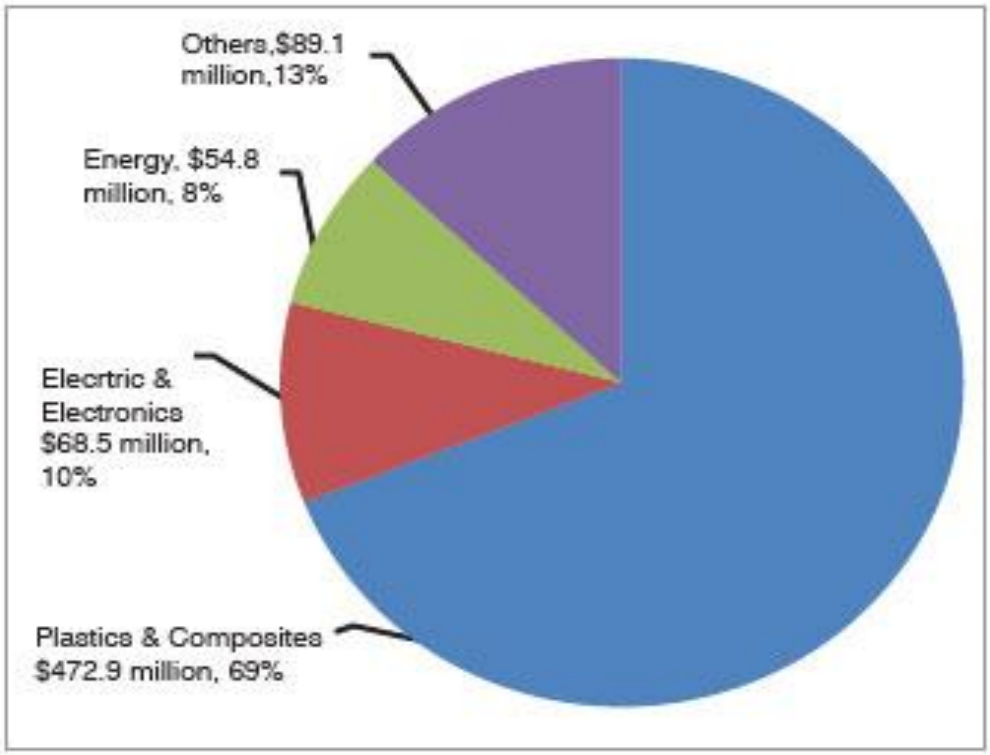

Figure 1.14: Global CNTs market by industry [35].

essential ingredient or reinforcement material for these industries, with its usage growing broadly in line with the global economy.

The largest share of global CNTs is accounted for by plastics and composites with sales of $472.9 million in 2010, representing 69% of the market (figure1.14). Plastics and composites will remain the most significant markets through to 2016. Electrical and electronics industries accounted for 10% of the CNTs market share followed by energy (8%). The electronics and data storage market is likely to see the biggest penetration by 2016, with the performance-enhancing properties of carbon nanotubes allowing electronics manufacturers to meet demanding market needs across a variety of applications, including interconnects, displays, memory, storage and others. The energy sector will also witness rapid growth, with enhanced performance requirements for batteries, wind turbine blades, photovoltaic cells and other applications in the next five to ten years [35].

CNT powders have already been incorporated in many commercial applications and are now entering the growth phase of their product life cycle. MWNTs were first used as electrically conductive fillers in plastics,

taking advantage of their high aspect ratio to form a percolation network at concentrations as low as 0.01 weight percent (wt %). Disordered MWNT-polymer composites reach conductivities as high as 10^4 S m^{-1} at 10 wt % loading. In the automotive industry, conductive CNT plastics have enabled electrostatic-assisted painting of mirror housings, as well as fuel lines and filters that dissipate electrostatic charge. Other products include electromagnetic interference (EMI)–shielding packages and wafer carriers for the microelectronics industry (figure 1.15).

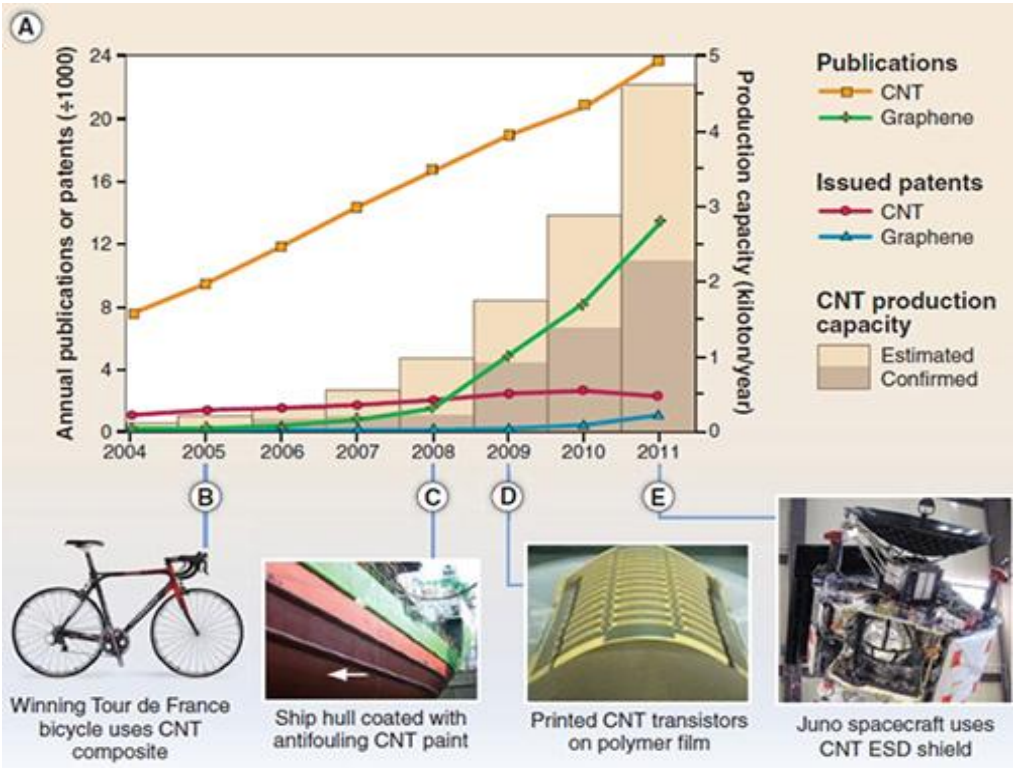

Figure 1.15: Trends in CNT research and commercialization. (A) Journal publications and issued worldwide patents per year, (B to E) Selected CNT related products: composite bicycle frame, antifouling coatings, printed electronics and electrostatic discharge shielding [36].

CNT yarns and laminated sheets made by direct CVD or forest spinning or drawing methods may compete with carbon fiber for high-end uses, especially in weight-sensitive applications requiring combined electrical and mechanical functionality. In scientific reports, yarns made from high-quality few-walled CNTs have reached a stiffness of 357 GPa and strength of 8.8 GPa but only for a gauge length that is comparable to

the millimeter-long CNTs within the yarn. Centimeterscale gauge lengths showed 2-GPa strength, corresponding to a gravimetric strength equaling that of commercially available Kevlar (DuPont). Because the probability of a critical flaw increases with volume, macroscale CNT yarns may never achieve the strength of the constituent CNTs. However, the high surface area of CNTs may provide interfacial coupling that mitigates these deficiencies, and, unlike carbon fibers, CNT yarns can be knotted without degrading their strength.

Last 2013, L Kurzepa et al. showed the performance of macroscopic insulated assemblies of carbon nanotube wires by substituting them for copper windings in a standard high frequency transformer (figure 1.16). The process of making nano cables begins with a lump of double-walled nanotubes that have been treated to remove impurities. The researchers add sulfuric acid to the nanotubes so they can spread them into a thin film. They then grasp the edge of the film with tweezers to start making a fiber, and pull with a steady force to yield a long cable—similar to how wool yarn is made by pulling and twisting fleece. They rinse the acid from the cable and expose it to iodine vapor at high temperatures. The iodine penetrates into the nanotubes within the cable and increases the cable's conductivity without compromising its mechanical properties. And the Rice group has shown that conductivity isn't affected when the cables are knotted together to make greater lengths [38].

For fuel cells, the use of CNTs as a catalyst support can potentially reduce Pt usage by 60% compared with carbon black, and doped CNTs may enable fuel cells that do not require Pt as catalyst. For organic solar cells, ongoing efforts are leveraging the properties of CNTs to reduce undesired carrier recombination and enhance resistance to photooxidation. In the long run, photovoltaic technologies may incorporate CNT-Si heterojunctions and leverage efficient multiple-exciton generation at p-n junctions formed within individual CNTs.

In the nearer term, commercial photovoltaics may incorporate transparent SWNT as window electrodes. CNTs are widely used for supercapacitors and Li-ion batteries [39, 40]. Membranes using aligned encapsulated CNTs with open ends permit flow through the interior of the CNTs, enabling unprecedented low flow resistance for both gases and liquids [41]. This enhanced permeability may enable lower energy cost for water desalination by reverse osmosis in comparison to commercial

polycarbonate membranes. However, very-small-diameter SWNTs are needed to reject salt at seawater concentrations [36, 42].

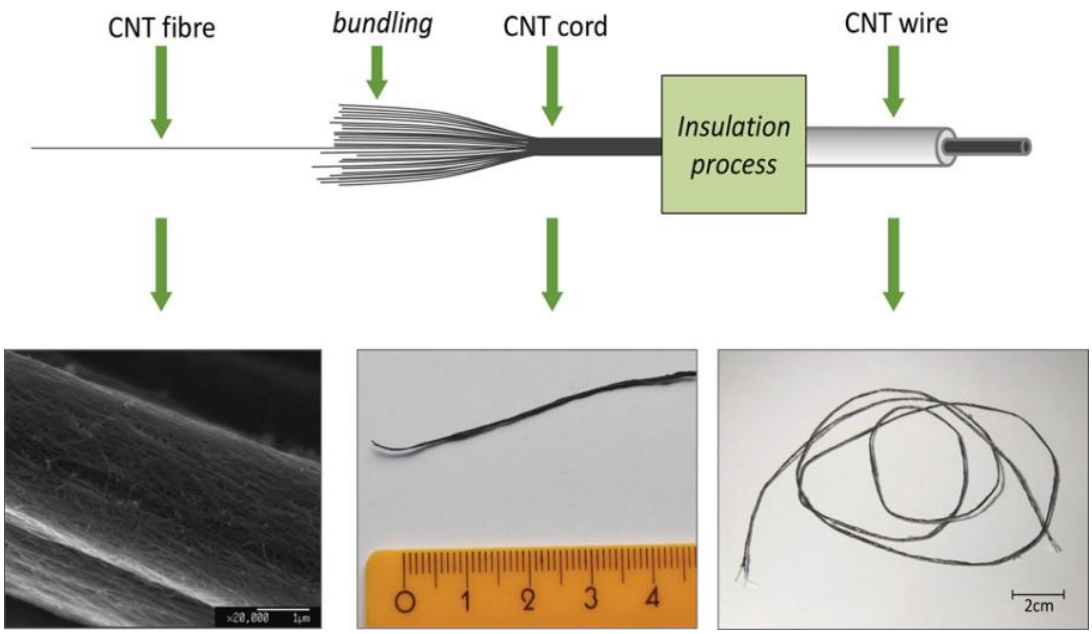

Figure 1.16: The process of production of CNT wire [36]

Researchers at Fraunhofer Institute have succeeded at coming up with a new material for electrodes that is on the same level as indium-tin-oxide (ITO) and on top of it is much cheaper. Its main components are CNTs and low–cost polymers. This new electrode foil is composed of two layers. One is the carrier, a thin foil made of inexpensive polyethylenterephthalate PET used for making plastic bottles. Then a mixture of CNTs and electrically conducting polymer is added that is applied to the PET as a solution and forms a thin film when it dries. In comparison to ITO, these combinations of plastics have not been particularly durable because of humidity, pressure or UV light put a strain on the polymers. The layers became brittle and broken down. Only CNTs have made them stable [43]. CNTs use as components of biosensors and medical devices are motivated by the dimensional and chemical compatibility of CNTs with biomolecules, such as DNA and proteins. At the same time, CNTs enable fluorescent and photoacoustic imaging, as well as localized heating using near-infrared radiation [36].

1.9. Supercapacitors

1.9.1. Introduction

A tsunami wave of small electronic devices is hitting the market as commonplace. There has been great interest in developing and refining more efficient energy storage devices. Electrical energy can be stored in two fundamentally different ways: (1) indirectly in batteries as potentially available chemical energy requiring Faradaic oxidation and reduction of the electrochemically active reagents to release charges that can perform electrical work when they flow between two electrodes having different electrode potentials; and (2) directly, in an electrostatic way, as negative and positive electric charges on the plates of a capacitor, a process known as non-Faradaic electrical energy storage [44]. Supercapacitors store and discharge energy very quickly and are being used in thousands of different applications and considered in a host of future applications. Supercapacitors complement a primary energy source like an internal combustion engine, fuel cell or battery, which cannot repeatedly provide quick bursts of power. The future horizon looks immense for supercapacitors as a green, alternative energy resource. Primary energy sources internal combustion engines, fuel cells and batteries work well as a continuous source of low power. However, they cannot efficiently handle peak power demands or recapture energy in today's applications because they discharge and recharge slowly. Supercapacitor/battery combinations in electric vehicles (EV) and hybrid electric vehicles (HEV) are well investigated. A 20 to 60% of fuel reduction has been claimed by recovering brake energy in EVs or HEVs [45].

1.9.2. Overview

Supercapacitors are called with several names such as electrochemical capacitors, ultra capacitors and electrochemical double-layer capacitors. In 1957 Becker proposed a capacitor based on porous carbon material with high surface area to store electrical energy for practical purposes. The principle involved was charging of the capacitance, C_{dl}, of the double layer, which arises at all solid/electrolyte interfaces, such as metal, semiconductors and colloid surfaces. After Becker, the Sohio Corporation in Cleveland, Ohio, also utilized the double layer capacitance of high-area materials in a non-aqueous solvent containing a dissolved

tetraalkylammonium salt electrolye [44]. In late 70's and 80's, Conway and coworkers made a great contribution to the capacitor research work based on RuO_2, which has high specific capacitance and low internal resistance. In the 90's, supercapacitors received much attention in the context of hybrid electric vehicles.

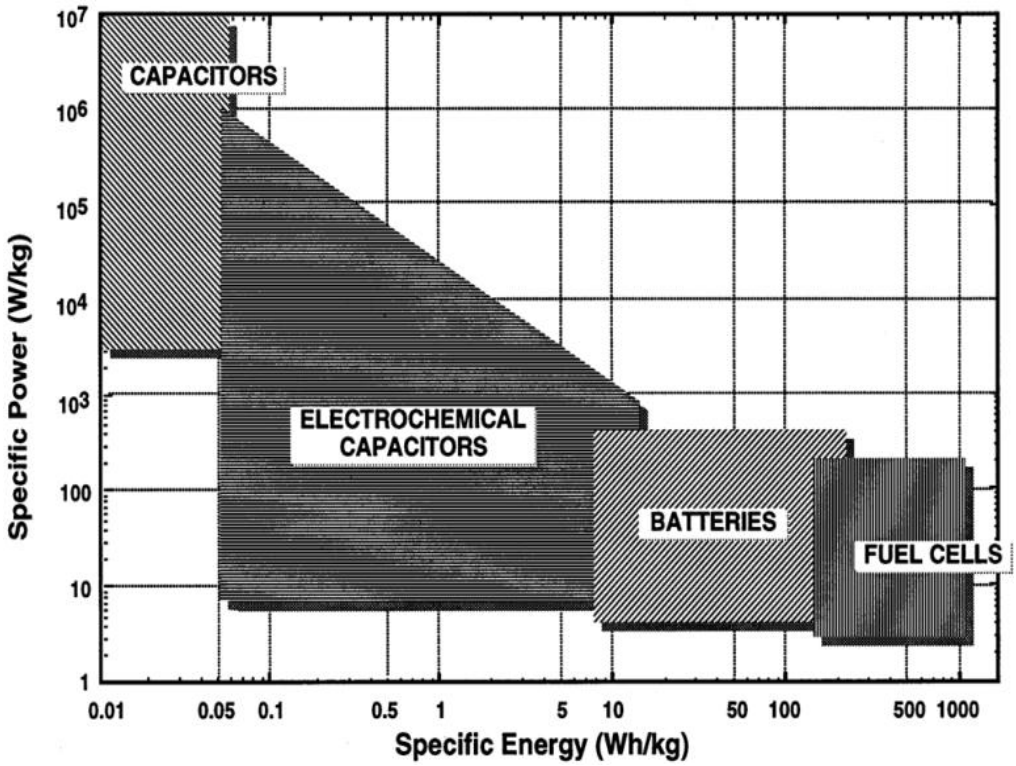

Figure 1.17: Sketch of Ragone plot for various energy storage and conversion devices. The indicated areas are rough guide lines [46].

Commercial productions of supercapacitors in nowadays markets are basically from the high surface area porous carbon materials as well as noble metal oxides systems. For instance, Matsushita Electric Industrial (Panasonic, Japan) developed gold capacitors, as high performance supercapacitors for military applications that were produced by Pinnacle Research (USA). The commercial supercapacitors are widely used as power sources for activators, elements for long time constant circuits, standby power for random access memory devices, and handphone equipments. A comparison of the properties and performance between battery, capacitor, and supercapacitor is given in (figure 1.17). Batteries are typically low power devices compared to conventional capacitors that have

power densities as high as 10^6 Wkg^{-1}, but low energy densities. From this point of view, supercapacitors (Ultracapacitors) combine the properties of high power density and higher energy density, and also show long life cycles due to the absence of chemical reactions [47]. A graphical taxonomy of the different classes and subclasses of supercapacitors is presented in (figure 1.18).

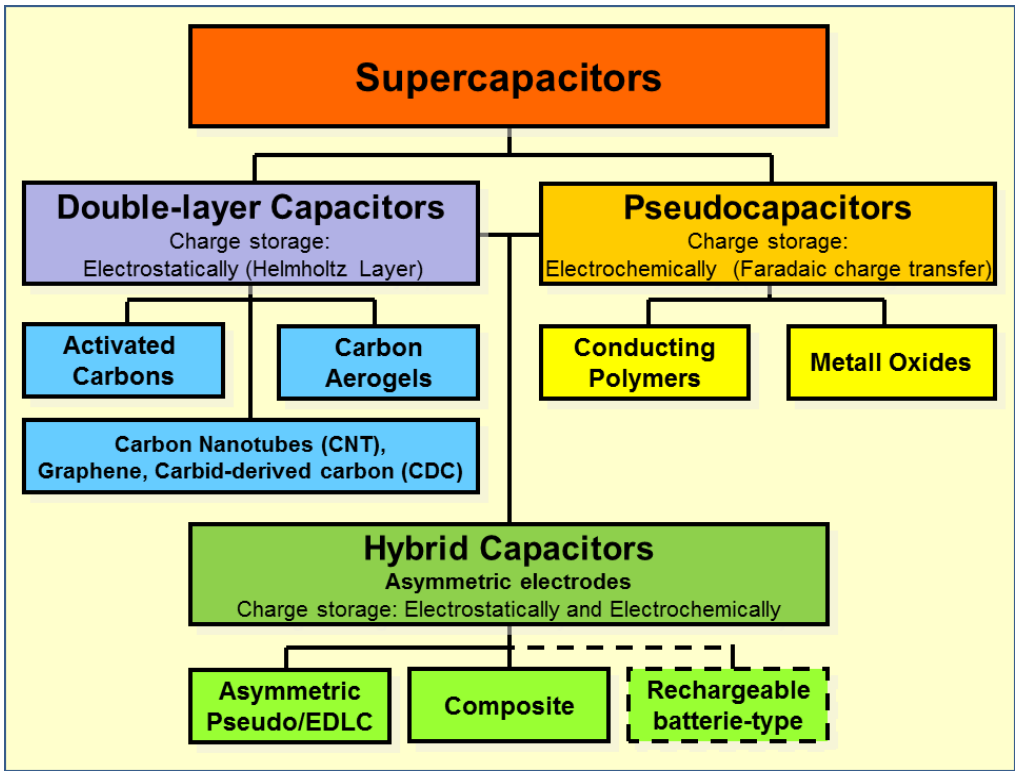

Figure 1.18: Taxonomy of supercapacitors [47]

1.10. References

[1] Taniguchi, Norio (1974). *On the Basic Concept of 'Nano-Technology'*. Proceedings of the International Conference on Production Engineering, Tokyo, 1974, Part II (Japan Society of Precision Engineering); and R Hoffmann, *For the first time you can see atoms*, (1993), American Scientists, 81, 11-12.

[2] L Dai, *Carbon nanotechnology. Recent Developments in Chemistry, Physics, Materials Science and Device Applications*, (2006), CH 1. ISBN: 978-0-444-51855-2

[3]Courses.washington.edu/overney/ChemE554_Course_Mat/course_material/1.2_overview_nanoscience_nanotechnology.htm

[4] R Saito, G Dresselhaus and M S Dresselhaus, *Physical properties of CNTs*, (1998) ISBN: 1-86094-0935.

[5] Timothy D. Burchell , *Carbon materials for advanced technologies*, (1999), CH 1, ISBN: 978-0-08-042683-9.

[6] M.S. Dresselhaus, G. Dresselhaus, Ph. Avouris, *Carbon nanotubes*, (2001), ISBN: 3-540-41086-4.

[7] F P Bunday, W A Bassett, M S Weathers, R J Hemley, H K Mao and A F Goncharov, *The pressure-temperature phase and transformation diagram for carbon; updated through 1994*, (1996), Carbon, 34,141-153.

[8] S Iijima and T Ichihashi, *Single-shell carbon nanotubes of 1 nm diameter*, (1993), Nature, 363, 603–5.

[9] R Kotz, M Carlen, *Principles and applications of electrochemical capacitors*, (2000), Electrochimica Acta, 45, 2483–2498.

[10] H-S P Wong and D Akinwande, *Carbon nanotube and Graphene device physics*, (2011), ISBN: 9780521519052.

[11] S Ijima, *Helical microtubules of graphitic carbon*, (1991), Letters to Nature, 354, 56-58.

[12] D S Bethune, C H Kiang, M S de Vries, G Gorman, R Savoy, J Vasquez and R Beyers, *Cobalt-catalysed growth of carbon nanotubes with single-atomic-layer walls*, (1993), Nature, 363, 605-607.

[13] M Naraghi, *Nanotechnology and Nanomaterials*, CH 3, (2011), ISBN: 978-953-307-566-2.

[14]http://courses.cs.washington.edu/courses/csep590a/08sp/projects/CarbonNanotubes.pdf.

[15] M S Dresselhaus,G Dresselhaus, and R. Saito, *Physics of carbon nanotubes*, (1995), Carbon, 33, 7, 883-891.

[16] R Saito, *Physical properties of carbon nanotubes*, (1998), Imperial College Press, ISBN: 1-86094-093-5.
[17] J P Lu, *Elastic properties of single and multilayered nanotubes*, (1997), J. Phy.Chem solids, 58, 11, 1649-1652.
[18] M M J Treacy, T W Ebbesen and J M Gibson, *Exceptionally high Young's modulus observed for individual carbon nanotubes*, (1996), Nature, 381, 678-680.
[19] A. Krishnan, E. Dujardin, T. W. Ebbesen, P. N. Yianilos and M. M. J. Treacy, *Young's modulus of single-walled nanotubes*, (1998), Physical Review B, 58, 15, 14013-14019.
[20] B Peng, M Locascio, P Zapol, S Li, S L Mielke, G C Schatz and H D Espinosa, *Measurements of near-ultimate strength for multiwalled carbon nanotubes and irradiation-induced crosslinking improvements*, (2008), Nature Nanotechnology, 3 626-631.
[21] B Ruelle, PhD thesis, *Functionalization of carbon nanotubes via plasma post-discharge surface treatment: Implication as nanofiller in polymeric matrices*, Année académique 2009-2010.
[22] M-F Yu, T Kowalewski and R S Ruoff, *Investigation of the Radial Deformability of Individual Carbon Nanotubes under Controlled Indentation Force*, (2000), Physical Review Letters, 85, 1456-1459.
[23] S Iijima, C Brabec,A Maiti, J Bernholc, *Structural flexibility of carbon nanotubes*, (1996), J. Chem. Phys, 104, 2089-2092.
[24] J Hone, M Whitney, and A Zettl, *Thermal conductivity of single-walled carbon nanotubes*, (1999), Synthetic Metals, 103, 2498-2499..
[25] P Kim, L Shi, A Majumdar, and P L McEuen, *Thermal Transport Measurements of Individual Multiwalled Nanotubes*, (2001), Physical Review Letters, 87, 215502-1-4.
[26] T Belin, F Epron, *Characterization methods of carbon nanotubes: a review*, (2005), Materials Science and Engineering B, 119, 105–118.
[27] E T Thostenson, Z Ren, Tsu-Wei Chou, *Advances in the science and technology of carbon nanotubes and their composites: a review*, (2001), Composites Science and Technology, 61, 1899–1912.
[28] A Bachtold, C Strunk, J P Salvetat,J M Bonard, L Forro, T Nussbaumer and C Schoenenberger, *Aharonov-Bohm oscillations in carbon nanotubes*, (1999), Nature, 397, 673-675.

[29] C Schönenberger, A Bachtold, C Strunk, J P Salvetat, L Forro, *Interference and Interaction inmulti-wall carbon nanotubes*, (1999), Appl. Phys. A, 69, 283–295.
[30] H J Li, W G Lu, J J Li, X D Bai and C Z Gu, *Multichannel Ballistic Transport in Multiwall Carbon Nanotubes*, (2005), Physical Review Letter, 95, 086601, 1-4.
[31] S Frank, P Poncharal, Z L Wang, W A de Heer, *Carbon Nanotube Quantum Resistors*, (1998), Science, 280, 1744-1746.
[32] S J Tans, M H Devoret, H Dai, A Thess, R E Smalley, L J Geerlings and C dekker, *Individual single wall carbon nanotubes as quantum wires*, (1997), Nature, 386, 474-477.
[33] C V Haesendonck, L Stockman, R J M Vullers, y Bruynseraede, L Langer, V Bayot, E Grivei, j-p. Issi, j p Heremans and C H Olk, *Nanowire bonding with the scanning tunneling microscope*, (1997), Surface Science, 386, 279-289.
[34]http://students.chem.tue.nl/ifp03/Wondrous%20World%20of%20Carbon%20Nanotubes_Final.pdf
[35] http://www.nanowerk.com/spotlight/spotid=23118.php
[36] Michael F. L. De Volder, Sameh H. Tawfick, Ray H. Baughman, A. John Hart, *Carbon* Nanotubes*: Present and Future Commercial Applications*, (2013), Science, 339 1 535-539.
[37] L Kurzepa , A Lekawa-Raus , J Patmore , and K Koziol, *Replacing Copper Wires with Carbon Nanotube Wires in Electrical Transformers*, (2013), Adv. Funct. Mat., 1-6.
[38] http://www.extremetech.com/extreme/145446-rice-creates-first-long-strong-flexible-and-conductive-carbon-nanotube-thread
[39] S Hussain, R Amade, E Jover, and E Bertran, *Water Plasma Functionalized CNTs/MnO_2 Composites for Supercapacitors*, (2013), The Scientific World Journal, Vol. 2013, ID 832581, 1-8.
[40] I Lahiri, S W Oh, J Y Hwang, S Chao, Y K Sun, R Banarjee, W Choi. *High capacity and excellent stability of Lithium ion battery anode using interface-controlled binder-free multiwall carbon nanotubes grown on copper*. (2010), ACS Nano, 4, 3440-3446.
[41] Jason K. Holt, Hyung Gyu Park, Yinmin Wang, Michael Stadermann, Alexander B. Artyukhin, Costas P. Grigoropoulos, Aleksandr Noy, Olgica Bakajin, *Fast Mass Transport Through Sub–2-Nanometer Carbon Nanotubes*, (2006), Science, 312, 1034-1037.

[42] B Corry, *Designing Carbon Nanotube Membranes for Efficient Water Desalination*, (2008), J. Phys. Chem. B, 112, 1427-1434.
[43] http://nextbigfuture.com/2011/01/touchscreen-made-in-part-from-carbon.html#more
[44] B.E. Conway, *Electrochemical Supercapacitors; Scientific Fundamentals and Technological Applications*, Kluwer Academic/ Plenum Publishers, NewYork, NY,USA, (1999), ISBN: 0306457369, 9780306457364
[45] http://en.wikipedia.org/wiki/Supercapacitor
[46] R Kotz, M Carlen, *Principles and applications of electrochemical capacitors*, (2000), Electrochimica Acta, 45, 2483–2498.
[47] M V Kiamahalleh and S H S ZEIN, *Multiwalled Carbon Nanotubes Based Nanocomposites For Supercapacitors: A Review Of Electrode Materials*, (2012), NANO: Brief Reports and Reviews, 7, 2, 1230002, 1-27.
[48] http://www.asdn.net/asdn/chemistry/carbon_nanotubes.shtml

PART II – EXPERIMENTAL DESCRIPTION

Chapter 2
Experimental techniques and setup

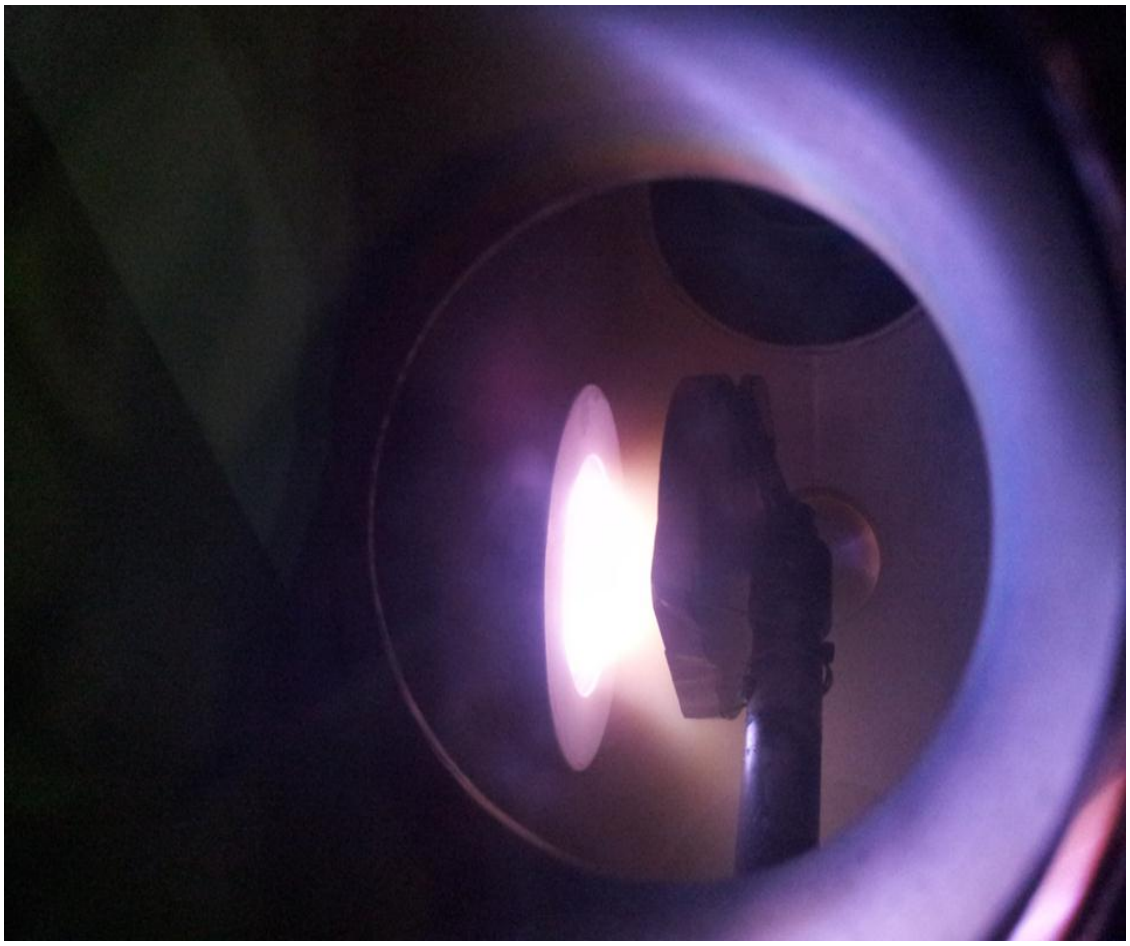

Figure 2: Photograph of Ar plasma.

Chapter 2: Experimental techniques and setup

As an approach to the production technology of carbon nanotubes (CNTs), we are going to give a short introduction to the main deposition technologies used during the development of this thesis. Plasma, sputtering, chemical vapor deposition (CVD) and plasma enhanced chemical vapor deposition (PECVD) have been introduced and the details of the reactor used to perform the experiments of deposition of thin films and CNTs, have been described.

2.1. Introduction to plasma: the fourth state of matter

Plasma is an ionized gas, a distinct fourth state of matter. "Ionized" means that at least one electron is not bound to an atom or molecule, converting the atoms or molecules into positively charged ions. As temperature increases, molecules become more energetic and transform matter in the sequence: solid, liquid, gas, and finally plasma, which justifies the title "fourth state of matter."

The free electric charges – electrons and ions – make plasma electrically conductive (sometimes more than gold and copper), internally interactive, and strongly responsive to electromagnetic fields. Ionized gas is usually called plasma when it is electrically neutral (i.e., electron density is balanced by that of positive ions) and contains a significant number of the electrically charged particles, sufficient to affect its electrical properties and behavior. In addition to being important in many aspects of our daily lives, plasmas are estimated to constitute more than 99% of the visible universe.

The term *plasma* was first introduced by Irving Langmuir (1928) because the multicomponent, strongly interacting ionized gas reminded him of blood plasma. Langmuir wrote: "Except near the electrodes, where there are sheaths containing very few electrons, the ionized gas contains ions and electrons in about equal numbers so that the resultant space charge is very small. Plasmas occur naturally but also can be effectively man-made in laboratory and in industry, which provides opportunities for numerous applications, including thermonuclear synthesis, electronics, lasers, fluorescent lamps, and many others practice. Most plasmas of practical significance, however, have electron temperatures of 1-20 eV, with electron densities in the range 10^{6}-10^{18} cm^{-3}. (High temperatures are

conventionally expressed in electron volts; 1 eV approximately equals 11,600 K). All particles need to be ionized in plasma; a common condition in plasma chemistry is for the gases to be only partially ionized. The ionization degree (i.e., ratio of density of major charged species to that of neutral gas) in the conventional plasma–chemical systems is in the range 10^{-7}-10^{-4}. When the ionization degree is close to unity, such plasma is called completely ionized plasma. When the ionization degree is low, the plasma is called weakly ionized plasma. Both natural and man-made laboratory plasmas are quasi-neutral, which means that concentrations of positively charged particles (positive ions) and negatively charged particles (electrons and negative ions) are well balanced.

As in any gas, temperature in plasma is determined by the average energies of the plasma particles (neutral and charged) and their relevant degrees of freedom (translational, rotational, vibrational, and those related to electronic excitation). Thus, plasmas, as multi-component systems, are able to exhibit multiple temperatures. In electric discharges common for plasma generation in the laboratory, energy from the electric field is first accumulated by the electrons between collisions and, subsequently, is transferred from the electrons to the heavy particles.

Electrons receive energy from the electric field during their mean free path and, during the following collision with a heavy particle, lose only a small portion of that energy (because electrons are much lighter than the heavy particles). That is why the electron temperature in plasma is initially higher than that of heavy particles. Subsequently, collisions of electrons with heavy particles (Joule heating) can equilibrate their temperatures, unless time or energy are not sufficient for the equilibration (such as in coronas and pulsed discharges) or there is an intensive cooling mechanism preventing heating of the entire gas (such as in wall-cooled low-pressure discharges). The temperature difference between electrons and heavy neutral particles due to Joule heating in the collisional weakly ionized plasma is conventionally proportional to the square of the ratio of the electric field (E) to the pressure (p).

A plasma source, which in most laboratory conditions is a gas discharge, represents the physical and engineering basis of the plasma chemistry. For simplicity, an electric discharge can be viewed as two electrodes inserted into a glass tube and connected to a power supply. The tube can be filled with various gases or evacuated. As the voltage applied

across the two electrodes increases, the current suddenly increases sharply at a certain voltage required for sufficiently intensive electron avalanches. If the pressure is low, on the order of a few torrs, and the external circuit has a large resistance to prohibit a large current, a glow discharge develops. This is a low-current, high-voltage discharge widely used to generate non-thermal plasma [1].

A similar discharge is known by everyone as the plasma source in fluorescent lamps. The glow discharge can be considered a major example of low-pressure, non-thermal plasma sources. In gases the process begins when a stray electron near the cathode carrying an initial current i_0 is accelerated toward the anode by the applied electric field (E). After gaining sufficient energy the electron collides with a neutral gas atom (A) converting it into a positively charged ion (A^+). During this impact ionization process, charge conservation indicates that two electrons are released, i.e., (equation 2.1).

$$e^- + A \rightarrow 2e^- + A^+ \tag{2.1}$$

These are accelerated and now bombard two additional neutral gas atoms, generating more ions and electrons, and so on. Meanwhile, the electric field drives ions in the opposite direction where they collide with the cathode, ejecting, among other particles, secondary electrons. These now also undergo charge multiplication. The effect snowballs until a sufficiently large avalanche current ultimately causes the gas to breakdown. In order for breakdown to occur, the distance (d) between electrodes must be large enough to allow electrons to incrementally gain the requisite energy for an ionization cascade. Also, the electrodes must be wide enough to prevent the loss of electrons or ions through sideways diffusion out of the interelectrode space.

The critical breakdown voltage (V_B) can be calculated as expressed by Paschen's Law, (equation 2.2).

$$V_B = \frac{APd}{\ln(Pd)+B} \tag{2.2}$$

where A and B are constants. At low values of Pd there are few electron-ion collisions and the secondary electron yield is too low to sustain ionization in the discharge. On the other hand, at high pressures there are

frequent collisions, and since electrons do not acquire sufficient energy to ionize gas atoms, the discharge is quenched. Thus at either extreme, ion generation rates are low and high voltages are required to sustain the discharge. In between, at typically a few hundred to a thousand volts, the discharge is self-sustaining. In most sputtering discharges the *Pd* product is well to the left of the minimum value [2].

2.2. Sputtering

Thin film fabrication has gained a great interest in the fields of microelectronics, optical coating and decorative parts. The properties of a material in the bulk form are different to those in the form of thin film. The properties of a synthesized thin film strongly depend on the adopted deposition techniques. Thin films can be deposited by physical process (thermal evaporation process and sputtering) or by chemical process (Plasma CVD and Laser CVD). In the physical processes thermal evaporation or physical vapor deposition (PVD) is performed in a high vacuum chamber where the atoms of the target material are evaporated from a crucible by heating it at high temperature, and are transported to deposit on the substrate. Sputtering is also a PVD technique where ion bombardment of a target is used to eject the atoms instead of high temperature. In the process the atoms are sputtered from a solid state target by bombarding its surface by energetic ions generated near the cathode (target) by collision with the electrons, which can be confined close to cathode by a magnetron. The sputtering process is performed in a vacuum system at a moderated vacuum (0.1 to 2 Pa). Sputtering was discovered by Grove in 1852 when he observed the cathodic material deposited on the anode in a glow discharge.

When a high energy electron (approximately 40 eV) collides with an Ar atom, it has a high probability of producing an Ar^+ ion and an additional electron that is (equation 2.3):

$$e^- + Ar = e^- + Ar^+ + e^- \tag{2.3}$$

In a sputtering process the cathode or target surface is bombarded by the high energy ions (usually, Ar^+). The incident ion actually becomes a neutral atom because Auger neutralization before impact; that is, it picks up an electron from the target, so that energetic Ar atom that shares its kinetic

momentum with target atoms. The target atom will get kinetic energy from the incident atom on a collision and will be displaced from its position deeper inside the material and will transfer its energy to other atoms of the material which also will displace from their positions. With the continuous impact and transfer of kinetic momentum from the incident energetic atoms to target, the atoms near the surface may be emitted by overcoming the surface binding energy. These ejected atoms are called sputtered atoms. In sputtering actually a transfer of momentum process take place between the incident Ar atom and target atom. In a single collision between Ar (mass M_1) and target atom (mass M_2), the maximum fraction of energy transfered to target atom is (equation 2.4) [4].

$$\frac{4M_1M_2}{(M_1+M_2)^2} \tag{2.4}$$

The sputtered atoms travels towards the substrate and on impact adsorbed on the surface by losing their velocity but due to difference in the thermal energies, atoms moves over the substrate surface. The moving atoms makes cluster by interacting with each other. These clusters or nuclei grow in size by attaching with each other and at a certain size becomes thermodynamically stable and nucleation barrier is said to be have been overcome. This is called *nucleation* stage. These grown nuclei are called island. These islands started to agglomerate and form bigger island in a process called *coalescence*. The empty spaces made by coalescence could be refilled by new nuclei. In this way a continuous film is formed [3].

The sputter yield *S*, is a parameter used to define the mean number of atoms or molecules removed from the surface of target material per incident ion. The sputter yield (*S*) for a given ion energy depends on the atoms density which should be higher in the target material and the mean free path should be shorter for higher yield (equation 2.5) [4].

$$S = \frac{k}{\lambda} \times \frac{4M_1M_2}{(M_1+M_2)^2} \times \frac{E_i}{E_b} \tag{2.5}$$

where λ is the mean free path of ions going against the target, which is a function of mass ratio, energy, and material property. The sputter yield is higher when incident angle between ion and target atom is between 45-75°. At higher ion energies usually > 40 keV, *S* becomes lower because of the

ion implantation in the target. *S* increases with atomic number (*Z*) but due to the binding energies differences, *S* is higer for nobel metals and lower for refractory metals. Sputtering yield (*S*) is given in atoms/ion, and the atoms have a given mass. These atoms are deposited. Thus, the sputtering and deposition rates are expressed in atoms·cm^{-2}s^{-1} or since atoms have a given mass, in g·cm^{-2}s^{-1}. However, rates are usually quoted in terms of thickness (e.g., μm/h or nm/s).

The sputtering rate can be increased by increasing the sputtering power but this will not affect the uniformity. However, changing the conditions, for example, pressure, may affect both deposition rate and uniformity.

A plasma discharge can be initiated by using direct current (DC), alternated current (AC), radiofrequency (RF) or pulsed-DC signals. The choice of the source of plasma power depends on the target material. The plasma is generated in the vacuum system by applying enough potential difference between the cathode and the anode in the presence of appropriate gas (Ar) density. Since the plasma functions electrically as a conductor, its potential is constant spatially across the chamber and only changes significantly at either the cathode or anode. The ions move with high energies towards the cathode and strikes there to eject the atoms of target material whereas electrons move towards the anode. The emission of secondary electrons from the cathode due to the ion bombardment maintains the plasma. This kind of plasma is called diode plasma. In the DC diode plasma the current densities at the cathode are about 0.01 mA·cm^{-2} and applied voltage is several kV. At low pressure (mTorr) plasma density is very low and the secondary electron can impact directly on the anode cause effect of the substrate. With the increase in the pressure (hundreds of mTorr) plasma density could be increased significantly but the deposition rate will become slow because of the increase in the collision between sputter atoms and gas.

DC sputtering system does not work when an insulated target is used, because sputtering glow discharge cannot be sustained due to immediate build-up of a surface charge of positive ions on the front side of the insulator. To overcome this problem alternating current (AC or RF) could be used so that target would alternately by positive ions and then by negative electrons so as to neutralize the charge. The applied frequency has mostly been set at 13.56 MHz. Rf potential provide two main advantages.

The first one is it facilitate the use of a dielectric target. The second advantage of a rf is that the coupling of a the energy from the electrons is better. Because of the oscillatory nature of the applied electric field, the electrons tend to be more readily retained in the plasma and their energy increased by a wave-coupling process [5].

The basic problems of the diode are due to long electron mean free path because electrons may reach the anode with high energy, heating the substrate but not producing the ions required for sputtering. Furthermore, using a low pressure discharge the sputter yield is low. These problems could be solved by using a magnetron sputtering system instead of diode systems. Magnetrons make use of the fact that a magnetic field configured parallel to the target surface can constrain secondary electron motion to the vicinity of the target. The magnets are arranged in such a way that one pole is positioned at the central axis of the target and second pole is formed by a ring of magnets around the outer edge of the target. The magnetic field *B* forces the electrons into semicircular orbits (these become cycloidal orbits when considering the crossed electric field closed to cathode). This is due to the magnetic component of the Lorentz force, (equation 2.6).

$$\vec{F} = -e(\vec{v} \times \vec{B}) \tag{2.6}$$

Where $\vec{v}$ is the velocity vector of the electron, charge $-e$, and $\vec{B}$ is the magnetic field. This field causes traveling electrons to spiral along magnetic flux lines near the substrate instead of being attracted toward the substrate. Trapping the electrons in this way substationally increases the probability of an ionizing electron-atom collision occurring. The increased ionization efficiency of a magnetron results in a dense plasma in the target region. This, in turn, leads to increased ion bombardment of the target, giving higher sputtering rates and, therefore, higher deposition rates at the substrate. In addition, the increased ionization efficiency achieved in the magnetron mode allows the discharge to be maintained at lower operating pressures (typically 10-3 mbar, compared to 10-2 mbar) and lower operating voltages (typically, -500 V, compared to -2 to -3 kV) than is possible in the basic sputtering mode [6].

Magnetron sputtering depends on the presence of a magnetic field above the target's surface. Ferromagnetic targets (Fe, Ni, Co, etc) of normal thickness have high magnetic permeabilities which traps the flux from the

source's normal magnet set. However, reducing the target's thickness causes it to saturate allowing the magnetic field to penetrate. Depending upon the magnetic saturation of the material, the thickness of the material must be made such that enables to transmit magnetic field over the target surface to maintain efficient plasma ionization. It is needed to change thin (0.5 mm) target frequently, because of fast resputtering [7].

In pulsed DC magnetron sputtering the frequency is much lower, typically 50-250 kHz depending upon the application. Generally, the discharge voltage cycles between a high negative voltage and a low positive voltage. The negative voltage part of the cycle is used to perform the sputtering, as the ions bombard the cathode. The low positive voltage part of the cycle is used to attract electrons to prevent charge buildup. Due to the higher mobility of the electrons, this part of the cycle can be relatively short compared to the total cycle time.

For the case of reactive deposition of oxides, it is usually sufficient simply to introduce oxygen into the deposition system: the oxidation reaction is sufficiently exothermic that the reaction occurs spontaneously at room temperature. As the deposition process proceeds, area on the target away from the main racetrack become covered with an insulating layer, as do the target earth shields. This coverage of the target with reaction product is called target poisoning. The poisoned layers charges up, until breakdown occurs in the form of an arc. Arc events during reactive sputtering are a serious problem, because the can affect the structure, composition and properties of the growing film and also lead to damage of the magnetron power supply. Pulsed Magnetron sputtering overcomes many of the problems encountered when operating a reactive sputtering mode. Pulsing the magnetron discharge in the medium frequency range (10-200 kHz) when depositing insulating films can significantly reduce the formation of arcs and consequently improve the film quality [5, 6].

2.3. Chemical Vapor Deposition

Chemical vapor deposition is a common name of the process in which elements in the vapor phase react chemically in an activated (heat, light, plasma) environment near or on a substrate surface to form a solid product. This method provides highly pure material at nanometer scale level. The history of CVD goes down to year 1893 when Lodyguine deposited W onto carbon lamp filament through the reduction of WCl_6 by

H_2. However it is only past 50 years a great understanding of CVD processes has been made. CVD techniques have been widely used in science and engineering fields. The CVD process is performed in vacuum condition to reduce the undesirable physical or chemical reactions from air constituents such as (oxygen or water vapors) and to increase the mean free path of the precursor gases to form uniform material on the substrate. The mean free path calculation (equation 2.7) is,

$$\lambda = \frac{kT}{\sqrt{2}\pi P d^2} \tag{2.7}$$

Where d is the molecular diameter, T is the temperature in Kelvin, k is Boltzmann constant and P is the pressure.

At room temperature we can use a simple equation to calculate the mean free path (equation 2.8).

$$\lambda(mm) = \frac{6.6}{P(Pa)} \tag{2.8}$$

where P is the pressure, λ varies moderately for usual gases.

It should be noted that mean free path is different from the average distance between the molecules. A normal CVD process is subject to very complicated fluid dynamics. The fluid (in this case a combination of gases), is forced through pipes, valves and various chambers and, at the same time, is the object of large variations in temperature and to a lesser degree of pressure, before it comes in contact with the substrate and the reaction takes place. The reaction is heterogeneous, which means that it involves a change of state, in this case from gaseous to solid. In some cases, the reaction may take place before the substrate is reached while still in the gas phase (gas phase precipitation).

CVD reaction can be classified into several major categories such as. (1) Thermal decomposition, in which a molecule is broken apart into its constituents or more elementary molecule. (2) Hydrogen reduction. Reduction is the process in which an element gains an electron. Hydrogen reduction has a major advantage in that the reaction generally takes place at lower temperature than equivalent decomposition reaction. Hydrogen has a supplementary role in reaction, which has not a primary function. Hydrogen is necessary to prevent the formation of oxides or carbides and

generally improve the characteristics and properties of the deposited material. CVD reactor main function is to heat the sample [8].

2.4. Atmospheric and low pressure reactor

At atmospheric pressure, the rate of gas-phase transport (i.e. the rate of diffusion through the boundary layer) of both reactant gases (diffusing in) and by-product gases (diffusing out) is low and the reaction is diffusion limited.

On the other hand, at low pressure (i.e. < 1 Torr), the rate of gas-phase transport of both reactants and by-products is increased in inverse proportion to pressure, by a factor of 100 if *P* is decreased from 760 to 7.6 Torr. However, one may not gain similarly if the pressure decrease is at the expense of the partial pressure of reactant gas, e.g., the kinetic rate (for first order reactions) may be directly proportional to the reactant partial pressure. Reduction of pressure by eliminating carrier gas is always beneficial. At low pressure, surface reaction is the rate determining step and the mass transfer variables are far less critical than at atmospheric pressure. In practical terms, this means that low pressure generally provides film with more uniformity, better step coverage and improved quality. Some reactants in atmospheric pressure reactors must be highly diluted with inert gases to prevent vapor phase precipitation while generally no dilution is necessary at low pressure.

CVD does not require as low pressures as those normally used by sputtering, ion implantation and other PVD processes. Consequently, the vacuum system is simpler and less costly. The main function of the CVD reactor is to heat the sample. The temperature during CVD is usually in the range of 500 to 2000°C. There are two kinds of reactors for the CVD process, hot wall or cold wall reactor. A hot wall reactor is an isothermal reactor in which temperature is controlled independent of the substrate temperature, whereas in the cold wall reactor which is also called adiabatic reactor the temperature is controlled directly by measuring the substrate temperature.

A CVD process assisted by plasma is called plasma enhanced chemical vapor deposition (PECVD). PECVD is an attractive alternative for depositing a variety of thin films at lower temperatures than those utilized in CVD reactors. The PECVD process employed in our research is a capacitively coupled RF power or pulsed-DC power. Plasma CVD

combines a chemical process with a physical process and, to some degree bridges the gap between CVD and physical vapor deposition (PVD). It is similar to the PVD processes operating in a chemical environment such as reactive sputtering. Power is driven to the small electrode (cathode), where the substrate is placed, and the reactor walls are usually grounded (anode). Electrical power (usually DC, RF or pulsed-DC) is used to initiate a glow discharge into a gas mixture. Electrical power at a sufficient high voltage to a gas at reduced pressure (< 1.3 kPa), results in the breaking down of the gas and generates a glow discharge consisting of radicals, ions, neutral atoms and molecules, and other highly excited species. The vapor reactants are ionized and dissociated by electron impact, and enhance generating chemically active ions and radicals that undergo the heterogeneous chemical reaction, depending the nature of these interaction, either ion etching or deposition processes occurs at the substrate. Since the formation of the reactive and energetic species occurs by the collisions in the gas phase, the substrate can be maintained at low temperature. Hence, film formation can occur on substrate at low temperature. The chemical reactions that occur during the glow discharges are complex and can be categorized into homogeneous gas phase collisions and heterogeneous surface interactions [8, 9].

2.5. Principles of plasma deposition

As the temperature of a gas increases, the atoms are gradually ionized, that is they are stripped of their electrons and a plasma is formed which consists of ions (with +ve charge), electrons (with –ve charge) and atoms that have not been ionized (neutral). Above some temperature, all gas molecules are dissociated into atoms which are increasingly ionized. However, to accomplish this, a very large amount of energy is required and, as a result, temperatures must be very high (> 5000K). A plasma generated by a combustion flame has a temperature limit of approximately 3700 K, which is not sufficient for complete ionization. In fact, such plasma is only 10% ionized.

A more convenient way to achieve high temperature is with a low frequency discharge. By increasing the electrical energy in a fixed amount of gas, all molecules are eventually dissociated and complete ionization is achieved. In such a low frequency discharge, both electrons and ions respond to the constantly changing field direction; they both acquire energy

and their temperature is raised more or less equally. The plasma is in equilibrium (isothermal). Isothermal plasmas are generated at relatively high pressure (100 Torr to 1 atm). At such pressure, the mean free path, which is the average distance traveled between collisions, is much reduced, collisions are more frequent and molecules and ions heat readily.

Arc discharge plasma requires a large amount of power and is extremely hot. For that reason, they have not been used to any extent in CVD deposition except for the very special and important case of diamond deposition or carbon nanoparticles production.

Another type of plasma of major interest in CVD is the non-equilibrium (or non-isothermal) plasma (glow discharge) which is generated in a gas by a high frequency electric field and operates at lower pressure than the isothermal plasma. In such plasma, the following events occur:

a) In the high energy frequency electric field, the gases are ionized into electrons and ions. The electrons, which are considerably lighter than other species, are quickly accelerated to high levels of energy (commonly 1 to 11 eV) corresponding to electronic temperatures of 11,500 to 130,000 K. In spite of these very high values, electrons have very low mass and they do not appreciably raise the plasma temperature.
b) The heavier ions with their greater inertia cannot respond to the rapid changes in the field direction, in contrast with their behavior in a low frequency field. As a result, their temperature and the temperature of plasma remains low (hence the name non-isothermal plasma).
c) The high energy electrons collide with the gas molecules with resulting dissociation and generation of reactive chemical species and the initiation of chemical reaction.

The current used high frequencies are radio frequency (RF) at 13.45 MHz and microwave (MW) frequency at 2.45 GHz [9].

2.6. Characteristics of plasma CVD process

Advantages

1. Plasma CVD has several advantages. It is capable of forming a deposit at temperatures (low) where, no reaction whatsoever would take place in thermal CVD.

2. Another advantage is that the effects of thermal expansion mismatch between substrate and coating and resulting stresses are reduced since the temperature of deposition remains low.
3. In addition, the deposition rates are usually increased and, since the pressure is low (in the case of glow discharge plasma CVD), the rate controlling factor is surface kinetics, which leads to greater uniformity.
4. The low temperature of deposition also favors the formation of amorphous or very fine polycrystalline deposits which usually have superior properties.

Limitations

1. It is difficult to obtain a deposit of pure material. In most cases, desorption of by-products and other gases, particularly hydrogen, remains as inclusion in the deposit. However in some cases it has advantage for instance, amorphous silicon used in solar cells has improved optoelectronic properties if hydrogen is present.
2. Plasma CVD tends to create undesirable compressive stresses in the deposit particularly at the lower frequencies. This may not be a problem in very thin films used in semiconductor application, but in thicker films typically metallurgical applications, the process carries peeling and cracking.
3. Another disadvantage is that fragile substrate used in VLSI, semiconductor materials, can be damaged by the ion bombardment from the plasma, particularly if the ion energy exceeds 20 eV. In addition, the plasma reacts strongly with the surface of the coating as it is deposited. This means that the deposition rate and often the film properties depend on the uniformity of the plasma. Areas of the substrate fully exposed will be more affected than the more sheltered ones.
4. The equipment is generally more complicated and more expensive [9].

2.7. CNTs synthesis technologies

Carbon nanotubes are generally produced by three main techniques, arc discharge, laser ablation and chemical vapour deposition. However,

scientists are researching more economic ways to produce these structures. In arc discharge, a vapour is created by an arc discharge between two carbon electrodes with or without catalyst. Nanotubes self-assemble from the resulting carbon vapour. In the laser ablation technique, a high-power laser beam impinges on a volume of carbon –containing feedstock gas (methane or carbon monoxide). At the moment, laser ablation produces a small amount of clean nanotubes, whereas arc discharge methods generally produce large quantities of impure material. In general, chemical vapor deposition (CVD) results in MWNTs or poor quality SWNTs. The SWNTs produced with CVD have a large diameter range, which can be poorly controlled. But on the other hand, this method is very easy to scale up, what favors commercial production.

2.7.1. Arc discharge

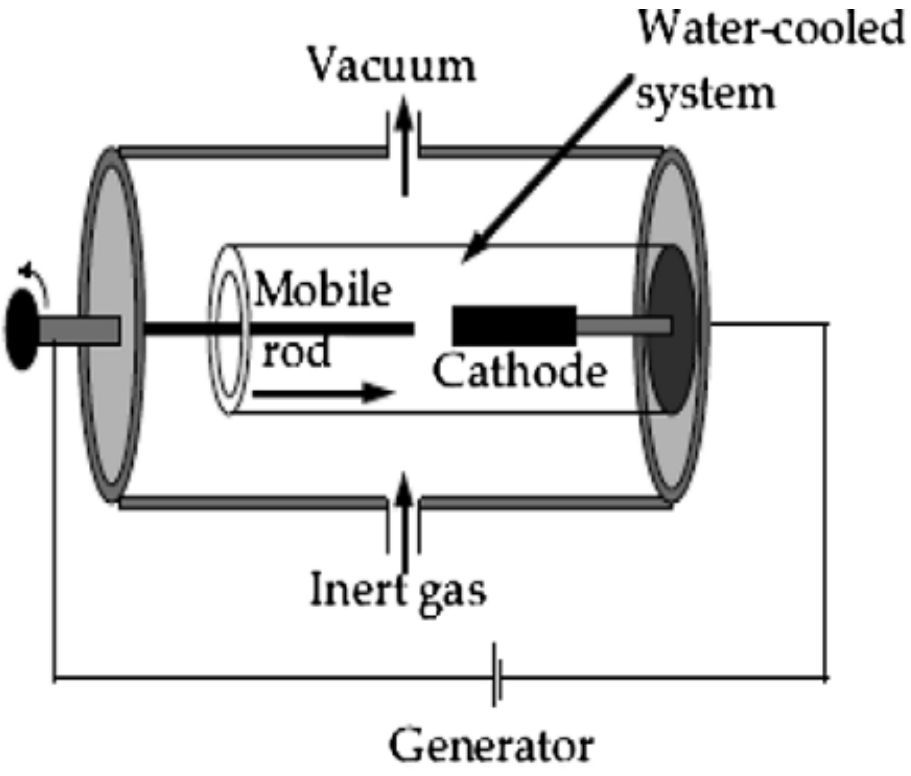

Figure 2.1: Experimental set-up of an arc discharge apparatus [10].

The arc discharge method (figure 2.1), initially used for producing C60 fullerenes, is the most common and perhaps easiest way to produce CNTs as it is rather simple to undertake. However, it is a technique that

produces a mixture of components and requires separating nanotubes from the soot and the catalytic metals present in the crude product [10].In this method an electric arc discharge is generated between two graphite electrodes under inert atmosphere of helium or argon. A very high temperature is obtained which allows the sublimation of the carbon. For the carbon nanotubes to be obtained, purification by gasification with oxygen or carbon dioxide is needed. For single wall nanotubes to be obtained a metal catalyst is needed. Process parameters involve small gaps between electrodes *(*~1 mm), high current (100 A), plasma between the electrode at about 4000 K and voltage range (30-35 V) under specified electrode dimensions [11].

2.7.2. Laser ablation

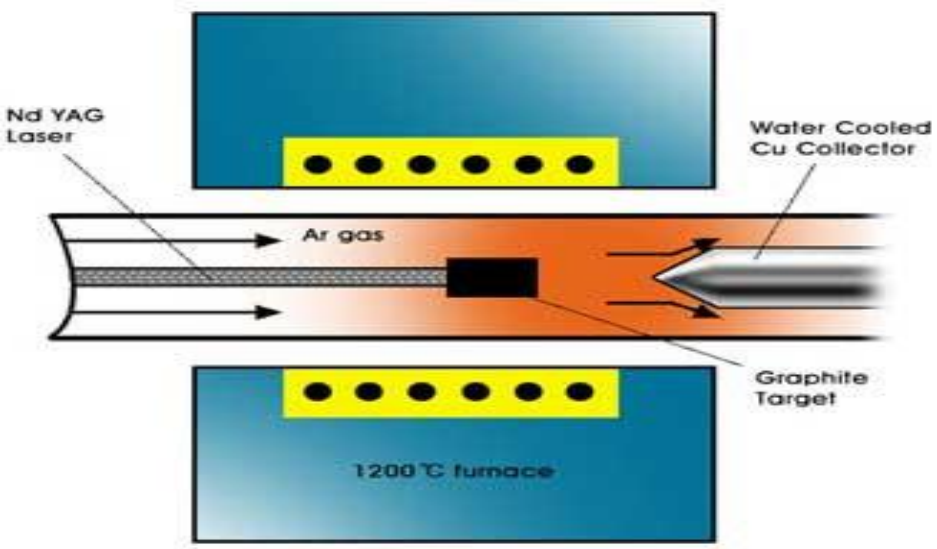

Figure 2.2: Schematic drawings of a laser ablation apparatus [10].

A pulsed or continuous laser (figure 2.2) is used to vaporize a graphite target in an oven at 1200°C. The oven is filled with helium or argon gas in order to keep the pressure at 500 Torr (6.7×10^4 Pa). A hot vapor plume forms, then expands and cools rapidly. As the vaporized species cool, small carbon molecules and atoms quickly condense to form larger clusters, sometimes including fullerenes. The catalysts also begin to condense, but more slowly at first, and attach to carbon clusters and prevent their closing into cage structures. Catalysts may even open cage

structures when they attach to them. From these initial clusters, tubular molecules grow into SWCNTs until the catalyst particles become too large, or until conditions have cooled sufficiently that carbon no longer can diffuse through or over the surface of the catalyst particles [10].

2.7.3. Thermal chemical vapor deposition

In this method Fe, Ni, Co or an alloy of the three catalytic metals are initially deposited on a substrate. After the substrate is etched in a diluted HF solution with distilled water, the specimen is placed in a quartz boat. The boat is positioned in a CVD reaction furnace, and nanometer-sized catalytic metal particles are formed after an additional etching of the catalytic metal film using NH_3 gas at a temperature of 750 to 1050°C. As carbon nanotubes are grown on these fine catalytic metal particles in CVD synthesis, forming these fine catalytic metal particles is the most important process. (Figure 2.3) shows a schematic diagram of thermal CVD apparatus in the synthesis of carbon nanotubes.

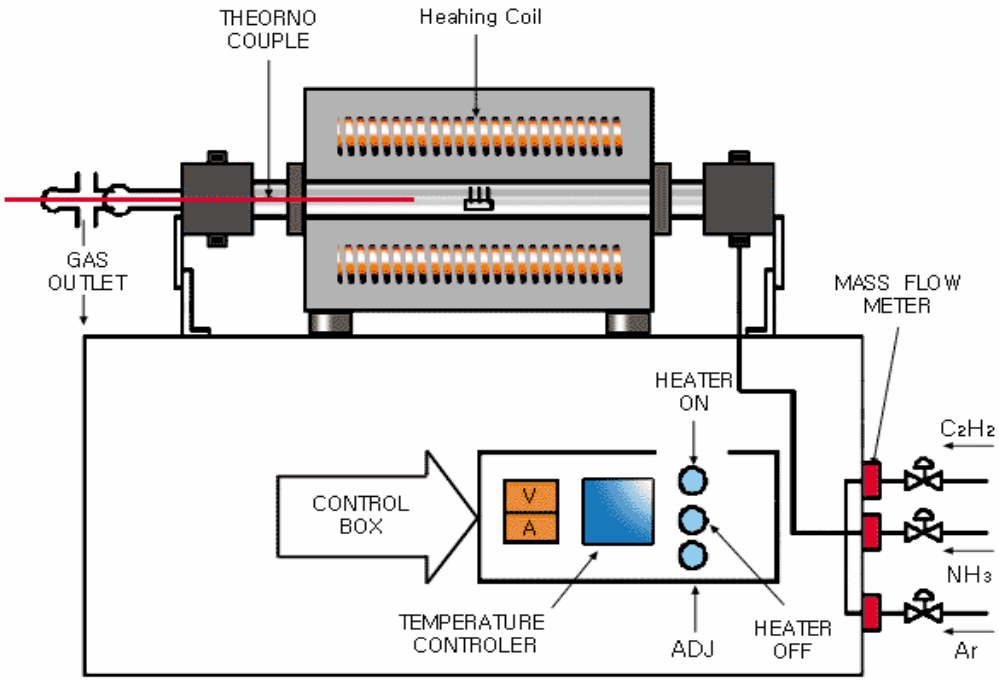

Figure 2.3: Schematic diagram of thermal CVD apparatus [10].

2.7.4. Vapour phase growth

Vapour phase growth is a synthesis method of carbon nanotubes, directly supplying reaction gas and catalytic metal in the chamber without a substrate. (Figure 2.4) shows a schematic diagram of a vapour phase

growth apparatus. Two furnaces are placed in the reaction chamber. Ferrocene is used as catalyst. In the first furnace, vaporisation of catalytic carbon is maintained at a relatively low temperature. Fine catalytic particles are formed and when they reach the second furnace, decomposed carbons are absorbed and diffused to the catalytic metal particles. Here, they are synthesized as carbon nanotubes. The diameter of the carbon nanotubes by using vapor phase growth are in the range of 2 – 4 nm for SWNTs and between 70 and 100 nm for MWNTs.

2.7.5. CNTs growth by Chemical vapor deposition (CVD)

Chemical vapor deposition (CVD) is the most prominent technique to synthesize the CNTs. It is also known as thermal CVD or catalytic CVD. As compared to arc-discharge and laser-ablation methods, CVD is a simple and economic technique for synthesizing CNTs at low temperature and ambient pressure. In crystallinity, arc- and laser-grown CNTs are superior to the CVD-grown ones (although CVD-grown MWCNTs possess inferior crystallinity, the crystallinity of SWCNTs grown by CVD is close to that grown by arc or laser methods). However, in yield and purity, CVD beats the arc and laser methods. And, when it comes to structure control or CNT architecture, CVD is the only answer. Arc discharge and laser vaporization can be classified as high temperature (> 3000 °C) and short time reaction (μs to ms) techniques, whereas catalytic CVD is a medium temperature (500-1100°C) and longtime reaction (typically minutes to hours) technique. The CVD method uses a carbon source in the gas phase and a heated coil, to transfer the energy to the gaseous carbon molecule. Commonly used carbon sources are methane, carbon monoxide and acetylene. The energy source cracks the molecule into atomic carbon. The carbon then diffuses towards the substrate, which is heated and coated with a catalyst (usually a first row transition metal such as Ni, Fe or Co) and binds to it [12]. CVD is versatile in the sense that it offers harnessing plenty of hydrocarbons in any state (solid, liquid or gas), enables the use of various substrates, and allows CNT growth in a variety of forms, such as powder, thin or thick films, aligned or entangled, straight or coiled nanotubes, or a desired architecture of nanotubes on predefined sites of a patterned substrate. It also offers better control on the growth parameters [13].

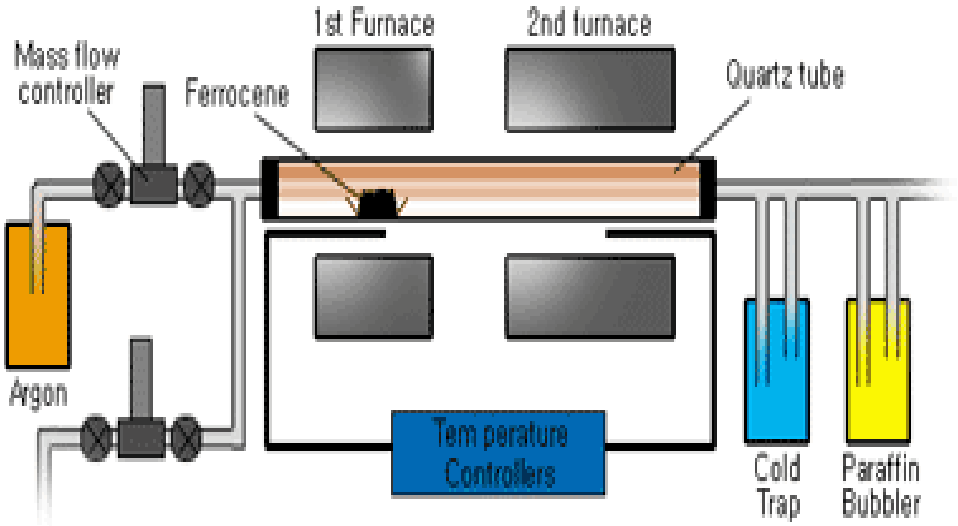

Figure 2.4: Schematic diagram of a vapor phase growth apparatus [10].

The growth mechanism of CNTs is still somewhat controversial. The suggested mechanisms for the growth of CNTs are VLS (vapor-liquid-solid) theory [14, 15, 16] and vapor-solid-solid (VSS) (figure 2.5) [17]. Few basic steps are generally acknowledged in chemical CNT production regardless of whether the growth takes place in the gas phase or on a supported surface. The catalyst is generally prepared by sputtering a transition metal onto a substrate, followed by etching by chemicals such as ammonia, or thermal annealing, to induce the nucleation of catalyst particles. Thermal annealing results in metal cluster formation on the substrate, from which the nanotubes grow. The temperature for the synthesis of nanotubes by CVD is generally in the 650–900°C range. Hydrocarbon vapor when comes in contact with the "hot" metal nanoparticles, first decomposes into carbon and hydrogen species; hydrogen flies away and carbon gets dissolved into the metal. After reaching the carbon-solubility limit in the metal at that temperature, as-dissolved carbon precipitates out and crystallizes in the form of a cylindrical network having no dangling bonds and hence energetically stable. Hydrocarbon decomposition (being an exothermic process) releases some heat to the metal's exposed zone, while carbon crystallization (being an endothermic process) absorbs some heat from the metal's precipitation zone. This precise thermal gradient inside the metal particle keeps the process on.

Chen et al. performed ethanol CVD directly on SiO_2 nanoparticles without any metal. Their results suggest that, during the CVD, SiO_2 does not form any SiC phase and the SWCNT nucleation and growth occur by carbon diffusion on solid SiO_2 particles, following a vapor-solid-solid (VSS) model [17].

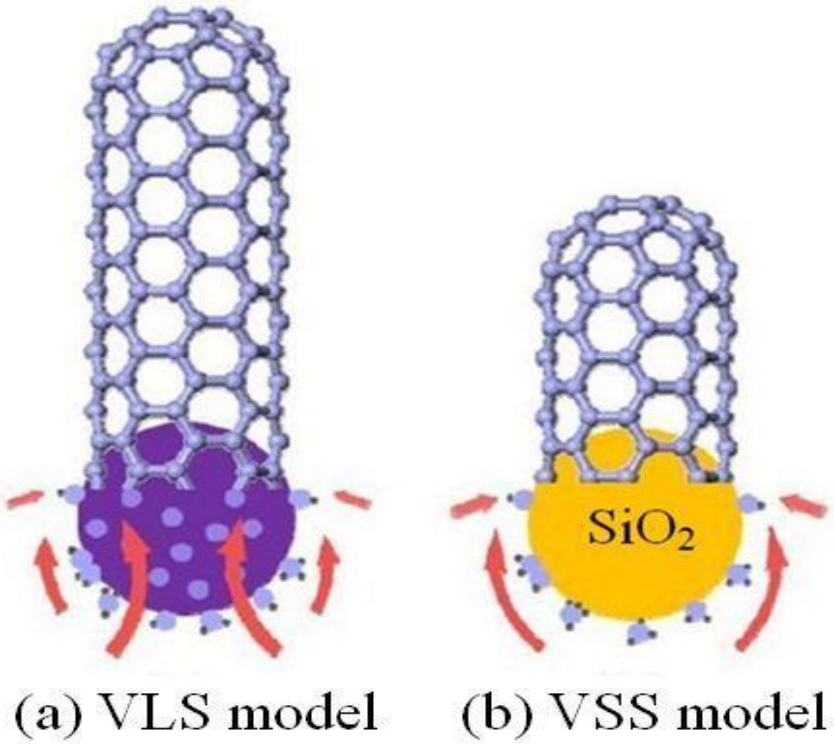

Figure 2.5: (a) The classical VLS mechanism during SWCNT growth by metallic catalyst. (b) The supposed VS mechanism during SWCNT growth from SiO_2 nanoparticles as nucleation centers [17].

There are two different growth mechanisms in a CVD process, tip growth and root growth. When the catalyst-substrate interaction is weak hydrocarbon decomposes on the top surface of the metal, carbon diffuses down through the metal, and CNT precipitates out across the metal bottom, pushing the whole metal particle off the substrate. As long as the metal's top is open for fresh hydrocarbon decomposition, the concentration gradient exists in the metal allowing carbon diffusion, and CNT continues to grow longer and longer. Once the metal is fully covered with excess carbon, its catalytic activity ceases and the CNT growth is stopped. This is known as "tip-growth model". In the other case, when the catalyst-substrate interaction is strong, initial hydrocarbon decomposition and carbon

diffusion take place similar to that in the tip-growth case, but the CNT precipitation fails to push the metal particle up; so the precipitation is compelled to emerge out from the metal's apex (farthest from the substrate, having minimum interaction with the substrate). At first, carbon crystallizes out as a hemispherical dome (the most favorable closed-carbon network on a spherical nanoparticle) which then extends up in the form of seamless graphitic cylinder. Subsequent hydrocarbon decomposition takes place on the lower peripheral surface of the metal, and as-dissolved carbon diffuses upward. Thus, CNT grows up with the catalyst particle rooted on its base; hence, this is known as "base-growth model" [13]. CNT synthesis involves many parameters such as hydrocarbon, catalyst, temperature, pressure, gas-flow rate, deposition time, reactor geometry.

2.7.6. CNTs growth by plasma enhanced CVD

In the field of microelectronic application, controllable assembly and directional in situ synthesis of CNTs are very crucial steps to incorporate CNTs directly into the integrated circuit. However, the synthesis of CNTs using CVD method requires undesirably high temperature, which damages the electronic chip. Plasma-enhanced chemical vapor deposition (PECVD) method offers a solution to low temperature synthesis of CNTs. The plasmatic energy efficiently dissociates gas molecules at lower temperatures, and the synthesis of carbon nanotubes might occur at lower temperature. PECVD has been investigated for its ability to produce vertically-aligned nanotubes. It has been suggested that in PECVD only VACNTs grown from the tip are aligned specifically due to the presence of the plasma electric field in the growth process, whereas VACNTs grown from the base are aligned mainly due to the crowding effect. The electrostatic force F creates a uniform tensile stress across the entire particle/CNT interface, regardless of where the particle is located tip or at base [18]. The plasma is composed of electrons, charged species and ions, and neutral atoms and molecules. The plasma remains electrically neutral as the ion density is balanced by the electron density. The electron density in the radio frequency generated plasma is typically ~10^8-10^9 cm^{-3} for a pressure range of 0.1-100 Torr. The electron temperatures are ~1-11 eV, while the ion temperatures are lower at ~50-100 meV. There is also a spontaneous but nonequilibrium conversion of neutral species into long

lived radicals. The plasma forms ‘‘sheaths’’, dark regions of very low electron density, with the electrodes [19].

The growth of CNTs synthesized using high temperature CVD methods had been proposed to be a vapour-liquid-solid mechanism. The catalyst was in a liquid drop state and carbon species from the chemical vapor dissolved into it. Carbon nanotubes were precipitated from the supersaturated eutectic liquid. The activated energy for (thermal) CVD (≤ 700 °C) was reported to be ~ 1.2-1.8 eV. Clearly, this proposed growth mechanism of CNTs was not suitable for low temperature growth (< 120 °C), whereby the catalysts might remain as solids at such low temperatures. Low activation energy of ~ 0.2-0.4 eV was reported for low-temperature plasma assisted growth of CNTs. In order to synthesize SWCNTs, it required the use of special plasma configuration such as remote plasma or point arc discharge, whereby the substrates were minimally exposed to the plasma sheath. In the plasma sheath, high density of plasma ion flux bombardment at sufficiently high energy caused C–C bond breakage. The presence of plasma radicals such as NH_x and H further chemically etched the surface of the carbon nanotubes. The growth mechanism of SWCNT in a PECVD process determines the endurance of the carbon nanotubes towards ion-etching effects. In the tip-growth mechanism, the catalyst at the tip of the vertically growing SWCNT, offered protection to walls of the nanotube from the ion etching effects. On the other hand, in base-growth mechanism, the catalyst adhered to the substrate, and the vertically growing SWCNTs had uncapped tips, which are easily destroyed by the impinging ions [19]. In a typical plasma, ions constitute only one part per million of the total number of the gas species, whereas the fraction of neutral radicals is of the order of 1%. Therefore, the growth is essentially due to the neutral radicals (and species that form due to mutual collisions of these radicals as they move towards the substrate across the dark space) [20, 21].

2.8. Catalysts for CNTs and their properties

It is well known that a 3d transition metal (Fe, Co, Ni) catalyst is complementary for the CVD growth of CNTs. It is because of the high solubility of carbon in these metals at high temperatures and high carbon diffusion rate in these metals. As well as these metals shows strong adhesion with growing nanotubes. Apart from the popular transition metals (Fe, Co, Ni), other metals of this group, such as Cu, Au, Ag, Pt, Pd were

also found to catalyze CNT growth from various hydrocarbons [22]. Noble metals (Au, Ag, Pt, Pd) also catalyze the growth of CNTs. In conclusion any metal can catalyze the growth of CNTs providing the right experimental condition [13].

In most of the cases a barrier layer could be metal (e.g. Al, Ti) or metal oxide, (e.g. Al_2O_3, SiO_2) is deposited on the top surface of the substrate to avoid the catalyst diffusion upon annealing at higher temperature. The heating is performed in an inert atmosphere such as under hydrogen flow to reduce the catalyst to metallic form during heating. At a desired temperature the thin catalyst film collapse and converts into nanometric size particles. The size of nanoparticles tells the diameter of the growing nanotube.

So starting from an oxide catalyst, a reduction of metal oxide takes place during decomposition of carbon precursor compound. As a result, a metallic particle forms through intermediate oxide states. Upon carbon dissolution, metal-carbon mixture or metal carbide is formed. Subsequent segregation results in the formation of graphitic carbon and metal particles. Bimetallic catalyst such as iron-cobalt alloy shows higher catalytic activity on the basis of lower melting temperature and an increase in carbon solubility [23, 22]. The size of metal particles explain the melting temperature of the metal, at a size of less than about 100 nm melting temperature can be lowered significantly and lower than 10 nm an exceptional decrease is observed. The reason is at nanometric size the ratio of surface atoms increase with respect to internal atoms. The surface atoms are electronically and coordinately unsaturated and thus are more reactive and mobile [22]. The melting temperature of iron, nickel, gold and silver as a function of particle diameter is shown in (figure 2.6).

The melting temperature of a metal particle (T_c) with radius r can be approximated by following (equation 2.9) [24].

$$T_c = T_0 - \frac{2T_0}{\Delta H_{fusion}\rho_s r}\left[\sigma_{sl} + (1 - \frac{\rho_s}{\rho_l})\sigma_l\right] \qquad (2.9)$$

where T_0 is the bulk melting temperature, ΔH_{fusion} is the latent heat of fusion, ρ_s and ρ_l are the densities of solid and liquid metal respectively, σ_l is the surface energy of the liquid.

Carbon solubility in metals is a temperature dependent property, which increases with increase in temperature. Due to the small size of

transition metals carbon solubility can be efficiently increased. The effect of particle size on solubility can be calculated as from below (equation 2.10).

$$S = S_0 \exp\left(\frac{2\sigma V}{kTr}\right) \quad (2.10)$$

where S and S_0 are solubilities in the particle and bulk material, respectively [22].

The eutectic temperature for the Fe -carbon in the bulk phase is 1153 °C but it decreased down to 732°C significantly at the nanometer scale. At higher temperature catalyst particle is more active and stay in liquid phase for longer time but it is important to grow the nanotubes at the temperature well below self-pyrolysis temperature and above the metal-carbon eutectic. The self-pyrolysis temperature depends on the stability of the carbon source used and the eutectic point decreases for all metals with the film thickness. The catalyst deactivation due to the amorphous carbon is a major problem which is the result of the self-pyrolysis of hydrocarbon or excessive carbon concentration [25, 22].

The chemical reactivity between metallic catalyst (e.g. Fe) and oxide support (e.g., Al_2O_3) influence the particle size distribution. The Al_2O_3 act as an oxygen "getter" for the Fe oxide, therefore it reduces the Fe to metallic Fe. The oxidation state of the catalyst depends on the gas used for the thermal annealing process and it determines the growth process of the CNTs. The catalyst activity increases in the following order: FeO < Fe_2O_3 < Fe_3O_4 < Metallic Fe [26]. Zhanbing He et al. stated that both Fe and Fe-C (generally Fe_3C) compounds catalyze the growth of CNTs. They proposed that formation of Fe_3C nanoparticles take place at the start of growth process and kept during the growth [27].

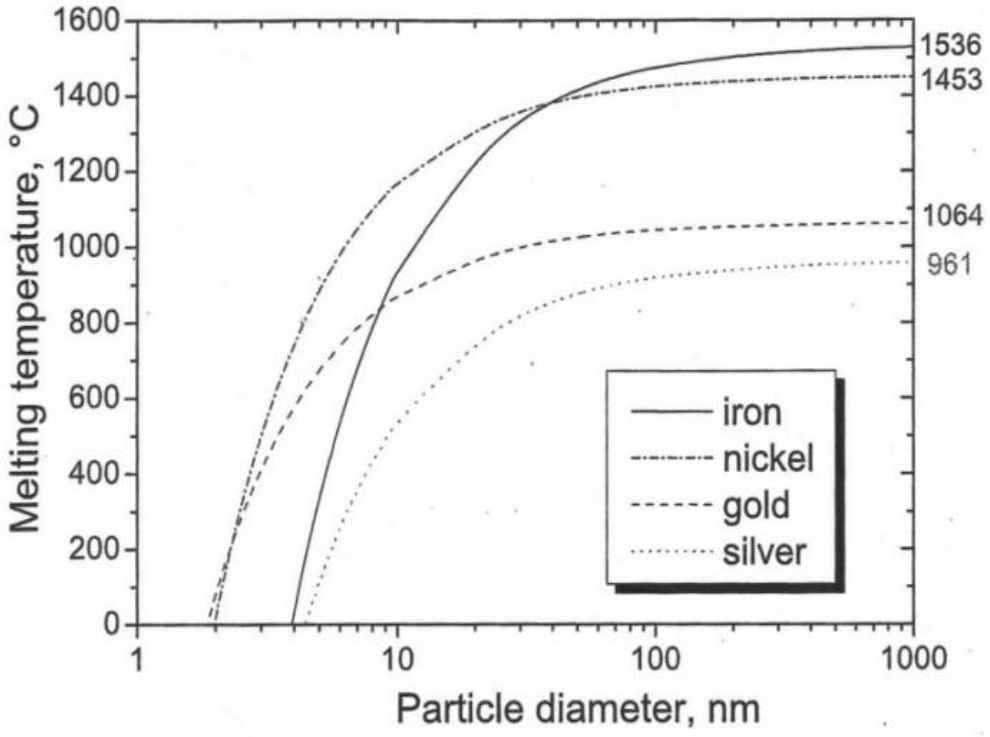

Figure 2.6: Melting temperature of selected metals as a function of particle diameter [22].

Porous Al_2O_3 has already been shown to facilitate CNT growth without any catalyst [28]. L Camilli et al. synthesized CNTs on a stainless steel substrate without support of catalyst material. They suggested that metallic composition and surface morphology of stainless steel substrate favor the growth of CNTs. This native metallic surface morphology is the principal ingredient that excludes the addition of external metallic catalyst [29]. Rummeli et al., found the continuous growth of CNTs even when Fe catalyst stops where cyclohexane was used as a carbon source CVD process at 800°C. An oxide, typically used as a catalyst support in CVD, is itself capable of forming graphene layers [30].

The catalytic CVD growth of CNTs is driven by the surface and bulk diffusion of the carbon to the catalyst nanoparticles. In 2007, Hofmann et al. reported an atomic-scale environmental TEM observation of CNT growth from acetylene decomposition on Ni particles at 480°C (figure 2.7). Initially, the Ni clusters had a round shape which transformed into an elongated shape (perpendicular to the substrate) surrounded by a thin carbon layer. This elongation was in contact with the substrate up to 0.8 s and suddenly (at 0.87 s), the Ni cluster left the substrate contact and contracted upward taking a round shape and leaving behind a hollow carbon tube. This elongation and contraction of Ni re-occurred alternately,

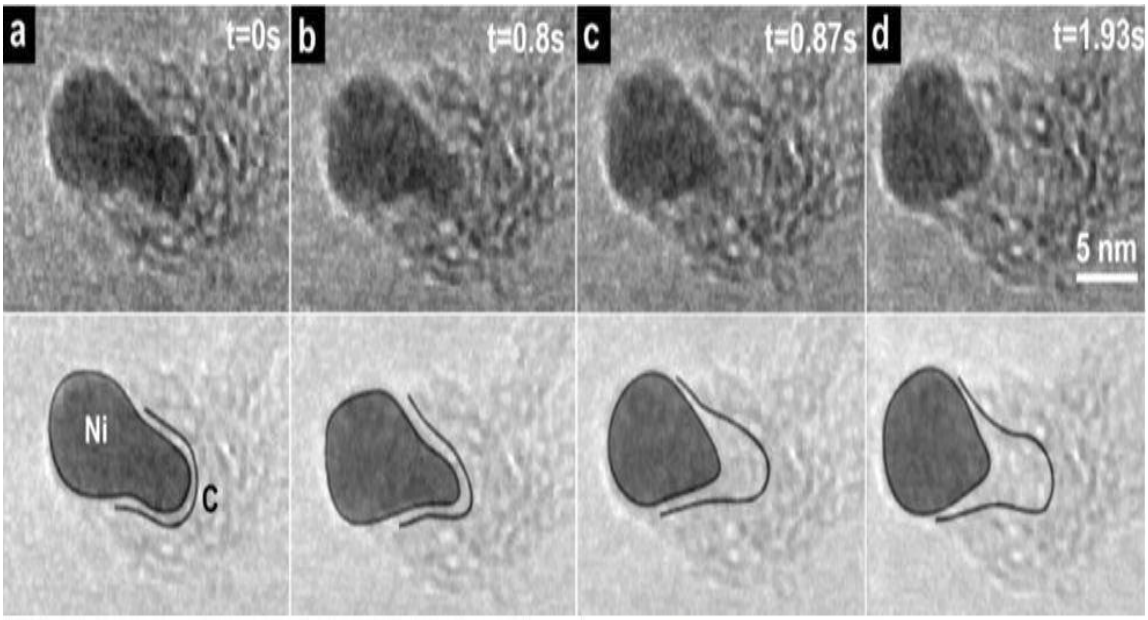

Figure 2.7: TEM image sequence showing a growing CNF in 3:1 NH_3:C_2H_2 at 1.3 mbar and 480 °C. The video was recorded at 30 frames/s, and the time of the respective stills is indicated. Drawings (lower row) indicate schematically the Ni catalyst deformation and C-Ni interface [31].

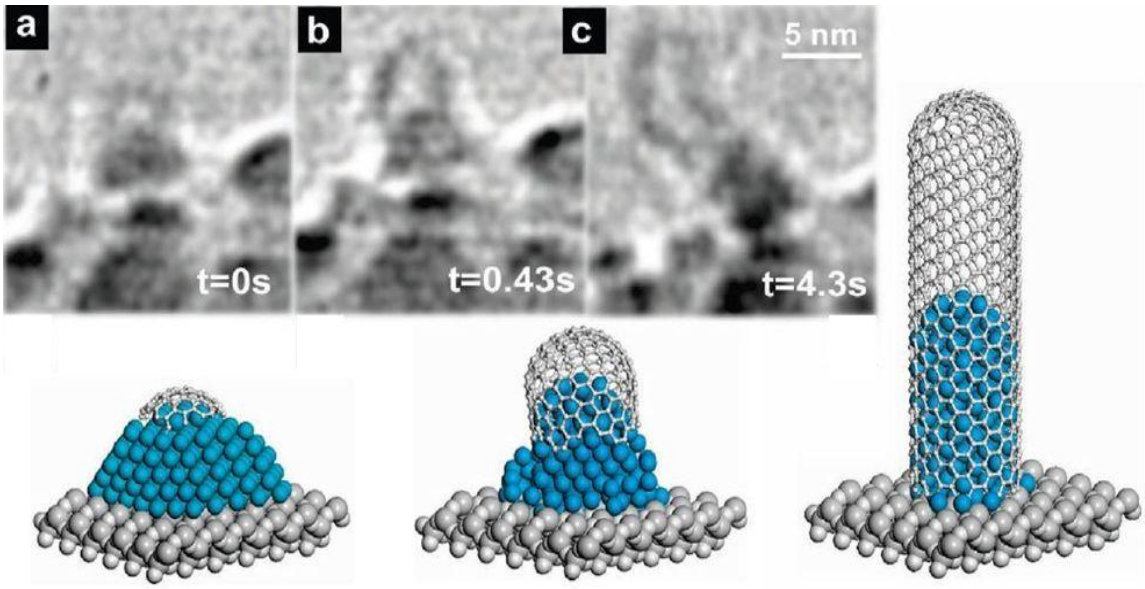

Figure 2.8: In-situ TEM image sequence showing a SWCNT nucleation and growth, and corresponding growth scheme [31].

moving ahead and leaving behind a bamboo-like MWCNT grown. The inner walls of the tube appeared to emerge from step-like stages of Ni cluster, suggesting that carbon atoms also diffuse deep inside the Ni cluster and crystallize in the form of inner tube walls when the Ni cluster moves up (contracts back to round shape at the CNT tip). In the base growth model, (figure 2.8) initially, a carbon cap emerged with a diameter smaller than the Ni cluster. Then, the apex portion of the cluster assumed a cylindrical shape, pushing the carbon cap off the cluster and forming a SWCNT. Finally, the CNTs network expanded upward by itself. These evidences also explain the general experience that small nanoparticles are crucial for SWCNT formation. Small metal clusters (1–2 nm) have sharp edges (atomic steps); hence they possess high catalytic activity and are capable to form high-strain SWCNTs. With the increasing cluster size, the sharpness of the atomic steps at the cluster boundary decreases and so does their catalytic activity. Therefore, bigger metal clusters (5–20 nm) form less strained MWCNTs. Too big clusters (viz. 100 nm) acquire almost spherical boundary with no sharp steps; that is why they do not form CNTs at all [31, 32].

2.9. Effect of various gases on the morphology of CNTs

In order to prevent the deposition of amorphous carbon ("a-C"), which inhibits the formation of nanotubes by poisoning the growth catalyst and can also cause short circuits on the substrate surface, the carbon source (typically, C_2H_2 or CH_4) is combined with a hydrogen-rich gas (typically, NH_3 or H_2), which produces reactive species in the plasma to remove any excess carbon. The use of etch gas during the growth process of CNTs is important. It has been widely reported that atomic hydrogen is the active species for the removal of excess carbon.

NH_3 has a key role in removing any excess carbon through the generation of reactive atomic hydrogen species, which combine with and carry away carbon atoms. At high NH_3 ratios, NH_3 decomposes preferentially over C_2H_2. This is because the chemical bonds that hold the NH_3 molecule together are weaker than those that hold C_2H_2 together. This allows the C_2H_2 to decompose slowly, generating the small amounts of carbon necessary for nanotube self-assembly. At high C_2H_2 ratios, there is insufficient NH_3 to effectively suppress C_2H_2 decomposition, resulting in higher levels of carbon generation and deposition of excess carbon as a-C.

NH_3 therefore has two key roles in the formation of carbon nanotubes: Not only does it generate atomic hydrogen species to remove any excess carbon, it also suppresses the decomposition of C_2H_2, limiting the amount of carbon generated in the first place. The gas-phase removal of carbon-containing species results in the production of gaseous HCN, which is detected in the mass spectra [33].

Etchant gas makes an impact on the morphology (cylindrical or bamboo like) of the CNTs. A. Gohier et al. study the effect of etchant gases (H_2 and NH_3) on the CNTs structure in a PECVD growth process. Ions produced in H_2 (H^+ or H_3^+) are significantly lighter than those generated in NH_3 (NH_3^+, NH_2^+, NH^+,…). Therefore, ion physical etching is drastically reduced and ion effects on the CNT structure is reduced (but not suppressed). Second, concerning the chemical etching, H_2 plasma produces less hydrogen radicals than NH_3 related to its higher dissociation energy (H-H:4.52 eV vs H-NH_2:1.92 V). Hence, there is reduction of carbon etching using H_2 plasmas compared to NH_3 plasma [34]. The role of nitrogen or nitrogen containing species based precursor gas and hydrogen on CNTs has been studied by Sanjay K et al.. They proposed morphology based growth model (figure 2.9) (bamboo like or hollow tubes) related to the nitrogen concentration in precursor etchant gas. Introduction of nitrogen facilitates the precipitation of graphite sheets at the top surface of the catalyst particles and formation of curved structures. Compartment formation occurs because of periodic precipitation of graphite sheets on the top of catalyst particle. Outer diameter of growing tube is confined by size of the catalyst particle. Shape of the tip is controlled by the local geometry of the catalyst particle seeding the growth of the tube. The particles are in liquid or semi-liquid state during the growth. The elongation of catalyst particles into a truncated cone shape could be due to interaction between inner graphitic walls of growing compartment and the catalyst particle to acquire minimum energy configuration. In C_2H_2/NH_3 plasma, H and CN keep the surface of iron catalyst clean in the nucleation as well as post nucleation stages by gas phase and surface reactions. This leads nucleation and growth of high density aligned CNTs. NH_3 can easily be dissociated due to weaker bonds compared to that of H_2 or N_2 [35].

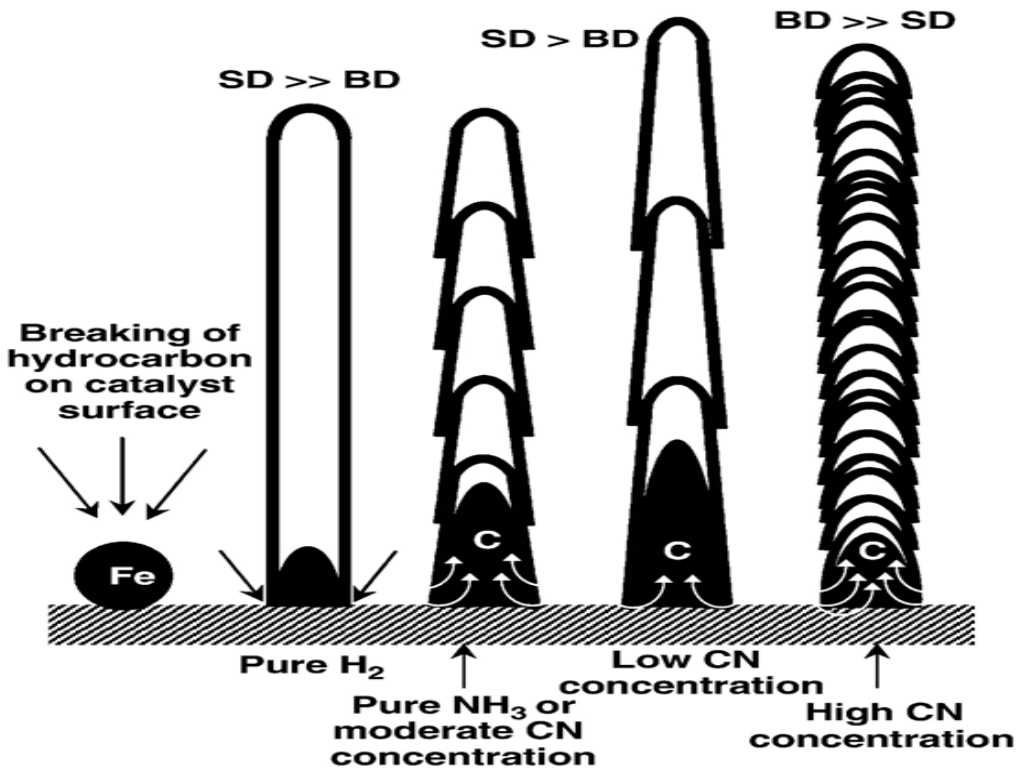

Figure 2.9: Schematic of growth model of bamboo-shaped CNTs in presence of nitrogen and hence CN at different plasma composition, depending on it occurs via surface diffusion (SD) and/or bulk diffusion (BD) of carbon species through catalyst particles [35].

The observation of bamboo-structure in nitrogen containing plasma and hollow tubes in nitrogen-free plasma suggests that nitrogen or CN played critical role in compartment formation. Further it is believed that CNTs growth occurs via surface diffusion (SD) and/or bulk diffusion (BD) of carbon species through catalyst particles.

It was suggested that CNTs growth was governed by both SD and BD in presence of nitrogen and hence CN. Compartment formation was controlled mainly via BD process. On the other hand SD was responsible for growth of nanotube walls. High concentration of CN promoted BD of carbon through Fe particles and suppressed SD by keeping the catalyst surface clean and hence, shorter compartment length (CL). There is a possibility of CN diffusion through the Fe particles as well. But CN or N has very limited solubility in Fe so the concentration of N or CN in Fe is supposed to be very less compared to carbon [35].

2.10. Post synthesis treatments of CNTs

Extraordinary properties of CNTs make them an attractive material for various applications such as in biology, electrochemistry, etc. However, it remains several drawbacks to be overcome such as their tendency to become aggregated. Indeed, CNTs form long bundles thermodynamically stabilized by numerous π-π interactions between sidewalls. As well as most of the desired applications require to craft their surface with desired functional groups in order to change their surface properties. Unrefined CNTs possess some degree of toxicity (in vivo and in vitro), predominately due to the presence of transition metal catalysts. Exposure to pristine CNTs has been shown to cause minimal cytotoxicity at higher concentrations (both in vivo and in vitro), while chemically functionalized CNTs enhanced for drug delivery have not demonstrated any toxicity thus far [36].

Synthesized CNTs present defects and usually, around 1-3% of carbon atoms of a nanotube are located at a defect site. The end caps of nanotubes can be composed of highly curved fullerene-like hemispheres, which are highly reactive as compared to the sidewalls. The sidewalls themselves contain defect sites such pentagon-heptagon pairs called Stone-Wales defects, sp3-hybridized defects and vacancies in the nanotube lattice [37]. The most frequently encountered type of defect is the so-called Stone-Wales (inclusion of five or seven membered ring) defect which leads to a local deformation of the nanotube curvature. Addition reactions are most favored at the carbon-carbon double bonds in these positions. The different typical defects are showed in the figure [38]. (Figure 2.10) shows five- or seven-membered rings in the carbon framework, instead of the normal six membered rings, leading to a bend in the tube (arrow A). The sp3-hybridized defects is indicated with the letter B (R=H and OH). Carbon framework can be damaged by oxidative conditions, which leaves –COOH groups on the edge of a hole (C). (D) shows open end of the SWNT terminated with –COOH groups. Other terminal groups, such as –OH, -H and =O, are also possible.

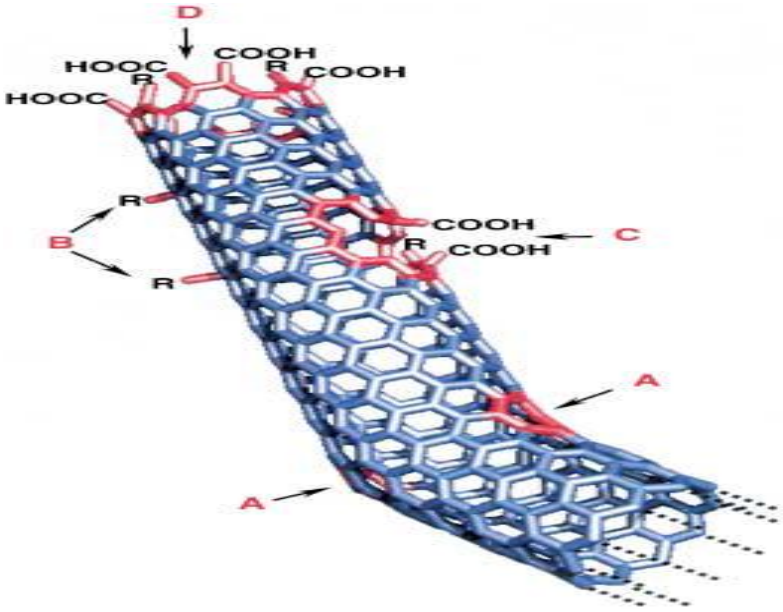

Figure 2.10: Typical defects in a SWNT. Five or seven carbons in a ring, bending tube (A), sp3-hybridized defects (B), –COOH groups on the edge of a hole (C) and open end of the SWNT terminated with –COOH groups (D) [38].

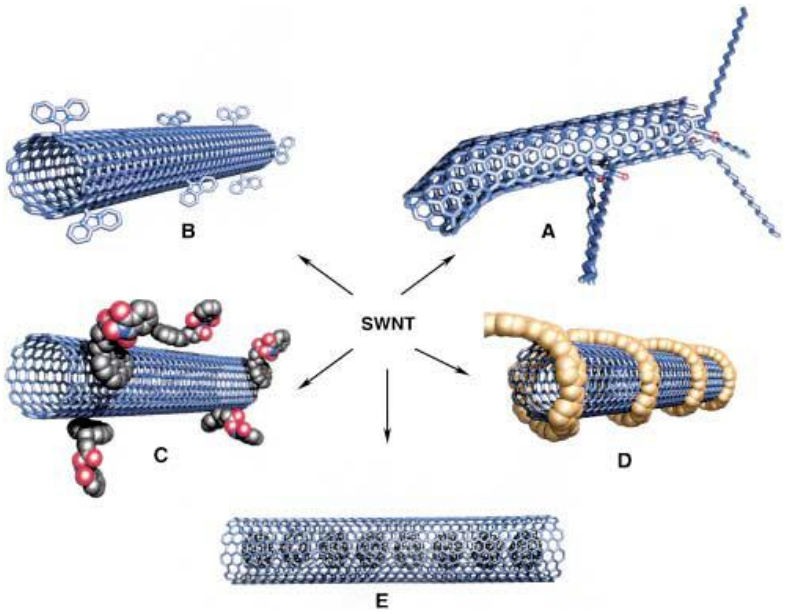

Figure 2.11: Functionalization possibilities for SWNTs: A) defect-group functionalization, B) covalent sidewall functionalization, C) noncovalent exohedral functionalization with surfactants, D) noncovalent exohedral functionalization with polymers, and E) endohedral functionalization with, for example, C_{60} [38].

The defect sites of CNTs are very reactive and when the samples are taken out from the reactor oxygen from air react with these defects and attached to them so readily. For certain applications like supercapacitor application using organic electrolytes it is desirable to remove these oxygen groups from the surface of the nanotubes. The oxygen groups like carboxylic acid and quinine groups can be decomposed from the surface of the nanotubes by heat treatment from 623 to 1073 K [39].

For most applications, like in biology and aqueous electrolytes for supercapacitor applications, it is important to have oxygen functional groups attached to the surface of the nanotubes. Physical or chemical methods can be adopted for the surface treatment of the CNTs. These methods can be divided into two major functionalization strategies. The first is "endohedral functionalization", in which the CNT functionalization is obtained by filling the inner cavity with guest nanoparticles or molecules. This can be achieved by using colloidal suspensions or applying special thermal or chemical conditions (called "wet chemistry"). The second strategy is the exohedral functionalization, which consists to graft molecules on the outer surface of carbon nanotubes (figure 2.11) [38]. During the functionalization, functional groups or nanoparticles can form a covalent (chemical) or a non-covalent (physical) bond with the CNT surface [40]. In addition post synthesis treatment also enables to remove the amorphous carbon and catalysts particles from the nanotubes.

Early work to modify the defective site of carbon nanotube surface is the oxidation reaction of CNTs at high temperature above 700°C in the presence of air, yielding hemispherical end-caps opening in CNTs [41]. This indicates that the hemispherical end-tips are more reactive than the sidewalls of CNTs. The CNTs, with opened endcaps, can be filled with foreign materials such as metal oxide nanoparticles into the hollow tubes. Purification of CNTs in gas-phase reaction with CNTs by using CO_2, N_2O, NO, NO_2, O_3 and has been shown that amorphous carbon impurities are more susceptible to gas-phase oxidation than CNTs. These oxidation reactions discussed above generate the various functional groups, such as -COOH, -OH, -C = O, at the opened end or defect sites of the CNTs [42]. Like graphite, CNT is relatively non-reactive, except at the nanotube caps which are more reactive due to the presence of dangling bonds. The reactivity of the side walls of the CNT π-system can also be influenced by the tube curvature or chirality (twist). The acid washings/sonication

commonly utilized to purify the nanotubes (separate the nanotubes from amorphous carbons and metallic catalysts impurities) create an open end termini in the structure, which are stabilized by –COOH and –OH groups left bonded to the nanotubes at the end termini and/or the sidewall defect sites. The –COOH are expected to covalently bond to CNT due to the strong interaction of CNT carbon atoms and the concentrated H_2SO_4 and/or HNO_3 used for the CNT purification. Very reactive elements like fluorine can also chemically bond to or functionalize nanotubes at room temperature and can lead to severe modification at higher temperatures of about 500-600°C. Also at the CNT end termini, the –COOH group can be coupled to various chemical groups depending on the choice of chemical, to further functionalize the nanotube. These chemicals can form covalent (or irreversible van der Waals) bonds with the nanotubes which could alter the sp^2 hybridization of CNTs to sp^3 hybridization. Strong and covalently bound atoms/molecules are expected to lead to a chemical shift in the CNT environment [43]. Oxygen-based functionalization by plasma techniques can lead to morphological and chemical modifications of the nanomaterials. In situations where one wishes to avoid wet chemical modifications or when it is desirable to confine a modification to the outermost surface, plasma techniques may be employed. A water-vapor plasma can be used to introduce defects in the CNT structure, removed catalyst particles present at the CNT tips after the CNT synthesis, and decreased the CNT diameter. Depending on the plasma parameters it is possible to choose the desired oxygen functional groups to graft on the surface of nanotubes [44]. Oxygen containing functional groups increase the hydrophilicity of the CNTs.

2.11. Experimental setup for CNTs growth

During this thesis two reactors were used to perform the experiments and these reactors are situated in the FEMAN lab. First one is the PEDRO reactor (figure 2.12) [45]. This reactor consists in a 304 stainless steel spherical chamber capable of reaching very high vacuum (10^{-5} Pa) whose gas feeds and vacuum system is fully computer controlled with RS-232 interfaces and through a digital output card. The seals are mainly of ISO-CF type (copper) and the chamber is pumped by a LEYBOLD TMP360C turbomolecular pump backed by one of two LEYBOLD TRIVAC rotary pumps, the selection of which depends on the pumped products:

combustibles. The gas feeds consist of six different lines each one equipped with pneumatic valves and mass flow controllers (MFC) which introduce the gases in the chamber. Three load-lock chambers are connected to the main spherical chamber. Two of them are used for entering water-cooled cathodes (for magnetron sputtering, PECVD or RIE) while the other is used to enter miscellaneous sample holder. Different sample holders can be used depending on the application (heated, multi-sample or for ion beam etching). Moreover, an ion source is located in front of the sample holder.

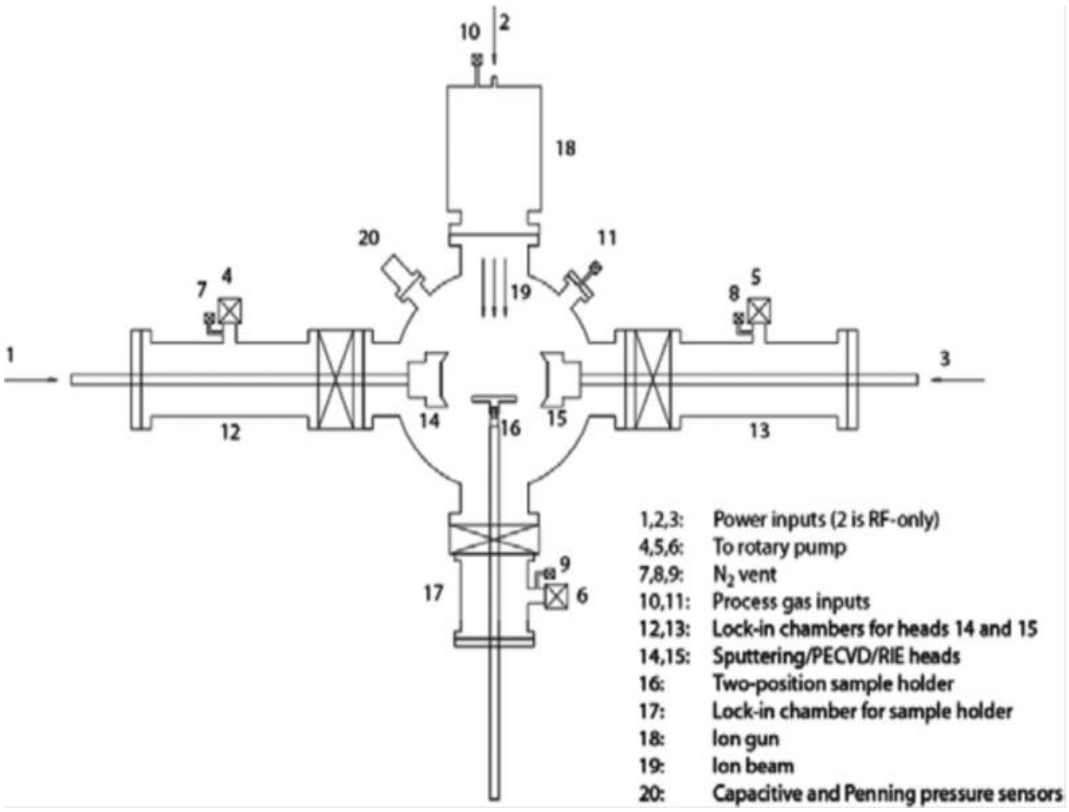

Figure 2.12: Schematic figure of PEDRO. Several techniques can be used: PECVD, magnetron sputtering, RIE, and IBE.

The reactor controller software was designed with LabView. It has two tabs: the "Control center" and the "Sequence configuration tab". The software can operate in two modes: manual or automatic. In the former, the following elements can be controlled as desired at any time:

- Bottle-side, bypass and reactor-side valves of the six different gas lines available
- Valve for the cold cathode pressure gauge

- Main valve between turbomolecular pump and chamber
- Valves between turbomolecular pump and backing pumps
- Butterfly valve: fixed position or pressure regulation
- MFCs' setpoint, on/off state and zero adjustment
- In addition, all pressure and flow readings are available all time and updated every two seconds:
- Full scale of the MFCs and actual flow
- Valve open/closed state
- Pressure in the chamber (two capacitive gauges with full scale of 133 Pa and
- 13 Pa plus one full range Pirani + cold cathode for down to 10^{-6} Pa) with numeric displays and a graphic plot of time evolution
- Pressure in the entry port of both backing pumps
- Manual mode includes a security switch in the "Sequence configuration" tab that watches over bad operation of the reactor by disabling certain actions:
- Open the bottle-side valve of a gas that could damage the cold cathode if its valve is opened
- Open the cold cathode valve if the bottle-side valve of any harmful gas is opened
- Open the bypass valve of any line if the bottle-side valve is also opened
- Entering combustible gases when pumping with the comburent pump and vice versa.

On the same tab, a program can be defined, or saved or loaded to/from a file.

When automatic mode is started, the program is run. Every step of the program defines the flow setpoint for every MFC, the pressure setpoint for the butterfly valve, the duration of the step and the state of the pulsed-DC power supply. In addition, every step has a "Gradient" switch. When on, flow setpoints are changed in the MFC linearly from the initial value to the defined setpoint. With this feature, layers with varying mixtures of different gases can carried out.

PEDRO reactor was used to sputter various thin films (Ni, Ti, Al_2O_3) on different substrates such as silicon wafer and copper foil, as well as to

remove the oxide layer by means of sputtering process from the surface of copper foil by hydrogen plasma.

The second reactor is plasma enhanced chemical vapor deposition (PECVD) reactor (figure 2.13), which is also located in the FEMAN lab. This reactor is a multi-purpose reactor, which can be used for the sputtering as well as for the vapor phase growth process. The reactor has a cylindrical shape. In the vertical axis is placed a rotatory system that permits to move the sample through four different stages. In one stage, plasma and heating systems for CVD and PECVD processes are placed. The other stages are equipped with three homemade magnetron sputtering systems (600 W of nominal RF power, water cooled and 3´´ targets of silicon, iron and copper, respectively.). In addition, the reactor has a load-lock prechamber system to avoid atmospheric contamination of the main chamber during the sample introduction. A view of the reactor can be seen in figure.

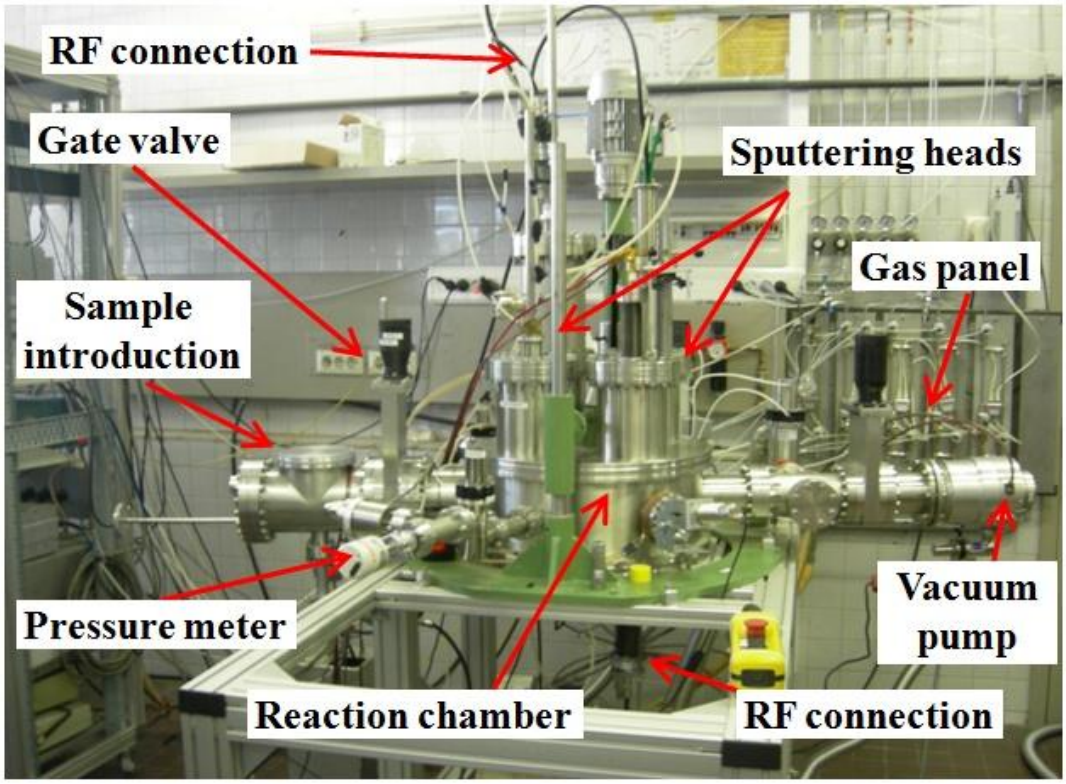

Figure 2.13: Plasma enhanced chemical vapour deposition (PECVD) reactor for CNTs growth.

The plasma in PECVD stage is achieved *via* electrically connecting the sample holder (cathode) to the RF power supply and matching network.

The same RF power supply and matching network is also used in the sputtering processes. The heating system consists in a graphite resistance connected to a DC power supply with a maximum voltage output of 60 V. The temperature is measured through an external pyrometer. It can only be measured in the PECVD stage where there is a quartz window.

The vacuum system is composed for three pumps. A primary rotatory pump for the first vacuum, a Roots pump with a butterfly valve to maintain the low pressure conditions during the processes and a turbomolecular pump for high vacuum. The final pressure that the system can achieve is ~2×10^{-4} Pa. The atmosphere composition is selected with six gas lines connected to the reactor; all equipped with mass flow controllers. The flux of gas, the different valves and the power of the heating and plasma systems are computer controlled with a LabView interface. The software interface permits to control different actuators independently. Also a specific schedule can be programmed in way that the actions with the reactor actuators are performed automatically during the process.

2.12. Introduction of double layer capacitance and experimental setup for electrochemical measurements

Conventional capacitors consist of two conducting electrodes of equal area *A* separated a distance *d* in vacuum. When a voltage is applied to a capacitor, opposite charges accumulate on the surfaces of each electrode. The charges are kept separate by the dielectric, thus producing an electric field that allows the capacitor to store energy.

Supercapacitors store energy in a similar way, but the charge does not accumulate on two conductors separated by a dielectric. Instead, the charge accumulates in the electric double layer at the interface between the surface of a conductor and an electrolyte solution. When charged, the negative ions in the electrolytes will diffuse to the positive electrode, while the positive ions will diffuse to the negative electrodes [46].

The electrochemical process for the double-layer capacitor can be written as:

Positive electrode:

$$E_s + A^- \leftrightarrow {E_s}^+ \,//\, A^{-1} + e^{-1} \tag{2.11}$$

Negative electrode:

$$E_s + C^+ + e^- \leftrightarrow {E_s}^+ \,//\, C^+ \quad (2.12)$$

Overall reaction:

$$E_s + E_s + C^+A^- \leftrightarrow {E_s}^+ \,//\, A^{-1} + {E_s}^+ \,//\, C^+ \quad (2.13)$$

where *E* represents the carbon electrode surface, // represents the double layer where charges are accumulated on the two sides of the double layer and *C* and *A* represent the cation and the anion of the electrolyte, respectively. As shown in (equations. 2.11 and 2.12), during the charge, electrons are forward from the positive electrode to the negative electrode through the external power sources; at the same time, positive and negative ions are separated from the bulk electrolyte and moved to the electrode surfaces. During the discharge, electrons move from the negative electrode to the positive electrode through the load, and ions are released from the electrode surface and moved back into the bulk of the electrolyte. As shown in the overall reaction, the salt (C^+A^-) in the electrolyte is consumed during charge, so the electrolyte can also be considered as an active material [47]. In view of this, only electrons would be transported to and from the electrode surfaces through the external circuit, and anions and cations of the electrolyte moved within the solution to the charged surfaces. Theoretically, no chemical or phase changes are involved or no charge transfer takes place on the interface of electrode and electrolyte [48]. Due to the purely physical formation of the EDL without electrochemical reactions, the charging of EDL capacitors (*EDLCs*) is very rapid. This fundamentally differs from batteries, where energy is stored through redox processes. *EDLCs* can deliver very high power densities (~15 kW/kg) compared to, for example, Li-ion batteries (up to about 2 kW/kg) [49].

The double-layer capacitance could be calculated by using the following (equation 2.14).

$$C = \frac{A\varepsilon}{4\pi d} \quad (2.14)$$

where *A* represents the surface area of the electrode, *d* represents the thickness of the double-layer, and ε represents the electrolyte dielectric constant. As shown in (figure 2.14), the charge accumulation is established across the double-layer, which is composed of a compact layer (Helmholtz

layer) with the thickness about 0.5-0.6 nm, equivalent to the diameters of the solvent molecules and ions reside on it, and a wider region of diffuse layer with dimensions over 1 to 100 nm, depending on the concentration of the electrolyte. It is just owing to the small thickness of the compact molecular interfacial layer that a quite larger *SC* could arise for an EDLC, compared to that of a conventional capacitor, where the separation distance is within the micro meter range.

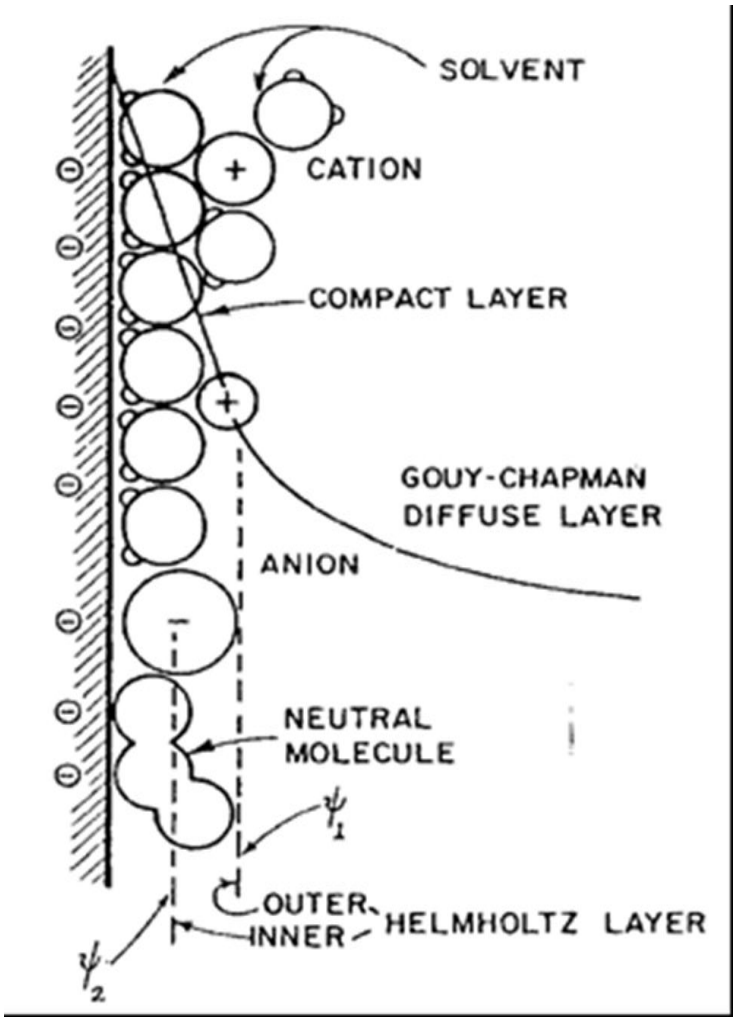

Figure 2.14: General representation of the structure of the double-layer [51].

The specific capacitance (C_{SP}) for one electrode in a supercapacitor can be calculated using the following (equation 2.15):

$$C_{sp}(Fg^{-1}) = \frac{4C}{M} \qquad (2.15)$$

where C is the measured capacitance for the two-electrode cell and m is the total mass of the active materials in both electrodes. The stored energy (E) and the power density (P) in a supercapacitor can then be calculated from (equations 2.16, 2.17) respectively.

$$E = \frac{(CV^2)}{2} \tag{2.16}$$

$$P = \frac{V^2}{(4R_S)} \tag{2.17}$$

where C (Fg^{-1}) is the total capacitance of the cell, V is the cell voltage, and R_S is the equivalent series resistance [50].

The electrochemistry studies the loss of electrons (oxidation) or gain of electrons (reduction) that a material undergoes during the electrical stimulation. The reduction and oxidation reactions are commonly known as redox reactions and can provide information about the concentration, kinetics, reactions mechanism, chemical status and other behavior of a species in solution, similar information can be obtained concerning the electrode surface. In an electrochemical experiment, we can measure one or more of four parameters [52].

(1) Potential (E) is the amount of electrical force or energy in a system. As the potential increases, more force is available to make a reaction happen. The base unit for potential is the volt (V).
(2) Charge (Q) is the measure of the number of electrons used per equivalent. Its base unit is the coulomb (C). We can measure the charge directly or calculate it by multiplying the current and the time.
(3) Current (I) is the magnitude of the electron flow in a system. Its base unit is amperes (A). Cathodic (i) is due to a reduction. Anodic (i) is due to an oxidation.
(4) The time (t) is a measure of duration. Its base unit is second (s). Electrochemical experiments may require time as short as microseconds or as long as days.

The response of a system depends on which parameter is used as the excitation signals. By plotting different parameters in different ways, we can get valuable information.

Electrochemical measurements are made in an electrochemical cell consisting of two or more electrodes and the electronic circuitry for controlling and measuring the current and the potential. The simplest electrochemical cell uses two electrodes. The potential of one electrode is sensitive to the analyte's concentration, and called the working electrode. The second electrode, is called counter electrode, completes the electrical circuit and provides a reference potential against which we measure the working electrode's potential. Ideally the counter electrode's potential remains constant so that we can assign to the working electrode any change in the overall cell potential. If the counter electrode's potential is not constant, we replace it with two electrodes: a reference electrode whose potential remains constant and an auxiliary (counter) electrode that completes the electrical circuit.

Because we cannot simultaneously control the current and the potential, there are only three basic experimental designs: (1) we can measure the potential when the current is zero, (2) we can measure the potential while controlling the current, and (3) we can measure the current while controlling the potential. Each of these experimental designs relies on Ohm's law,

Which states that a current, *i*, passing through an electrical circuit of resistance *R*, generates a potential, *E* [53].

$$E = i \cdot R \tag{2.18}$$

In a CV experiment, the potentiostat applies a potential ramp to the working electrode to gradually change potential and then reverses the scan, returning to the initial potential (see figure 2.15). During the potential sweep, the potentiostat measures the current resulting from the applied potential. These values are then used to plot the CV graph of current versus the applied potential. A single CV is also useful in determining the number of electrons transferred in a reaction. If you assume the reaction is reversible (i.e., follows the Nernst equation) you can calculate the number of electrons transferred during the oxidation/reduction.

In a typical CV study, we vary the scan rate in a series of experiments to determine the diffusion coefficient of a species. In this approach, plot the I_{pc} versus the square root of the scan rate. For a reversible system, the peak height will increase linearly with the square root of the scan rate. The slope of the resulting line will be proportional to the diffusion coefficient, as shown in the Randles-Sevcik equation.

$$i_p = (2.69\times10^5)\cdot n^{3/2}\cdot A\cdot D^{1/2}\cdot \nu^{1/2}\cdot C \qquad (2.19)$$

at 25°C, where F is Faraday´s constant (96458 C/mol), R is universal gas constant in J·mol/K, T is temperature in K, n is the number of electrons transferred, A is the electrode active surface area in cm^2/S, ν is the scan rate in V/s and C is the bulk concentration of the species in mol/cm^3.

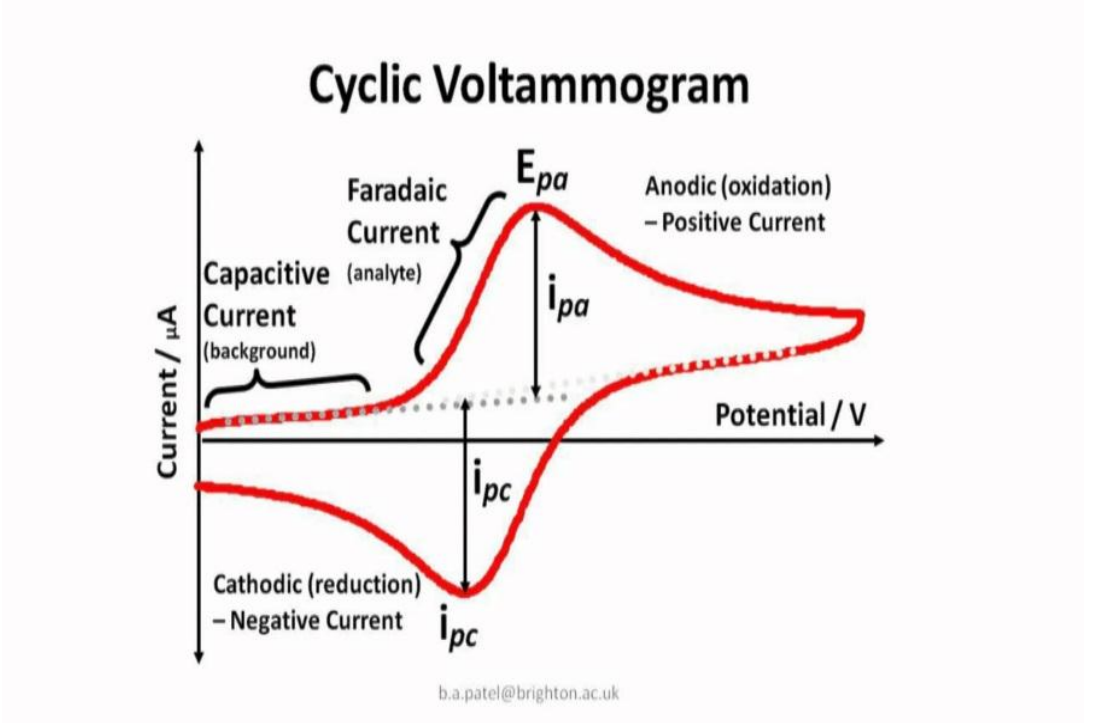

Figure 2.15: cyclic voltammogram.

Electrochemical characterization of electrodes based on CNTs, and composite of CNTs/MnO_2 for supercapacitor was performed in three electrode cell and two electrode configurations (cell). The three electrode system consists of (working electrode (W), reference electrode (R) and counter electrode (C)). Working electrode (W) was CNTs or composite of

CNTs/MnO_2. The reference electrode (R) is an electrode which has a stable and well-known electrode potential and it is used as a point of reference in the electrochemical cell for the potential control and measurement. The high stability of the reference electrode potential is usually reached by employing a redox system with constant (buffered or saturated) concentrations of each participants of the redox reaction. Moreover, the current flow through the reference electrode is kept close to zero (ideally, zero) which is achieved by using the CE to close the current circuit in the cell together with a very high input impedance on the electrometer (> 100 GΩ). The counter electrode (also known as auxiliary electrode), is an electrode which is used to close the current circuit in the electrochemical cell. It is usually made of an inert material (e.g. Pt, Au, graphite, glassy carbon) and usually it does not participate in the electrochemical reaction. Because the current is flowing between the WE and the CE, the total surface area of the CE (source/sink of electrons) must be higher than the area of the WE so that it will not be a limiting factor in the kinetics of the electrochemical process under investigation [54].

For electrochemical measurement to analyze the working electrodes several techniques were adopted, cyclic voltammetry (CV), galvanostatic charge/discharge and electrochemical impedance spectroscopy.

The redox-reaction measurements were carried out in a three-electrode cell. An Ag/AgCl electrode (3M KCl internal solution) and a Pt-ring electrode were used as the reference and counter electrode, respectively. The working electrode was untreated and water plasma treated MWCNTs. The area of the working electrode was set to a constant value of 0.78 cm^2, A solution of 5 mM $K_3[Fe(CN)_6]$ in 0.1 M Na_2SO_4 was used during the study of the Fe^{3+}/Fe^{2+} redox process. The combination of solvent, electrolyte and specific working electrode material determines the range of the potential. Cyclic voltammetry is characterized by a linear increase of the working electrode potential from one potential limit to another and back. For supercapacitor measurements two different types of electrolyte were used during these experiments; aqueous electrolyte (Na_2SO_4) in different concentrations and the 1.0-molar liquid electrolyte solution consisted of lithium perchlorate ($LiClO_4$) (99%, Fluka BioChemica) dissolved in ethylene carbonate (EC) and diethyl carbonate (DEC) (both 99%, anh. from Sigma-Aldrich) mixed in 1:1 volumetric proportions.

For organic electrolyte, the capacitors were fabricated in a MBRAUN Unilab dry glove box by sandwiching an organic electrolyte soaked separator (Whatmann glassy-fiber GF/A) between two carbon nanotube electrodes sample D. The area of each electrode was 0.56 cm^2.
The specific capacitance of the samples was calculated from the cyclic voltammograms using (equation 2.20).

$$C_s = \frac{q_a + |q_c|}{2m\Delta V} \tag{2.20}$$

where C_s is the specific capacitance in Fg^{-1}, m is the mass of the active material in g, ΔV is the voltage window in V, q_a and q_c are the anodic and cathodic charge in C, respectively.
Galvanostatic charge/discharge measurements were performed and the specific capacitance was calculated from the discharge curve using (equation 2.21).

$$C_s = \left[\frac{I}{(\Delta V/\Delta t).m}\right] \tag{2.21}$$

where C_s specific capacitance in Fg^{-1}, ΔV is the voltage difference during the discharge curve in V, I is the current in A and Δt is the discharge time in s.

Electrochemical impedance measurements were also performed. Electrochemical impedance spectroscopy (EIS), measures the dielectric properties of a medium as a function of frequency. It is based on the interaction of an external field with the electric dipole moment of the sample, often expressed by permittivity. This technique measures the impedance of a system over a range of frequencies, and therefore the frequency response of the system, including the energy storage and dissipation properties, is revealed. Often, data obtained by EIS is expressed graphically in a Bode plot or Nyquist plot [55].

2.13. References

[1] Alexander Fridman, *Plasma Chemistry*, (2008), ISBN-13 978-0-511-39857-5

[2] Milton Ohring, *Materials Science of Thin Films, Deposition and Structure,* Second Edition, (2002). ISBN: 978-0-12-524975-1

[3] Kiyotaka Wasa, Shigeru Hayakawa, *Handbook of sputter deposition and technology: Principles, technology and applications*, (1992). ISBN: 0-8155-1280-5

[4] Willian D. Westwood, *Sputter Deposition*, (2003), Published by AVS, ISBN: 0-7354-0105-5

[5] S. M. Rossnagel, Thin film deposition with physical vapor deposition and related technologies, *J. Vac. Sci. Technol*. A 21.5., Sep/Oct 2003, S74-S87.

[6] P J Kelly, R D Arnell, *Magnetron sputtering: a review of recent developments and applications*, (2000), Vacuum, 56, 159-172.

[7] A Iljinas, J Dudonis, R Brucas, A. Meskauska, *Thin ferromagnetic films deposition by facing target sputtering method*, (2005), Nonlinear analysis: Modelling and control, 10, 1, 57-64.

[8] Hugh O. Pierson, *Handbook of chemical vapor deposition (CVD), principles, technology, and applications*, Noyes, Park Ridge, NJ, 1992. ISBN: 0-8155-1300-3

[9] K L Choy, *Chemical vapour deposition of coatings*, (2003), Progress in Materials Science, 48, 57–170.

[10]http://students.chem.tue.nl/ifp03/Wondrous%20World%20of%20Carbon%20Nanotubes_Final.pdf

[11] M Paradise, T Goswami, Carbon nanotubes-Production and industrial applications, (2007), Materials and Design 28, 1477–1489.

[12] C N R Rao and A Govindaraj, *Nanotubes and Nanowires*, 2nd Edition, RSC Nanoscience & Nanotechnology, (2011), doi:10.1039/9781849732840-00001.

[13] M Kumar and Y Ando, *Chemical Vapor Deposition of Carbon Nanotubes: A Review on Growth Mechanism and Mass Production*, (2010), Journal of Nanoscience and Nanotechnology, 10, 3739–3758.

[14] R T K Baker and D J C Yates, *Filamentous Carbon Formation over Iron Surfaces*, (1983), doi: 10.1021/bk-1983-0202.ch001. ISBN13: 9780841207455 eISBN: 9780841209848

[15] A. Gorbunov, O. Jost, W. Pompe, A. Graff, *Solid–liquid–solid growth mechanism of single-wall carbon*, (2002), Carbon, 40, 113–118.
[16] E F Kukovitsky, S G Lvov, N A Sainov, *VLS-growth of carbon nanotubes from the vapor*, (2000), Chemical Physics Letters, 317, 65–70.
[17] Y Chen, J Zhang, Diameter controlled growth of single-walled carbon nanotubes from SiO_2 nanoparticles, (2011), Carbon 49, 3316–3324.
[18] M Meyyappan, L Delzeit, A Cassell and D Hash, *Carbon nanotube growth by PECVD:*
a review, (2003), Plasma Sources Sci. Technol. 12, 205–216.
[19] S H Lim, Z Luo, Z Shen, J Lin, *Plasma-Assisted Synthesis of Carbon Nanotubes*, (2010), Nanoscale Res Lett, 5, 1377–1386.
[20] V I Merkulov, A V Melechko, M A Guillorn, D H Lowndes, M L Simpson, *Growth rate of plasma-synthesized vertically aligned carbon nanofibers*, (2002), Chemical Physics Letters, 361, 492–498.
[21] Z Luo, S Lim, Y You, J Miao, H Gong, J Zhang, S Wang, J Lin and Z Shen, *Effect of ion bombardment on the synthesis of vertically aligned single-walled carbon nanotubes by plasma-enhanced chemical vapor deposition*, (2008), Nanotechnology, 19, 255607 (6pp).
[22] A Moisala, A G Nasibulin and E I Kauppinen, *The role of metal nanoparticles in the catalytic production of single-walled carbon nanotubes - a review*,(2003), J. Phys Condens. Matter, 15 S3011–S3035.
[23] E Flahaut, A Govindaraj, A Peigney, Ch Laurent, A Rousset, C N R Rao, *Synthesis of single-walled carbon nanotubes using binary (Fe, Co, Ni) alloy nanoparticles prepared in situ by the reduction of oxide solid solutions*, (1999), Chemical Physics Letters, 300 236–242.
[24] Ph. Buffat and J-P. Borel, *Size effect on the melting temperature of gold particles*, (1976), Physical review A, 13 6 2287-2298.
[25] A Gruneis, C Kramberger , D Grimm, T Gemming, M H Rummeli, A Barreiro, P Ayala, T Pichler, Ch Schaman, H Kuzmany, J Schumann, B Buchner, *Eutectic limit for the growth of carbon nanotubes from a thin iron film by chemical vapor deposition of cyclohexane*,(2006), Chemical Physics Letters, 425, 301–305.
[26] E Teblum, Y Gofer, C L Pint, and G D Nessim, *Role of Catalyst Oxidation State in the Growth of Vertically Aligned Carbon Nanotubes*, (2012), J. Phys. Chem. C, 116, 24522−24528.

[27] Z He, J L Maurice, A Gohier, C S Lee, D Pribat,and C S Cojocaru, *Iron Catalysts for the Growth of Carbon Nanofibers: Fe, Fe_3C or Both?* (2011), Chemistry of materials, dx.doi.org/10.1021/cm202315j.
[28] J J Schneider, N I Maksimova, J Engstler, R Joshi, R Schierholz, R Feile, *Catalyst free growth of a carbon nanotube–alumina composite structure*, (2008), Inorganica Chimica Acta., 361, 1770–1778.
[29] L Camilli, M Scarselli, S D Gobbo, P Castrucci, F Nanni, E Gautron, S Lefrant, M D Crescenzi, *The synthesis and characterization of carbon nanotubes grown by chemical vapor deposition using a stainless steel catalyst*, (2011), *Carbon*, 49, 3307-3315.
[30] M H Rummeli, F Schaffel, C Kramberger, Thomas Gemming, A Bachmatiuk, R J Kalenczuk, B Rellinghaus, B Buchner, and T Pichler, *Oxide-Driven Carbon Nanotube Growth in Supported Catalyst CVD*, (2007), J. AM. CHEM. SOC. 129, 15772-15773.
[31] S Hofmann, R Sharma, C Ducati, G Du,C Mattevi, C Cepek, M Cantoro, S Pisana, A Parvez, F C Sodi, A C Ferrari, R Dunin-Borkowski, S Lizzit, L Petaccia, A Goldoni, and J Robertson, *In situ observations of catalyst dynamics during surface-bound carbon nanotube nucleation*, (2007), Nano Letters, 73, 602-608.
[32] Siva Yellampalli, *Carbon nanotubes – Synthesis, Characterization, Applications*, CH 8, (2011), ISBN 978-953-307-497-9
[33] M S Bell, K B K Teo, R G Lacerda, W I Milne, D B Hash, and M. Meyyappan, *Carbon nanotubes by plasma-enhanced chemical vapor deposition*, (2006), Pure Appl. Chem,78, 6, 1117-1125.
[34] A Gohier, T M Minea, M A Djouadi, and A Granier, *Impact of the etching gas on vertically oriented single wall and few walled carbon nanotubes by plasma enhanced chemical vapor deposition*, (2007), Journal of Applied Physics, 101, 054317.
[35] S K Srivastava, V D Vankar, V Kumar, *Growth and microstructures of carbon nanotube films prepared by microwave plasma enhanced chemical vapor deposition process*, (2006), Thin Solid Films, 515, 1552–1560.
[36] S K Smart, A I Cassady, G Q Lu, D J Martin, *The biocompatibility of carbon nanotubes*, (2006), Carbon, 44, 1034–1047.
[37] J C Charlier, *Defects in Carbon Nanotubes*, (2002), Acc. Chem. Res. 35, 1063-1069.

[38] A Hirsch, *Functionalization of single-walled carbon nanotubes*, (2002), Angew. Chem. Int. Ed, 41, 11, 1853-1859.
[39] A Kuznetsova, D B Mawhinney, V Naumenko, J T Yates Jr., J Liu, R E Smalley, *Enhancement of adsorption inside of single-walled nanotubes: opening the entry ports*, (2000), Chemical Physics Letters, 321, 292–296.
[40] E V Hooijdonk, C Bittencourt, R Snyders, and J F Colomer, *Functionalization of vertically aligned carbon Nanotubes*, (2013), Beilstein J. Nanotechnol, 4, 129–152.
[41] P M Ajayan, T W Ebbesen, S Ijima, K tanigaki, H Hiura, *Opening carbon nanotubes with oxygen and implications for fillings*, (1993), Nature, 362, 522-525.
[42] L Dai, *Carbon nanotechnology*, (2006), CH 8.
[43] T I T Okpalugo, P Papakonstantinou, H Murphy, J McLaughlin, N M D Brown, *High resolution XPS characterization of chemical functionalized MWCNTs and SWCNTs*, (2005), Carbon, 43, 153–161.
[44] S. Hussain, R. Amade, E. Jover, and E. Bertran, *Functionalization of carbon nanotubes by water plasma*, (2012), Nanotechnology, 23, 1–8.
[45] Miguel Rubio Roy, *Surface Properties of Hard Fluorinated Amorphous Carbon Films Deposited by Pulsed-DC Discharges*, PhD thesis, (2010).
[46] M V Kiamahalleh and S H S ZEIN, *Multiwalled carbon nanotubes based nanocomposites for supercapacitors: A review of electrode materials*, (2012) NANO: Brief Reports and Reviews, 7, 2 1230002 (27 pages).
[47] J P Zheng, J Huang, and R Jow, *The limitations of energy densily for electrochemical capacitors*, (1997), J. Electrochem. Soc., 144, 6, 2026-2031.
[48] Yaohui Wang, *Manganese dioxide based composite electrodes for electrochemical supercapacitors*, (2012), PhD thesis.
[49] F Béguin, V Presser, A Balducci, and E Frackowiak, *Carbons and electrolytes for advanced supercapacitors*, (2014), Adv. Mater. DOI: 10.1002/adma.201304137
[50] T Chen and L Dai, *Carbon nanotubes for high-performance supercapactors*, (2013), Materials Today, 16, 7/8 272-280.
[51] B. E. Conway, *Electrochemical Supercapacitors; Scientific Fundamentals and Technological Applications*, Kluwer Academic/ Plenum Publishers, NewYork, NY,USA, 1999.

ISBN 0-306-45736-9
[52]http://goals.usim.edu.my/moodle/pluginfile.php/118191/mod_resource/content/1/Review%20Techniques%20for%20Electrochemical%20Analysis.pdz
[53]http://www.asdlib.org/onlineArticles/ecourseware/Analytical%20Chemistry%202.0/Text_Files.html
[54]http://www.ecochemie.nl/download/Applicationnotes/Autolab_Application_Note_EC08.pdf
[55] http://en.wikipedia.org/wiki/Dielectric_spectroscopy

Chapter 3
Characterization techniques

Chapter 3- Characterization techniques

3.1. Electron Microscopy

The minimum distance (resolution or resolving power) between two points that can be resolved by human eyes is about 0.1-0.2 mm. A microscope could be used to study the details of finer objects below the size of 0.1 mm. Electron microscopy (EM) is widely used technique that uses a beam of electrons to produce highly magnified image of a specimen. An EM has greater resolving power than a light microscope and can reveal the structure of smaller objects because electrons have wavelengths about 100,000 times shorter than visible light photons.

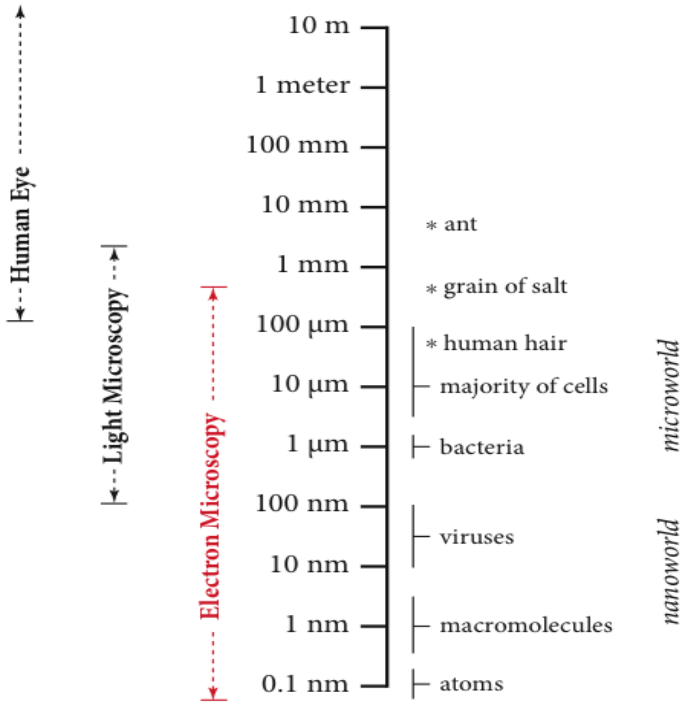

Figure 3.1: Resolving power of unaided eye versus light and electron microscopy [2].

In an electron microscope magnetic lenses are used to direct electrons much as the optical lens are used to direct light in a light microscope. The resolution of a microscope depends on two factors,

wavelength of the illumination source (λ) and the numerical aperture of the lens (N.A.) (equation 3.1) [1].

$$limits\ of\ resolution = \frac{0.61\,\lambda}{N.A.} \tag{3.1}$$

The maximum value of N.A. for light microscope is approx. 1.4; it is obvious, therefore, that even the short blue light (λ = 436 nm) of the visible spectrum will yield a resolution of only 190 nm. The electron microscope, however, utilizes electrons for illumination. Electrons have the characteristics of both particles and waves. The wavelength λ of the incident electron can be determined by the kinetic energy of the electrons, *k*, which follow the Broglie´s expression (equation 3.2).

$$\lambda = \frac{h}{p} = \frac{h}{\sqrt{2mk}} \tag{3.2}$$

where *h* is the Planck's constant, *p* is the momentum of the electron, and *m* is the electron mass [1]. (Figure 3.1) shows a comparison of seeing objects between human eye, light microscopy and electron microscopy [2].

3.1.1. Scanning Electron Microscopy

Scanning electron microscopy (SEM) is a non-destructive tool to gain the knowledge about the surface topography, chemical composition, and crystalline structure of a specimen by scanning it with focused beam of electrons. SEM can magnify a specimen from about 10 - 300,000 times. The SEM has high resolution better than 1 nm and in comparison the light microscope has resolution of 200 nm. The SEM has high field depth more than 300 times to light microscopy.

A SEM consists of an electron gun (cathode) at the top, a column which consists of anode, magnetic lens, scanning coils through which the electrons travel and a specimen holder at the base see (figure 3.2). Lenses in the SEM are not a part of the image formation system but are used to demagnify and focus the electrons beam onto the sample surface. This gives rise to two of the major benefits of the SEM: range of magnification and depth of filed in the image. Depth of field is that property of SEM images where surfaces at different distances from the lens appear in focus, giving the image a three dimensional information.

Typical energy produced by the electrons from the electron gun in SEM is usually in between 2-40 keV. Three types of electron guns (filaments) are typically used. (1)Tungsten hairpin filament, which is heated up to 2500°C to produce thermal emission of electrons from its tip. (2) Lanthanum hexaboride (LaB_6) works on the sample principle as for tungsten but has advantage over tungsten by providing larger maximum beam current and longer life time. The current density obtained from a thermionic source is described by the Richardson formula (equation 3.3).

$$J = A.T^2.e^{-\frac{\emptyset}{kT}} \quad (3.3)$$

Where both *A* and the "work function" *Φ*, are material-constants, *T* is the temperature (in Kelvin) and *k* is Boltzmann's constant. *J* can be increased either by increasing *T* or by reducing *Φ*. Only a few refractory (high melting temperature) materials (like W) can withstand the required high temperature to obtain reasonable current density and increase of the temperature beyond saturation reduces cathode lifetime with minor gain in current. Materials with lower work function (like LaB_6 or CeB_6) can be operated at lower temperatures and still produce higher brightness. (3) Field emission electron gun consists of a sharp metal (tungsten) tip with a radius of less than 100 nm. A potential difference (V_1 = extraction voltage) is established between the first anode and the tip. The electron emission is promoted by the concentrated electric field at the tip. The potential difference between the tip and the second grounded anode determines the accelerating voltage (V_0) of the gun. The penetration power of the electrons depends on the accelerating voltage.

There are two types of field emission electron guns (FEGs). (1) Cold, (2) Thermally assisted. In the cold filed emission electron gun the electric field produce by the extraction voltage lowers the work function barrier and allows electrons to directly tunnel through it as a result facilitating emission. A field emission gun operates at 10^{-8} to 10^{-9} Pa to keep the cathode clean. The gun contains two anodes. The first one provides the "extraction field" and the second accelerates the electrons to the required energy. Due to this construction the brightness does not depends significantly on the accelerating voltage. Although the brightness is the highest for FEGs, the maximum emitted current (needed for low magnification operation) is the lowest for them and thermionic cathodes

surpass FEGs in that respect. Long term stability is also poorer with FEGs (< 5% / hour with feedback regulating electronics). The thermally assisted filed emission gun (Schottky field emitter) uses heat and chemistry (nitride coating) in addition to voltage to overcome the potential barrier level. A comparison of different properties of electrons guns is shown in (table 3.1).

Table 3.1: comparison of different properties of electrons guns [26].

	Tungsten	LaB_6	Thermal Filed Emission Gun	Cold Field Emission Gun
Brightness(A/cm^{2}str)	10^5	10^6	10^8	10^8
Life time (hours)	40-100	200-1000	> 1000	> 1000
Source size	30-100 m	5-50 µm	< 5 nm	< 5 nm
Energy spread (eV)	1-3	1-2	1	0.3
Current stability (% hr)	1	1	5	5
Vacuum (Torr)	10^{-5}	10^{-7}	10^{-11}	10^{-11}

The filament is heated resistively by a current to achieve a temperature between 2000-2700 K. This results in an emission of thermionic electrons from the tip over an area about 100 µm × 150 µm. The electron gun generates electrons and accelerates them to energy towards the sample. A series of lenses focus the electron beam on to the sample where it interacts with the sample.

The principle images produced by SEM are of three types: secondary electron images, backscattered electron images and elemental X-ray maps. Secondary and backscattered electrons are conventionally separated according to their energies. When the energy of the emitted electron is less than about 50 eV, it is referred as a secondary electron and backscattered electrons are considered to be the electrons that exit the specimen with energy greater than 50 eV. Detectors of each type of electrons are placed in the microscope in proper positions to collect them.

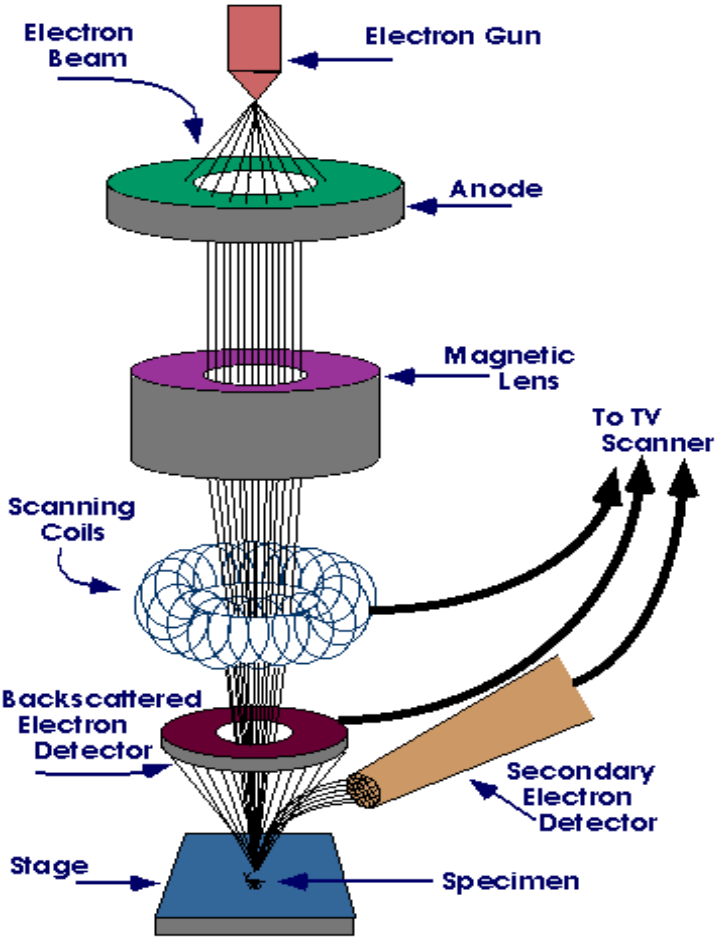

Figure 3.2: Geometry of SEM [4].

The SEM electron beam is a focused probe of electrons accelerated to moderately high energy and positioned onto the sample by electromagnetic field. The SEM optical column is utilized to ensure that the incoming electrons are of similar energy and trajectory. These beams electrons interact with atoms in the specimen by a variety of mechanism when they impinge on a point on the surface of specimen. For inelastic interaction, energy is transferred to the sample from the beam, while elastic interactions are defined by a change in trajectory of the beam electrons without loss of energy. The signals resulting from these interactions will each have different depths within the sample from which they can escape due to their unique physical properties and energies. For example, a secondary electron (SE) is a low-energy (2 to 5 eV) electron ejected from the outer shell of a sample atom after an inelastic interaction. These low-energy electrons can escape the surface only if generated near the surface.

These electrons are influenced more by surface properties than by atomic number. The term secondary refers to the fact that this signal is not a scattered portion of the probe, but a signal generated within the specimen due to the transfer of energy from the beam to the specimen. In practice, secondary electrons are arbitrarily defined as those electrons with < 50 eV energy. Secondary electrons are generated by both the beam entering the specimen and back scattered electrons as they escape the specimen; however secondary electron generation is concentrated around the initial probe diameter. Secondary electron intensity is a function of the surface orientation with respect to the beam and the secondary electron detector and thus produces an image for the specimen morphology. Backscattered electrons are electrons from the incident probe that undergo elastic interaction with sample, change trajectory, and escape the sample. The depth from which backscattered electron escape the specimen is dependent upon the beam energy and specimen composition. The intensity of backscattered electron signal is a function of the average atomic number (z) of the specimen, with higher atomic elements (Z) producing more backscattered electrons [3].

Image construction in the SEM is accomplished by mapping intensity of the signals from secondary electrons or backscattered electrons. There is a point to point transfer of this intensity information, since SEM scan generator simultaneously drives an electron beam across the surface of the specimen and an electron beam on the viewing cathode-ray tube (CRT) or recording device. The SEM image conveys three-dimensional information due to the depth of field in the image. The depth of the field depends upon the electron divergence angle, which is defined by the diameter of the objective lens aperture and the distance between the specimen and the aperture. Depth of field is increased by reducing the beam divergence angle, which can be done by increasing the working distance or decreasing the aperture diameter.

Linear magnification is calculated by the (equation 3.4).

$$M = \frac{L}{I} \tag{3.4}$$

Where L is the raster's length of the cathode ray tube (CRT) monitor and I the raster's length on the surface of the sample [4, 5, 6]. A conductive

substrate is used for the preparation of sample to avoid the accumulation of electrons on the surface, which might diverge the incident beam.

3.1.2. High resolution transmission electron microscopy

A specimen's morphology, composition and crystallography can be studied by using transmission electron microscope (TEM). A TEM is the most powerful microscope use high energy electrons. High-resolution transmission electron microscopy (HRTEM) is an imaging mode of the transmission electron microscope (TEM) that allows for direct imaging of the atomic structure of the specimen. A layout of basic TEM is shown in (figure 3.3).

TEM works on the principle similar to that of an optical microscope with the key difference that it uses electrons and not photons as the source.

In a TEM, the electrons are accelerated at high voltage (100-1000 kV) to a velocity approaching the speed of light (0.6-0.9 *c*); they must therefore be considered as relativistic particles.

The uncertainty principle sets a fundamental limit on the spatial resolution while using a beam of particles with de Broglie wavelength. Thus, smaller the wavelength of the source, higher will be the resolution of the system. The associated wavelength is five orders of magnitude smaller than the light wavelength (0.04-0.008 Å). Nevertheless, the magnetic lens aberrations limit the convergence angle of the electron beam to 0.5° (instead of 70° for the glass lens used in optics), and reduce the TEM resolution to the Å order. This resolution enables material imaging and structure determination at the atomic level.

Thin samples below than 60 nm in size are required due to the important absorption of the electrons in the material. High acceleration voltage reduces the absorption effects but can cause radiation damage (estimated at 170 kV for Al). In a working way electron gun produce electrons which are transmitted towards specimen in an evacuated column through the electromagnetic lenses below and above the specimen. The transmitted electrons could be elastically or in elastically scattered or unscattered by the specimen are used to form an image on phosphorescent screen or CCD camera as shown in figure .When an electron beam encounter crystalline structure diffraction will occurs. The conditions for diffractions are given by Bragg (equation 3.5).

$$n\lambda = 2dsin\theta \tag{3.5}$$

where λ is the electron wavelength, d is the spacing of the diffracting planes, and θ is the angle between the planes and electron beam [7, 8].

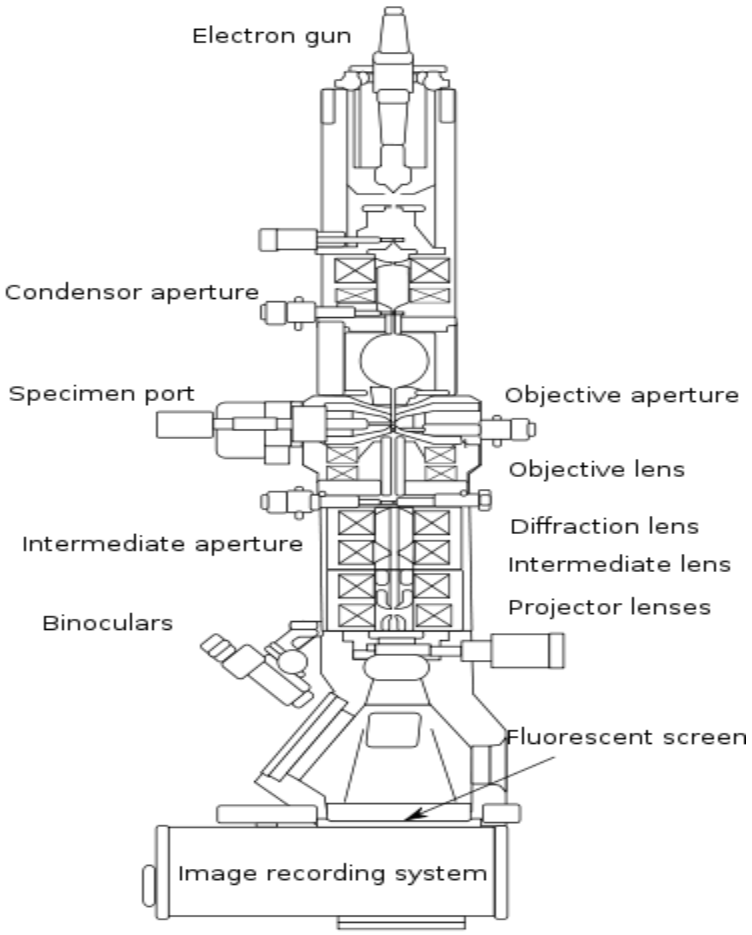

Figure 3.3: Layout of optical components in basic TEM [9].

Electrons being charged in nature can be easily deflected using an external electric or magnetic field and can be accelerated using external potential. As the electrons travel through the sample, they are either scattered or are transmitted unaffected through the sample. The probability of scattering is described in terms of the interaction cross-section or the mean free path and can be elastic or inelastic. This results into a nonuniform distribution of electrons in the beam that comes out of the sample, which contains all the structural information of the sample. The scattered (diffracted) electrons deflected away from the optical axis of the

microscope are blocked using an aperture and thus the transmitted electron beam generates a contrast on the fluorescent screen depending on its varying intensity. In the case of nanomaterials, the crystalline structures interact with the electron beam mainly by diffraction rather than absorption, though the intensity of the transmitted beam depends largely on the density and thickness of the material though which it passes. The intensity of the diffraction thus depends on the orientation of the planes of atom in the crystal relative to the electron beam. Angular distribution of electrons due to diffraction can be viewed in the form of scattering patterns, usually called diffraction patterns, and spatial distribution of electrons can be observed as contrast in images of the sample. The transmitted electron beam strikes the fluorescent screen and generates an image with varying contrast. The darker areas with higher contrast are those from where fewer electrons have been transmitted due to high density or thickness of the sample while the areas of lower contrast show the areas in the sample, which have less density or thickness, and thus more number of transmitted electrons are present.

In this thesis samples for HRTEM were prepared as follows. CNTs which were grown by the plasma enhanced chemical vapor deposition (PECVD) technique were scratched from the silicon wafer and dispersing in the absolute ethanol using an ultrasound bath for 30 s. Ultra long CNTs which were prepared by water assisted chemical vapor deposition were scratched from silicon wafer immersed in absolute ethanol and for the dispersion of the nanotubes we had to perform ultrasound bath for more than 48h. The reason behind this long time ultrasound was the water assisted nanotubes grown in very strong bundles and is little difficult to separate them. A few drops of the resultant suspension were added onto a holey carbon grid and let it to dry at room temperature. The dispersed nanotubes were deposited on the holy carbon TEM grid and analyzed by HRTEM JEOL 2100.

3.2. Raman Spectroscopy

Light is an electromagnetic wave which carries both energy and momentum. Light propagate straight through the optically homogenous medium, however when the in homogeneities of the material are comparable to the size of the wavelength of the light the radiation will

scattered into various directions. The scattering of light could be elastic or inelastic scattering.

Raman spectroscopy is a spectroscopic technique based on inelastic scattering of monochromatic light, usually from a laser source, the frequency of photons in monochromatic light changes upon interaction with a sample. Photons of the laser light are absorbed by the sample and then reemitted. Frequency of the reemitted photons is shifted up or down in comparison with original monochromatic frequency, which is called the Raman effect. This shift provides information about vibrational, rotational and other low frequency transitions in molecules or atoms. Raman spectroscopy can be used to study solid, liquid and gaseous samples. To observe the Raman scattering, the molecules or atoms must be polarizable. The incident electromagnetic wave induces a dipole moment during the light material interaction. The strength of dipole moment, P, is given by the following (equation 3.6).

$$P = \alpha \bar{E} \tag{3.6}$$

where α is the polarizability, which is a material property that depends on the molecular structure and nature of the bonds and $\bar{E}$ is the electric field strength of the incident electromagnetic wave.

When monochromatic radiation of frequency ν_0 is passed through a transparent medium, most of it is transmitted, some of it is absorbed and a small amount is scattered (less than 10^{-5} of the intensity of the exciting source). Most of this scattered light is at the same frequency as the incident radiation (called elastic or Rayleigh scattering) whilst a very small amount (10^{-3} to 10^{-4} of the Rayleigh intensity) is scattered at a frequency higher or lower than that of the incident radiation. It is this inelastic scattering that is referred as Raman Scattering.

Molecules are continuously vibrating. Raman spectroscopy detects and analyzes the energy of the different vibrations that take place in the molecule, which will produce a spectrum. Every molecule or crystal has its own specific and unique Raman spectrum. Raman spectroscopy uses a single frequency source to irradiate the sample and it is the scattered light from the molecule which is detected in the Raman experiment. The Raman scattering process can be easily explained by a simple quantum mechanical description (see figure 3.4): a photon of energy $h\nu_0$ colliding with a

molecule can either be scattered elastically (Rayleigh) or inelastically (Raman). In the latter case, the collision with photons induces the molecule to undergo a transition between two vibrational energy levels of the molecule and the resulting scattered radiation has a different frequency than the incident photon. If during the collision, the molecule gains some energy $h\nu_{vib}$, the photon will be scattered at the frequency $h\nu_0$- $h\nu_{vib}$, which is referred to as Stokes Raman scattering. Conversely, if the molecule loses some energy by relaxing from an excited vibrational level to the ground state, then the scattered energy will be at $h\nu_0$+ $h\nu_{vib,}$ i.e. anti-Stokes Raman scattering. Raman spectra are usually represented in wavenumbers shift (ν_{vib}), relative to the excitation line. The advantage of using such a shifted scale is that it allows working with a spectrum that gives directly the frequency of the molecular vibrations.

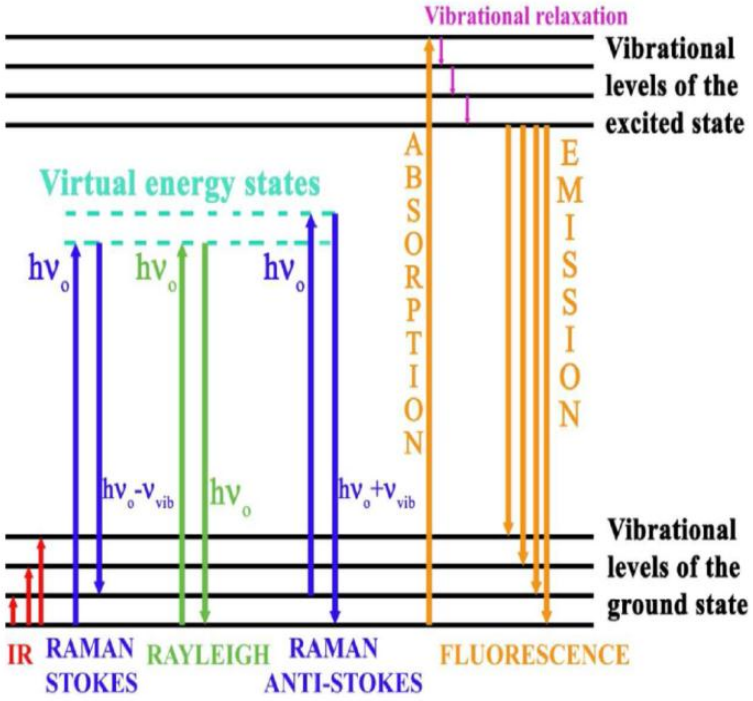

Figure 3.4: Vibrational and electronic energy-level diagram of a molecule showing the processes of IR absorption, Raman and Rayleigh scattering and fluorescence emission [10].

The relative intensities of the two processes depend on the population of the various states of the molecules, which is given by Boltzmann distribution. At room temperature, the probability to have molecules in an excited vibrational state is low, therefore anti-Stokes

scattering will be weak compared to Stokes intensity, and will become weaker as the frequency of the vibration increases. This is why the Raman spectrum is usually limited to the Stokes region. In some cases, both Stokes and anti-Stokes band intensities are measured in order to determine the temperature *in situ* at the microscopic level in some specific positions of the sample [10].

A Raman system typically consists of four major components:

1. Excitation source (laser).
2. Sample illumination system and light collection optics.
3. Wavelength selector (filter or spectrophotometer).
4. Detector (photodiode array, CCD or PMT).

Typical measurements use a back scattering configuration and 50×, 80×, and 100× objective lenses (~1 μm spot for the 100× objective).

Raman spectroscopy is easy, fast and non-destructive qualitative technique to study the physical properties of the carbon materials at room temperature.

The frequency of the Raman band depends on the masses and positions of the atoms, the interatomic forces (i.e. force constants of the bonds) and the bond length. Therefore, any effects altering these features will produce a change in the frequency of the band. For instance, this is the reason why the band position is sensitive to the presence of stresses or strains: a tensile stress will determine an increase in the lattice spacing and, hence, a decrease in the wavenumber of the vibrational mode. Further, the presence of crystalline disorder and chemical impurities in crystalline network produce changes in the wavenumber.

Raman bandwidth and bandshape are closely related to the crystalline order. In principle the bandwidth is related to the lifetime of the phonons. The presence of crystalline disorder produces a decrease of the phonon lifetime, which thus generates an increase of the bandwidth. Therefore the density of defects can be evaluated from the bandwidth.

The intensity of the Raman band is also very sensitive to the structure of crystals and as a result significant information can be obtained from intensity measurements. Damage in the lattice leads to a decrease of the intensity of the Raman modes, related to the breaking of bonds and changes in atomic forces displacements, and, hence produces a decrease of the Raman polarizability tensors. Raman spectra of graphite and Single wall CNTs gives us general information about their physical properties

such as electronic structure, phonon structure and defects. During the inelastic scattering of light in the Raman spectroscopy, (1) an electron is excited from the valence energy band to the conduction band by absorbing a photon, (2) the excited electron is scattered by emitting (or absorbing) phonon, and (3) the electron relaxes to the valence band by emitting a photon. By measuring the intensity of scattered light as a function of frequency downshift of the scattered light, we can calculate the phonon frequencies of the material.

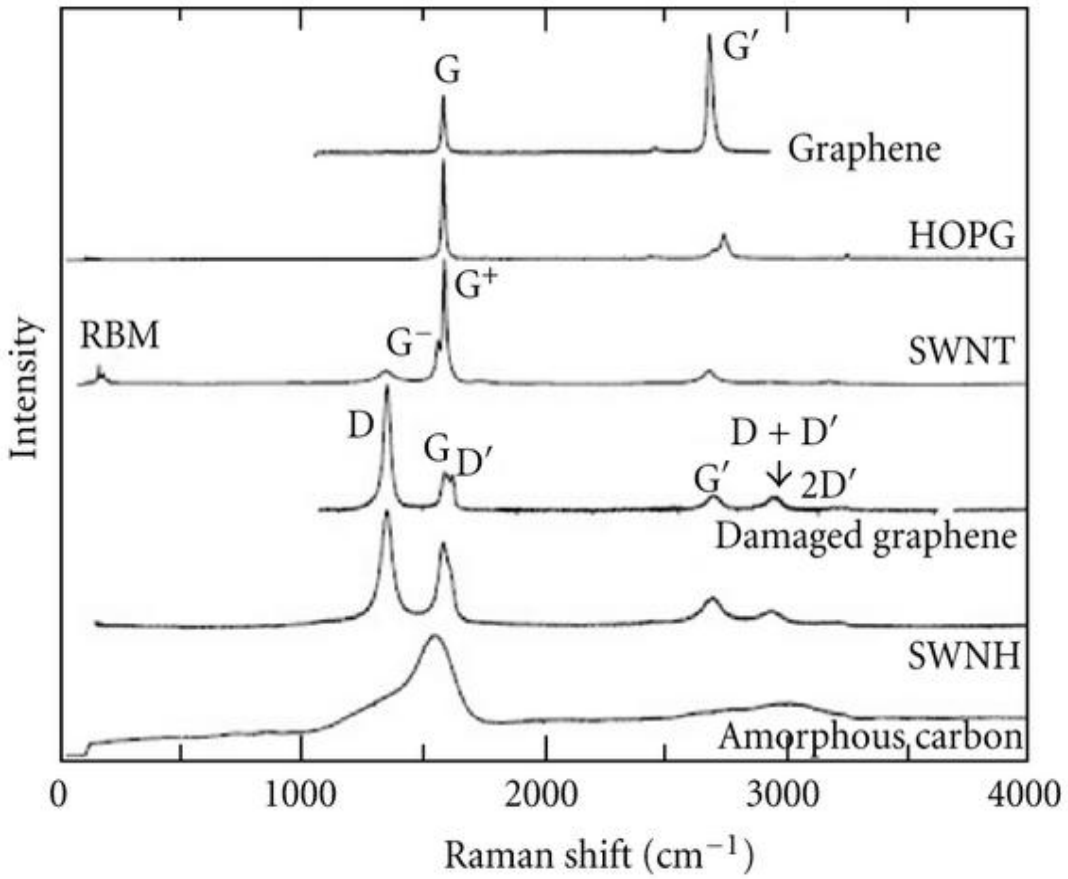

Figure 3.5: Raman spectra from different types of sp^2 nanocarbons [12].

In the Raman inelastic scattering process of light, not only the phonon but also magnon and plasmon can be involved in scattering process [11]. The number of emitted phonon before relaxation of the lattice can be one, two and so on, which we call respectively, one phonon, two phonon and multi phonon Raman processes. The order of a scattering event is defined as its number in the sequence of the total scattering events, including elastic scattering by an imperfection (such as defect or edge) of the crystal. (Figure 3.5) shows the Raman spectra of different types of

nanocarbon. G band has the E_{2g} symmetry around ~ 1582 cm^{-1} which is the stretching of C-C bond in the graphitic materials is the first order Raman peak. This mode does not require the presence of six fold ring. Radial breathing mode (RBM) at the lower frequencies (100-400cm^{-1}) is a unique phonon mode appears only in carbon nanotubes is the unique feature of G band splitting is direct evidence that sample contains the SWCNTs. D band around ~ 1360 cm^{-1} and G´ around ~ 2700 cm^{-1} are due to one and two phonon, second order Raman scattering process. The appearance of D mode is due to the defects, disorder or amorphous carbon in the graphitic material. The D band is the A_{1g} symmetry breathing mode. The G´ band spectra are free from defect effects [11, 12, 13].

3.3. X-ray photoelectron spectroscopy (XPS)

X-ray photo electron spectroscopy (XPS) is also known as electron spectroscopy for chemical analysis (ESCA) or X-ray photoemission spectroscopy is a powerful technique frequently used to study the materials electronic structure, elemental composition and element oxidation state.

A target solid material is irradiated by the X-ray photons whose energy ($h\nu$) is high enough to knock out the electron from the *K* shell of the atom. The *K*-shell electron would be ejected from the surface as a photoelectron with a kinetic energy E_k. We can calculate the binding energy of the atom's photoelectron (E_B) by the following (equation 3.7).

$$E_B = h\nu - E_k - \phi \tag{3.7}$$

Where h is Plank's constant, ν is the frequency, φ represents the energy required for an electron to escape from the material. The φ depends on both the sample material and the spectrometer. The XPS process is schematically represented in (figure 3.6) for the emission of an electron from the 1s shell of an atom.

XPS uses the spectroscopic notation: first the principal quantum number (n = 1, 2, 3, …), then l = 0, 1, 2, … indicated as s, p, d, …, respectively, and finally the j value given as a suffix (1/2, 3/2, 5/2, …) [14].

X-ray radiation is commonly not exactly monochromatic. The photoelectron emission can also be excited by continuous X-rays, which are commonly associated with characteristic X-ray radiation. Such photoelectron emission generates a background in the low binding energy

of the spectrum. XPS is performed in the environment with a vacuum pressure is the range of 10^{-8}-10^{-10} mbar to keep the surface of the sample free from contaminants and reduce the chance of low energy electrons being scattered by gas molecules on their way to reach the detector. Scattering will reduce signals intensity and increase background noise in spectra. In XPS soft characteristic X-ray Al*K*α and Mg*K*α are generated by X-ay anode materials Al and Mg, whose energies 1.4866 and 1.2536 keV are used. XPS requires a line width less than 1.0 eV to ensure good energy resolution. Both Al*K*α and Mg*K*α exhibits line width less than 1.0 eV and also have sufficient energies. A concentric hemispherical analyzer (CHA) also called hemispherical sector analyzer (HSA) is used to analyze the electron energy to obtain the XPS spectra. An XPS spectrum can have three types of peaks on a back ground: photo-emission from core electron levels, photo emission from valance levels and Auger emission excited by X-rays.

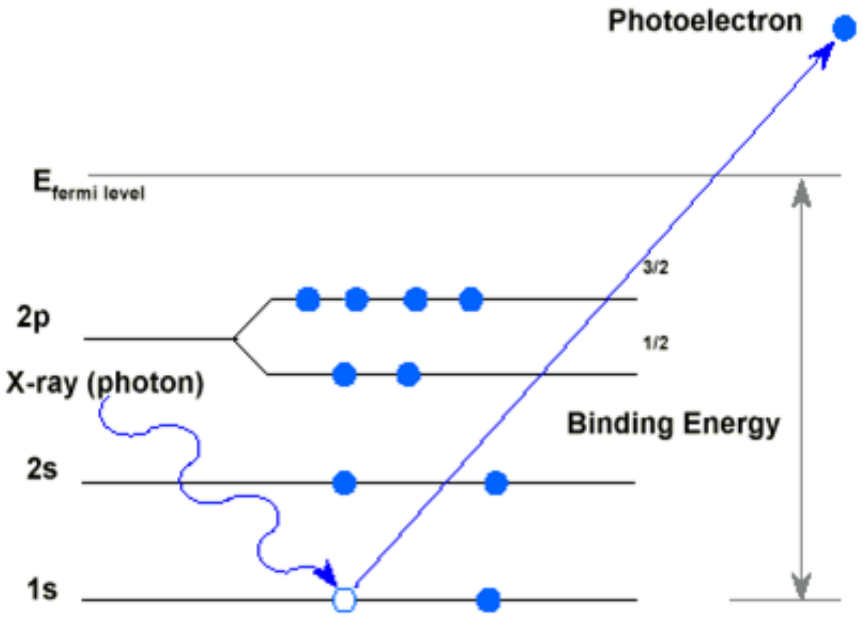

Figure 3.6: Schematic representation of the XPS process [14].

XPS spectra have a step like background, increasing with binding energy. They result from inelastic scattering of photoelectrons in a solid. The XPS spectrum can also include extra, or satellite, peaks associated with a main core-level peak.

Shake-up satellites are the extra peaks which result from interaction between a photoelectron and a valence electron. A photoelectron can excite

(shake-up) a valence electron to a higher energy level and thereby lose a few electron volts of kinetic energy. This will create a satellite peak associated with a core level peak of photoelectrons. Multiplet splitting of a core level peak may occur in a compound that has unpaired electrons in its valence level.

XPS is extremely sensitive to chemical changes occurring at the surface, with a depth resolution close to atomic dimensions. XPS provides the elemental composition information of the surface (top 1-10 nm usually). The binding energies for electrons in the outermost shell of an atom are strongly affected by the chemical state for example the binding energy difference between C-C and C=O is about 3 eV. Chemical shifts can also reveal the degree of oxidation in molecular solids. The larger the number of electrons transferred, the higher the chemical shift. Chemical shifts are less obvious in metallic and semiconductive elements because the shifts decrease with increasing atomic number. For example the shift range of Si *2p* is less than 6 eV.

The binding energy of an electron does not only depend upon the energy level of emission but also upon the oxidation state of the concerned atom and the local surrounding to that atom. A change in either of the two factors results in a shift of the peak for that atom in the spectrum, which is called as chemical shift. Atoms of a higher positive oxidation state exhibit a higher binding energy due to the extra coulombic interaction between the photoemitted electron and the ion core. Similarly, presence of an electronegative atom in the surrounding of the atom in question, a net partial positive charge is imparted to that atom.

Thus, emission of an electron from such an atom will require higher energy, which shifts the peak to higher binding energy. This ability to discriminate between different oxidation states and chemical environments is one of the major strengths of the XPS technique.

Hydrogen and Helium within solids are not detectable by XPS because their photoelectron cross sections (yields) are below XPS detection limits. This arises from a combination of effects namely, that

(a) Photoelectron cross-section (these governs intensities) from stationary states (energy levels) of a specific principle quantum number decrease with decreasing atomic number.

(b) XPS is not highly sensitive to valence electrons (hydrogen and helium only have valence electrons, while XPS analysis is optimized towards core electrons) [15, 16].

3.4. X-ray diffraction (XRD)

Material properties are generally related to the arrangements of the atoms in its crystal structure. X-ray diffraction is non destructive, most effective technique to determine the crystal structure of materials. This technique is also useful to identify chemical compounds from their crystalline structure. X-rays are short-wavelength and high energy beams of electromagnetic radiation. X-ray energy is characterized either by wavelength or photon energy. X-rays are produced by high speed electrons accelerated by a high voltage field colliding with a metal target. Rapid deceleration of electrons on the target enables the kinetic energy of electrons to be converted to the energy of X-ray radiation. The wavelength of X-ray radiation (λ) is related to the acceleration voltage of electrons (V) as (equation 3.8).

$$\lambda = \frac{1.2398\times10^{3}}{V}(nm) \tag{3.8}$$

X-ray wavelength is in the order of 0.1 nm. In a physical point of view of X-ray generation an incident electron with sufficient energy excite an electron from inner shell of the an atom to a higher energy state, the vacancy left in the inner shell will be filled by tan electron in an outer shell. As the electron falls in the inner shell, energy will be released by emitting an X-ray with a specific wavelength or photons with specific energy.

X-ray diffraction methods are based on the phenomenon of wave interference. Two light waves with the same wavelength and traveling in the same direction can either reinforce or cancel each other, depending on their phase difference. When they are a phase difference $n\lambda$ (n is an integer), called in phase, constructive interference occurs as shown in figure. When they have a phase difference of $n\lambda/2$, called completely destructive interference occurs. X ray beam incident on a crystalline solid will be diffractive by the crystallographic planes as shown in figure will be in phase following Bragg´s relationship (equation 3.9).

$$n\lambda = 2dsin\theta \tag{3.9}$$

By knowing the spacing of crystallographic planes by diffraction method, we can determine the crystal structure of materials. XRD instrument is called an X-ray diffractometer. X-ray diffractometer is often used to examine powder samples, polycrystalline solid samples and even liquids. Importantly, a sample should contain large number of tiny crystals (or grains) which randomly orient in three-dimensional space because standard X-ray diffraction data are obtained from powder samples of perfectly random orientation. A diffractometer records changes of diffraction intensity with *2θ*. The diffractometer record the diffraction intensity starting from a low *2θ* and ending at a high *2θ*. Commonly a range of about 5-65° is necessary with an unknown material. Copper kα is the most popular radiation source used in diffractometry because of its short wavelength [17, 18].

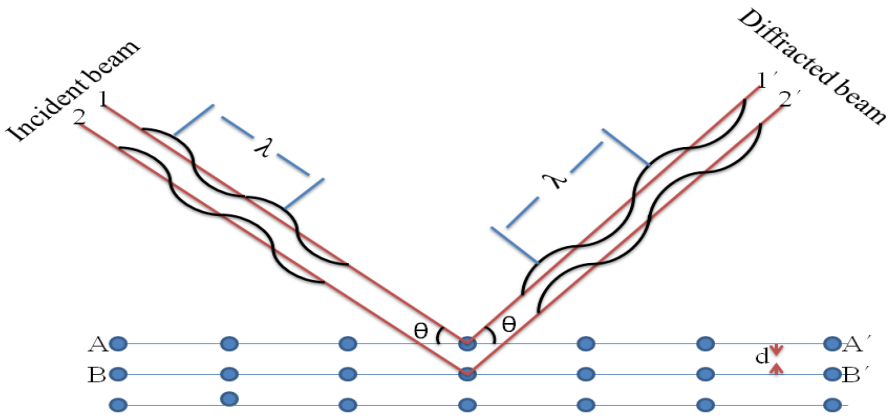

Figure 3.7: Bragg´s law of diffraction

3.5. Energy dispersive X-ray spectroscopy (EDX)

Energy Dispersive X-ray spectroscopy is a non destructive qualitative and quantitative X-ray microanalytical technique in which an electrons beam is used to excite the emission of characteristic X-rays from the sample atoms. When a high energy particle, such as photon, electron or neutron strikes an electron in the inner shell (such as K shell) of an atom, the energy of the particle can be high enough to knock an electron out of its original position in an atom. The atom becomes ionized. The knocked-out electron leaves

the atom as a free electron and the atom become ionized. Because ionization is an excited state, the atom will quickly return to its normal state after refilling the inner electron vacancy by an outer shell (L shell) electron. The excessive energy is emitted as a characteristic X-ray photon. The energy of the X-ray is characteristic of the sample atomic number from which it is derived. There is another possibility after refilling the K shell hole by L shell electron, the excessive energy could also be transferred to another electron in L shell which is subsequently ejected as and Auger electron. Two types of X-ray results from the interaction between high energy electron and sample: Bremsstrahlung X-rays which means 'braking radiation' and are also referred to as continuum or background X-rays, and characteristic X-rays. The frequency of characteristic X-ray is determined by the change in the energy level of the electrons by (equation 3.10).

$$E = hf \tag{3.10}$$

And the frequency of Bremsstrahlung is determined by change in the kinetic energy of the electron (equations 3.11, 3.12).

$$E_{k_i} = E_{k_f} + E_{X-ray} \tag{3.11}$$

$$E_{X-ray\,(\max)} = E_{k_i} \tag{3.12}$$

A parameter, Fluorescent yield (ω) is used to measure the relative effectiveness of X-ray generation. Fluorescent yield (ω) variation in *K*, *L* and *M* series is different for each element and energy of K series higher than L and M series as shown in figure. Fluorescent yield increased with atomic number. The typical resolution of EDS is about 150-200 eV. Elements below (Z=8) O are not detectable from EDS. The detector which is used is Si(Li) diode.

EDS in an electron microscopy is suitable for analyzing the chemical elements in microscopic volume. Instead of using the primary X-ray source beam, a high energy electron beam is used [19].

3.6. Optical emission spectroscopy (OES)

Emission spectroscopy is a spectroscopic technique which examines the wavelength of the photons emitted by atoms or molecules during their transition from an excited state to a lower energy state. These excited atoms and ions in the discharge plasma create a unique emission spectrum specific to each element. A single element generates numerous characteristic emission spectral lines as shown in (figure 3.8) for hydrogen atom. Radiation is emitted from atoms in discrete quanta, called photons, whose energy ΔE is equal to the difference in energy between the initial i and final f stationary states of the atom, and proportional to the frequency, *v,* (equation 3.13).

$$\Delta E = E_i - E_f = h\nu \tag{3.13}$$

In optical spectroscopy we normally use wavelength rather than frequency, hence the observed wavelength in vacuum, λ_{vac}, (equation 3.14).

$$\lambda_{vac} = \frac{c}{\nu} = \frac{ch}{\Delta E} \tag{3.14}$$

where *c* is the speed of light in vacuum.

The frequency of EM filed associated with photon does not change when it travel from one medium to another but both speed and wavelength do change. The refractive index of a medium is defined as the ratio of the speed of light in vacuum to the speed of light in the medium. The difference in the wavelength is air and vacuum is given by (equation 3.15).

$$\lambda_{vac} - \lambda_{air} = (n_{air} - 1)\lambda_{air} \tag{3.15}$$

where n_{air} is the refractive index of air. Since n_{air} is slightly greater than 1. λ_{air} is slightly less than λ_{vac}. The refractive index of air varies with the composition of air and its density, i.e. it varies with the purity of the air and its pressure and temperature. The refractive index of nitrogen is very close to that of air, except that high purity nitrogen transmits wavelength below 180 nm that air will not.

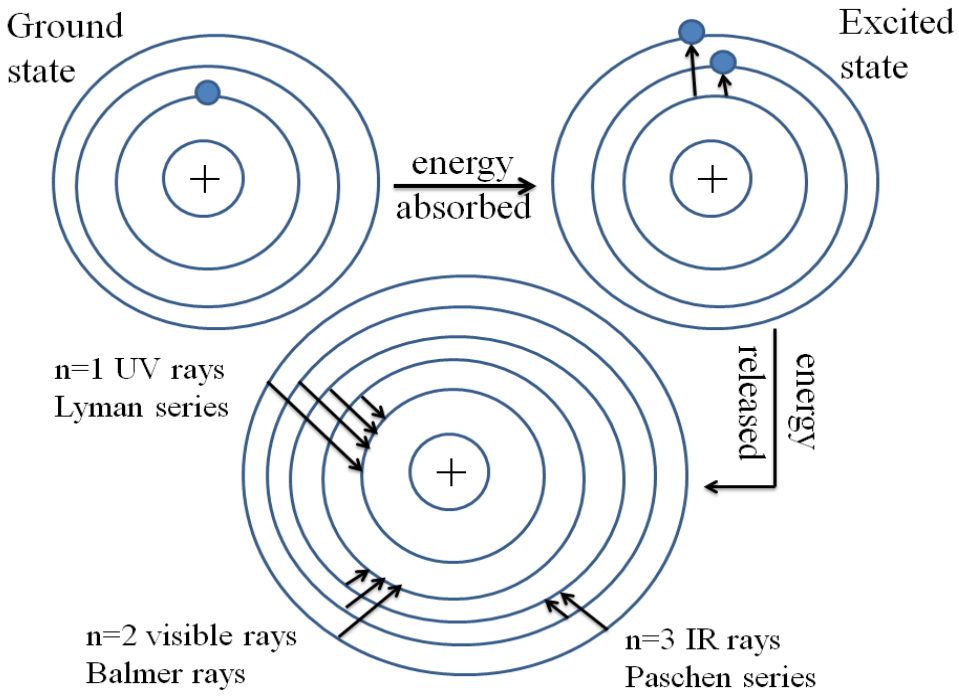

Figure 3.8: characteristic line for hydrogen.

By convention, the emission lines above 200 nm are labeled by their values in air. This is done even when the wavelengths are measured in vacuum and then converted to air values. Below 200 nm emission lines are labeled by their values in vacuum. Theoretical spectra are available for atoms and their first ionic states for virtually all elements in the periodic table. Such spectra assume that emitting atoms are in local thermodynamic equilibrium (LTE). This assumption is necessary to estimate the population of atoms and ions in their various excited states, according to Boltzmann statistics. The wavelength of emission line depends on the difference in energy between the initial (excited) and final (de-excited) state of the atom and in analytical plasmas is largely unaffected by the plasma. The intensity of emission line is proportional to the number of atoms in excited state. The GD plasma is not in LTE. This means while the wavelengths of emission lines will be nearly the same as those from other plasma (neglecting the small pressure effects), the intensities, and especially the ratio neutral to ionic lines, may be quite different.

For nearly pure single element materials it is relatively straightforward to determine the strongest lines of the elements.

The main complication is the presence of Ar lines. A rapid way to identify Ar lines is to record the spectra from two different pure materials remove a constant background and then multiply the two spectra. Since the Ar line will be in both spectra, the multiplied spectra will highlight the Ar lines.

It is much more difficult to determine the most intense lines for elements that are not available for as suitable single element materials. Spectral interferences are not usually a major problem in GDOES, but they do occur in particularly when spectrometers with low resolving power are used [20, 21].

3.7. Contact angle

The contact angle is the angle; conventionally measured through the liquid, where a liquid/vapor interface meets a solid surface. This technique gives us information about the variation of wettability of the solid surface by a liquid via the Young equation (equation 3.16).

$$\gamma_{sg} = \gamma_{sl} + \gamma_{lg} Cos\theta \tag{3.16}$$

where the surface energies correspond to the solid-gas interface, γ_{sg}, to the liquid-gas interface, γ_{lg}, and to the solid-liquid interface, γ_{sl}. A given system of solid, liquid, and vapor at a given temperature and pressure has a unique equilibrium contact angle. The wettability of the CNTs surface is an important property, governed both by chemical composition and by the geometrical microstructure of the contact surface, which can play a key role in the CNTs performance during their applications. We measured the static contact angle by using the device CAM200 to check the surface properties of CNTs [22].

3.8. Quadrupole mass spectrometry

Mass spectrometry is one of the most popular analysis methods today. A mass spectrometer analyzes the composition of chemical substances by means of partial pressure measurement (figure 3.9). The quadrupole mass analyzer or residual gas analyzer is one type of mass analyzer used in mass spectrometry. As the name implies, it consists of four cylindrical rods, set parallel to each other. The residual gas analyzer (RGA) consists of an ion source, a mass spectrometer, and a measurement section. The residual gas is ionized when it collides with the thermoelectrons discharged from the

high-temperature filament, and the ions that are thereby created accelerate and converge onto the mass spectrometer. At the mass spectrometer, direct and alternating current voltages are applied to the four cylindrical electrodes (quadrupole mass analyzer is a quadrupolar lens acting as a mass filter. A suitable DC+RF signal creates a quadrupolar electric field allowing selecting each *q/m* ratio into a mass-to-charge range of 300 uma. Then, ions can be separated by mass and counted by an electrode mounted inside a Faraday cup. The measured ion current is proportional to the charge (partial pressure) at a given particle mass of the residual gas. The lower limit of partial pressures which can be detected with such an instrument is about 10^{-14} mbar. In the RGA the following chemical species can be detected:

1. Fragments of several hydrocarbons, such as mechanical pump oil, diffusion pump oil, vacuum grease, cutting oil, and organic solvents.

2. Fragments of several *chlorinated hydrocarbons* such as *carbon tetrachloride, trichloroethylene* and many freons.

3. Fragments from both straight chain hydrocarbons and benzene ring hydrocarbons.

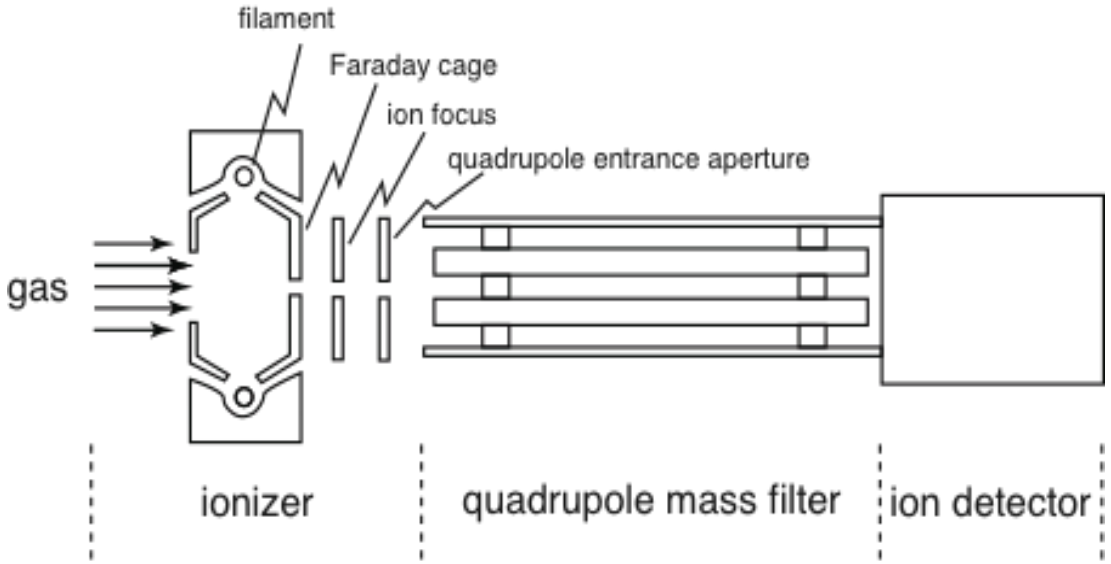

Figure 3.9: Schematic figure of QMS [23].

3.9. Ultraviolet/visible spectroscopy

The human eye is only sensitive to a tiny proportion of the total electromagnetic spectrum between approximately 380 and 780 nm and

within this area we perceive the colors of the rainbow from violet through to red. The full electromagnetic spectrum is shown in (figure 3.10). The energy of visible light depends on its frequency, and is approximately equivalent to 170 kJ mol^{-1} (mole of photons) for red light and 300 kJ mol^{-1} for blue light. The promotion of electrons to different energy levels is not restricted to electromagnetic radiation in the visible part of the spectrum; it can also occur in the ultraviolet region.

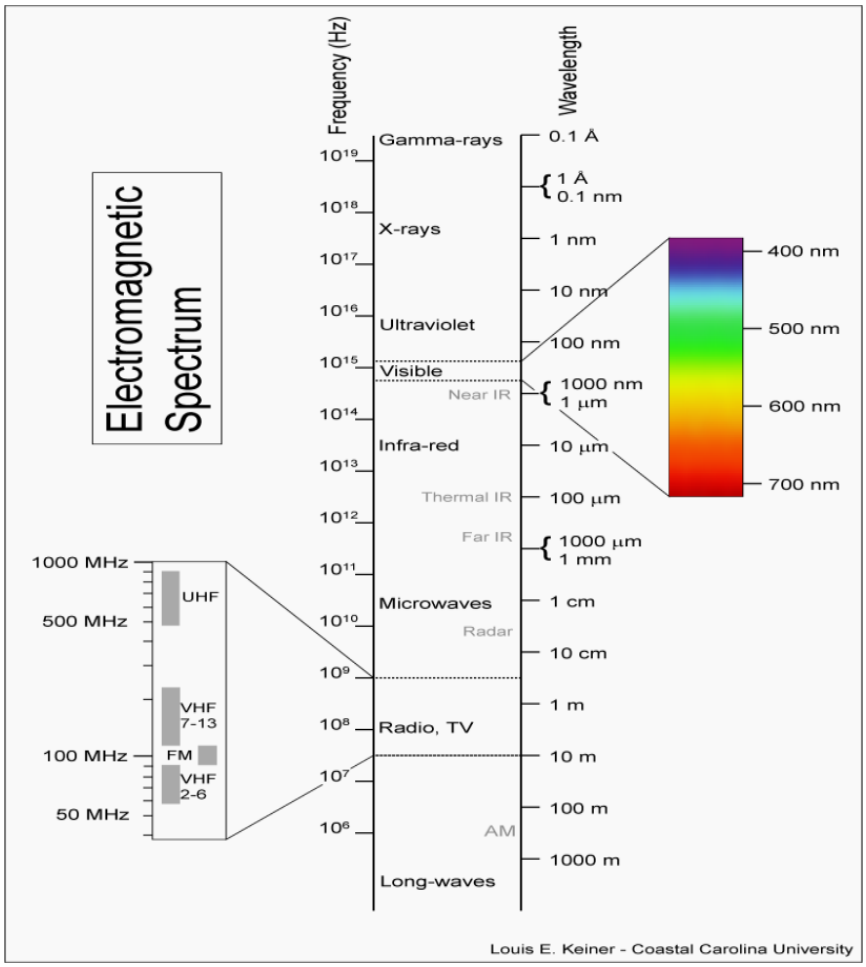

Figure 3.10: The ful electromagnetci spectrum [24].

A spectrophotometer is employed to measure the amount of light that a sample absorbs. The instrument operates by passing a beam of light through a sample and measuring the intensity of light reaching a detector. The interaction of electromagnetic radiation with solids, liquids or gases produces various effects, such as absorbance, reflectance or scattering.

UV VIS spectroscopy exclusively investigates the interaction of radiation with matter in the ultraviolet and visible range. When atoms or molecules absorb electromagnetic radiation they are transformed from a ground state into an energetically excited state. Energy of a specific wavelength is absorbed in this process. The various molecular states have a relatively broad energy range in comparison with atoms. Rotation and vibration of a molecule can be stimulated in the infrared range. The absorbance of defined packets of energy (quanta) by the valence electrons is observed in the range of visible and ultraviolet light. The energy of these quanta can be specified as the wavelength of the radiation. The shorter the wavelength, the greater will be the energy of the quanta. The location of the absorbance points and the relative magnitudes of absorbance can be determined with UV VIS spectrophotometers.

Beer's law tells us that absorption is proportional to the number of absorbing molecules – i.e. to the concentration of absorbing molecules (this is only true for dilute solutions) – and Lambert's law tells us that the fraction of radiation absorbed is independent of the intensity of the radiation. Combining these two laws, we can derive the Beer-Lambert Law: The Bouguer-Lambert-Beer law describes the relationship between absorbance and concentration (equation 3.17).

$$log_{10}\frac{I_0}{I} = \varepsilon lc \tag{3.17}$$

where I_o = the intensity of the incident radiation

I = the intensity of the transmitted radiation

$\varepsilon = a$ constant for each absorbing material, known as the molar absorption coefficient (called the molar extinction coefficient in older texts) and having the units mol^{-1} dm^3 cm^{-1}, but by convention the units are not quoted

l = the path length of the absorbing solution in cm

c = the concentration of the absorbing species in mol dm^{-3}

Calibration means measuring samples with known concentration (standards) and the measured absorbance values are entered against the respective concentrations. The Lambert-Beer law applies within the linear range of the calibration curve [25].

3.10.References

[1] Ellen Rosenberg and Michael Weis, *Introduction to Electron Microscopy*, CH5, http://www.ableweb.org/volumes/vol-10/5-rosenberg.pdf

[2] http://bsp.med.harvard.edu/node/219

[3] Elton N Kaufmann, *Charcterization of materials* (volume 2). Printed in USA. ISBN 0-471-26882-8

[4] Bettina Voutou and Eleni-Chrysanthi Stefanaki, *Electron Microscopy*: The Basics, Physics of Advanced Materials Winter School 2008.

[5] J L Labar, *Introduction to electron microscopes: electron optics, interactions and signals*, (2002), http://www.mfa.kfki.hu/~labar/Introduction.pdf

[6] K D Vernon-Parry, *Scanning electron microscopy: an introduction*, (2000), Analysis, 13, 4, 40-44.

[7] K D Vernon-Parry, *TEM: an introduction*, (2000), Analysis, 13, 6, 36-40.

[8] http://cbe.ivic.ve/mic250/pdf/thesebook-chap3.pdf

[9] http://en.wikipedia.org/wiki/Transmission_electron_microscopy

[10] Tariq Jawhari, Handbook of instrumental techniques from CCiTUB, *Raman spectroscopy as a powerful analytical tool: probing the structure of matter*, CH2. (2012)

[11] M S Dresselhaus, G Dresselhaus, R Saito, A Jorio, *Raman spectroscopy of carbon nanotubes*, (2005), Physics Reports, 409, 47–99.

[12] M S Dresselhaus, A Jorio, M Hofmann, G Dresselhaus, and R Saito, *Perspectives on Carbon Nanotubes and Graphene Raman Spectroscopy*, (2010), Nano Lett., *10*, 751–758.

[13] A C Ferrari and J Robertson, *Interpretation of Raman spectra of disordered and amorphous carbon*, (2000), Physical review B, 61, 20, 14095-14107.

[14] http://webhost.ua.ac.be/mitac4/micro/micro_xpsaes.pdf

[15] http://www.casaxps.com/help_manual/manual_updates/xps_spectra.pdf

[16] http://csacs.mcgill.ca/francais/docs/CHEM634/XPS_Paynter_t.pdf

[17] http://www.microscopy.ethz.ch/bragg.htm

[18] Cullity, B.D. *Elements of X-ray diffraction*, Addison-Wesley Publishing Co.Inc. 1978.

[19]http://cime.epfl.ch/files/content/sites/cime2/files/shared/Files/Teaching/EDX/Introduction%20to%20EDS.pdf
[20]http://books.google.es/books?id=RMXMaI9o7gMC&printsec=frontcover&source=gbs_ge_summary_r&cad=0#v=onepage&q&f=false
[21] http://www.shimadzu.com/an/elemental/oes/oes.html
[22] Carles Corbella Roca, *Thin film structures of diamond-likecarbon prepared by pulsed plasma techniques*, (2005), PhD thesis.
[23] http://philiphofmann.net/ultrahighvacuum/ind_RGA.html
[24] http://quibb.blogspot.com.es/2011/01/electromagnetic-spectrum.html
[25] Analytik Jena AG, *Fundamentals, Instrumentation and techniques of UV VIS Spectroscopy*, www.analytik-jena.com
[26] http://www.charfac.umn.edu/sem_primer.pdf

PART III- EXPERIMENTAL RESULTS

Chapter 4
Growth of vertically aligned carbon nanotubes by plasma enhanced chemical vapor deposition and water plasma functionalization

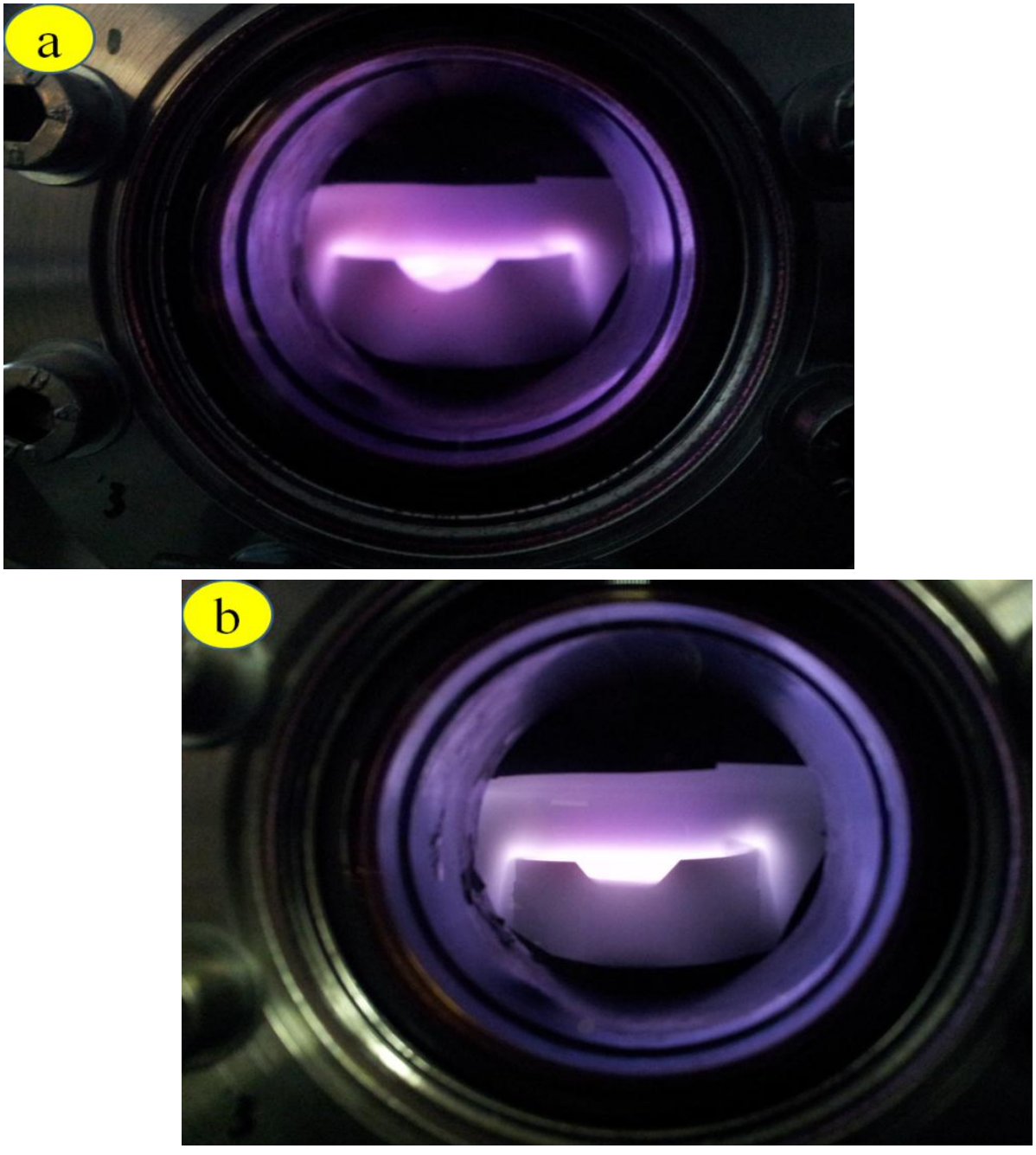

Figure 4: Water plasma photographs (a) 75 W, 135 Pa, (b) 140 W, 135 Pa.

Chapter4- Growth of Vertically aligned carbon nanotubes by Plasma enhanced chemical vapor deposition and water plasma functionalization

4.1. Introduction

Owing to the attractive size-dependent properties of nanophase materials, the development of nanoscience and nanotechnology has opened up unique significant and applied frontiers in material science and engineering. CNTs are considered an essential contributor to the field of nanotechnology and have found a wide range of applications like, e.g., as electrode material in supercapacitors, as transparent conductors, in various kinds of sensors and field emission displays.

Growth of MWCNTs by CVD is a very promising technology that allows precise control over the length, diameter and positioning [1]. Particularly, plasma enhanced chemical vapor deposition (PECVD) [2] is an excellent technique to grow vertically aligned carbon nanotubes (VACNTs), which are suited for many applications.

The poor solubility of CNTs in solvents and the inertness of their surface is a big obstacle in real-world applications [3, 4]. Therefore, it is important to be able to functionalize the surface of CNTs through the incorporation of different chemical groups. CNTs can be functionalized by different types of treatments like air oxidation, ozone oxidation [5], photo oxidation [6], plasma oxidation [7-12] or by electrowetting [13]. Furthermore the treatment of CNTs with certain acids (e. g. refluxing in HNO_3 or H_2SO_4) was proved to open nanotubes tips and introduce oxygen containing groups [14-16]. The main purpose of the oxidative treatment is the removal of metallic catalyst particles used in the synthesis of nanotubes and of the amorphous carbon generated as a synthesis byproduct.

Most treatment methods involve long procedures with very low yield of pure nanotubes [17]. It is desirable that the treatment should be surface exclusive so that the bulk properties are preserved. Plasma technique is an effective, rapid and versatile technique, with limited effects on the surface and adjacent areas of the CNTs that can be easily tuned through its intensity [18, 19]. The excited species, radicals, electrons, ions, and UV light within the plasma strongly interact with the surface of CNTs, breaking the C=C bond and creating active sites where chemical groups are bonded.

Depending on the plasma parameters such as power, pressure, gas mixture and treatment time a wide range of functional groups can be introduced.

4.2. Growth of VA-MWCNTS

CNT production was carried out on p-type boron doped silicon wafers (0.01-0.02 Ω cm range) by PECVD technique. Prior to every vacuum process, the pressure in the corresponding reactor was lowered to the level below 4×10^{-4} Pa to ensure clean deposition conditions. In first step sputtering of Fe catalyst on Si wafer was use to deposit 3 nm with the presence of 2 Pa and 50 W Ar plasma. PECVD was chosen as a better process to grow vertically aligned CNTs. Growth process with PECVD was done at 680°C, 900 s and 50 W RF power in the presence of NH_3/C_2H_2 mixture where NH_3 is using as a carrier gas and C_2H_2 is a precursor gas (table 4.1).

Table 4.1: Summary of VACNTs growth conditions.

Parameter	Value
Catalyst layer thickness	3 nm
Annealing time	870 s
PECVD process temperature	680 ºC
PECVD process plasma power	50 W
PECVD process time	900 s

It is generally accepted that VLS description presented by Baker et al. [20] for carbon filament growth is also applicable to carbon nanotube growth, at least when metal catalyst particles are employed. The tubular structure of the CNTs was verified by HRTEM. (Figure 4.1 (a)) shows the nanotubes with catalyst on their top surfaces. The side walls of CNTs contains the amorphous carbon which is a usually a byproduct during the PECVD growth. (Figure 4.1 (b)) show the elongated catalyst particle at the tip of the CNT; clearly indicates the tip growth mechanism. The arrows inside the nanotube (Figure 4.1 (b)) demonstrate the graphene layers inside the nanotube at certain distances. This kind of structure defines as the bamboo-like shape of the CNTs rather than the hollow cylindrical shape in which the nanotube from inside is empty. A bamboo-shaped nanotube consists of regular cone shaped compartments. Compartment formation in the bamboo like structure occurs because of periodic precipitation of graphite sheets on

the top of catalyst particle. NH_3 can easily be dissociated due to weaker bonds compared to that of H_2. Martin S. Bell et al. Found bamboo-structure in nitrogen containing plasma and hollow tubes in nitrogen-free plasma suggests that nitrogen or CN played critical role in compartment formation. They found CN plays a critical role in the formation of bamboo like structure. Further, it is believed that CNTs growth occurs via surface (SD) and/or bulk diffusion (BD) of carbon species through catalyst particles. High concentration of CN promoted BD of carbon through Fe particles and

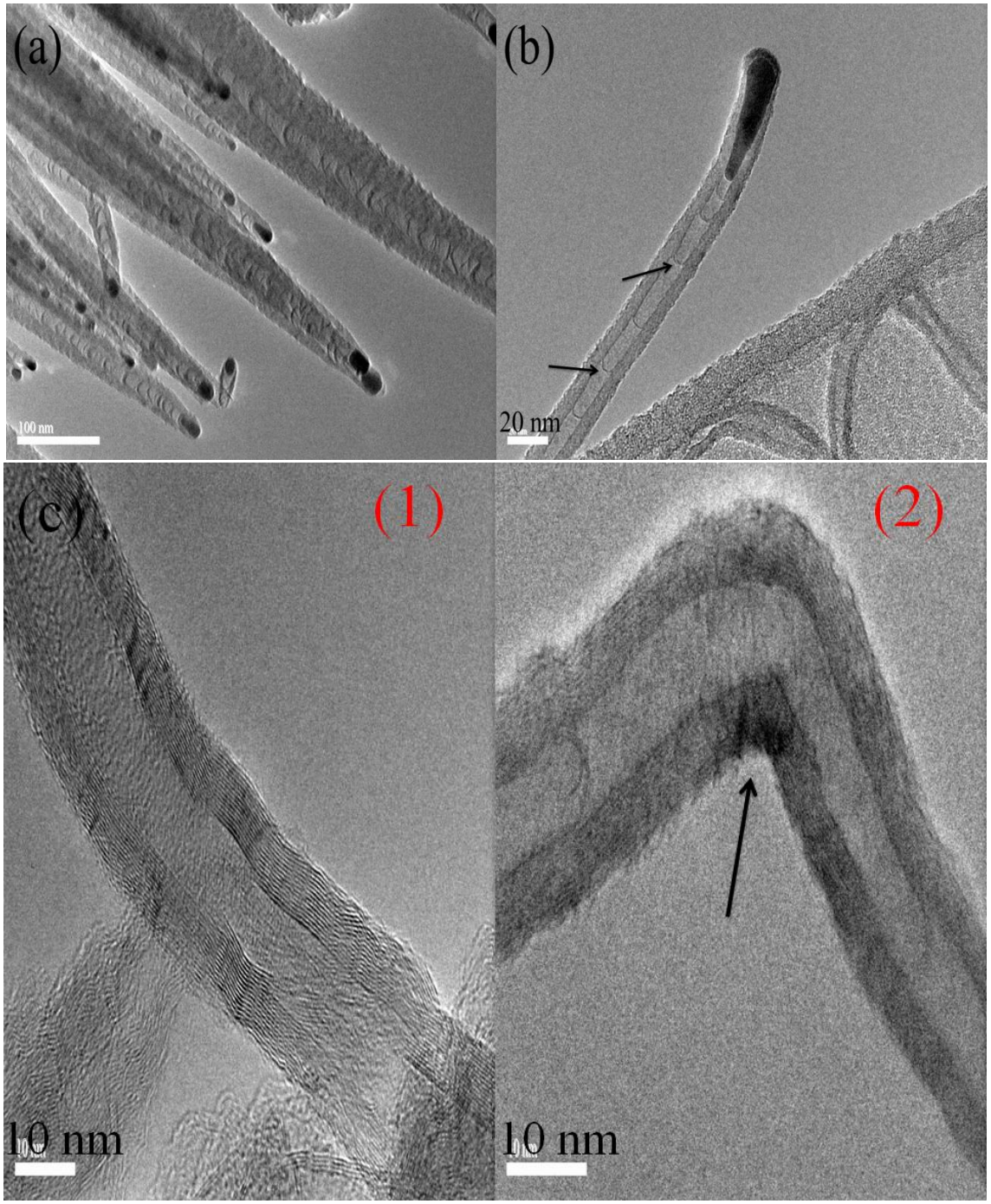

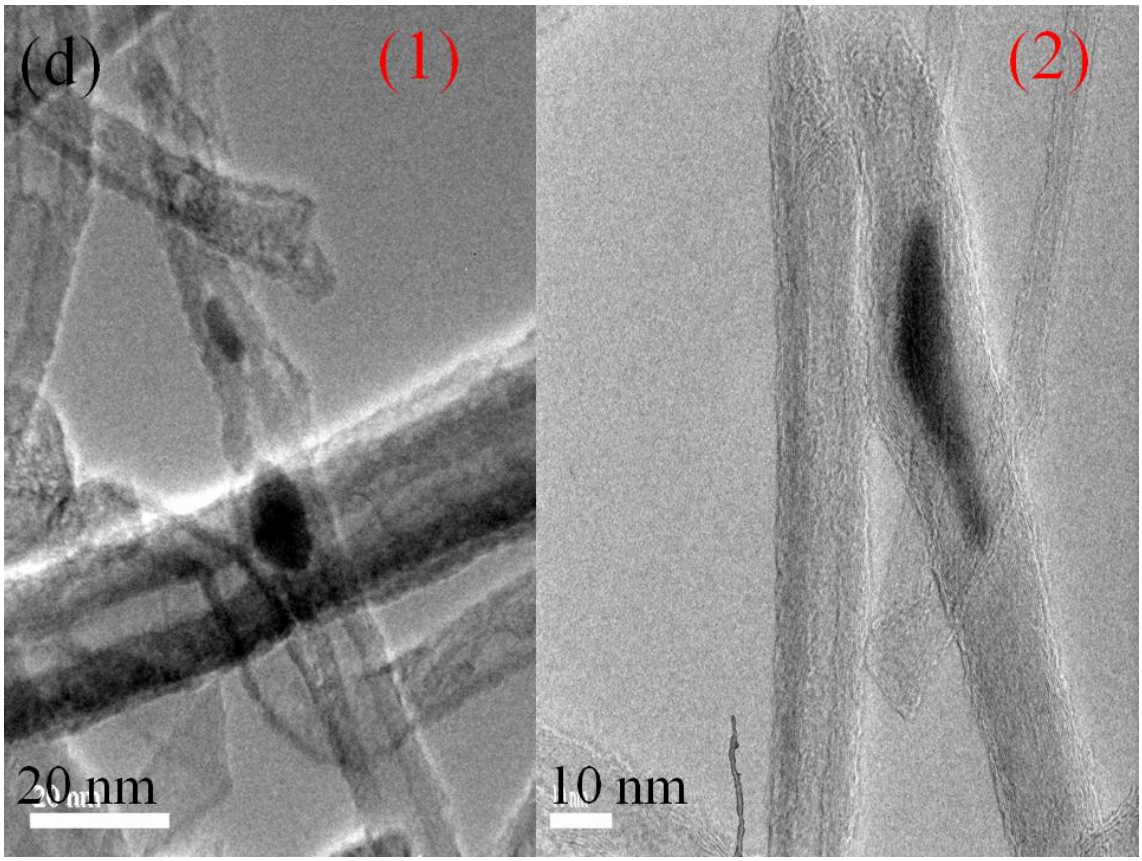

Figure 4.1: HRTEM images of PECVD grown MWCNTs.

suppressed SD by keeping the catalyst surface clean and hence, shorter CL. There is a possibility of CN diffusion through the Fe particles as well [21]. But CN or N has very limited solubility in Fe so the concentration of N or CN in Fe is supposed to be very less compared to carbon. Outer diameter of growing tube is confined by size of the catalyst particle. Shape of the tip is controlled by the local geometry of the catalyst particle seeding the growth of the tube [22]. The production of nanotubes requires a controlled deposition of carbon, which can then self-assemble into an energetically favored nanotube form. This controlled deposition rate is achieved through the combination of two reactions: the dissociation of a carbon-rich gas (in our case, C_2H_2) and the removal of excess carbon, which would otherwise lead to amorphous carbon deposits.

The main role of NH_3 was to hinder the formation of amorphous carbon and dilute the C_2H_2. At high NH_3 ratios, NH_3 decomposes preferentially over C_2H_2 due to the relative weakness of its molecular bonds. This allows the C_2H_2 to decompose slowly, generating the controlled amounts of

carbon necessary for nanotube formation and giving rise to clean, well-aligned carbon nanotubes. At high C_2H_2 ratios, there is insufficient NH_3 to effectively suppress C_2H_2 decomposition, resulting in higher levels of carbon generation and the deposition of amorphous carbon onto the substrate. NH_3 has a key role in removing any excess carbon through the generation of reactive atomic hydrogen [23]. Figure c (1) shows the graphitic nature of the CNTs with amorphous carbon on side walls the nanotube. The planes are clearly visible with a plane to plane distance of 0.34 nm. It is known that metal atoms become mobile at Tamman temperature (Half the melting temperature in kelvin). R Sharma et al. proposed a model for the growth mechanism of the CNT growth by using Ni as a catalyst. They suggested CNT growth is related to the certain crystallographic surface. The particles rotate and melt and re-crystallize [24]. As shown in the (figure 4.1 C (2)) change in the inner diameter and direction. These changes in the inner diameter could be due to the change in the crystallographic structure of the Fe catalyst. (Figure 4.1 d (1)) shows the 2 catalyst particles reside in the nanotube. Possibly catalyst particles brake during the growth, which proves the catalyst was in liquid state during the growth.

4.1. Functionalization of VA-MWCNTs

Basically, CNTs have two areas with different reactive sites: the fullerene-like tube ends and the less reactive hexagonal cylindrical tube walls. The carbon bonds at the tips are under higher strain due to their large curvature and provide an area of enhanced reactivity and lower activation energy for oxidation reactions; therefore, oxidation is expected to start at the tips rather than at the cylindrical walls [25].

H_2O plasma technique was used to remove amorphous carbon, Fe particles and to functionalize the surface of CNTs by introducing various oxygen functional groups such as carboxyl and hydroxyl groups. These functional groups on the side walls of CNTs are favourable to contribute as a faradaic capacitance in total capacitance of the supercapacitor in aqueous solution. While for nonaqueous solutions they are not good because they are easily decomposed at 1.2 V and release some gases [26]. H_2O vapor was supplied through a mass flow controller using a water flask. The plasma treatment time was set to 120 s for each experiment.

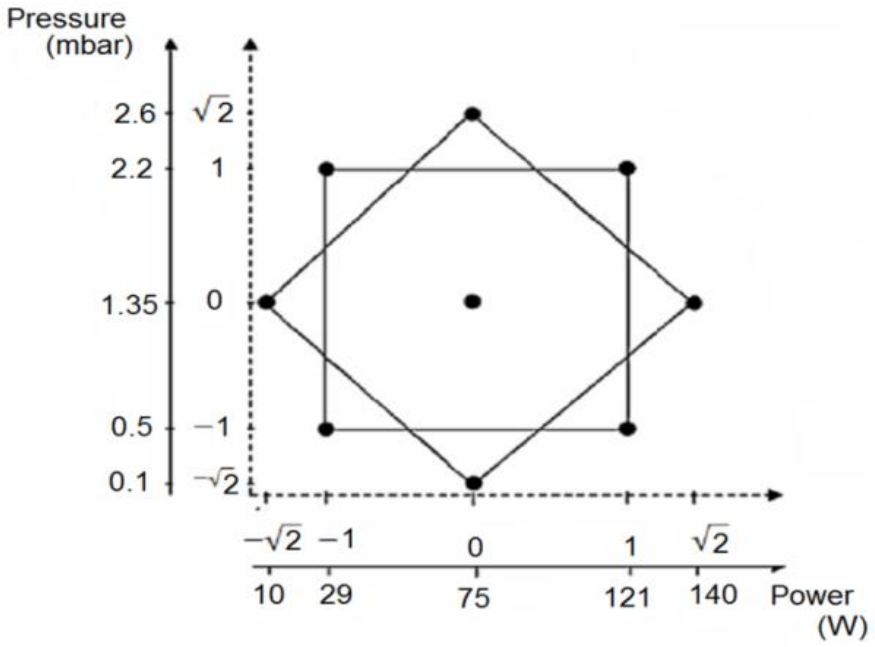

Figure 4.2: Box-Wilson experimental design samples distribution for two main parameters (RF power and water pressure).

In this work vertically aligned MWCNTs were treated with pure H_2O plasma. Previous reports by other researcher have used an Ar/H_2O mixture [7–10]. The pure water plasma interacts chemically with the nanotubes and physically by an intense protonic bombardment, while an argon mixture includes physical effects (sputtering) and reduces the chemical effects. Furthermore, we used radio frequency (RF) power to ignite the plasma instead of microwave power, as reported in most of the Ar/H_2O plasma articles [7-10]. RF plasma [18] appears very stable and homogeneous in a large area at very low power densities (0.5 W cm^{-2}).

The optimization of the different operational parameters such as water pressure and RF power was addressed adopting a Box-Wilson experimental design. According to Box-Wilson graph distribution, 9 conditions were chosen to perform the 13 experiments (figure 4.2). The experimental design allows the simultaneous optimization of two operating parameters taking into account possible interactions between them. The central point of the design was replicated 5 times in order to evaluate the intrinsic standard deviation of the process. A wide range of dependent variables were evaluated using the Box-Wilson experimental design, such as diameter,

length, crystallinity, relative content of oxygen groups, hydrophobicity of the CNTs and species present in the plasma. Using this method, a second degree polynomial equation including first level interactions was obtained for each dependent variable, (equation 4.1):

$$X = a_0 + a_1 A + a_2 B + a_3 A^2 + a_4 AB + a_5 B^2 \quad (4.1)$$

where X is the dependent magnitude, a_n are constant coefficients obtained by statistically adjusting these polynomial equations, A is the plasma power and B the water pressure.

4.1. Results and discussion

4.1.1. Optical emission spectroscopy (OES)

The chemical species generated in the plasma emit at different wavelengths according to their nature and can be determined by optical emission spectroscopy (OES). The spectrum of the water plasma obtained at different conditions of water pressure and plasma power were analyzed with this technique. The outcoming light from the discharge was collected through a quartz optical fiber and led to a spectrophotometer (Stellarnet EPP2000C), which operated centered in the UV–VIS range (185–850 nm).

We supposed that the high RF energy break up the 1st OH bond and 2nd OH bond in H_2O molecules at low power. As more RF power is supplied the remaining OH molecules are further dissociated into hydrogen and oxygen atoms that rapidly recombine to form hydrogen and oxygen molecules. (Figure 4.3 (a)) shows that at low power only the OH peak (309 nm) appears, however with increasing power the intensity of the peaks becomes higher and two new peaks appear at 655 nm (Hα) and 486 nm (Hβ). Moreover, at high pressures the intensities of the Hα and Hβ peaks are lower and even disappear in the case of the Hβ peak (Figure 4.3 (b)). (Table 4.2) shows the intensities of OH, H_α and H_β.

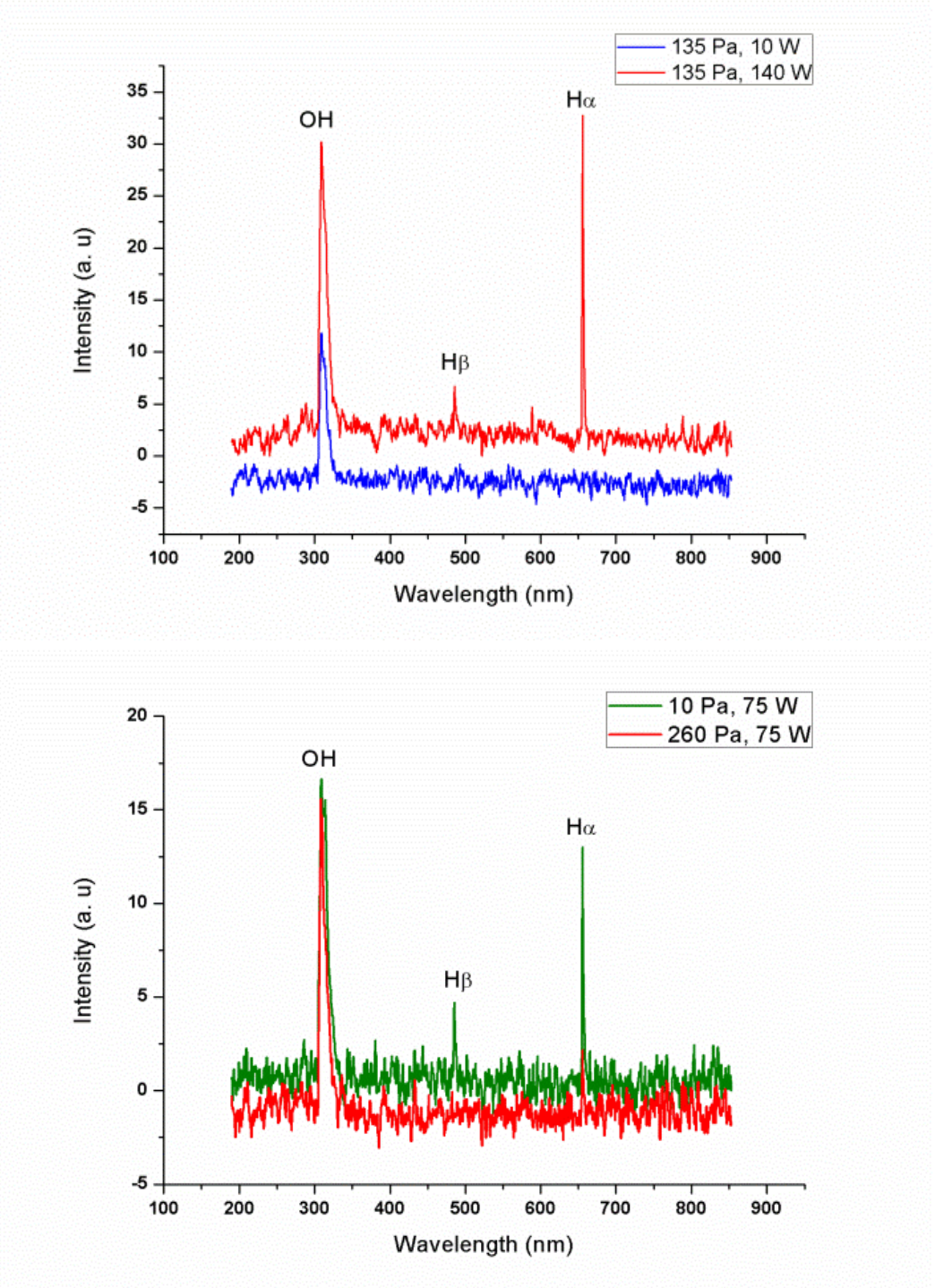

Figure 4.3: (a) OES spectra with low and high RF power at constant water pressure, (b) OES spectra at low and high water pressure at constant RF.

Table 4.2: Optical emission spectroscopy intensities in a.u.

H_2O RF-Plasma	OH (a.u.)	H_α (a.u.)	H_β (a.u.)
10 W, 135 Pa	11.84	0	0
29 W, 50 Pa	39.18	13.1	0
29 W, 220 Pa	14.69	0	0
75 W,10 Pa	16.64	13	4.421
75 W, 135 Pa	32.16	18.82	0
75 W, 260 Pa	15.6	2.17	0
121 W,50 Pa	66.42	42.06	11.42
121 W, 220 Pa	20.77	15.61	0
140W, 135 Pa	30.19	32.77	6.69

4.4.2. Scanning electron microscopy

Field Emission Scanning Electron Microscopy (FE-SEM) studies were performed on a Hitachi S-4100 (Japan) and (FE-SEM) (FEI Nova NanoSEM 230, USA). The FE-SEM images clearly show the effect of water plasma treatment on changing the power and pressure (see figure 4.4). (Figure 4.4 (a)) corresponds to an untreated sample of MWCNTs. The nanotubes are vertically well aligned, with a length of about 8 μm, highly dense and homogeneous. The inset displays the amorphous carbon on the top surface of the CNTs. (Figure 4.4 (b)) corresponds to a water plasma treated sample with 75 W power and 135 Pa pressure. A slight decrease in the length of the CNTs is observed due to plasma etching effects, but the nanotubes still remain vertically aligned, homogeneously distributed and with a high density. The inset clearly shows the surface is without amorphous carbon after plasma treatment. When using an extreme conditions (140 W, 135 Pa), relatively low density and short nanotubes cannot resist these conditions, most of the nanotubes were destroyed, their density and length decreases (figure 4.4 (c)). This is because smaller tubes are more easily etched due to their higher curvature energy and higher strain. Whereas high density, long nanotubes can survive even after this harsh treatment, structural disorder increases a lot and the nanotubes become completely free of amorphous carbon and catalyst particles as can be seen from (figure 4.4 (d)) HRTEM, Raman and XPS results.

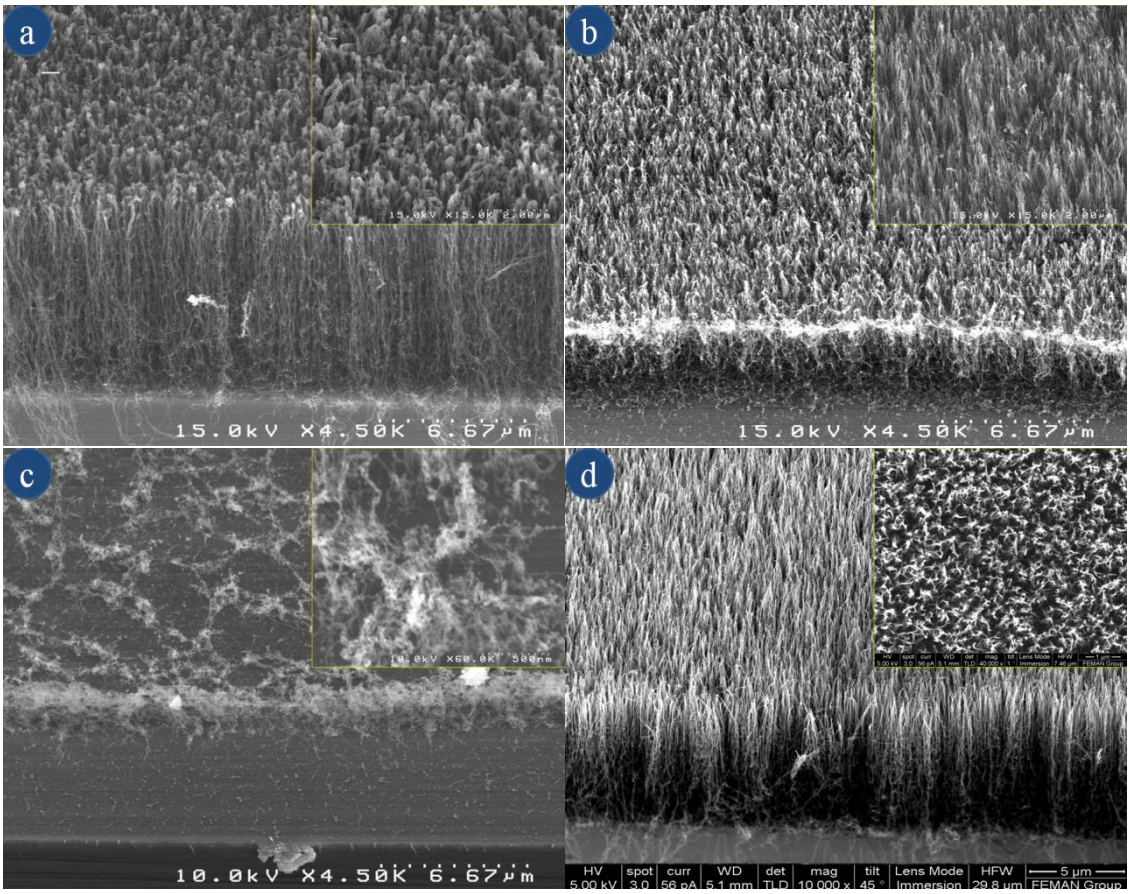

Figure 4.4: FE-SEM images of MWCNTs before and after water plasma treatments; (a) untreated MWCNTs, (b) water plasma treated CNTs (75 W, 135 Pa) (c, d) water plasma treated at extreme conditions (140 W, 135 Pa).

4.4.3. High resolution transmission electron microscopy (HRTEM)

High resolution electron microscopy (HRTEM) analysis was performed to see differences in the number of CNT walls, removal of amorphous carbon and opening of nanotube tips between the untreated and water plasma treated CNTs. (Figures 4.5 (a) and (b)) show Fe catalyst particles at the tips of the nanotubes and a layer of amorphous carbon covering the outer walls of the nanotubes. The number of walls was in the range of 15–37. The central point sample in the Box–Wilson experimental design showed more than 90% of the nanotube tips open and presented a clear multiwall crystalline structure with 10–20 layers (figures 4.5 (c) and (d)). It should be noted that high power plasma treatment reduces the number of walls and may completely destroy the nanotubes.

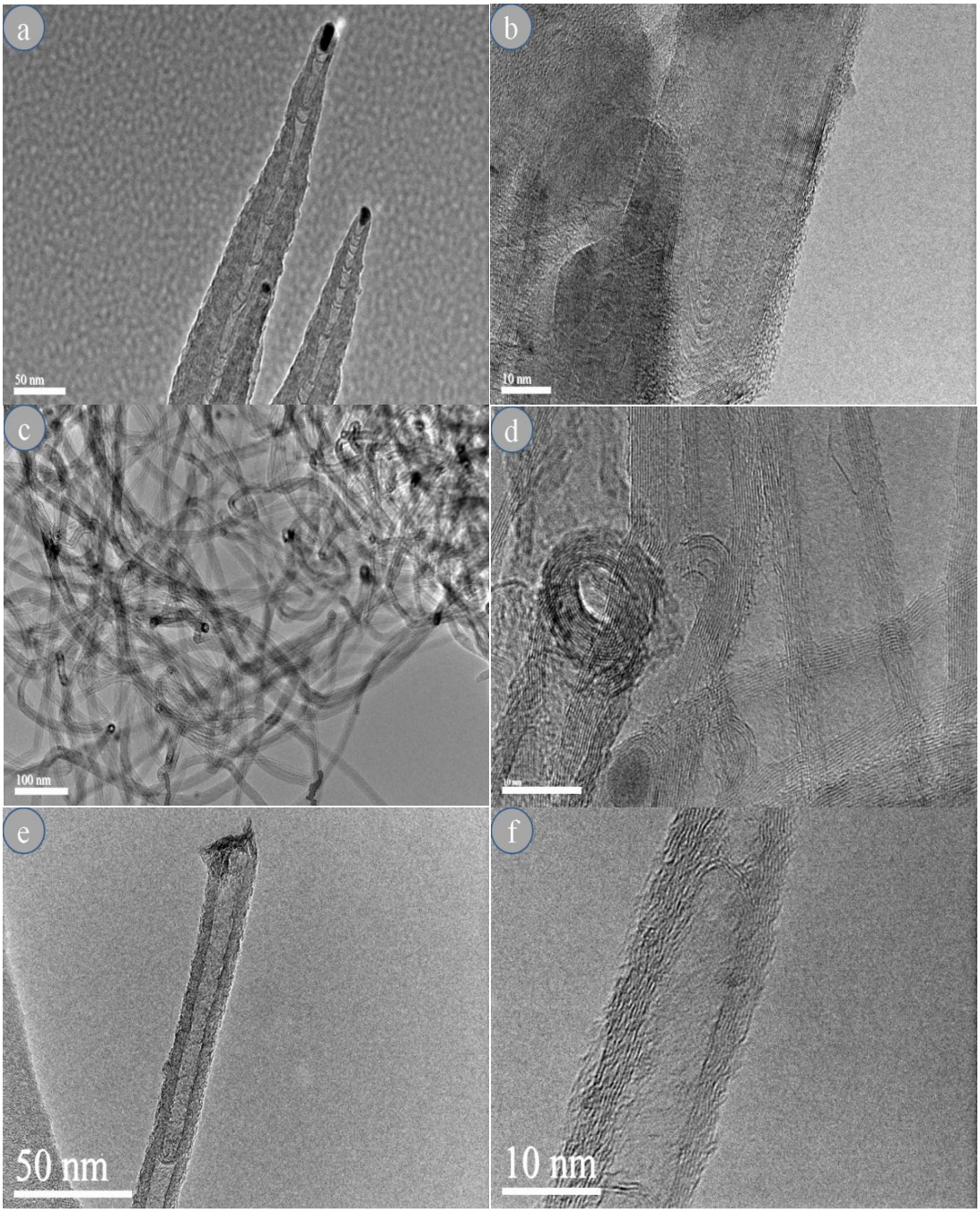

Figure 4.5: HRTEM images of (a, b) untreated samples of CNTs, (c, d) water plasma treated CNTs (75 W, 135 Pa), (e, f) water plasma treated CNTs (140 W,135 Pa).

The CNTs treated with water plasma at high power showed mainly open tips and strongly etched walls of the nanotubes with no amorphous carbon (figures 4.5 (e) and (f)). High magnification images (b, d, f) show well defined graphene planes parallel to tubes axis confirms the tubular nature of the nanotubes.

4.4.2. Raman spectroscopy

Raman Spectroscopy was used to evaluate the quality of CNTs in untreated and H_2O plasma treated samples. Raman spectra of CNTs mostly display three characteristic bands, the tangential stretching G mode (1500-1600 cm^{-1}), the D mode (1330-1360 cm^{-1}) and the radial breathing modes (RBM, 100-400 cm^{-1}) [27]. MWCNTs exhibit an additional Raman band at ~ 1615 cm^{-1} called $D^{/}$ that corresponds to defects on the side walls of CNTs [28] and which is similar to the D band. $D^{/}$ is a double resonance Raman feature induced by disorder, defects or ion intercalation between the graphitic walls [29]. However, MWCNTs do not show any RBM signal [30] since the signal from large diameter tubes is usually too weak to be observed.

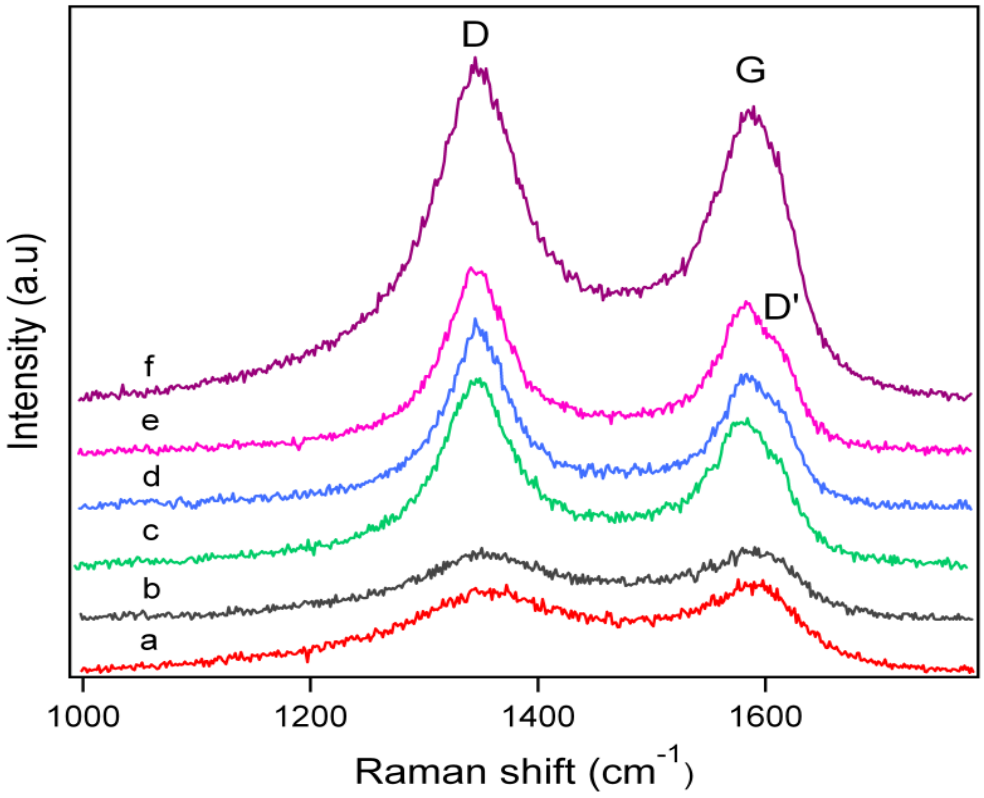

Figure 4.6: Raman spectra of untreated (a) and H_2O plasma treated CNTs under different conditions (b: 10 W, 1.35 mbar, c: 75 W, 1.35 mbar, d: 121 W, 0.5 mbar, e: 121 W, 2.2 mbar, f: 140 W, 1.35 mbar).

The position close to that of ~1580 cm^{-1} corresponds to the symmetric E_{2g} vibrational mode in graphite-like materials [31]. The D band is a double resonance Raman mode that can be understood as a

measurement of structural disorder coming from amorphous carbon and any other defects [29]. The ratio of intensities between the D and G bands, R= I_D/I_G, can be used to evaluate the extension of defects within CNTs [32]. As the I_D/I_G ratio decreases, so does the number of structural defects present in the CNTs.

Table 4.3: RAMAN feature of untreated and plasma treated MWCNTs.

	D band			G band			
	Position (cm^{-1})	**Intensity (a.u.)**	**FWHM (cm^{-1})**	**Position (cm^{-1})**	**Intensity (a.u.)**	**FWHM (cm^{-1})**	**R=I_D/I_G**
Untreated CNTs	1356.6 ± 1.4	1.13 ± 0.08	178.6 ± 10.4	1594.8 ± 1.0	1.06 ± 0.10	85.2 ± 6.0	1.07 ± 0.17
10 W, 135 Pa	1355.8 ± 1.2	0.97 ± 0.01	184.5 ± 4.0	1596.8 ± 1.1	0.87 ± 0.04	74.1 ± 4.0	1.12 ± 0.06
29 W, 50 Pa	1352.3 ± 0.4	1.79 ± 0.02	88.6 ±1.5	1588.3 ± 0.4	1.72 ± 0.02	78.2 ± 1.4	1.04 ± 0.04
29 W, 220 Pa	1356.7 ± 1.0	1.12 ± 0.01	171.3 ± 3.3	1595.3 ± 0.9	1.09 ± 0.05	75.8 ± 3.1	1.06 ± 0.06
75 W, 10 Pa	1354.6 ± 1.8	1.31 ± 0.02	138.3 ± 13.0	1593.2 ± 1.7	1.33 ± 0.03	80.9 ± 10.5	0.99 ± 0.04
75 W, 135 Pa	1352.2 ± 0.3	2.44 ± 0.01	76.2 ± 1.0	1588.6 ± 0.3	2.09 ± 0.03	81.8 ± 2.8	1.17 ± 0.02
75 W, 260 Pa	1353.0 ± 0.8	1.53 ± 0.02	125.1 ± 6.1	1583.8 ± 3.2	1.28 ± 0.22	71.3 ± 9.7	1.19 ± 0.22
121 W, 50 Pa	1353.6 ± 0.4	2.66 ± 0.02	93.1 ± 1.3	1583.2 ± 0.1	2.03 ± 0.04	80.9 ± 1.8	1.31 ± 0.04
121 W, 220 Pa	1349.1 ± 0.2	2.54 ± 0.03	79.1 ± 1.9	1591.9 ± 0.4	2.19 ± 0.03	79.1 ± 1.9	1.16 ± 0.03
140 W, 135 Pa	1350.0 ± 0.3	4.41 ± 0.12	92.0 ± 2.1	1583.6 ± 3.4	3.35 ± 0.26	65.5 ± 4.5	1.32 ± 0.14

The G and D bands for H_2O plasma treated CNTs at different water pressures and RF powers were fitted using two Lorentzian peaks, which vary in the range of 1583-1594 cm^{-1} and 1349-1356 cm^{-1}, respectively (figure 4.6). These variations suggest a dependency between structured defects and the two operational parameters; water pressure and RF power. (Figure4.6) shows the Raman spectra of untreated CNTs and H_2O plasma treated CNTs at different conditions of water pressure and RF power. (Table 4.3) shows the D and G band position variations and ratio between

their intensities R, which can be used to determine the relative amount of induced defects at different conditions. The downshift in the frequencies of the G and D vibrational modes are related to the diameter of the nanotubes; after the water plasma treatment the diameter decreases as the D band moves to lower frequencies and its FWHM decreases (see table 4.3) [33].

HRTEM analysis agrees with this observation. The H_2O plasma treatment etches the surface of CNTs and decreases the number of walls at a higher or lower rate depending on the treatment parameters (RF power and water pressure). $D^{/}$ is not observed in untreated MWCNTs indicating that this sample is more graphitic [29] and has a lower amount of defects.

The I_D/I_G ratio for the untreated CNTs was 1.06 and increases up to 1.31 for water plasma treated CNTs. This observation is also related to the decrease in the diameter of the CNTs. Furthermore, the water plasma treatment increases the structural disorder, incorporates oxygen groups and removes amorphous carbon. It is known that larger diameter CNTs show reduced tip curvature and, in turn, less structural defects [34]. Table 4.3 clearly shows a decrease in the diameter of CNTs as the I_D/I_G ratio increases.

At very low and high water pressures, and using a relatively low RF power, it is difficult to remove amorphous carbon as observed from the FWHM of the D band. At high water pressures this behavior is assumed to be related to a layer of condensed water on the surface of the nanotubes that protects them from being etched by the active species in the plasma, while at low pressures is related to a lower reactivity of the plasma.

4.4.3. X-ray photoelectron spectroscopy

In our study XPS was performed to analyze the oxygen containing groups on the CNTs. By changing two operational parameters of the water plasma treatment, it was possible to tune the distribution of oxygen groups on the surface of the nanotubes. Depending on the conditions of plasma power and water pressure used, the nanotubes were preferentially decorated with a given functional group. During the plasma treatment, the excited species, radicals, electrons, ions, and UV light interact with the surface of CNTs breaking C–C and C=C bonds and creating active sites for bonding oxygen and hydrogen atoms present in the plasma. During highly energetic plasma treatments, sputtering phenomena can occur, breaking and eventually destroying the nanotubes [35].

Before H_2O plasma treatment the relative oxygen content on the CNT surface was 3%, which is assumed to be introduced when the sample enters in contact with ambient air and moisture.

After H_2O plasma treatment, the relative oxygen content on CNT surfaces can reach up to 19%. The RF power is the most prominent oxidation parameter. At a water vapour pressure of 135 Pa the oxygen content increases with plasma power from 4.06% up to 19.53 % (figure 4.7). It was also noticed that high pressure plasma treatments have a negative effect on the oxygen content, which means that high amounts of water protect the surface of the nanotubes from plasma etching.

XPS can also be used to determine the groups attached to the surface of MWCNTs. (Figure 4.8 (a, b)) show high resolution XPS C1s spectra of untreated and H_2O plasma treated MWCNTs, which are deconvoluted into five component Gaussian peaks to explain the process of oxidation.

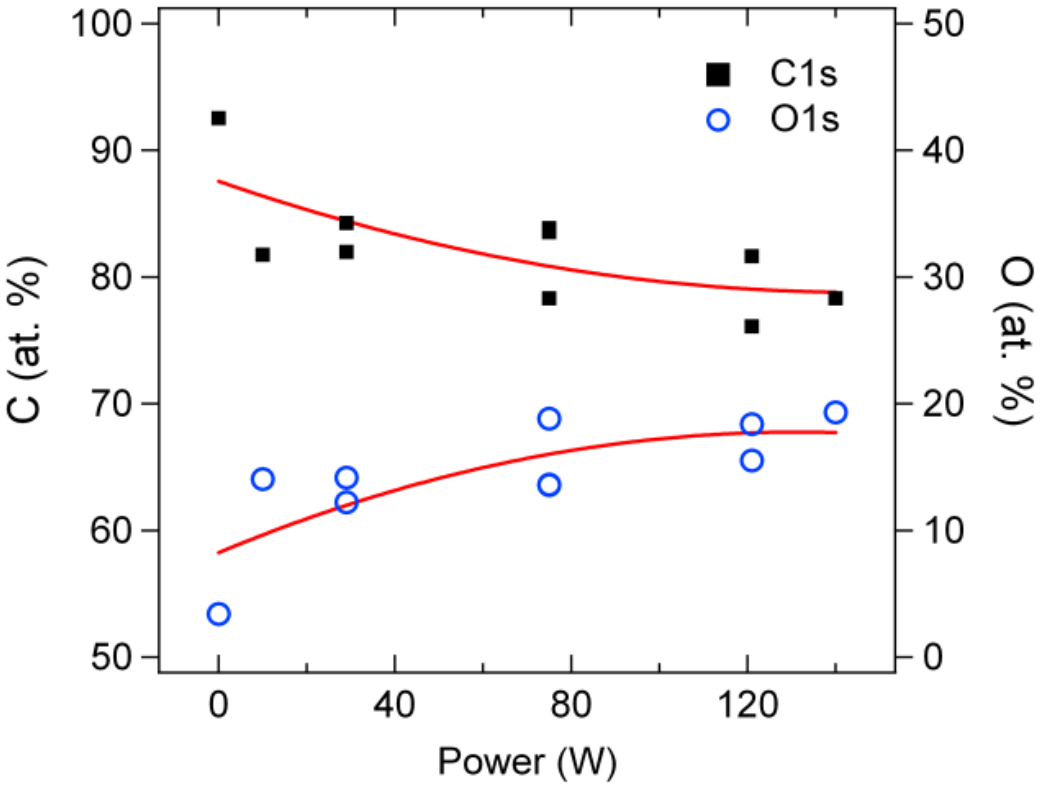

Figure 4.7: Influence of plasma power on the relative carbon and oxygen content of the samples. The solid lines are drawn to guide the eyes.

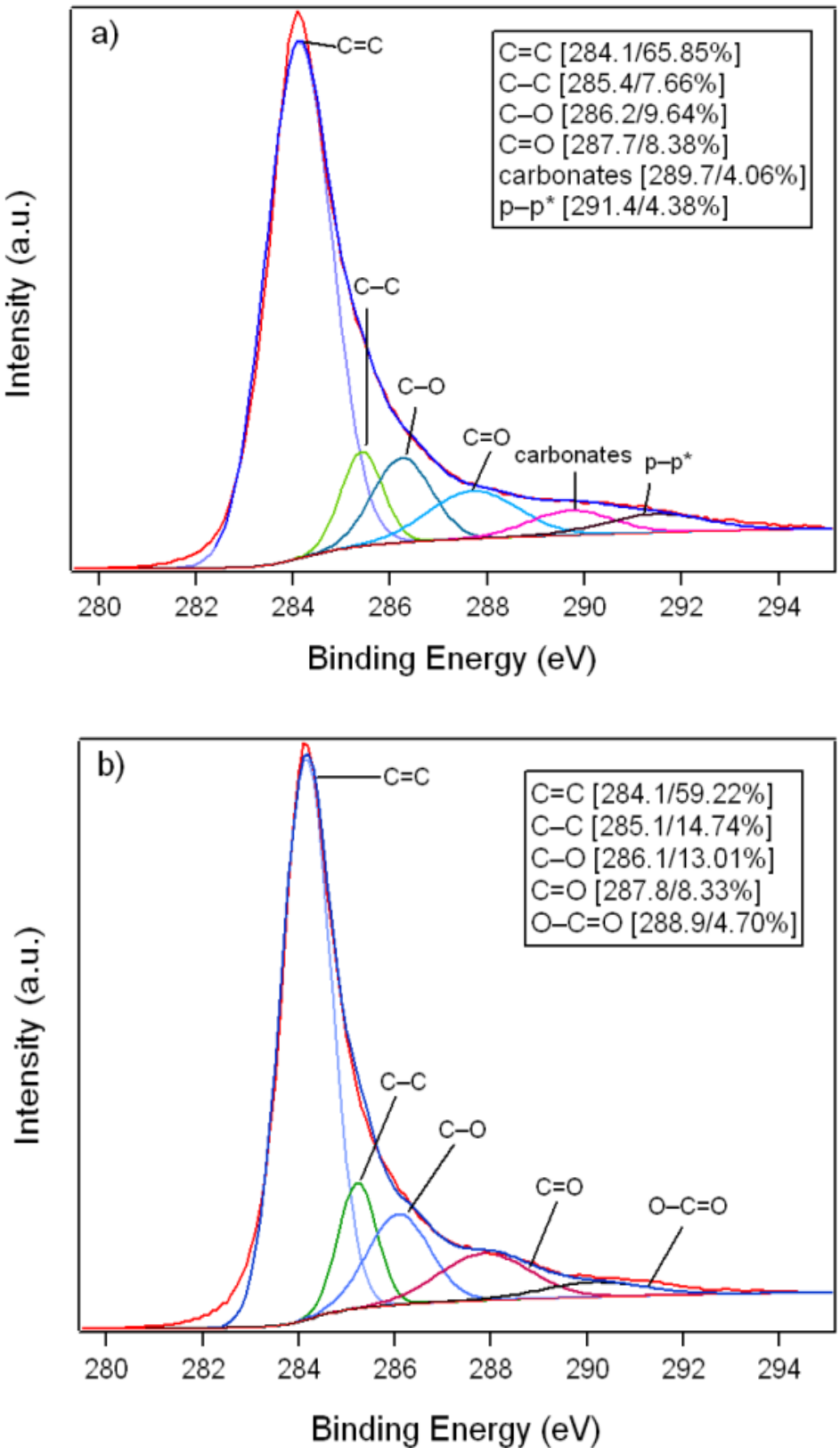

Figure 4.8: (a) XPS spectra of untreated MWCNTs and (b) H_2O plasma treated MWCNTs at 140 W and 135 Pa.

The main peak at 284.10 ± 0.2 eV corresponds to sp^2-hybridized graphite like carbon atom (C=C), the peak centered at 285.10 ± 0.2 eV is an indication of sp^3-hybridized carbon atom (C–C), the peaks at 286.2 ± 0.2 eV, 287.7 ± 0.2 eV and 288.9 ± 0.2 eV are considered to originate from carbon atoms linked to one or more oxygen atoms that induce a positive charge on the carbon atom. Hence, they correspond to C–O (e.g., alcohol, ether), C=O (e.g., ketone, aldehyde) and O–C=O (e.g., carboxylic, ester) species, respectively [36]. For untreated MWCNTs spectral deconvolution of C1s region is further complicated by the presence of π-π^* shakeup feature at (291.60 eV) that must be taken into account [37]. The area of this region in the untreated sample was 4.70 %.

Since the π bonds in the sp^2-hybridized graphite-like carbon within the CNT lattice are active and chemically unstable due to their lack of rotation around the C=C bond and its non-saturation, they are more susceptible to plasma attack [38]. As a consequence a decrease in the relative content of C=C bonds after the plasma treatment takes place. During the plasma treatment the radicals are first generated on the dissociated C=C π bonds, which then further react with active OH radicals originated from H_2O dissociation. The OH radicals are highly reactive and have the possibility to form covalent bonds upon reaction with dangling bonds or defects. A quantitative analysis of the carbon bonds present before and after the different water plasma treatments is provided in (table 4.4). It can be observed that the % area of sp^2 C=C bond decreases after the H_2O plasma treatment, whereas the % area of the C-O, C=O and O–C=O bonds increase. These results indicate that the C=C bonds are oxidized and new groups are generated on the surface of MWCNTs by plasma oxidation.

In order to study the oxidation mechanism that takes place on the CNT surface during the plasma treatment, the relative content of the different functional groups was fitted using (equation 4.1) for each XPS signal. As an example, for the relative content of C=C bond the polynomial model was found to be statistically significant ($p < 0.05$) explaining 86 % of the samples variation with $\alpha_0 = 61.8$, $\alpha_1 = -0.13$, $\alpha_2 = -0.30$, $\alpha_3 = 0.001$, $\alpha_4 = -0.015$ and $\alpha_5 = 1.4$.

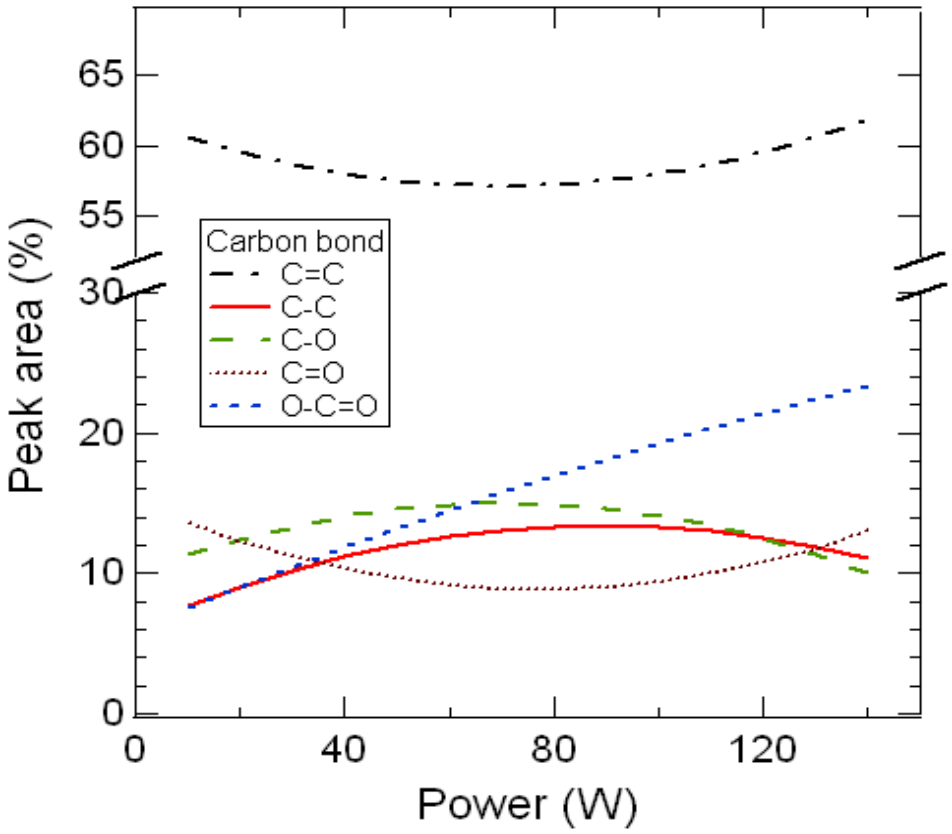

Figure 4.9: Percentage area of different carbon-carbon and carbon-oxygen bonds as a function of plasma power at a constant pressure of 50 Pa, obtained from the polynomial model

From the statistical analysis of the XPS bands it was possible to determine the effect of plasma power and water pressure on the oxidation of the nanotubes. (Figure 4.9) represents the variation of the functional groups with plasma power obtained from the fitting of the polynomial model, at a constant pressure of 50 Pa. It can be seen that as the relative amount of O-C=O bonds increases, that of C=O bonds decreases. This is in agreement with a two-step oxidation mechanism in which the carbon atoms are oxidized to C=O in a first step, and finally to O-C=O in a second step. This mechanism has been already proposed in the literature [43]. Not surprisingly, the relative content of C=C bonds decreases as that of C-C and C-O bonds increases, indicating that the C=C bonds are broken and oxidized during the treatment.

Table 4.4: Percentage area of the different bonds obtained from XPS C1s spectra.

MWCNTs	sp^2 (%)	sp^3 (%)	C–O (%)	C=O (%)	O–C=O (%)
untreated MWCNTs	68.13	6.18	8.65	7.17	5.17
10 W, 135 Pa	63.72	7.81	8.63	13.88	6.46
29 W, 50 Pa	57.59	10.89	13.63	10.77	7.12
29 W, 220 Pa	62.66	10.66	11.95	9.25	7.63
75 W, 10 Pa	58.25	12.21	15.26	9.91	4.48
75 W, 135 Pa	57.17	14.78	15.32	6.55	6.18
121 W, 50 Pa	59.01	11.22	11.07	11.98	5.73
75 W, 260 Pa	63.76	8.72	11.89	9.10	6.52
121 W, 220 Pa	61.79	9.23	13.31	9.09	6.58
140 W, 135 Pa	62.69	10.76	12.61	9.52	4.42

4.4.2. Contact angle

The static contact angle of the samples was measured by adopting sessile drop method to confirm the decrease in the hydrophobicity of H_2O plasma treated CNTs. Water droplets of 6 µl were deposited by using micro syringes and images were recorded to evaluate the liquid-solid interface on both sides (left (L) and right(R)) of the droplet. The contact angle was evaluated by using Young/Laplace method. The images show apparently the transformation of the hydrophobic surface to hydrophilic surface depending on the parameters of water plasma treatment (Figure 4.10). The image of untreated MWCNTs (Figure 4.10 (a)) indicates that the CNTs are hydrophobic with a contact angle of 113º ± 5º. From (Figure 4.10 (b, c, d)) it is evident how H_2O plasma increase the hydrophilicity of CNTs and contact angle changes depends on the plasma treatment conditions.

Statgraphics model shows the relationship between water pressure and RF power has fitted explained more than 87 % of the variability of the contact angle. We noticed that estimated surface response indicates, water pressure has positive and negative effects and power has positive effect on decreasing of the hydrophobicity of CNTs (figure 4.11).

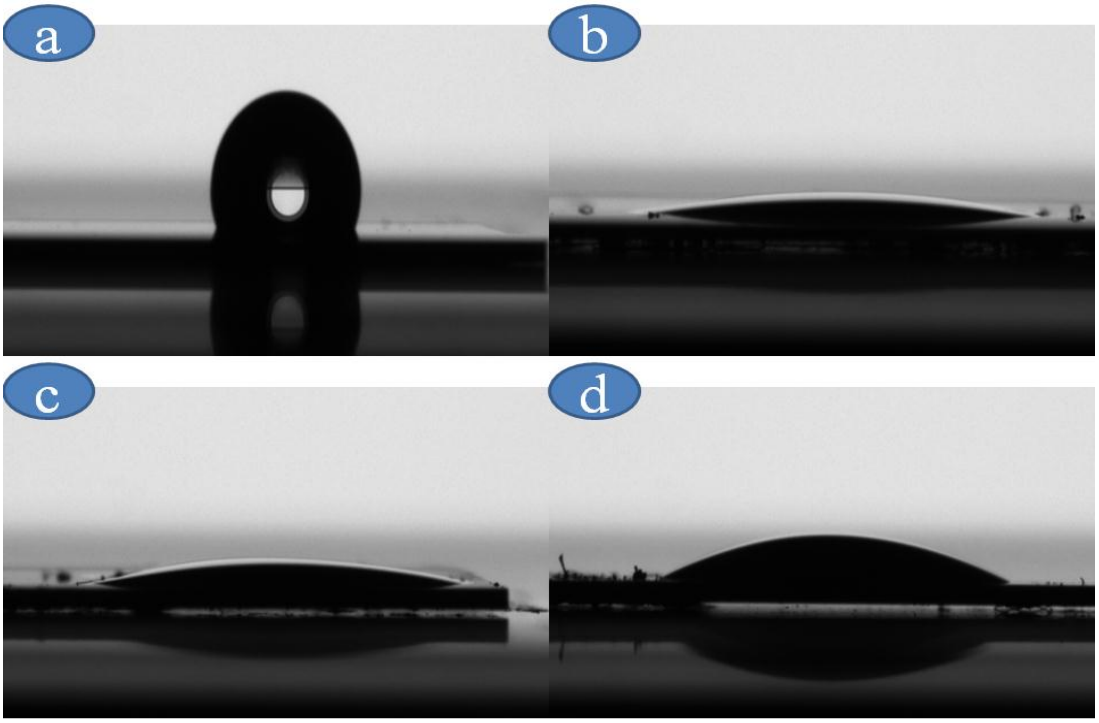

Figure 4.10: Showing the increase in hydrophilicity of the MWCNTs by the H_2O plasma treatment. Contact Angle (a) Untreated sample (b) H_2O plasma treated with power 29 W and water pressure 50 Pa, (c) H_2O plasma treated with power 75W and water pressure135 Pa and (d) H_2O plasma treated with power 75W and water pressure 260 Pa.

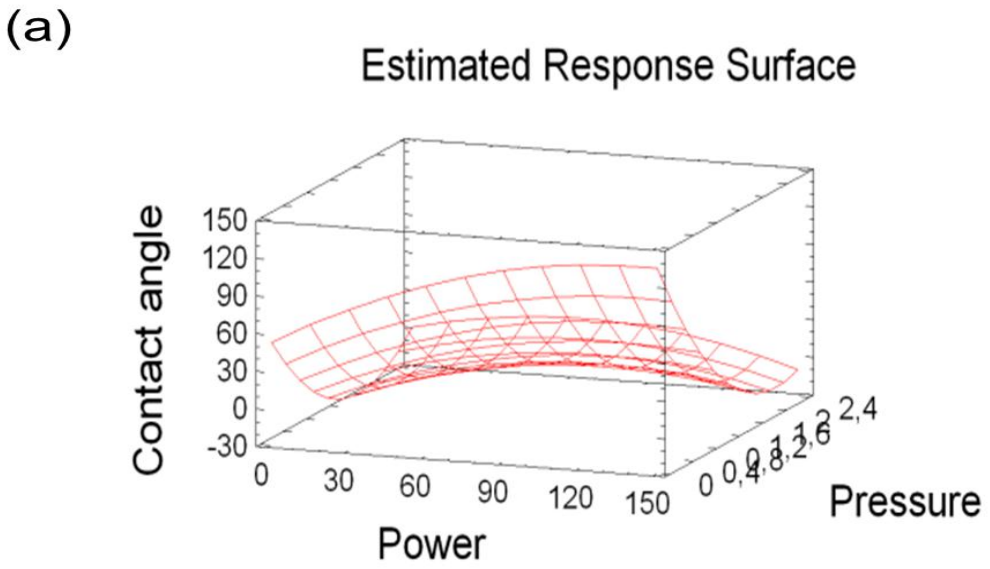

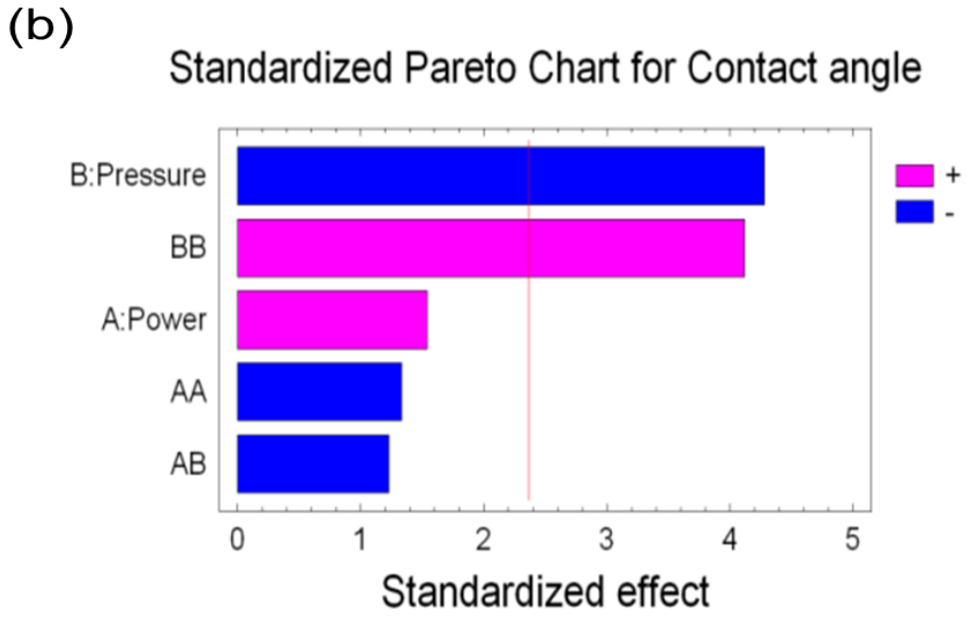

Figure 4.11: a) Interaction between power and pressure for decreasing the contact angle. (b) Pareto diagram of standardized effects of the different parameters A(RF power) and B (water pressure) on the H_2O treated CNTs.

4.4.2. Cyclic Voltammetry

The active surface area of the samples was determined from the slope of the linear fit obtained by plotting the peak current vs. the square root of scan rate, as shown in (figure 4.12 (a)). Using (equation 3.18) an active surface area of 1.24 cm^2 was found for untreated MWCNTs. For H_2O plasma treated carbon nanotubes the active area increased for the entire samples depending on the plasma treatment conditions. The highest active surface area was found to be 1.91 for the sample treated at 29 W (plasma power) and 220 Pa (water pressure).

The average specific capacitance of the samples in 0.1 M Na_2SO_4 solution was determined from the cyclic voltammograms using the following (equation 3.19). (Figure 4.12 (b)) shows the cyclic voltammograms at a scan rate of 50 mVs^{-1} of untreated MWCNTs and water plasma treated MWCNTs. Untreated CNTs present typical rectangular-shape voltammograms associated with double layer capacitance. The other voltammograms show a slight deviation from this shape, which are related to pseudocapacitive (faradaic) processes. This pseudocapacitance is related to the introduction of oxygen functionalities.

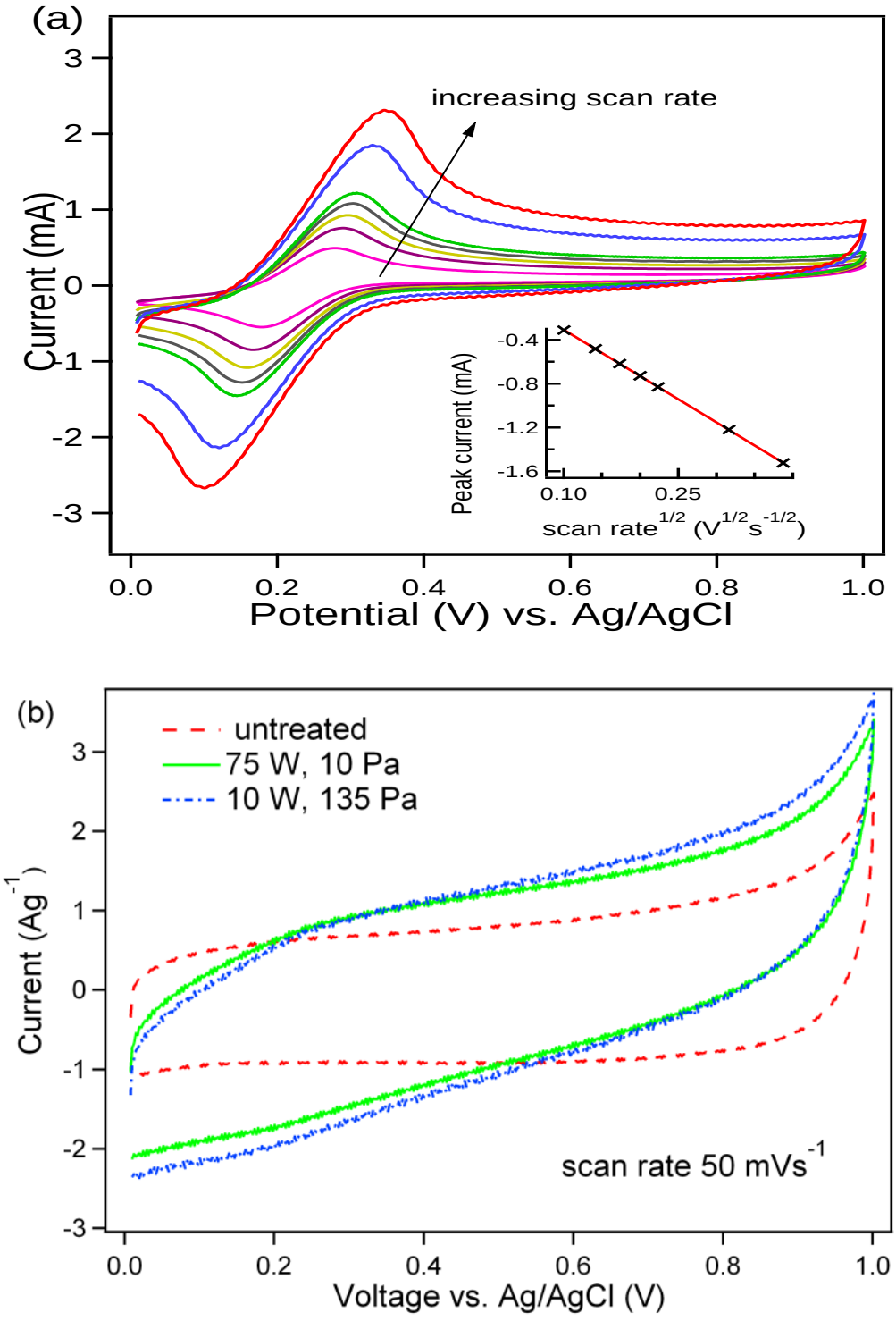

Figure 4.12: (a) CV of water plasma treated MWCNTs at a plasma power of 29 W and a water pressure 220 Pa applying different scan rates (10, 20, 30, 40, 50, 100 and 150 mVs^{-1}) and peak current versus square root of the scan rate (inset graph). (b) Comparison between the cyclic voltammograms of untreated and water plasma treated CNTs at a scan rate of 50 mVs^{-1}.

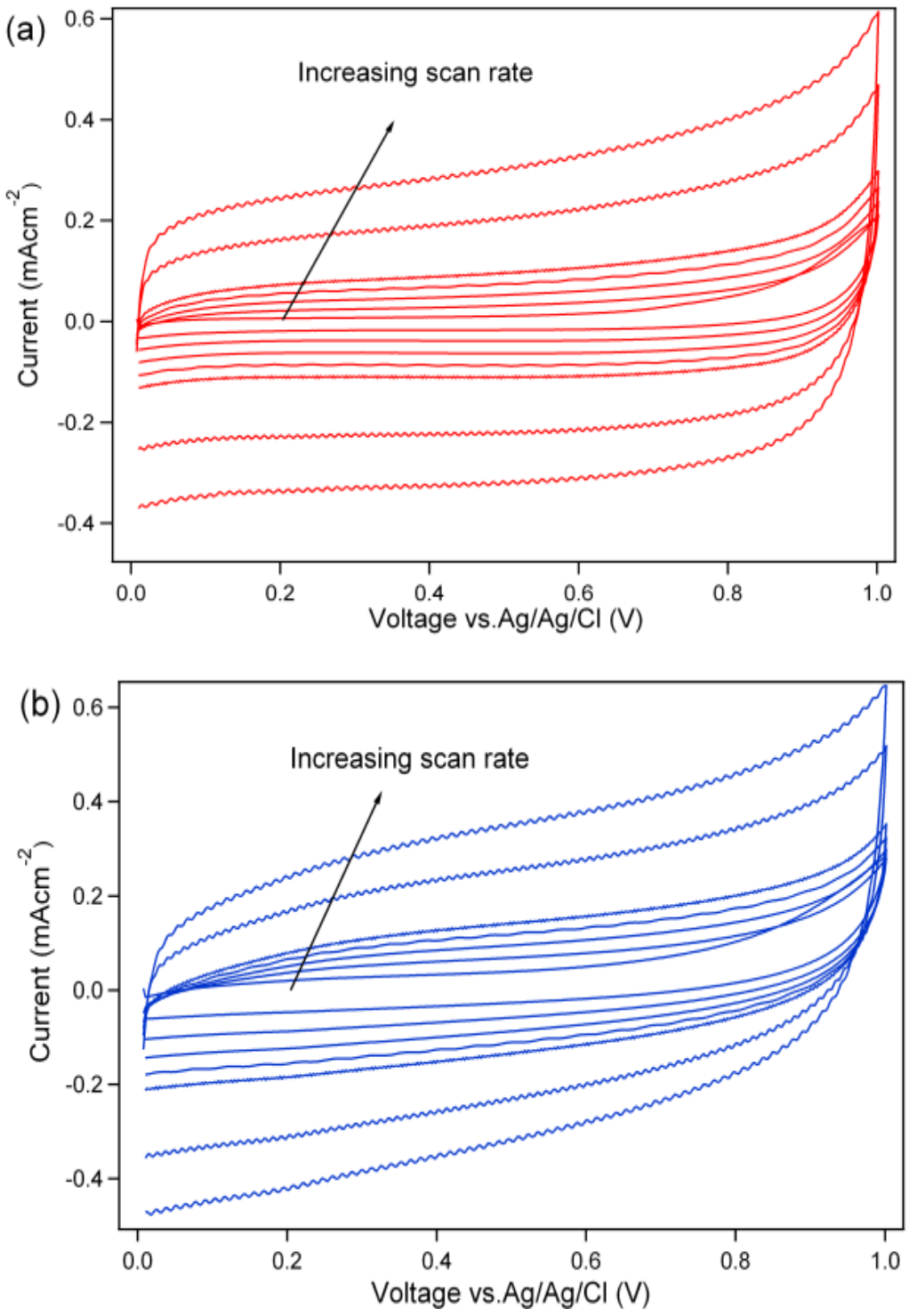

Figure 4.13: cyclic voltammograms at different scan rates (10, 20, 30, 40, 50, 100 and 150 mVs $^{-1}$), (a) Untreated CNTs, (b) H_2O treated CNTs.

The incorporation of pseudocapacitance is also evident at higher scan rates, as can be seen in (figure 4. 13) more evident for plasma treated

CNTs. The specific capacitance increases for all the water plasma treated MWCNTs from 23 up to 68 F g^{-1} at a scan rate of 10 mVs^{-1} (see table 4.5).At low power and middle pressures the treatment seems to be only specific to the removal of amorphous carbon without etching the walls or oxidizing too much the surface of the CNTs. MWCNTs obtained under high power conditions show poor electronic transfer properties and low specific capacitance. From the Raman analysis we can see that the diameter of the MWCNTs shows a significant effect on the specific capacitance of the MWCNTs. As the FWHM of the D band decreases the specific capacitance of the MWCNTs also decreases. Larger diameter MWCNTs show higher capacitance.

Table 4.5: Specific capacitance of untreated and water plasma treated MWCNTS at a scan rate of 10mVs^{-1}.

Sample	Fg^{-1}	Sample	Fg^{-1}
Untreated MWCNTs	22.5	75 W, 135 Pa	26.58
10 W, 135 Pa	66.75	75 W, 260 Pa	40.53
29 W, 50 Pa	29.16	121 W, 50 Pa	23.99
29 W, 220 Pa	44.74	121 W, 220 Pa	37.31
75 W, 10 Pa	57.56	140 W, 135 Pa	22.36

The cyclic voltammetry measurements reveal that the water plasma treatment improves the specific capacitance of MWCNTs. In particular, those samples with larger diameters (see Table 4.3), i.e. soft etching, present higher capacitance values. On the other hand, samples with smaller diameters, i.e., more etched, do not present such a significant increase in the capacitance. Therefore, from these results it can be assumed that once the layer of amorphous carbon is removed, the surface of the nanotubes is increased but also functionalized with different oxygen groups, which inhibit a good electronic transfer with the electrolyte. By tuning the plasma operational parameters the oxidation process and the resulting properties of the nanotubes can be controlled. Depending on the conditions we can remove the amorphous carbon without etching the nanotubes, which results in an increase of the specific capacitance of the nanotubes, or reduce their number of walls and further oxidize them by introducing different oxygen functional groups. Furthermore, contact angle measurements indicate that most of the samples present super-hydrophilicity after the plasma

treatment, which is especially interesting for biosensors and electrochemistry experiments, in which a low wettability can limit the efficiency of CNTs.

4.5. Conclusions

VA-MWCNTs were grown by the PECVD technique and functionalized by H_2O plasma treatment, which introduced different oxygen containing chemical groups. Based on the comprehensive experimental design used, we have obtained a better insight into the functionalization mechanism. Since the main operating parameters of the water plasma are easy to modify (plasma power and water pressure), we have been able to tune the functionalization process. Non-functionalized and functionalized MWCNTs were characterized by different techniques and it was noticed that the power is the main operational parameter, while high water pressures have a negative effect on the crystallinity. This observation was attributed to a layer of water on the surfaces of the nanotubes that protects them from plasma etching. Morphological characterization suggests that after plasma treatment the MWCNT surfaces become rough and the number of defects is enhanced. Furthermore, it was observed that most of the catalyst particles on the tips of the nanotubes were removed. Raman analysis shows a shift in the frequencies of the D and G bands, which corresponds to an increase in the number of defects and a decrease in the diameter of the MWCNTs after the H_2O plasma treatment. X-ray photoelectron spectroscopy results show that by changing the two operational parameters it is possible to decorate the MWCNTs with desired functional groups like, e.g., carboxyl or hydroxyl. The electrochemical properties of the nanotubes can be tailored by tuning the water plasma operational parameters. In particular, the optimum conditions to remove amorphous carbon while improving the charge storage properties were found to be 10 W plasma power and 135 Pa water plasma pressure. Under these conditions a specific capacitance of 68 Fg^{-1} was obtained.

4.5. References

[1] Kumar M and Ando Y, *Chemical vapour deposition of carbon nanotubes: a review on growth mechanism and mass production*, (2010), J. Nanosci. Nanotechnol. 10, 3739-3758.

[2] Hofmann S, Ducati C and Robertson J, *Low-temperature growth of carbon nanotubes by plasma-enhanced chemical vapour deposition*, (2003), Appl. Phys. Lett. 83 (1) 135-137.

[3] Min B G, Chae H G, Minus M L and Kumar S, *Polymer/carbon nanotube composite fibers - an overview Functional composites of carbon nanotubes and applications* ed. K P Lee et al. (2009), (Kerala: Transworld research network) pp 43-73.

[4] Han Z J, Tay B K, Shakerzadeh M and Ostrikov K, *Superhydrophobic amorphous carbon/carbon nanotube nanocomposites*, (2009), Appl. Phys. Lett., 94, 223106.

[5] Simmons J M, Nichols B M, Baker S E, Marcus M S, Castellini O M, Lee C S, Hamers R J and Eriksson M A, *Effect of ozone oxidation on single-walled carbon nanotubes*, (2006), J. Phys. Chem. B, 110, 7113-18

[6] Lebron-Colon M, Meador M A, Lukco D, Sola F, Santos- Perez J and McCorkle L S, *Surface oxidation study of single wall carbon nanotubes*, (2011), Nanotechnology, 22, 455707.

[7] Chen C, Liang B, Ogino A, Wang X and Nagatsu M, *Oxygen functionalization of multiwall carbon nanotubes by microwave-excited surface-wave plasma treatment*, (2009), J. Phys. Chem. C, 113, 18, 7659-65.

[8] Chen C, Ogino A, Wang X and Nagatsu M, *Oxygen functionalization of multiwall carbon nanotubes by Ar/H_2O plasma treatment*, (2011), Diam. Relat. Mater. 20, 153-6.

[9] Lee S, Peng J W and Liu C H, *Probing plasma-induced defect formation and oxidation in carbon nanotubes by Raman dispersion spectroscopy*, (2009), Carbon, 47, 3488-97

[10] Chen C, Ogino A, Wang X and Nagatsu M, *Plasma treatment of multiwall carbon nanotubes for dispersion improvement in water*, (2010), Appl. Phys. Lett. 96 131504.

[11] Kalbacova M, Broz A, Kromka A, Babchenko O, Kalbac M, *Controlled oxygen plasma treatment of single-walled carbon nanotube*

films improves osteoblastic cells attachment and enhances their proliferation, (2011), Carbon, 49, 2926-34.
[12] Falten A, Bitencourt C and Pireaux J J, *Gold clusters on oxygen plasma functionalized carbon nanotubes: XPS and TEM studies*, (2006), *Nanotechnology*, 17, 1954-59.
[13] Han Z, Tay B, Tan C, Shakerzadeh M and Ostrikov K, *Electrowetting control of Cassie-to-Wenzel transitions in superhydrophobic carbon nanotube-based nanocomposites*, (2009), ACS Nano, 3, 3031–6.
[14] Rosca I D, Watari F, Uo M and Akasaka T, *Oxidation of multiwalled carbon nanotubes by nitric acid*, (2005), *Carbon*, 43, 3124-31.
[15] Datsyuk V, Kalyva M, Papagelis K, Partgenios J, Tasis D, Siokou A, Kallitsis I and Galiotis C, *Chemical oxidation of multiwalled carbon nanotubes*, (2008), Carbon, 46, 833-40.
[16] Martinex M T et al. *Modifcation of single-wall carbon nanotubes upon oxidative purification treatments*, (2003), Nanotechnology, 14, 691-95.
[17] Sun Y P, Fu K, Lin Y and Huang W, *Functionalized carbon nanotubes: properties and Applications*, (2002), Acc. Chem. Res.35 1096-104.
[18] Abbas G, Papakonstantinou P, Iyer G R S, Kirkman I W and Chen L C, *Substitutional nitrogen incorporation through rf glow discharge treatment and subsequent oxygen uptake on vertically aligned carbon nanotubes*, (2007), Phys. Rev. B 75 195429.
[19] Okpalugo T I T, Papakonstantinou P, Murphy H, Mclaughlin J and Brown N M D, *Oxidative functionalization of carbon nanotubes in atmospheric pressure filamentary dielectric barrier discharge (APDBD)*, (2005), Carbon, 43, 2951–9.
[20] R T K Baker and D J C Yated, *Filamentous carbon formation over iron surfaces*, (1983), doi: 10.1021/bk-1983-0202.ch001.
[21] M S Bell, K B K Teo, R G Lacerda, W I Milne, D B Hash, and M Meyyappan, *Carbon nanotubes by plasma-enhanced chemical vapor deposition*, (2006), Pure Appl. Chem. 78, 6, 1117–1125
[22] S K Srivastava, V D Vankar, V Kumar, *Growth and microstructures of carbon nanotube films prepared by microwave plasma enhanced chemical vapor deposition process*, (2006), Thin Solid Films, 515, 1552–1560.

[23] M S Bell, K B K Teo and W I Milne, *Factors determining properties of multi-walled carbon nanotubes/fibres deposited by PECVD,* (2007), J. Phys. D: Appl. Phys. 40, 2285–2292

[24] R Sharma, P Rez, M M J Treacy and S J. Stuart, *In situ observation of the growth mechanisms of carbon nanotubes under diverse reaction conditions*, (2005), Journal of Electron Microscopy 1 of 7, doi:10.1093/jmicro/dfi037.

[25] Fischer J E, *Carbon nanotubes: structure and properties Nanotubes and Nanofibers*, (2006), ed Y Gogotsi (Boca Raton, FL: Taylor Francis) p 36.

[26] Y Yu, C Cui, W Qian, Q Xie, C Zheng, C Kong and Fi Wei, *Carbon nanotube production and application in energy storage*, (2013), Asia-Pac. J. Chem. Eng, 8, 234–245.

[27] Korneva G, *Functionalization of carbon nanotubes*. (2008), PhD Thesis Drexel University

[28] Wang Z, Huang X, Xue R and Chan L, *Dispersion effects of Raman lines in carbon*, (1998), J. Appl. Phys. 84, 227–31.

[29] Osswald S, Havel M and Gogotsi Y, *Monitoring oxidation of multiwalled carbon nanotubes by Raman spectroscopy,* (2007), J. Raman Spectrosc. 38 728–36

[30] Jorio A, Pimenta M A, Filho A G S, Saito R, Dresselhaus G and Dresselhaus M S, *Characterizing carbon nanotube samples with resonance Raman scattering*, (2003), New J. Phys. 5 1–17

[31] Han Z J and Ostrikov K, *Uniform dense arrays of vertically aligned, large-diameter single-walled carbon nanotubes,* (2012) J. Am. Chem. Soc. 134 6018–24

[32] Dresselhaus M S, Dresselhaus G, Saito R and Jorio A, *Raman spectroscopy of carbon nanotubes*, (2005), Phys. Rep. 409 47–99.

[33] Costa S, Borowiak-Palen E, Kruszynska M, Bachmatiuk A and Kalenczuk R J, *Characterization of carbon nanotubes by Raman spectroscopy*, (2008), Mater. Sci.-Poland 26 433–41.

[34] Antunes E F, Lobo A O, Corat E J and Trava-Airoldi V J, *Influence of diameter in Raman spectra of aligned multi-walled carbon nanotubes*, (2007), Carbon, 45, 913–21.

[35]Felten A, Bittencourt C and Pireaus J J, *Radio-frequency plasma functionalization of carbon nanotubes surface O_2, NH_3, and CF_4 treatments*, (2005), J. Appl. Phys. 98, 074308.

[36] Okpalugo T I T, Papakonstantinou P, Murphy H, McLaughlin J and Brown N M D, *High resolution XPS characterization of chemical functionalized MWCNTs and SWCNTs*, (2005), Carbon, 43, 153–61.
[37] Jones C and Sammann E, *The effect of low power plasmas on carbon fiber surfaces*, (1990), Carbon, 28, 509–14.
[38] Chen C, Liang B, Ogino A, Wang X and Nagatsu M, *Oxygen functionalization of multiwall carbon nanotubes by microwave-excited surface-wave plasma treatment*, (2009), J. Phys.
Chem. C 113 7659–65.

Chapter 5
Water plasma functionalized MWCNTs /MnO_2 composites for supercapacitor applications

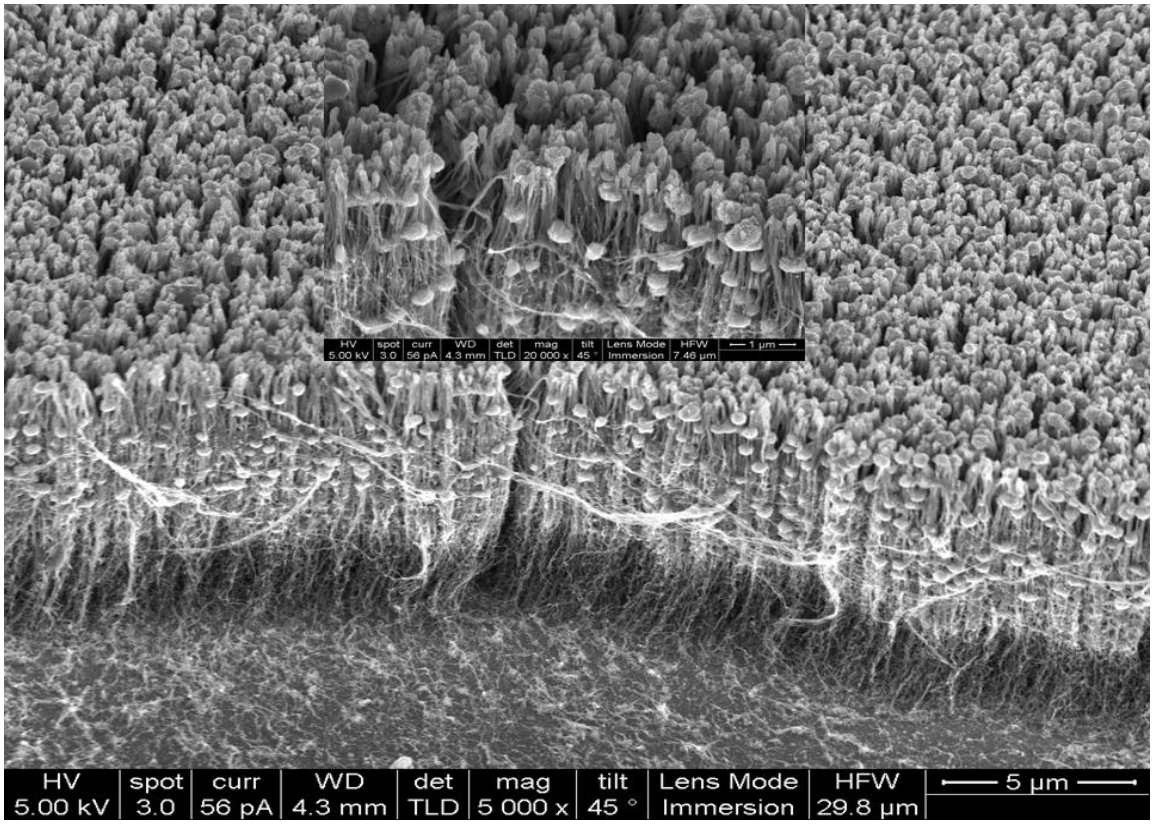

Figure 5: *Image of MnO_2 nanoflowers deposited on CNTs*

Chapter 5- Water plasma functionalized MWCNTs /MnO_2 composites for supercapacitor applications

5.1. Introduction

In EDLC the capacitance is mainly attributed to the physical adsorption of ions at the electrode/electrolyte interface as a non-faradic behaviour, with a contribution of 1-5% pseudocapacitance in the case of carbon DLC. While in faradic capacitors (pseudocapacitors) the charge storage mechanism is mainly provided by the contribution of reversible redox reactions that take place on the electrode surface involving various oxidation states of metal oxides and the physical adsorption of ions [1].

Capacitance enhancement of carbon electrodes can be achieved by surface specific treatments that introduce various kinds of functional groups such as oxygen and nitrogen based functionalities. As a result, the electrodes exhibit an increase of the double layer capacitance, and also, of reversible faradic reactions that contribute to the charge storage as a pseudocapacitance [2, 3].

Generally, pseudocapacitance is associated with reversible faradic redox processes in various oxidation states of transition metal oxides (RuO_2, MnO_2, NiO, V_2O_5, IrO_2). Among them, RuO_2 presents highest theoretical capacitance values (about 1400 Fg^{-1}). However, due to its low cost, environmental friendliness and more importantly, its faradic response with rectangular voltammograms, MnO_2 appears to be more suitable for high power applications [4].

Regarding the oxidation/reduction mechanism in MnO_2 pseudocapacitors, Mathieu Toupin et al. suggested that H^+ and C^+ (Na^+, K^+ , La^+) are intercalated and de-intercalated upon reduction and oxidation in the bulk of MnO_2 and C^+ adsorbed on the surface of MnO_2 as shown by (equations 5.1 and 5.2) [5].

$$MnO_2 + H^+ + e^- \leftrightarrow MnOOH \quad (5.1)$$

or

$$MnO_2 + C^+ + e^- \leftrightarrow MnOOC \quad (5.2)$$

This procedure includes a redox reaction between Mn^{3+} and Mn^{4+} oxidation states [9]. Since only the surface is involved in the charge storage mechanism, a thinner film of MnO_2 shows a higher capacitance than a thicker one. However, a compromise must be achieved to obtain the optimum thickness since usually a thinner layer of manganese dioxide undergoes mechanical instability and, as a result, delivers poor energy density [6]. Therefore, for supercapacitor applications it is important that the electrode material possess high surface area, high porosity as well as very low electrical resistance. A suitable configuration is CNTs/MnO_2 composite electrodes, in which a thin layer of MnO_2 provides high pseudocapacitance due to faradic redox reactions taking place on large surface area electrodes. CNTs provide high electrical conductivity and mechanical stability to the 3D-electrode [7, 8]. Although the highest reported capacitance obtained with such composite electrodes, in which MnO_2 is deposited on the outer surface of CNTs, is as high as 790 Fg^{-1} [9], it is still well below the theoretical value for MnO_2 (about 1370 Fg^{-1}) [5].

Several techniques have been used to prepare MnO_2/CNTs composite electrodes; electrophoretic deposition [10], wet chemistry method using capillary forces of the nanotube [9], layer by layer deposition of MnO_2 on CNTs [11], electrodeposition [8, 12, 13], potentiostatic and galvanostatic deposition [14]. Nevertheless, there is no report in the literature about the use of water plasma treated CNTs/MnO_2 composite electrodes for supercapacitor applications.

Herein, this chapter is related to the study of nanocomposite materials consisting of water plasma-treated CNTs covered with a layer of electrochemically deposited MnO_2 (MnO_2/wpCNTs) as electrodes for supercapacitor devices. Moverover we studied the effect of different potentials on the change in morphology of MnO_2 as deposited in nanoflower to layer like or to needle like structure and change in oxidation state.

5.2. Experimental section

Growth and water plasma functionalization of CNTs was performed following the same procedure as described in chapter 4. A Box-Wilson experimental design was adopted to explore the influence of plasma treatment parameters such as rf power and water pressure on the capacitance of MnO_2/CNTs composite electrodes. According to the Box–

Wilson graph distribution, nine conditions were chosen to perform 13 experiments; central point experiment was replicated 5 times in order to evaluate the intrinsic standard deviation of the process (see figure 5.1). This experimental design allows us to adjust the tested variables with a second degree polynomial equation (5.3).

$$X = \alpha_0 + \alpha_1 A + \alpha_2 B + \alpha_3 A^2 + \alpha_4 AB + \alpha_5 B^2 \quad (5.3)$$

where X is the dependent magnitude, α_n are constant coefficients obtained by statistically adjusting these polynomial equations, A is the plasma power and B the water pressure.

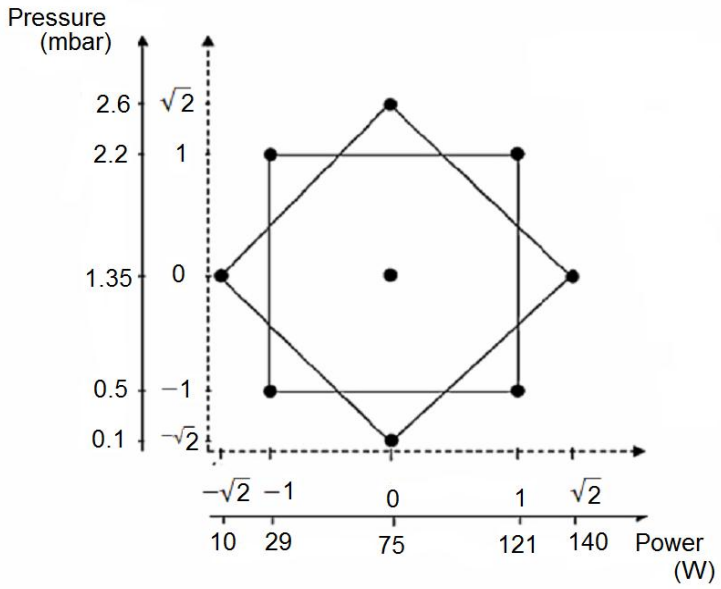

Figure 5.1: Box-Wilson experimental design samples distribution for two main parameters (RF power and water pressure).

The galvanostatic method was adopted to electrochemically deposit manganese dioxide on the surface of CNTs. The galvanostatic method was carried out in order to deposit the manganese oxide. In this case a two electrode cell was used [16]. The CNTs electrode was used as the anode and a graphite electrode as the cathode. About 0.5cm^3 of a 0.2 M $MnSO_4 \cdot H_2O$ solution was introduced drop wise through hole in the cathode during the deposition, as explain by Fan et al. (figure 5.2) [16]. The optimum conditions were found to be constant current of 1 mAcm^{-2} and 2 min of deposition time.

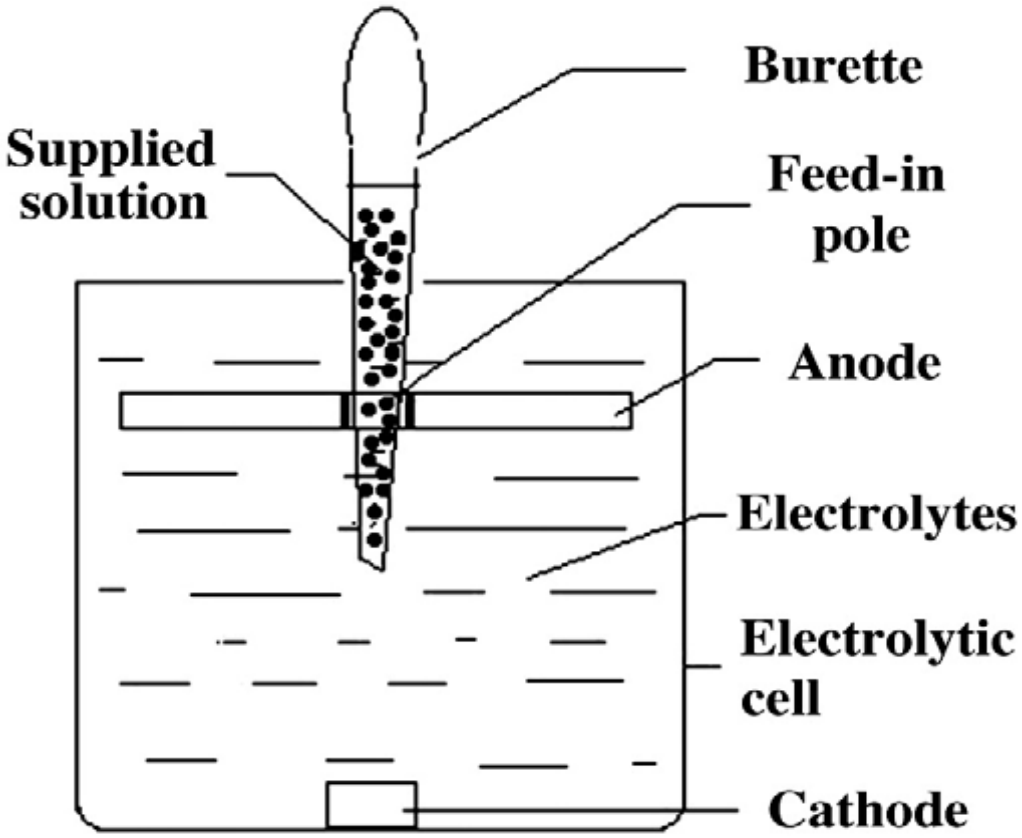

Figure 5.2: Schematic diagram of the electrolytic cell for deposition of manganese oxide [16].

The amount of manganese dioxide deposited on the CNTs was determined by oxidizing the manganese ions to MnO^{4-} and measuring its absorbency at 525 nm. The concentration of permanganate ions was obtained from UV-vis spectrophotometry and the deposited mass of MnO_2 was calculated from this value, which equalled (16.5 ± 1.5) μg. This amount corresponds to about 23% of the total mass of MnO_2/CNTs nanocomposite. The charge storage mechanism of MnO_2/CNTs composite electrodes was studied by means of cyclic voltammetry (CV), electrochemical impedance spectroscopy (EIS) and constant current charge/discharge cycling in a 0.1 M Na_2SO_4 aqueous solution using a potentiostat/galvanostat (AutoLab, PGSTAT30, USA). All experiments were carried out in a typical three-electrode cell at 25ºC. An Ag/AgCl electrode (3M KCl internal solution) and a Pt-ring electrode were used as the reference and counter electrode, respectively. The working electrode

was a sample of CNTs or MnO_2/CNTs composite. The geometrical area of the working electrode was set to a constant value of 0.57 cm^2.

5.3. Results and discussion

5.3.1. Scanning electron microscopy

The morphological analysis of the CNTs was performed by field emission scanning electron microscopy (FE-SEM) (FEINova NanoSEM 230, USA). (Figures 5.3 (a) and (b)) show SEM images of untreated CNTs and water plasma-treated CNTs (wpCNTs) at 75Wrf power and 135 Pa pressure, respectively. The CNTs vertical alignment is preserved after all the treatments.

Clearly, the CNTs surface becomes cleaner after the water plasma-treatment and presents less amorphous carbon, which is a by-product generated during the CNTs growth (inset of Figures 5.3(a) and 5.3(b)). (Figures 5.4(a) and (b)) show scanning electron micrographs of wpCNTs/MnO_2 composite before and after 2000 charge/discharge cycles, respectively, in the potential range of 0-1V. Before cycling, the MnO_2 presents nanoflower or nanosphere-like structures that are well distributed on the CNTs tips and inside the voids of CNTs bundles reaching the bottom part of the CNTs mat (see Figure 5.4(a)).

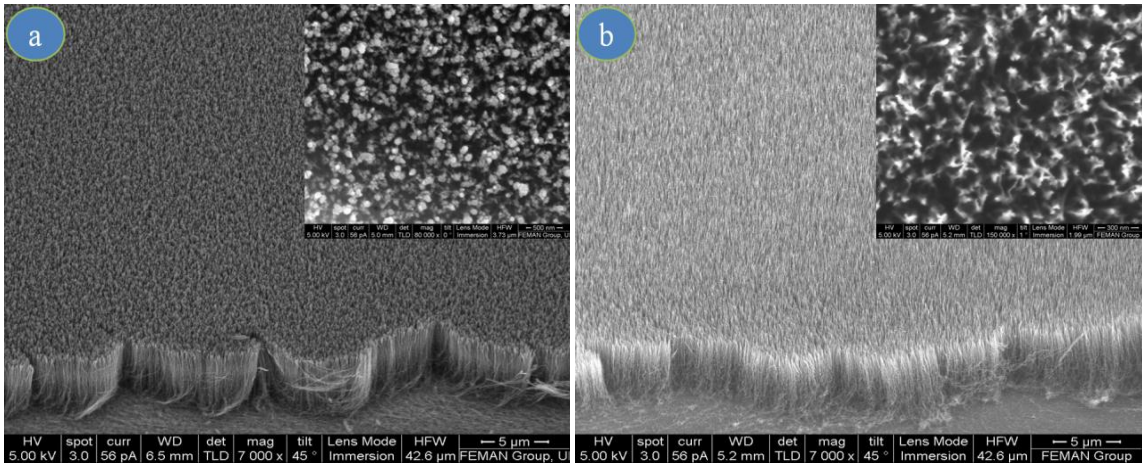

Figure 5.3: SEM images of untreated CNTs (a) and wpCNTs (b). Inset graphs show top view of the CNTs mat.

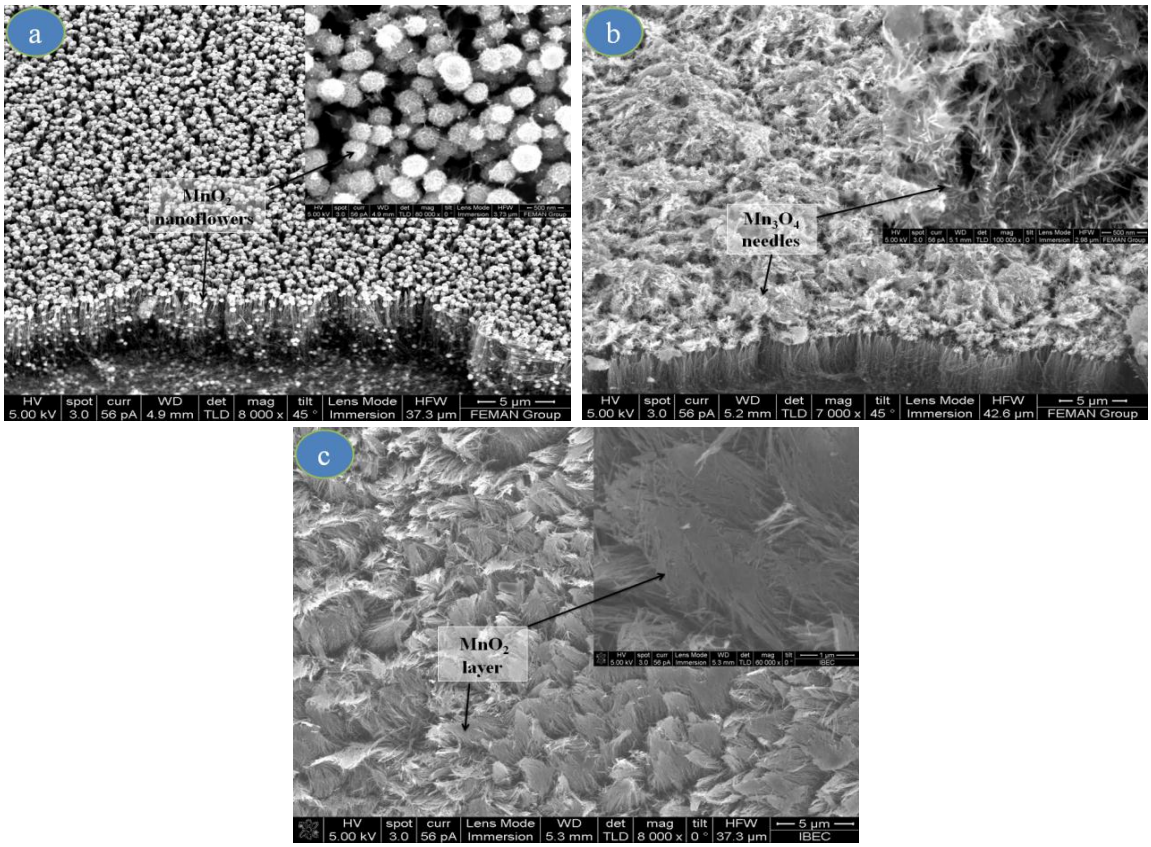

Figure 5.4: SEM images of wpCNTs/MnO_2 before electrochemical cycling (a), wpCNTs/MnO_2 after electrochemical cycling (0-1V) (b), and wpCNTs/MnO_2 after electrochemical cycling (0.1– 0.8 V) (c). Inset graphs show top view of the CNTs mat.

After 2000 cycles and within the potential window of 0 to 1V, the morphology of MnO_2 has changed from nanoflower to needle-like structure, which corresponds to Mn_3O_4 as indicated by X-ray photoelectron spectroscopy (XPS) and Raman spectroscopy (see further below). Furthermore, the Mn_3O_4 has agglomerated on the top surface of the CNTs mat creating a thick layer of the oxide (Figure 5.4(b)), whereas after 2000 charge/discharge cycles in a smaller potential window (0.1–0.8 V), nanoflower-structured MnO_2 is transformed into a thin layer-like structure, resembling a paste coating the surface of the CNTs (see Figure 5.4(c)).

5.3.2. Raman spectroscopy

Structural and chemical information about the carbon nanotubes and their composites was provided by Raman spectroscopy measurements.

Information regarding the CNTs structure is usually obtained from three Raman peaks that appear in the region between 1000 cm^{-1} and 1800 cm^{-1}. After the deposition of manganese dioxide on untreated and water plasma-treated CNTs, new Raman peaks emerge in the frequency region from 200 to 650 cm^{-1}. The peaks observed in the 200–500 cm^{-1} region are assigned to distortion of Mn–O–Mn chains inMnO_2 octahedral lattices, while peaks in the 500–650 cm^{-1} region are characteristic of Mn–O vibration in the basal plane of MnO_6 groups [17]. MnO_2 Raman spectrum consists of three main distinguished peaks at 523, 576, and 650 cm^{-1} and three smaller peaks, not always detected, at 392, 490, and 776 cm^{-1} [18].

(Figure 5.5) shows Raman spectra of untreated CNTs, wpCNTs (75 W, 135 Pa), and wpCNTs/MnO_2 (75 W, 135 Pa) composite before and after electrochemical cycling in small and large voltage windows. Before cycling, the peaks at 490, 560, and 640 cm^{-1} are very well pronounced and their positions are similar to those described in the literature for MnO_2 Raman spectra, as well as the two small peaks observed below 400 cm^{-1} [18, 19].After 2000 electrochemical charge/discharge cycles in the range of 0 to 1V, a very sharp and high intensity peak is observed at 640 cm^{-1} along with a combination of smaller peaks at 260, 350, and 480 cm^{-1}. The high intensity of the Raman peak at 640 cm^{-1} [19] is the signature of the Mn_3O_4 phase and characteristic of all needle-like structures, while a low intensity peak at this frequency cannot be assigned to Mn_3O_4 [18, 20]. In view of these results, we assume that dissolution of manganese species from the electrode in the solution and a slow phase transformation process from MnO_2 to Mn_3O_4 take place during constant current charge/discharge cycling owing to irreversible redox reactions that occur in the region around 0 V [21]. In agreement with this assumption, Gao et al. reported the thermal transformation of MnOOH into Mn_3O_4 phase [22]. Moreover, the above results are consistent with the morphological changes observed with SEM (see Figures 5.4 (a) and (b)) since the Raman signals at ~1360 and ~1580 cm^{-1} are very weak due to the formation of a thick layer of Mn_3O_4 at the CNTs top surface.

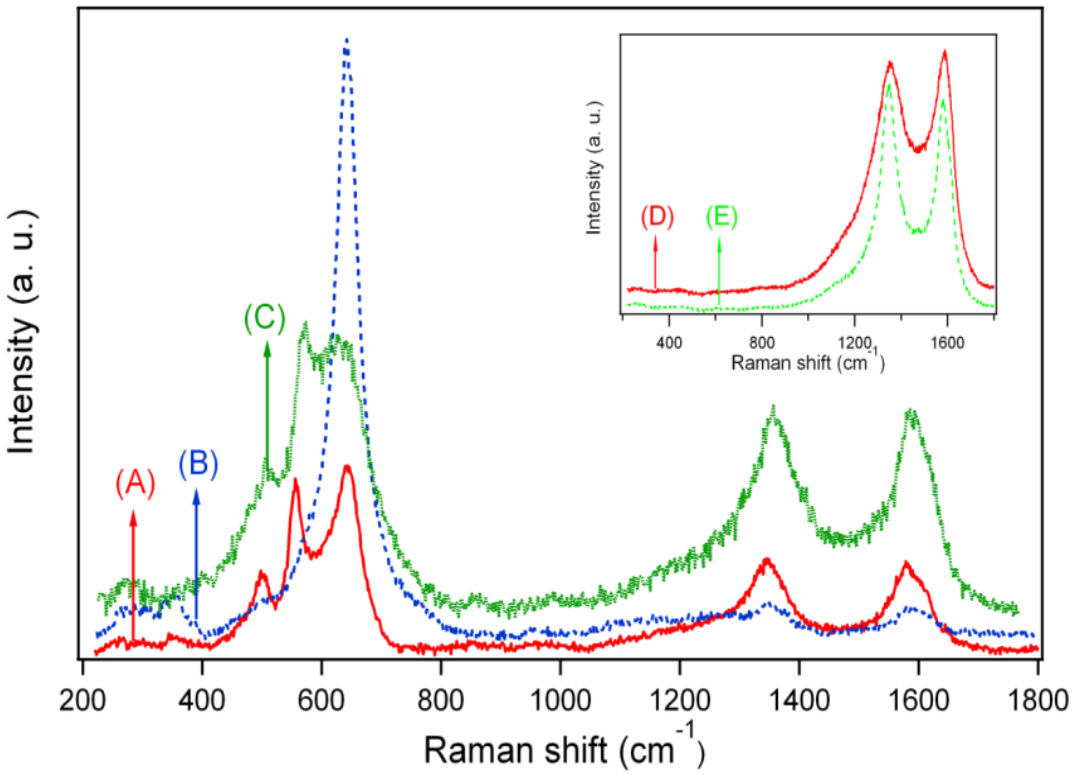

Figure 5.5: Raman spectra of (A) wpCNTs/MnO_2 (75W, 135 Pa) before cycling, (B) wpCNTs/MnO2 (75W, 135 Pa) after 2000 cycles (between 0-1V), and (C) wpCNTs/MnO_2 (75W, 135 Pa) after 2000 cycles (between 0.1–0.8 V). Inset figure shows Raman spectra of (D) untreated CNTs and (E) wpCNTs (75W, 135 Pa).

Raman spectra of samples cycled in the potential range of 0.1–0.8 V present peak positions and intensities that cannot be attributed to a change in the oxidation state of MnO_2.
Therefore, only a morphological change from nanoflower to layer-like structure, as proved by SEM images, occurs after cycling in this voltage window (0.1–0.8 V).

5.3.3. X-ray photoelectron spectroscopy

XPS was used to evaluate the elemental composition and oxidation states of manganese before and after electrochemical charge-discharge cycling within different potential limits. (Figure 5.6 (a)) shows Mn 2p spectra of different samples. The Mn 2p spectrum of sample wpCNTs/MnO_2 (75W, 135 Pa) before cycling exhibits three peaks; Mn $2p_{3/2}$ was positioned at (641.85 ± 0.1) eV, Mn $2p_{1/2}$ at (653.5 ± 0.1) eV [36],

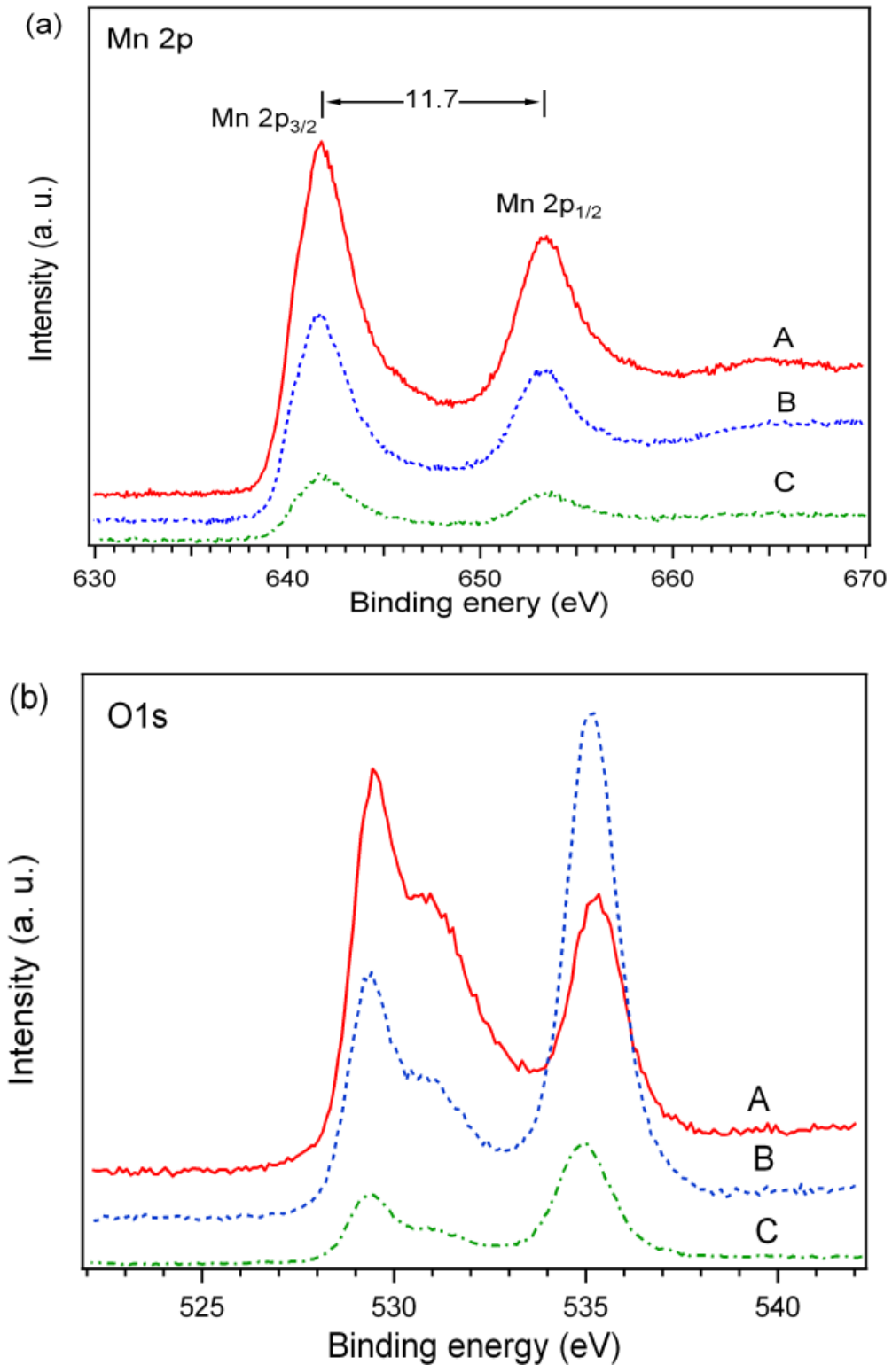

Figure 5.6: XPS spectra of (a) Mn 2p and (b) O1s, (A) wpCNTs/MnO_2 (75W, 135 Pa) before cycling (B) wpCNTs/MnO_2 (75W, 135 Pa) after 2000 cycles (between 0-1V), and (C) wpCNTs/MnO_2 (75W, 135 Pa) after 2000 cycles (between 0.1–0.8 V).

and a shoulder appears at around 644.5 eV. The binding energy difference between the Mn $2p_{3/2}$ and Mn $2p_{1/2}$ peaks is about 11.7 eV, which is very much like the reported values in other studies [24]. These results indicate that manganese is in the Mn^{4+} oxidation state [25]. After 2000 charge-discharge cycles in the potential range of 0-1V, the binding energy of the Mn $2p_{3/2}$ peak is shifted downward to a lower valence state of Mn at (641.5 ± 0.1) eV (see Figure 5.6 (b)). This peak position reveals the transformation of MnO_2 into Mn_3O_4 due to the irreversible potential limits used during the cycling process [25], whereas when the cycling was performed in the potential range of 0.1–0.8 V, there was almost negligible shift of the binding energies of the Mn 2p spectra in comparison with the sample without cycling, confirming that manganese is still in the Mn^{4+} state. The decrease observed in the intensities of the peaks could be related to the transition of MnO_2 from flower-like to (sheet) layer-like structure on the nanotubes surface (see Figure 5.4(c)).

Table 5.1: Peak position and percentage area of different bonds obtained from XPS O1s spectra.

Sample		(BE) (eV)	% area
wpCNTs/MnO_2 before cycling	**Mn-O-Mn**	**529.44**	**33.79**
	Mn-O-OH	530.88	24.36
	H-O-H	532.39	13.89
	Chemisorbed oxygen	535.26	27.96
wpCNTs/MnO_2 (0 – 1 V) after 2000 cycles	Mn-O-Mn	529.29	20.88
	Mn-O-OH	530.71	13.69
	H-O-H	523.36	7.68
	Chemisorbed oxygen	535.07	57.75
wpCNTs/MnO_2 (0.1 – 0.8 V) after 2000 cycles	Mn-O-Mn	529.31	23.17
	Mn-O-OH	530.84	17.37
	H-O-H	532.55	3.7
	Chemisorbed oxygen	534.91	55.75

The chemical environment of the oxygen atoms was examined by deconvoluting the O1s spectra in 5 peaks (see Figure 5.5(b)). The peak located at (529.30 ± 0.1) eV can be ascribed to (Mn–O–Mn). Peaks around (530.9 ± 0.1) eV, (532.7 ± 0.2) eV, and (535.10 ± 0.2) eV could be attributed to (Mn–O–H), (H–O–H), and chemisorbed oxygen, respectively [26, 27]. Table 5.1 shows the deconvoluted O1s spectra peak position and relative area percentage of oxide species. The amount of the OH/H_2O is higher in the sample without cycling. Thus, higher hydroxide content implies higher effective area as well as increased Na^+ and H^+ diffusion in the electrode [28]. The above XPS measurements are also in accordance with both SEM and Raman results previously discussed.

5.3.4. Electrochemical characterization

Specific capacitance of the wpCNTs/MnO_2 composite electrodes was calculated using equation (2.12). Highest specific capacitance (750 Fg^{-1}) was obtained using plasma-treated CNTs with 10W rf power and 135 Pa water pressure as the nanocomposite electrode. The increase in capacitance is related to the removal of amorphous carbon, soft etching, that is, less structural defects in comparison with other water plasma-treated carbon nanotubes, and the addition of oxygen functional groups [15]. Under these water-plasma conditions (10 W, 135 Pa), the existence of C=O (quinone) groups on the CNTs surface is especially high [15].This type of groups promotes the adsorption of protons, which is in agreement with the non-perfect rectangular shape of the CV curves (i.e., a non-truly horizontal value of the current) [29] (see Figure 5.7(a)).

As a result, the specific capacitance significantly increases due to the additional contribution of faradic currents (I_F). Samples treated under other plasma conditions clearly show a redox peak in the potential region from 0.4 to 0.6 V that corresponds to reversible redox reactions between Mn^{4+} and Mn^{3+} (Figure 5.6(a)). With increasing scan rate, the specific capacitance of the wpCNTs/MnO_2 (10 W, 135 Pa) composite decreases below that of the other samples. Since the shape of the CV curves becomes more rectangular at higher scan rates (Figure 5.7(b)), we assume that, for this sample, the I_F contribution to the total capacitance decreases due to slow Faradic processes taking place at the CNTs/MnO_2 surface.

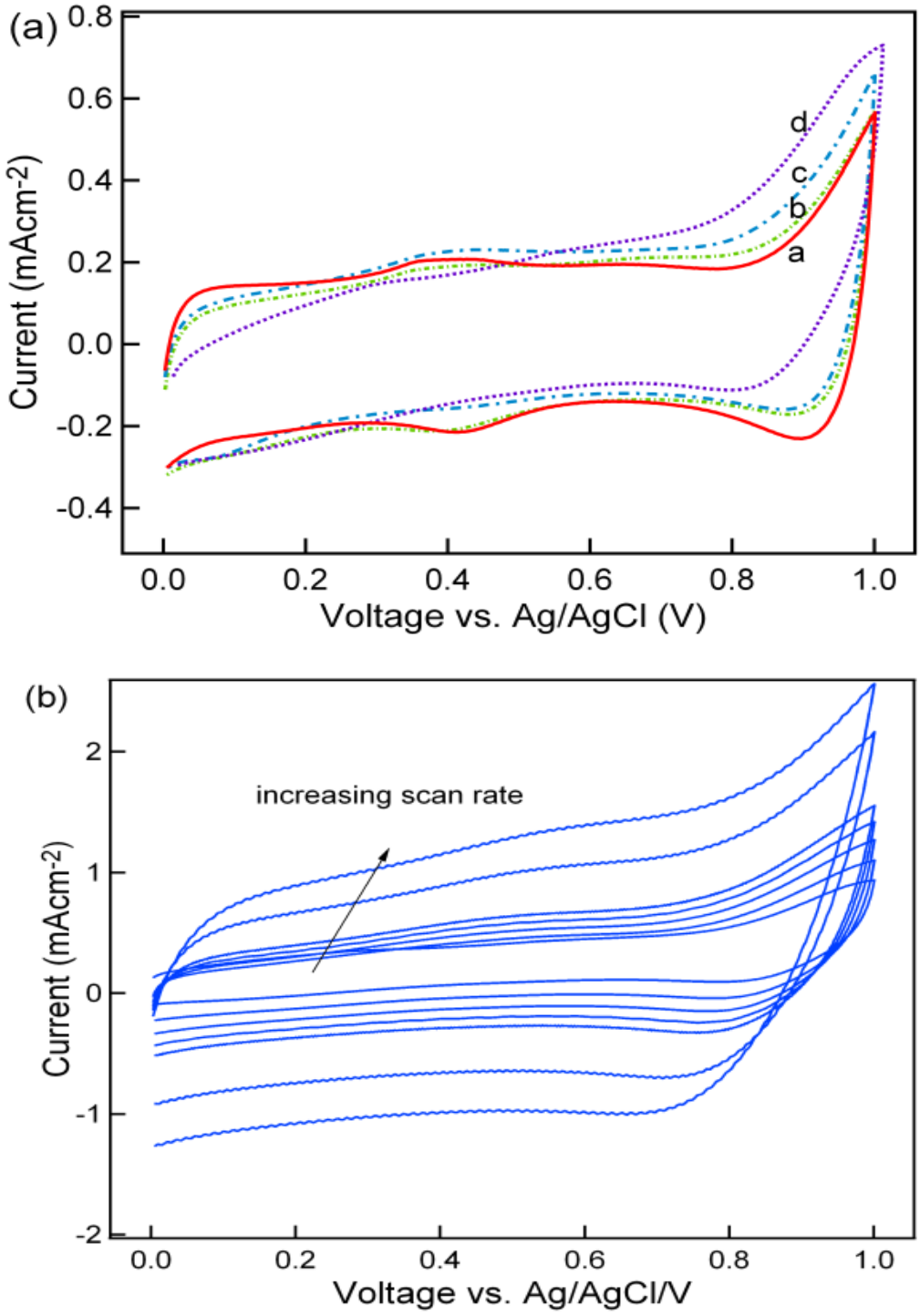

Figure 5.7: (a) Cyclic voltammograms obtained at a scan rate of 10mVs^{-1} for untreated MWCNTs/MnO_2 and wpCNTs/MnO_2 under different plasma conditions ((a): untreated, (b): 75W, 135 Pa, (c): 140 W, 135 Pa, (d): 10 W, 135 Pa). (b) Cyclic voltammograms of nanocomposite wpCNTs/MnO_2 (10 W, 135 Pa) at different scan rates, 10, 20, 30, 40, 50, 100, and 150 mVs^{-1}.

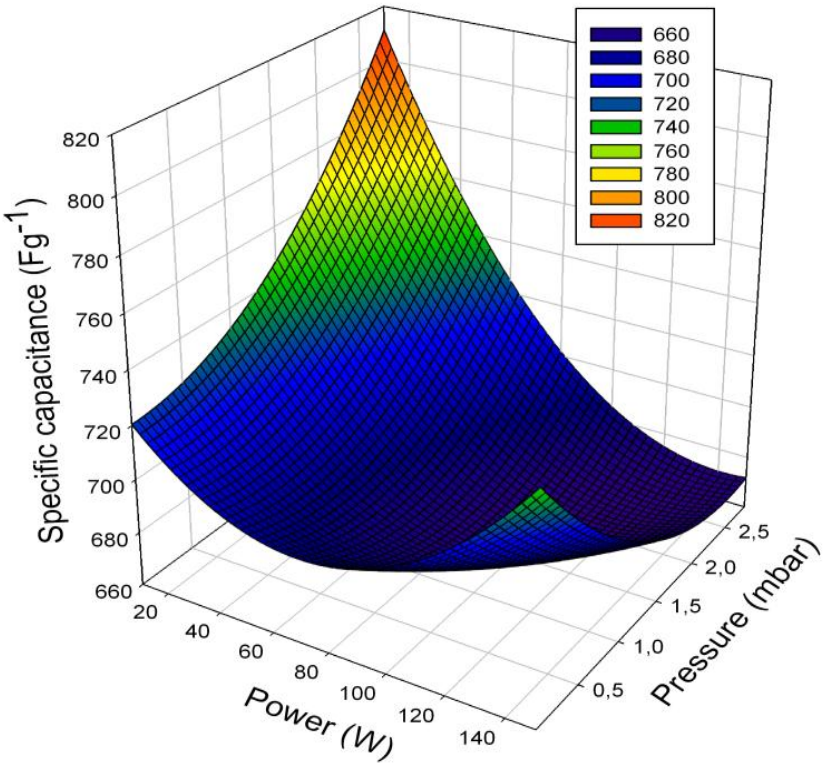

Figure 5.8: 3-dimensional graph of the specific capacitance of water plasma-treated CNTs/MnO_2 electrodes with respect to rf-power and water pressure.

Based on the experiments carried out, a second degree polynomial equation was adjusted for the specific capacitance (equation 1). The polynomial model was found to be statistically significant ($p<0.05$) explaining 76.6 % of the samples variation with a_0 = 730.935, a_1 =-1.134, a_2 =4.723, a_3 =0.008, a_4 = -0.415 and a_5 = 11.365. (Figure5.8) is a 3D graph obtained using these parameters. The interaction between plasma power and water pressure, and their influence on the specific capacitance of wpCNTs/MnO_2 composite electrodes is clearly shown. Optimum conditions of the plasma treatment that provide improved specific capacitance values of the composites are located at low plasma powers and high water pressures.

Electrochemical impedance spectroscopy was performed to investigate the kinetics behaviour of hybrid electrodes. The internal

components of the capacitor (e.g., current collectors, electrodes, dielectric material, and solution) contribute to the equivalent series resistance (ESR), which is above 65 ohm for all of the samples (see Figure 5.9). The ESR of all the wpCNTs/MnO_2 composites is lower than that of untreated CNTs/MnO_2 composite (83 ohm) because of the removal of amorphous carbon and increased wettability. The Nyquist plot of the samples present an almost straight line parallel to the imaginary axis that describes exactly polarized systems [1]. Deviation from this vertical line at low frequencies to smaller slopes corresponds to a higher contribution of the ionic diffusion resistance.

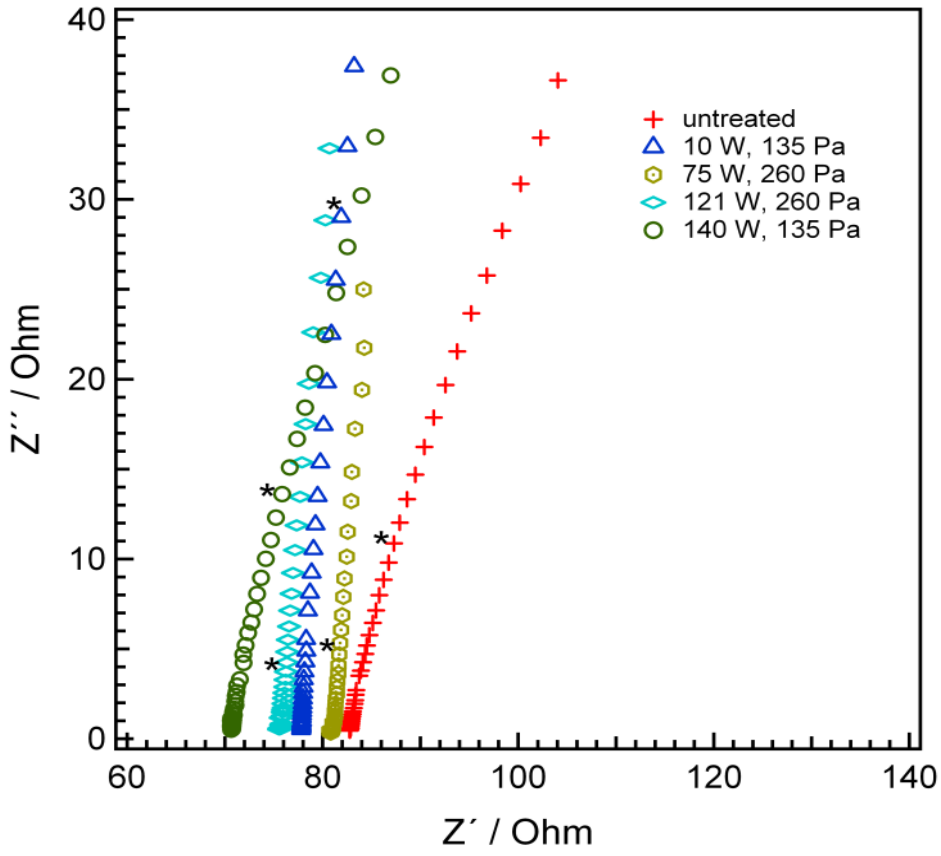

Figure 5.9: Nyquist plot of untreated and different wpCNTs/MnO_2 samples. Asterisks correspond to a frequency of 9.32 Hz.

The cycling stability of nanocomposite electrodes was investigated applying galvanostatic charge/discharge cycles. A constant current density of 0.52 mA cm^{-2} in a potential window from 0 to 1 V, and of 1.75 mA cm^{-2} between 0.1 and 0.8 V was applied during 2000 cycles. The specific capacitance was calculated from the discharge curve using (equation 2.13).

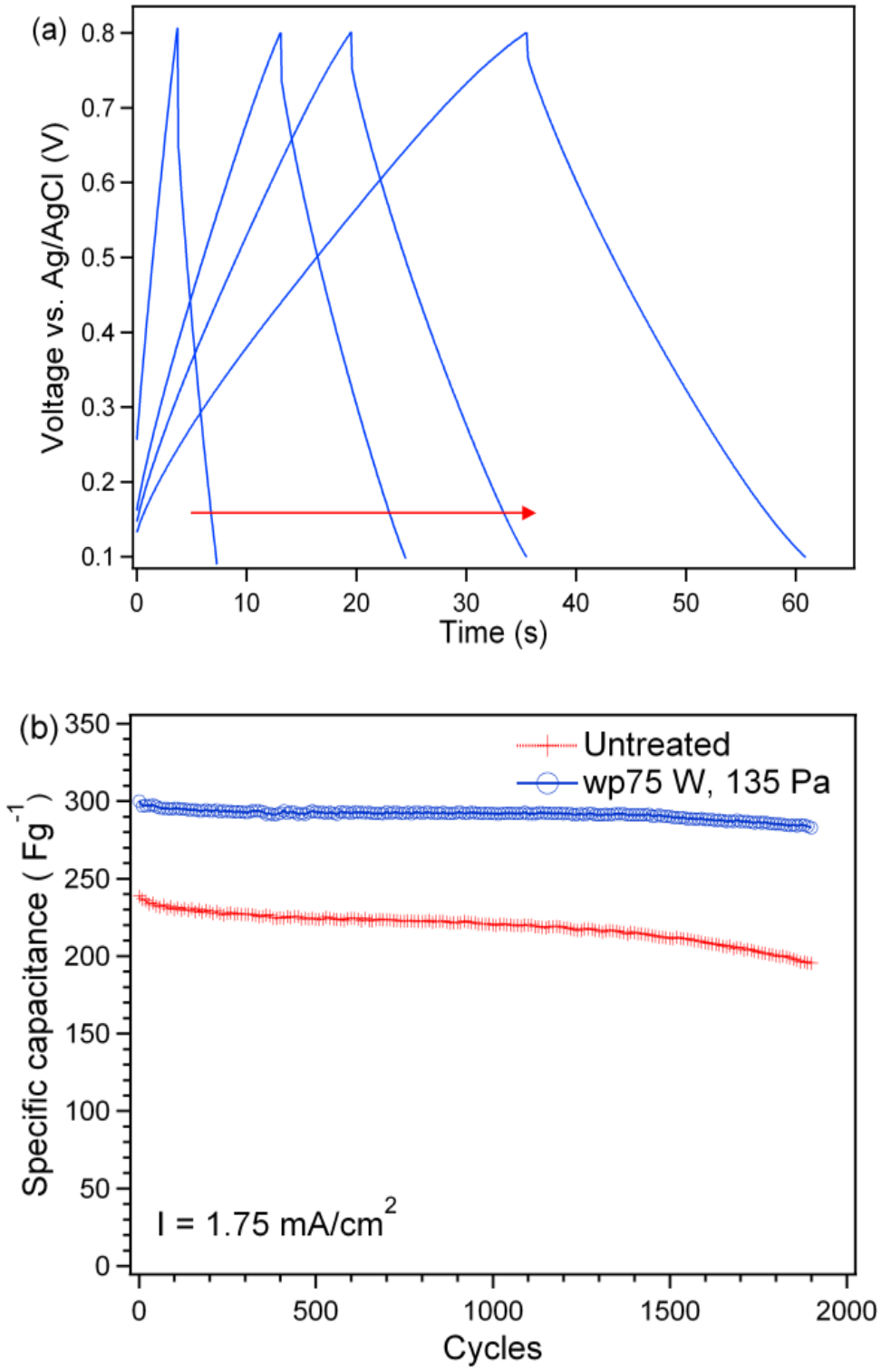

Figure 5.10: (a) Charge/discharge curves at different current densities from1.75, 0.70, 0.52, and 0.35 mAcm^{-2}, as indicated by the arrow, for wpCNTs/MnO_2 (75 W, 135 Pa). (b) Galvanostatic charge/discharge cyclic stability in the 0.1–0.8 V potential.

Galvanostatic charge/discharge curves were measured applying various current densities from1.75 to 0.35 $mAcm^{-2}$. (Figure 5.10 (a)) shows charge/discharge curves of wpCNTs/ MnO_2 (75 W, 135 Pa) nanocomposite between 0.1 and 0.8 V. As with the EIS measurements, the ohmic drop of the curves indicates a high series resistance related to the contact between silicon substrate and nanotubes, current collectors, and solution resistance. (Figure 5.10 (b)) shows the cycling stability of nanocomposite electrodes in the voltage range of 0.1 to 0.8 V at a current density of 1.75 $mAcm^{-2}$. It is evident that water plasma-treated CNTs/MnO_2 exhibits both a higher capacitance and capacitance retention in comparison with untreated CNTs/MnO_2. On the other hand, charge/discharge cycling of untreated CNTs/MnO_2 nanocomposite electrode in the voltage window of 0 to 1V (Figure 5.11) gives higher capacitance than wpCNTs/MnO_2 samples. However, it only lasts up to 700 cycles. In the case of wpCNTs/MnO_2 samples, a continuous fading in the capacitance was observed. The reason for this poor cyclability in both composites with untreated and plasma-treated CNTs is related to irreversible reduction/oxidation reactions of Mn^{4+} to Mn^{2+} and Mn^{7+} in the voltage region around 0V and 1V, respectively. Additionally, oxygen evolution reaction starts to take place around 0.8 V, which could also affect the reversibility of redox reactions [7]. These irreversible redox reactions cause the dissolution of manganese in the electrolyte and fading of the capacitance [30] (see Figure 5.11(b)).

From the above results, we assume that some processes occur during cycling in the potential regions around 0 V and 1 V, namely, dissolution of MnO_2 nanoflowers, coalescence, and upward drag of the oxide forming a thick layer of material on top of the CNTs, and morphological modification of the nanoflowers to a needle-like structure that corresponds to hausmannite Mn_3O_4.The dense and thick layer of Mn_3O_4 on the CNTs mat generated during the cycling process appears to be the reason for the capacitance fading. Furthermore, the presence of Mn_3O_4 proved by Raman spectroscopy and XPS is known to significantly decrease the reversibility of the system [21]. SEM images and cyclability experiments reveal that highly porous CNTs/MnO_2 composite electrodes, with good electronic conduction and, most importantly, separated MnO_2 nanoflowers, and/or layer-like structure are the desired conditions for a suitable capacitive behavior.

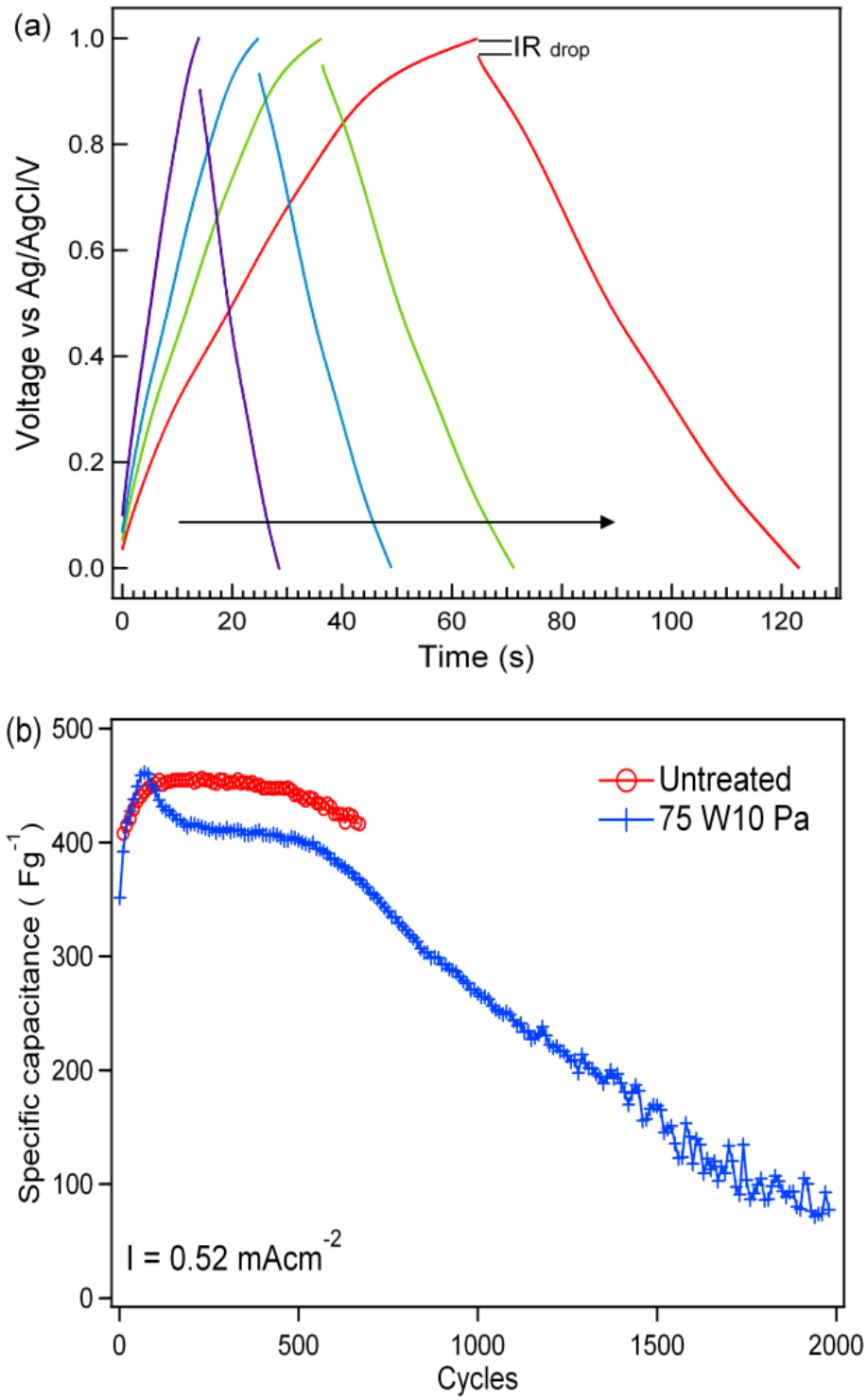

Figure 5.11: (a) Charge/discharge curves obtained at different current densities from 0.1, 0.2, 0.3, 0.4 mAcm^{-2}, as indicated by the arrow for wpCNTs/MnO_2 (10 W, 135 Pa) and (b) charge/discharge cyclic stability between 0 and 1 V for untreated and water plasma treated CNTs/MnO_2 electrodes.

5.4. Conclusions

Water plasma treatment performed on CNTs removes amorphous carbon and introduces several oxygen functional groups on the CNTs surface. MnO_2/CNTs nanocomposite electrodes were obtained after galvanostatic deposition of MnO_2 on untreated and water plasma-treated CNTs. SEM images confirm the removal of amorphous carbon and reveal nanoflower-structured MnO_2 deposited on the CNTs. Raman spectroscopy and XPS results indicate that electrochemical cycling in the potential range from 0-1V converts MnO_2 to Mn_3O_4, which corresponds to a change in the metal oxide morphology observed with SEM. On the other hand, a voltage window between 0.1–0.8 V does not change the oxidation state of MnO_2 and only induces a morphological change from nanoflower to layer-like structure of the oxide. High specific capacitance values were achieved under optimum water-plasma conditions; low rf plasma powers and high water pressures. A high specific capacitance of 750 Fg^{-1} was obtained for wpCNTs/MnO2 (10W, 135 Pa) nanocomposite electrode.

5.5. Refrences

[1] B. E. Conway, *Electrochemical Supercapacitors; Scientific Fundamentals and Technological Applications*, Kluwer Academic/ PlenumPublishers, NewYork, NY,USA, (1999).

[2] G. Lota, K. Lota, and E. Frackowiak, "*Nanotubes based composites rich in nitrogen for supercapacitor application*," (2007), Electrochemistry Communications, 9, 7, 1828–1832.

[3] S. Hussain, R. Amade, E. Jover, and E. Bertran, "*Nitrogen plasma functionalization of carbon nanotubes for supercapacitor applications*," Journal of Materials Science, (2013), 48, 7620–7628.

[4] K. Fic, E. Frackowiak, and F. Beguin, "*Unusual energy enhancement in carbon-based electrochemical capacitors*," (2012), Journal of Materials Chemistry, 22, 24223–24213.

[5] M. Toupin, T. Brousse, and D. B´elanger, "*Charge storage mechanism ofMnO_2 electrode used in aqueous electrochemical capacitor*," (2004), Chemistry of Materials, 16, 16, 3184–3190.

[6] S. R. Sivakkumar, J.M. Ko, D. Y. Kim, B. C. Kim, and G. G.Wallace, "*Performance evaluation ofCNT/polypyrrole/MnO_2 composite electrodes for electrochemical capacitors*," (2007), Electrochimica Acta, 52, 25, 7377–7385.

[7] E. Raymundo-Pinero, V. Khomenko, E. Frackowiak, and F. Beguin, "*Performance of manganese oxide/CNTs composites as electrode materials for electrochemical capacitors*," (2005), Journal of the Electrochemical Society, 152, 1, A229–A235.

[8] H. Zhang, G. Cao, Z.Wang, Y. Yang, Z. Shi, and Z. Gu, "*Growth of manganese oxide nanoflowers on vertically-aligned carbon nanotube arrays for high-rate electrochemical capacitive energy storage*," (2008), Nano Letters, 8, 9, 2664–2668.

[9] W. Chen, Z. Fan, L. Gu, X. Bao, and C. Wang, "*Enhanced capacitance of manganese oxide via confinement inside carbon nanotubes*," (2010), Chemical Communications, 46, 22, 3905–3907.

[10] Y. Wang and I. Zhitomirsky, "*Electrophoretic deposition of manganese dioxide-multiwalled carbon nanotube composites for electrochemical supercapacitors*," (2009), Langmuir, 25, 17, 9684–9689.

[11] H. Zheng, F. Tang, Y. Jia et al., "*Layer-by-layer assembly and electrochemical properties of sandwiched film of manganese oxide nanosheet and carbon nanotube*," (2009), Carbon, 47, 6, 1534–1542.

[12] Z.Chen, Z. Chen,A.Yu, R. Ahmed, H.Wang, andH. Li, "*Manganese dioxide nanotube and nitrogen-doped carbon nanotube based composite bifunctional catalyst for rechargeable zinc-air battery*," (2012), Electrochimica Acta, 69, 295–300.
[13] Y. Wang, H. Liu, X. Sun, and I. Zhitomirsky, "*Manganese dioxide-carbon nanotube nanocomposites for electrodes of electrochemical supercapacitors*," (2009), Scripta Materialia, 61,11, 1079–1082.
[14] R. Amade, E. Jover, B. Caglar, T. Mutlu, and E. Bertran, "*Optimization of MnO_2/vertically aligned carbon nanotube composite for supercapacitor application*," (2011), Journal of Power Sources, 196, 13, 5779–5783.
[15] S. Hussain, R. Amade, E. Jover, and E. Bertran, "*Functionalization of carbon nanotubes bywater plasma*," (2012), Nanotechnology, 23, 1–8.
[16] Z. Fan, J. Chen, B. Zhang, B. Liu, X. Zhongand, and Y. Kuang, "*High dispersion of γ-MnO_2 on well-aligned carbon nanotube arrays and its application in supercapacitors*," (2008), Diamond and Related Materials, 7, 1943–1948.
[17] C. Julien, M. Massot, R. Baddour-Hadjean, S. Franger, S. Bach, and J. P. Pereira-Ramos, "*Raman spectra of birnessite manganese dioxides*," (2003), Solid State Ionics,159, 3-4, 345–356.
[18] M.-C. Bernard, A. H.-L. Goff, B. V. Thi, and S. C. De Torresi, "*Electrochromic reactions in manganese oxides*," (1993), Journal of the Electrochemical Society, 140, 11, 3065–3070.
[19] F. Buciuman, F. Patcas, R. Craciun, and D. R. T. Zahn, "*Vibrational spectroscopy of bulk and supported manganese oxides*," (1999), Physical Chemistry Chemical Physics, 1, 1, 185–190.
[20] C. Julien, M. Massot, S. Rangan, M. Lemal, and D. Guyomard, "*Study of structural defects in γ-MnO_2 by Raman spectroscopy*," (2002), Journal of Raman Spectroscopy, 33, 4, 223–228.
[21] K.-W. Nam, M. G. Kim, and K.-B. Kim, "*In situ Mn Kedge X-ray absorption spectroscopy studies of electrodeposited manganese oxide films for electrochemical capacitors*," (2007), Journal of Physical Chemistry C, 111, 2, 749–758.
[22] T. Gao, H. Fjellvag, and P. Norby, "*A comparison study on Raman scattering properties of α- and β-MnO_2*," (2009), Analytica Chimica Acta, 648, 235–239.

[23] M. C. K. Sellers, B. M. Castle, and C. P. Marsh, "*Threedimensional manganese dioxide-functionalized carbon nanotube electrodes for electrochemical supercapacitors*," (2013), Journal of Solid State Electrochemistry, 17, 175–182.
[24] J. Shen, A. Liu, andY.Tu, "*Asymmetric deposition of manganese oxide in single walled carbon nanotube films as electrodes for flexible high frequency response electrochemical capacitors*," (2012), Electrochimica Acta, 78, 122–132.
[25] H. W. Nesbitt and D. Banerjee, "*Interpretation of XPS Mn(2p) spectra of Mn oxyhydroxides and constraints on the mechanism ofMnO2 precipitation*," (1998), American Mineralogist, 83, 3-4, 305–315.
[26] D. P. Dubal, D. S. Dhawale, R. R. Salunkhe, and C. D. Lokhande, "*Conversion of chemically prepared interlocked cubelike Mn_3O_4 to birnessite MnO_2 using electrochemical cycling*," (2010), *Journal of the Electrochemical Society*, 157, 7, A812–A817.
[27] S. Biniak, G. Szyma´nski, J. Siedlewski, and A. Swiatkoski, "*The characterization of activated carbons with oxygen and nitrogen surface groups*," (1997), Carbon, 35, 12, 1799–1810.
[28] S.-E. Chun, S.-I. Pyun, and G.-J. Lee, "*A study onmechanism of charging/discharging at amorphousmanganese oxide electrode in 0.1 M Na_2SO_4 solution*," (2006), Electrochimica Acta, 51, 28, 6479–6486.
[29] C.-T. Hsieh and H. Teng, "*Influence of oxygen treatment on electric double-layer capacitance of activated carbon fabrics*," (2002), Carbon, 40, 5, 667–674.
[30] C.-C. Hu and C.-C. Wang, "*Nanostructures and capacitive characteristics of hydrous manganese oxide prepared by electrochemical deposition*," (2003), Journal of the Electrochemical Society, 150, 8, A1079–A1084.

Chapter 6
Nitrogen plasma functionalization of VA-MWCNTs for supercapacitor applications

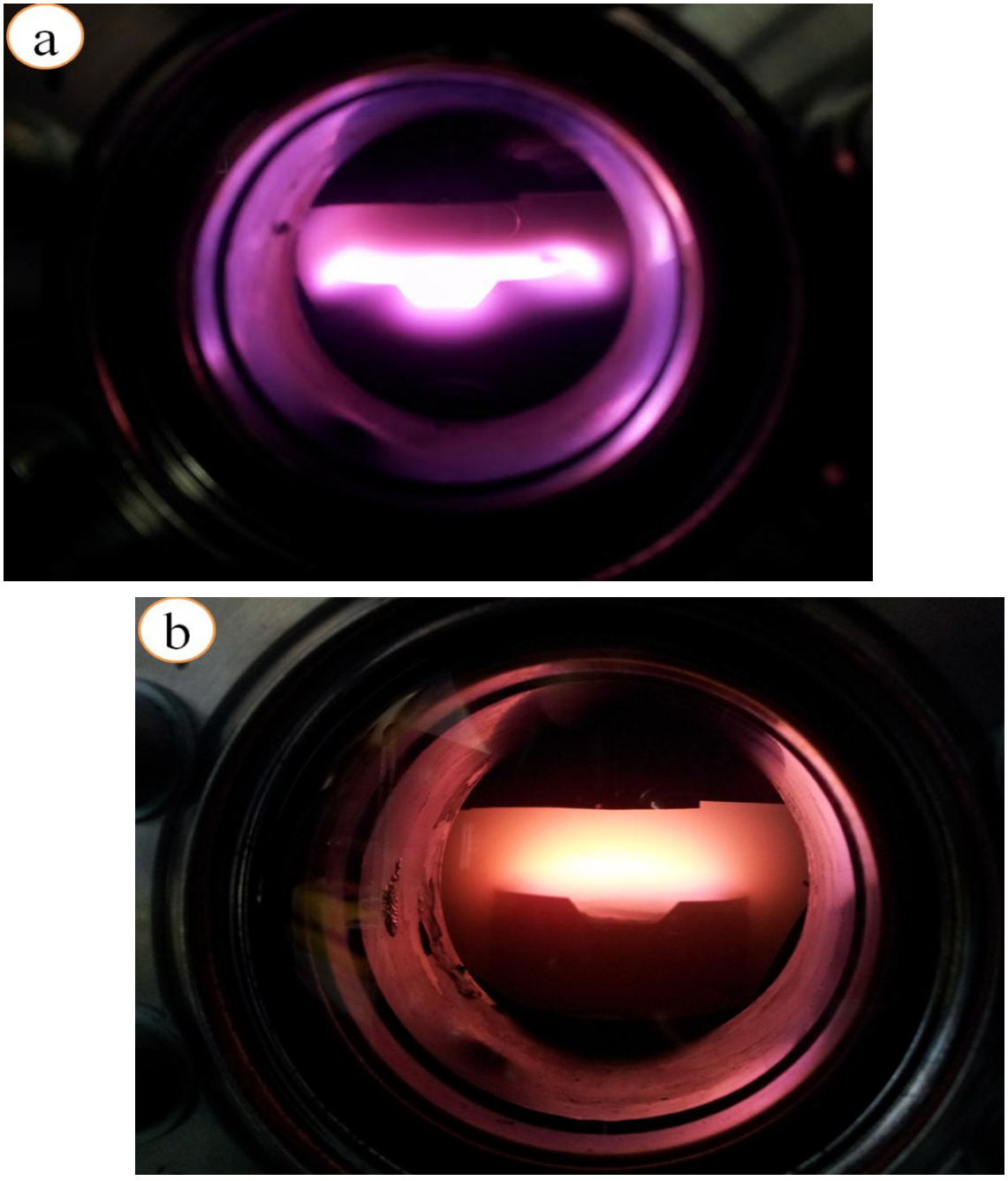

Figure 6: Nitrogen plasma photographs at (a) 29 W, 50 Pa (b) 75 W, 10 Pa.

Chapter 6- Nitrogen plasma functionalization of VA-MWCNTs for supercapacitor applications

6.1. Introduction

In order to get profit from the extraordinary properties of CNTs it is important to modify its surface chemistry and remove the amorphous carbon. The generated surface functionalities produce the acid-base quality [1] in CNTs that can boost their capacitance owing to the additional pseudocapacitive effect obtained [2], which acts in combination with the non faradaic currents and condensation of ionic charges at the electrode/electrolyte interface. The introduction of nitrogen containing functional groups onto the CNTs surface is known to promote faradaic pseudocapacitive reactions [3]. Among these functional groups pyridinic and pyrrolic enhance the capacitive behavior, while quaternary nitrogen and pyridinic–n-oxide improve the electronic transfer [3, 4]. On this subject, different methodologies have been applied to introduce nitrogen functionalities on the CNTs surface; ammonia plasma, N_2^+ Ar microwave plasma, atomic nitrogen plasma, N_2 plasma and urea treatments [5-8]. However, these methods involve long procedures and an in-depth study of the effects of plasma power and nitrogen pressure on the properties of CNTs has not been reported yet.

6.2. Nitrogen plasma functionalization

Vertically aligned multiwall carbon nanotubes (VA-MWCNTs) were grown on p-type boron doped silicon wafers (0.01-0.02 Ωcm range) by PECVD technique. Detailed condition of growth parameters are explained in chapter 4. Radio frequency (rf) nitrogen plasma was used to remove amorphous carbon and to decorate the surface of MWCNTs with nitrogen functionalities. The plasma treatment time was set to 120 s for each experiment, and the flow of pure nitrogen gas was set to 100 sccm. Optimization of the treatment effects was accomplished adopting a Box-Wilson experimental design, with rf-power and nitrogen pressure as the main operational parameters. In accordance with Box-Wilson distribution 9 conditions were chosen to perform 13 experiments (figure 6.1). In order to determine the possible intrinsic deviation of our experimental set-up the central point of the design was repeated 5 times. This approach allows us to

optimize two operating parameters simultaneously taking into account possible interactions between them. A statistical analysis of the results provides a second order (quadratic) model for the response variables that describes how the plasma operating parameters affect the CNTs properties (equation (6.1)).

$$X = a_0 + a_1 A + a_2 B + a_3 A^2 + a_4 AB + a_5 B^2 \quad (6.1)$$

where X is the dependent magnitude, a_n are constant coefficients obtained by statistically adjusting these polynomial equations, A is the plasma power and B the nitrogen pressure.

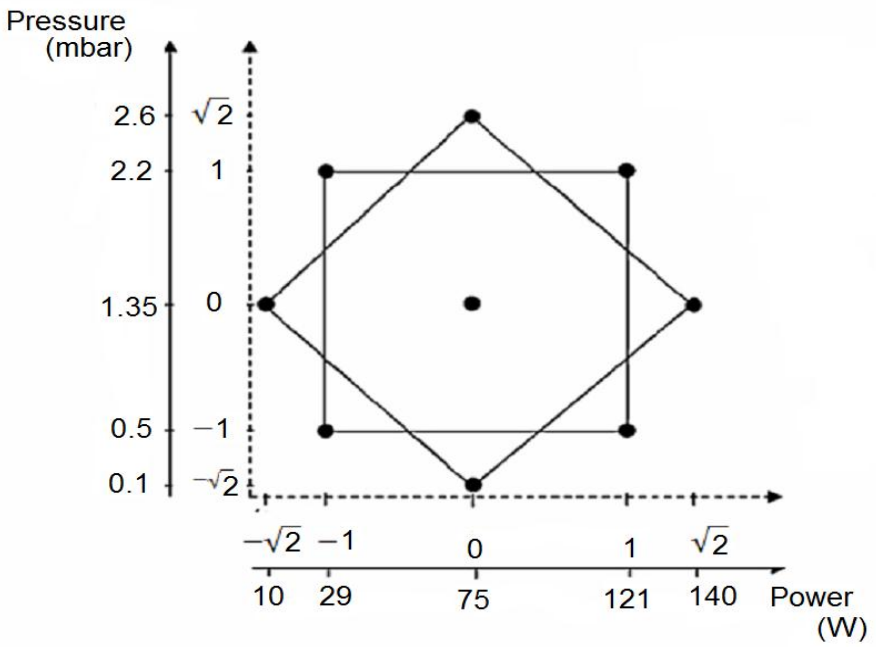

Figure 6.1: Box-Wilson experimental design samples distribution for two main parameters (RF power and nitrogen pressure).

6.3. Results and discussion

6.3.1. Morphological characterization

The morphology and structure of MWCNTs was analyzed by field emission scanning electron microscopy (FE-SEM) (Hitachi S-4100, Japan). Morphological characterization of untreated CNTs revealed vertically-

aligned nanotubes with a length of about 14 μm (figure 6.2 (a)) and a number of walls in the range of 25-45. After nitrogen-plasma treatment most of the amorphous carbon was totally removed from the samples and, although there was a slight decrease in the number of walls, the length of the CNTs remained almost unaltered (see figure 6.2 (b)). The slight decrease in the length due to the surface bombardment by the nitrogen-based ions (in nitrogen plasmas, a molecular ion N_2^+ is usually more abundant than N^+) or other plasma–surface interactions [9].

HRTEM analysis of a sample treated at 75 W plasma power and 260 Pa nitrogen pressure reveals catalyst particles still stuck on the tips of the nanotubes, but the graphitic walls and edges on the outer side of the planes can be clearly seen (figure 6.2 (c)). On the other hand, (figure 6.2 (d)) shows CNTs treated at a lower plasma power and nitrogen pressure (10 W, 135 Pa). Under these conditions the nanotubes preserve the catalyst particle on their tips as well as most of the amorphous carbon.

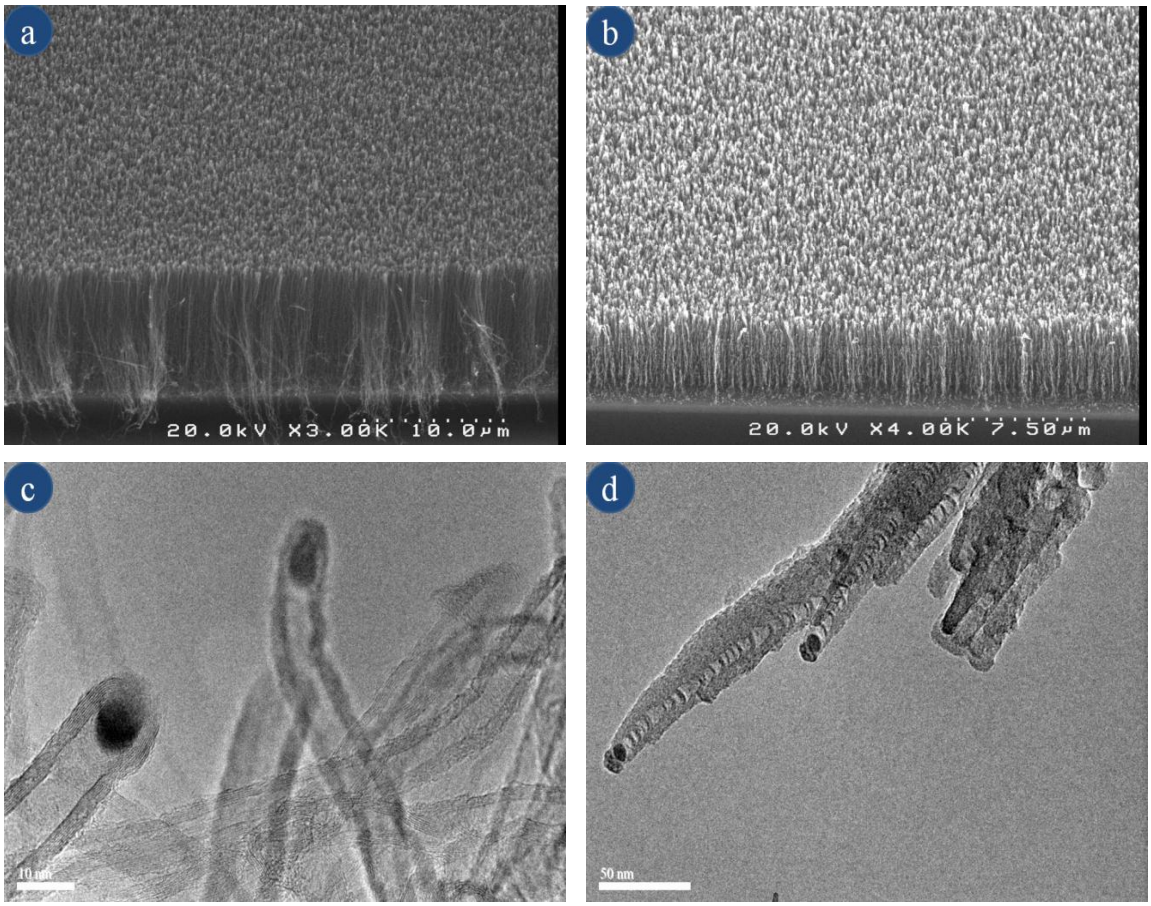

Figure 6.2: FE-SEM images of (a) untreated CNTs, (b) nitrogen plasma treated. HRTEM images of (c) nitrogen-plasma treated CNTs at 75 W

plasma power, 260 Pa nitrogen pressure and (d) nitrogen-plasma treated CNTs at 10 W plasma power, 135 Pa nitrogen pressure.

6.3.2. X-ray photoelectron spectroscopy (XPS)

The study of XPS elucidates the comparative percentage of C, N, and O before and after the nitrogen plasma treatment. A small N1s peak corresponding to a concentration of 4.28% appears in the untreated MWCNTs spectra, which is assumed to be a consequence of using ammonia during the PECVD growth of CNTs. This concentration increases up to 21.26% at different treatment conditions of nitrogen plasma power and pressure. The amount of oxygen in the untreated MWCNTs was 2.82% as a result of ambient air oxidation. After the plasma treatment it increases up to 10.58%. The dependency between the relative percentages of oxygen and nitrogen with the nitrogen pressure, at constant power (75 W), was gained using a second degree polynomial equation (equation (6.1)) (figure 6.3). The polynomial model was found to be statistically significant ($p< 0.05$) explaining more than 80 % of the sample variation with a_0= 23.74, a_1= $6.2\cdot10^{-3}$, a_2= $-1.3\cdot10^{-4}$, a_3= -10.78, a_4= 2.65, a_5= $1.79\cdot10^{-2}$ for N1s, and a_0= 9.97, a_1= $1.67\cdot10^{-2}$, a_2= $-3.8\cdot10^{-5}$, a_3=-4.11, a_4= 0.737, a_5= $1.13\cdot10^{-2}$ for O1s.

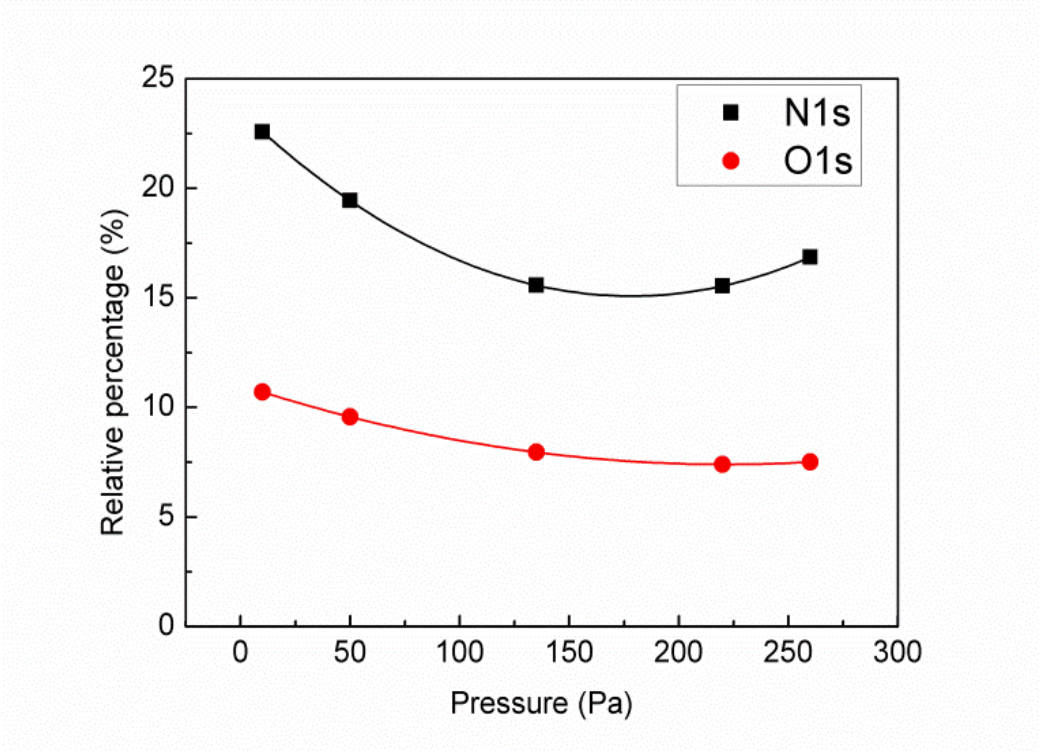

Figure 6.3: Relative contents of nitrogen and oxygen at a constant plasma power of 75 W against nitrogen pressure obtained from the polynomial model (see (6.1)).

A possible reason behind the simultaneous increase in oxygen content with respect to nitrogen content is the increase in polarity, high porosity and low density of CNx (carbon nitride) materials [10]. At relatively low plasma pressures both the nitrogen and oxygen concentrations are high. Under these conditions the low pressure discharge incorporates nitrogen, but also generates long-lived surface free radical sites [11], which eventually react with oxygen or ambient moisture while handling the samples for the XPS measurements. In addition, the plasma treatment produces numerous defect sites that may interact with oxygen outside the reactor [11, 12].

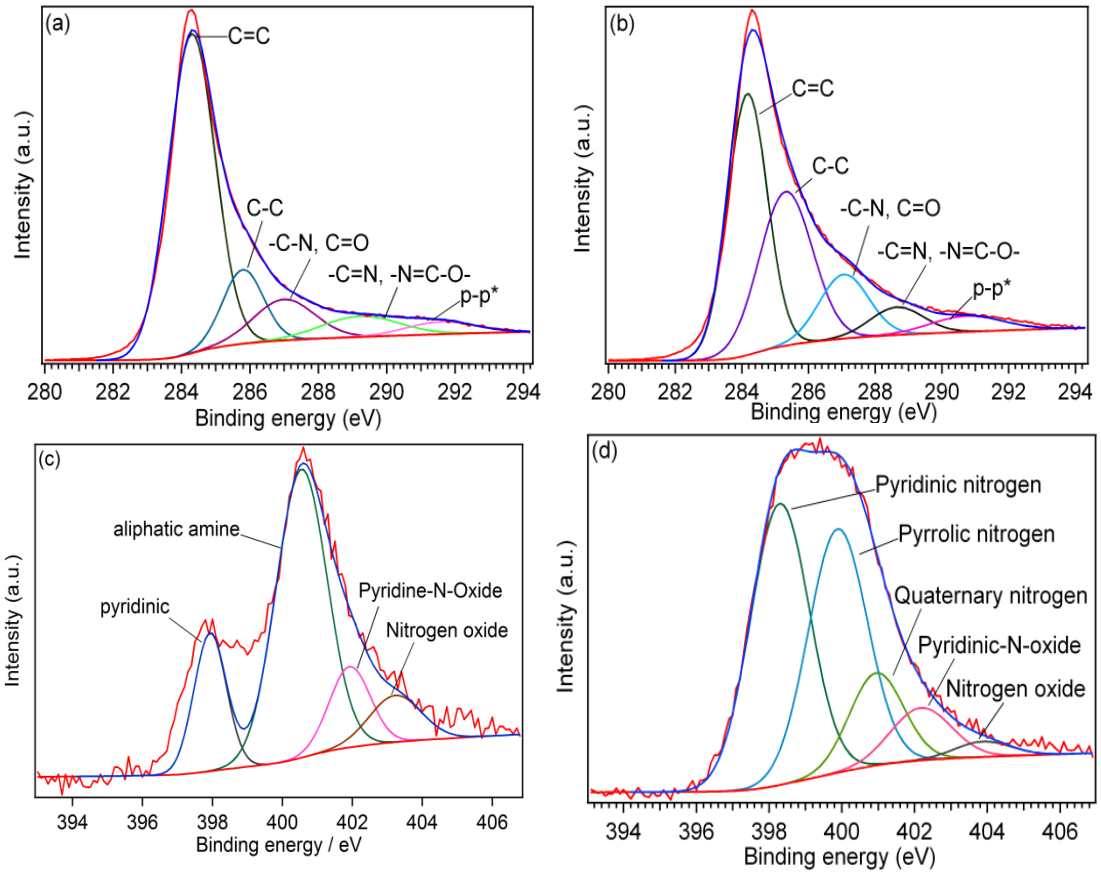

Figure 6.4: (a, c) high resolution deconvoluted C1s and N1s spectra, respectively, of untreated MWCNTs. (b, d) high resolution deconvoluted C1s and N1s spectra, respectively, of nitrogen-plasma treated MWCNTs.

Red and blue curves correspond to experimental data and obtained fitting, respectively.

After the nitrogen plasma treatment we observed an upshift in the C1s binding energy from 284.2 eV to 284.6 eV (figures 6.4 (a) and (b)) respectively, and the peak becomes more asymmetric and broad. The upshift in the binding energies is related to the incorporation of nitrogen in MWCNTs and the graphitic structure of CNTs [10, 13]. For the deconvolution of the C1s peak the position at 284.3 eV was taken as a reference, which is assigned to highly oriented pyrolytic graphite (HOPG) [14]. (Figures 6.4 (a) and (b)) show high resolution C1s spectra of untreated and nitrogen plasma treated MWCNTs deconvoluted into five Gaussian peaks. The peak at (284.3 ± 0.2) eV was assigned to sp^2 hybridized graphite-like carbon (C=C) and the peak in the region of (285.5 ± 0.2) eV has a contribution of sp^3 hybridized carbon atoms (C-C). The peaks observed at (287.3 ± 0.2) eV and (288.8 ± 0.3) eV indicate the presence of the following bonds; –C-N, C=O, and –C=N, -N=C-O-, COOC-, respectively. The assignment of the peaks is complete with the last peak at (290.8 ± 0.2) eV, which is related to π–π* interaction in aromatic ring [15]. The relative percentages of the bonds before and after the different plasma treatments are given in Table 2. Not surprisingly, the C=C hybridized into C-C and the intensities of the C1s spectra decreased after the nitrogen plasma treatments.

In order to study the different types of nitrogen incorporated in MWCNTs high resolution N1s spectra were deconvoluted into 4 and 5 peaks for untreated and nitrogen plasma treated MWCNTs, respectively (Figures 6.4 (c)and 6.4 (d)). The peaks of untreated MWCNTs found at (398.1 ± 0.2) eV, (400.5 ± 0.2) eV, (401.8 ± 0.2) eV and (403.6 ± 0.2) eV are assigned to pyridinic nitrogen functionalities, aliphatic amine [16], pyridine-N-oxide and nitrogen oxide [15, 18], respectively. For nitrogen plasma treated MWCNTs the peaks observed at (398.1 ± 0.2) eV, (399.6 ± 0.2) eV, (400.8 ± 0.2) eV, (401.9 ± 0.2) eV and (403.6 ± 0.2) eV were assigned to pyridinic nitrogen [19], pyrrolic nitrogen [19], quaternary nitrogen [17] pyridinic-N-oxide and nitrogen oxide, respectively. It should be noted that the quaternary nitrogen peak arises due to the presence of nitrogen substitutes in the aromatic graphene sheet. Except for this

functionality, all nitrogen containing groups introduced on the CNTs are located at the edges of graphene layers.

Table 6.1: Relative percentages of the bonds obtained after fitting the XPS C1s spectra

MWCNTs	sp2 (%)	sp3 (%)	-C-N, C=O (%)	-C=N, -N=C-O-, COOC- (%)	π–π* (%)
Untreated	65.0	13.2	10.9	7.1	3.8
10 W, 135 Pa	42.7	32.8	12.7	6.4	5.4
29 W, 50 Pa	36.2	35.9	16.2	7.4	4.3
29 W, 220 Pa	48.3	30.1	11.1	6.1	4.4
75 W, 10 Pa	43.5	30.3	18.3	4.5	3.4
75W, 135 Pa	37.4	35.4	14.9	7.0	5.3
75 W, 260 Pa	39.5	34.7	14.1	6.9	4.8
121W, 50 Pa	46.8	29.3	16.4	4.9	2.7
121W, 220Pa	41.0	34.6	13.0	6.9	4.4
140W, 135 Pa	43.3	34.1	12.3	5.9	4.5

From the obtained results (see Table 6.1 and Table 6.2) it is clear that the nitrogen plasma treatment produces new functionalities like quaternary and pyrrolic-like nitrogen and increases the concentration of pyridine functionalities [15].

(Figure 6.5) shows the concentration of different nitrogen groups as a function of nitrogen pressure at a constant power of 75 W obtained from the polynomial model. At low pressure the relative amount of pyridinic nitrogen is high, and presents a minimum at a pressure of 220 Pa, while the relative percentages of pyrrolic and quaternary nitrogen show a maximum at middle pressures. On the contrary, no big change is observed in the relative percentages of pyridinic-N-oxide and molecular nitrogen. Only a slight increase can be appreciated for oxygenated nitrogen at higher pressures.

In view of these results we assume that at low pressures a small amount of nitrogen replaces carbon atoms in the six-fold ring forming pyridinic nitrogen, which stops the propagation of further nitrogen functionalities [20]. With increasing nitrogen pressure the plasma becomes more effective resulting in an increase of the pyrrolic and quaternary

nitrogen amounts at the edge and basal planes respectively. At higher pressures the percentage of pyridinic nitrogen and pyridinic-N-oxide increases again resulting in a decrease of the pyrrolic and quaternary nitrogen, which is in agreement with previous reports on annealed coals and carbonized nitrogen-containing model compounds [21].

Table 6.2: Relative percentages of the bonds obtained after fitting the XPS N1s spectra.

MWCNTs (NP)	Pyridinic nitrogen (%)	Pyrrolic nitrogen (%)	Quaternary nitrogen (%)	pyridine-N-oxide (%)	Nitrogen oxide (%)
Untreated	20.54	[a]54.64	-	15.51	9.31
10 W, 135 Pa	41.26	35.76	12.41	7.94	2.63
29 W, 50 Pa	39.93	38.54	11.96	6.78	2.78
29 W, 220 Pa	38.74	37.34	12.67	7.15	4.14
75 W, 10 Pa	44.57	36.68	9.97	5.84	2.92
75W, 135 Pa	38.9	36.51	14.24	7.51	2.84
75 W, 260 Pa	40.56	36.17	7.27	7.27	2.32
121W, 50 Pa	46.23	34.86	10.81	5.19	2.92
121W, 220Pa	41.36	38.17	10.3	7.37	2.78
140W, 135Pa	46.67	36.54	6.67	6.97	3.06

[a] For this sample the percentage corresponds to aliphatic amine.

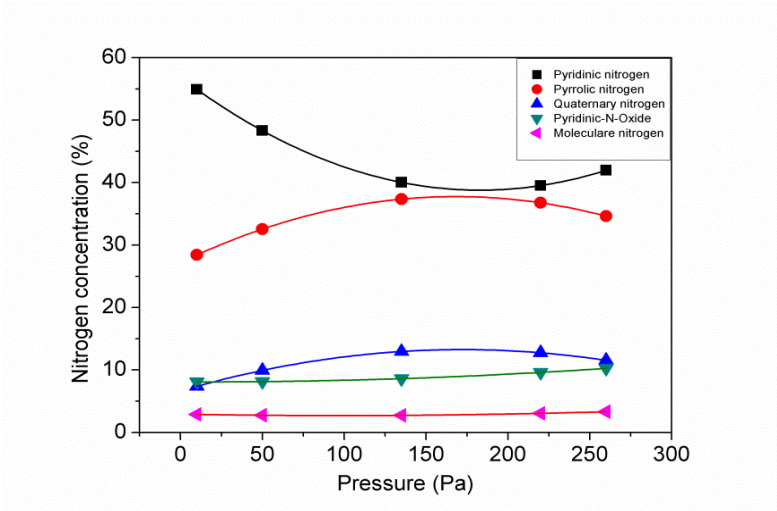

Figure 6.5: Nitrogen concentrations at a constant power of 75 W against nitrogen pressure, obtained from the polynomial model (see (6.1)).

6.3.3. Raman spectroscopy

Raman spectroscopy was performed to evaluate the quality of the nanotubes using a micro-Raman system (Horiba LabRam HR800, Japan). A green laser 532 nm wavelength, 0.5 mW power and a 50LWD objective was used during the measurements.

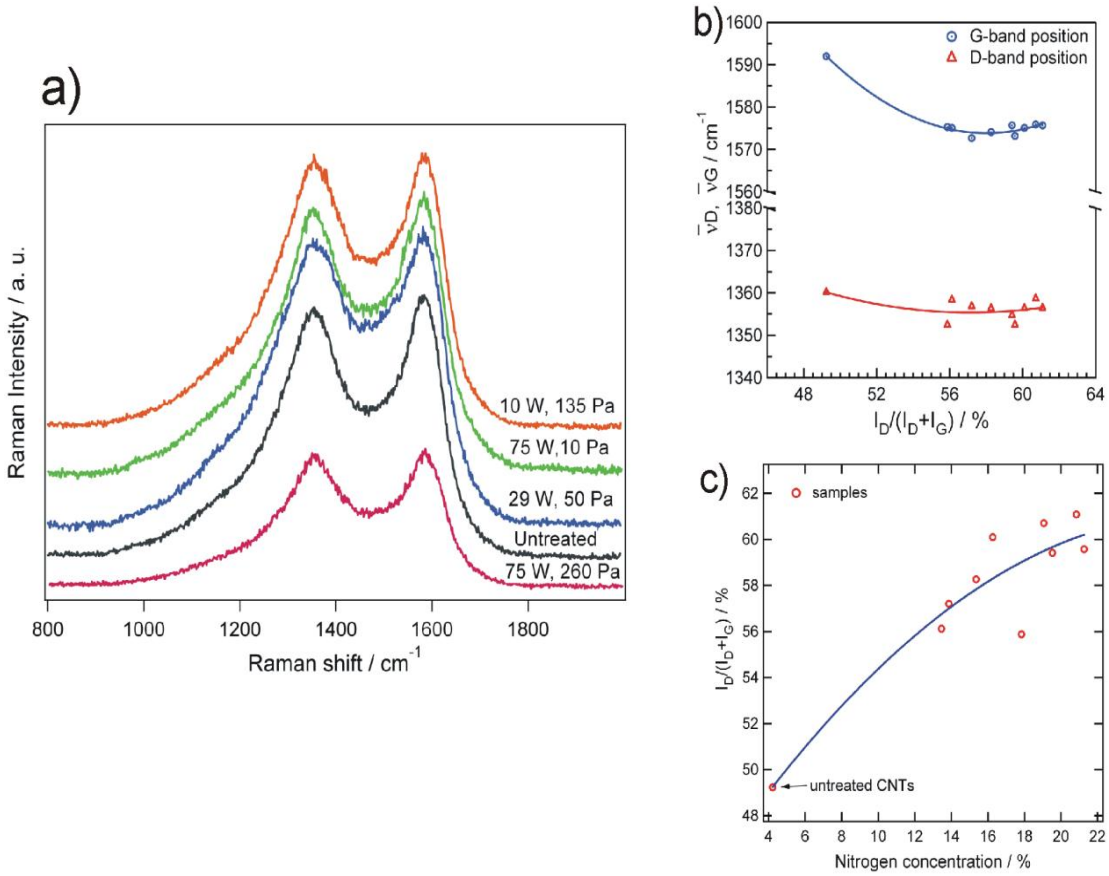

Figure 6.6: (a) Raman spectra of several samples obtained at different conditions of nitrogen plasma treatment. (b) Variation in the wavenumber of D and G peaks with respect to the disorder, (c) Structural disorder with respect to the nitrogen concentration. The solid lines are drawn to guide the eyes.

(Figure 6.6 (a)) shows Raman spectra of several samples evidencing broader peaks after the plasma treatment. Traditional fitting of the measured spectra into D and G band seemed to be neglecting some minor shoulders in the peaks and the error was very high. To improve the fitting we added some more peaks that are in agreement with those already assigned in the literature. The peak near 1610 cm^{-1} called $D^{/}$ corresponds to defects on the side walls of CNTs. $D^{//}$ appears near 1500 cm^{-1} wavenumber and is related to stacking defects in the graphene layer [17]. I band was

observed around 1210 cm^{-1} and is attributed to impurities in the graphite lattice [22], and incorporation of nitrogen in CNTs [17].

Analysis of the D and G band positions, FWHM (full width at half maximum) of the Raman peaks and ratio between relative intensities reveals information about the structure of CNTs. Since the D band is related to disorder and the G band to graphitic order, the relationship between their intensities gives us information about the structural disorder. In order to evaluate the structural disorder the following ratio was adopted, $(I_D/(I_D + I_G))\cdot 100$, with $I_D + I_G < 100\%$ due to the existence of minor bands in the first order spectrum [22, 23].

The downshift in the wavenumber of the G band from (1593 ± 0.56) cm^{-1} to (1572.7 ± 1.69) cm^{-1} is related to nitrogen doping or incorporation of nitrogen in CNTs (Figure 6.6 (b)) [24]. With higher nitrogen concentration the downshift in the G bands increases and also the structural disorder. As a consequence, a downshift in the D band frequency is observed [25]. The D band is displaced from (1356.9 ± 0.73) cm^{-1} for untreated MWCNTs down to (1352.4 ± 0.48) cm^{-1} for nitrogen plasma treated MWCNTs (see Figure 6.6 (b)). The FWHM of D band decreases from (184.56 ± 4.61) cm^{-1} for untreated MWCNTs, down to (149.4 ± 2.14) cm^{-1} for nitrogen plasma treated MWCNTs (75 W, 260 Pa). The decrease in the FWHM of the D band corresponds to a decrease in the diameter of MWCNTs [26], clearly related with a higher structural disorder. In agreement with these results TEM images show a reduction in the number of walls and the removal of amorphous carbon, suited for enhanced electrochemical properties.

As seen in (figure 6.6 (c)) the structural disorder increases with nitrogen concentration. In untreated MWCNTs the relative percentage of N1s obtained from XPS measurements is 4.23%, as a result of using ammonia during the growth of MWCNTs, and the structural disorder is 49%. With increasing nitrogen concentration the disorder increases up to 61%, which is related to a higher density of structural defects and distortion on the CNTs walls. Thus, relatively higher nitrogen concentrations produce more structural defects and decrease the crystallinity of CNTs [24].

6.3.4. Electrochemical characterization

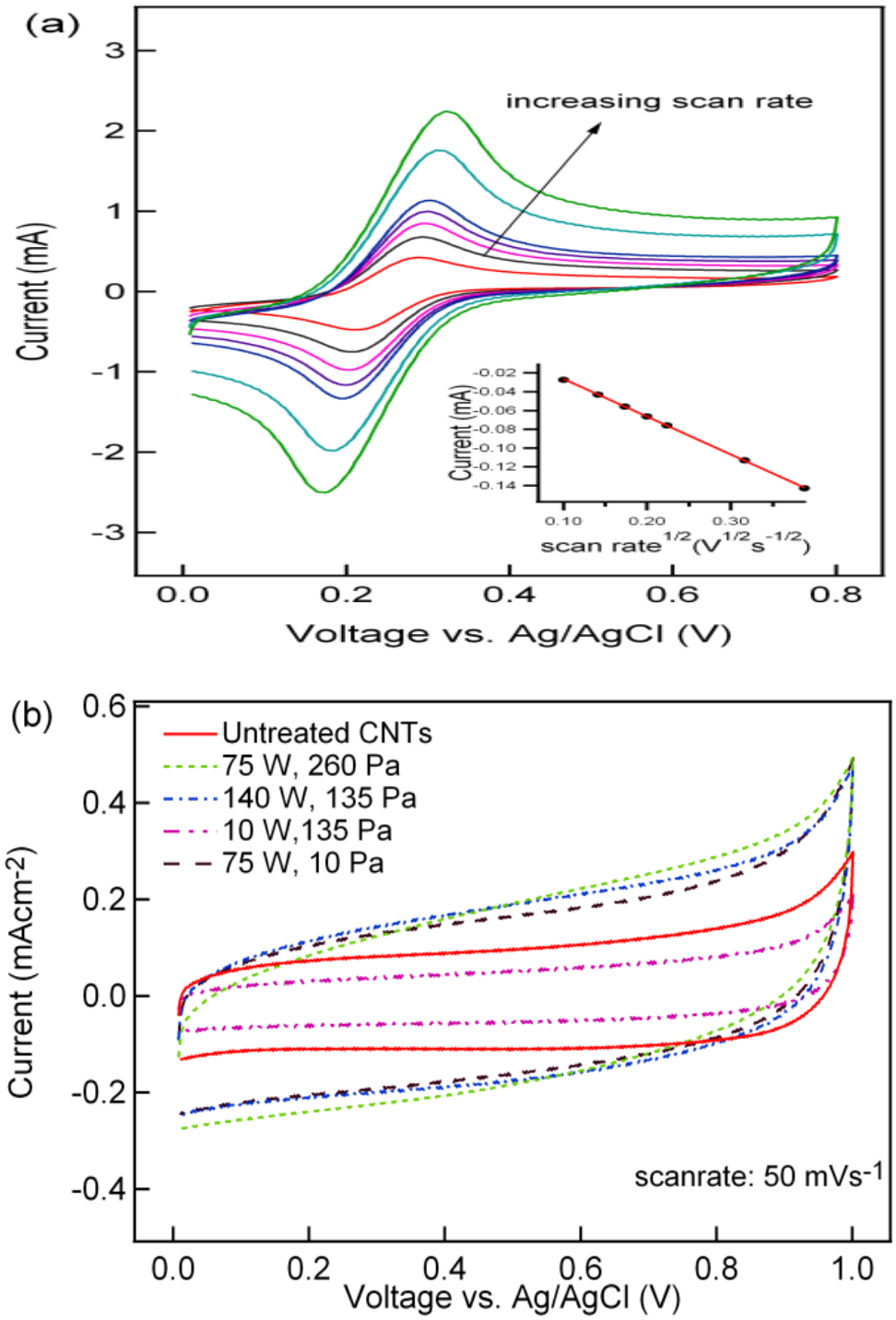

Figure 6.7: (a) CV of nitrogen plasma treated MWCNTs at a plasma power of 29 W and a nitrogen pressure 50 Pa applying different scan rates (10, 20, 30, 40, 50, 100 and 150 mVs^{-1}) and peak current versus square root of the scan rate (inset graph). (b) Comparison between the cyclic voltammograms of untreated and nitrogen plasma treated CNTs at a scan rate of 50 mVs^{-1}.

The electrochemical characterization of the samples was performed by cyclic voltammetry (CV). The electrochemical behavior of the Fe^{3+}/Fe^{2+} redox couple was studied at the surface of the nanotubes. A solution of 5 mM $K_3[Fe(CN)_6]$ in 0.1 M Na_2SO_4 was used during the study of the Fe^{3+}/Fe^{2+} redox process. The charge storage capability of the CNTs electrodes were analyzed using a 0.1 M Na_2SO_4 aqueous solution. The geometrical area of the working electrode was set to a constant value of 0.57 cm^2.

Analysis of the electrochemical properties of MWCNTs, before and after the nitrogen plasma treatment, shows that nitrogen functionalities enhance the charge storage properties of the nanotubes. Moreover, the functional groups affect the electron transfer properties of the obtained electrodes. The separation between the cathodic and anodic peak potentials (ΔE_p) of the Fe^{2+}/Fe^{3+} redox reaction is shown in (Table 6.3) for untreated and nitrogen-plasma treated MWCNTS. The untreated nanotubes present a high voltage difference (102 mV) at a scan rate of 10 mVs^{-1}, related to non-ideally reversible reduction/oxidation processes [27, 28]. The separation between the peaks decreases down to 75.7 mV for the sample treated with 29 W plasma power and 50 Pa nitrogen pressure. Hence, the nitrogen plasma effectively improves the reversibility of the reduction/oxidation processes at the electrode electrolyte interface (Figure 6.7 (a)).

Aqueous solution Na_2SO_4 0.1 M and 0.5 M were used to check the capacitive behavior of the untreated and nitrogen plasma treated CNTs. The specific capacitance of the samples was calculated from the cyclic voltammograms using (equation 2.12). (Table 6.3) shows the specific capacitance of untreated and nitrogen plasma treated MWCNTs at a scan rate of 10 mVs^{-1} in aqueous solution of 0.1 M Na_2SO_4. The specific capacitance increases from 22 Fg^{-1} for untreated MWCNTs up to 55 Fg^{-1} for plasma treated MWCNTs. Although containing a relatively higher nitrogen concentration than untreated CNTs, the sample treated at 10 W plasma power and 135 Pa nitrogen pressure presents a specific capacitance below that of untreated nanotubes (16 Fg^{-1}) (see Table 6.2 and 6.3). Under these conditions the plasma treatment seems to effectively introduce nitrogen groups in the amorphous carbon but not to remove it, therefore blocking the pores and in turn the flow of electrolyte through the nanotubes (see Figure 2(d)). The rest of the treated samples present higher capacitance values than untreated CNTs. Hence, the functional groups introduced by

the treatment increase the charge storage capabilities of the nanotubes, whose wettability is further improved through the removal of amorphous carbon by the plasma [29]. (Figure 6.7 (b)) shows cyclic voltammograms of untreated and nitrogen plasma treated CNTs at a scan rate of 50 mVs^{-1}. Untreated CNTs and nitrogen plasma treated nanotubes (10 W, 135 Pa) present typical rectangular-shape voltammograms associated with double layer capacitance. The other voltammograms show a slight deviation from this shape, which are related to pseudocapacitive (faradaic) processes. The presence of nitrogen functionalities revealed by XPS analysis supports this assumption.

Table 6.3: Specific capacitance in aqueous solution 0.1 M Na_2SO_4 and potential difference between cathodic and anodic peaks untreated and plasma treated samples in aqueous solution.

Sample	C_s (Fg^{-1})	ΔE_p (mV)	Sample	C_s (Fg^{-1})	ΔE_p (mV)
MWCNTs	22	102	75 W, 135Pa	34	100
10 W,135 Pa	16	97.6	75 W, 260 Pa	55	95
29 W,50 Pa	46	75.7	121 W, 50 Pa	41	89.2
29 W,220 Pa	37	102	121 W, 220 Pa	46	94.6
75 W,10 Pa	52	90.3	140 W, 135 Pa	50	100

The above results point out that both pyridinic and pyrrolic nitrogen functionalities enhance the capacitance significantly due to their positive charge and their electrochemical activity [30, 31]. Moreover, nitrogen containing groups in carbon have been proven to increase the porosity of carbon materials [32], which is also consistent with the enhanced capacity obtained in our results. Whereas when we used 0.5 M Na_2SO_4 aqueous solution specific capacitance increases to 25 Fg^{-1} for untreated CNTs and for nitrogen plasma treated (75 W, 10 Pa) to 74 Fg^{-1}.

Manganese dioxide deposited onto NP (75 W, 10 Pa) CNTs samples, show higher specific capacitance than those obtained without deposition (MnO_2 deposition conditions are explain in chapter 5). The electrochemical properties of the obtained NPCNTs/MnO_2 nanocomposites were explored using cyclic voltammetry, and electrochemical impedance spectroscopy. A comparison of the cyclic voltammograms of untreated MWCNTs, NP (75 W, 10 Pa) CNTs, and NP (75 W, 10 Pa) CNTs/MnO_2 obtained at a

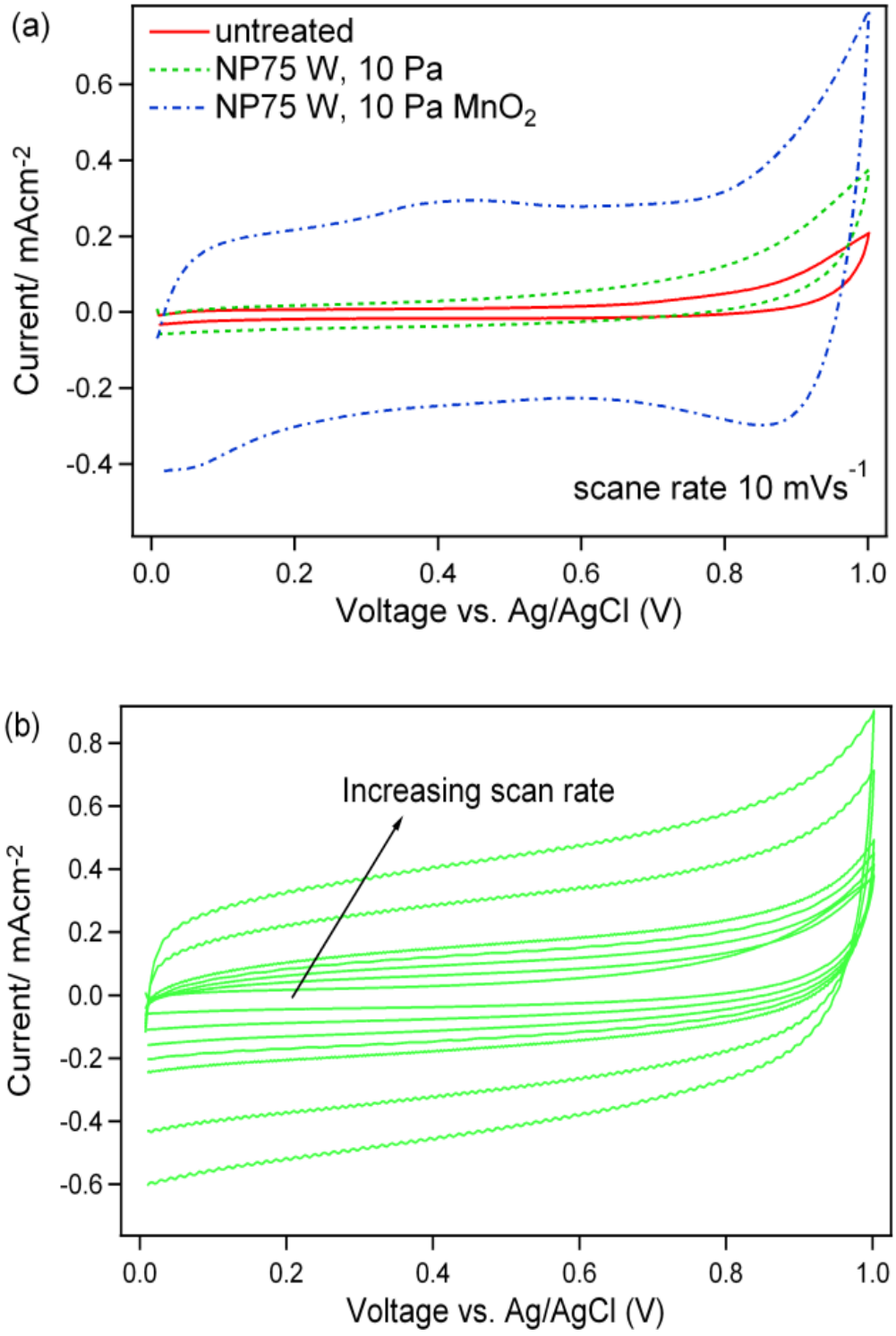

Figure 6.8: (a) Comparison of the cyclic voltammograms obtained at a scan rate of 10 mVs^{-1} for untreated MWCNTs, NPCNTS, and NPCNTs/MnO_2. (c) Cyclic voltammograms of nanocomposite NPCNTs/MnO_2 at different scan rates; 10, 20, 30, 40, 50, 100 and 150 mVs^{-1}.

scan rate of 10 mVs^{-1} is shown in (figure 6.8 (a)), considering carbon as the active material for the first two, and MnO_2 for the latter. Cyclic voltammograms of NP (75W, 10 Pa)CNTs/MnO_2 obtained at different scan rates show almost rectangular shapes even at high scan rates, which accounts for a fast current response to the change in voltage sweep direction (Figure 6.8 (b)). The MWCNTs treated with 75 W plasma power and 10 Pa nitrogen pressure, and further functionalized with MnO_2, exhibit highest specific capacitance of 955 Fg^{-1} at 10 mVs^{-1}. This value is almost 87% of the theoretical value for MnO_2 [33] and, to the best of our knowledge, is the highest value obtained until now for a NPCNTs/MnO_2 nanocomposite. Furthermore, the nanocomposite shows up to 575 Fg^{-1} even at a high scan rate of 150 mVs^{-1}.

6.4. Conclusions

Radio frequency nitrogen plasma can significantly introduce nitrogen containing groups in MWCNTs and remove amorphous carbon. Nitrogen functionalities such as quaternary nitrogen at the basal planes and pyrrolic nitrogen at the edge surface were significantly introduced on the MWCNTs. Raman spectroscopy results show that structural disorder increases with increasing nitrogen concentration. Middle to high plasma pressures (150–260 Pa) are suitable for the introduction of pyrrolic nitrogen, while low plasma pressures (10 Pa) for the introduction of pyridinic functionalities. An increase in the specific capacitance of MWCNTs is related to an increase in the structural disorder and the introduction of both pyridinic and pyrrolic functionalities. An increase in the specific capacitance from 22 to 55 Fg^{-1} was obtained in aqueous solution at a scan rate of 10 mV s-1 after applying a 75 W and 260 Pa nitrogen plasma treatment. Frackowiak et al., obtained highest capacitance of 137 F g^{-1} (in 6 M KOH solution) from MWCNTs purified with 69 % nitric acid at 80 °C. However, these CNTs present limited applications due to self-discharge processes [34]. Electrochemical treatments increase the capacitance of CNTs up to 56 Fg^{-1} in 6 MKOH aqueous solution [35], and heat treated modified CNTs present a specific capacitance as high as 80 F g^{-1} in an electrolytic solution of 1 M H_2SO_4 [36]. In comparison to these studies, the present work has the advantage of using a relatively fast treatment, and an environmentally friendlier and safer electrolyte such as 0.1 M Na_2SO_4 aqueous solution. A high specific capacitance of 955 Fg^{-1}

was obtained at a scan rate of 10 mVs^{-1} for a NPCNTs/MnO_2 (75 W, 10 Pa) nanocomposite.

6.5. References

[1] Li W, Chen D, Li Z, Shi Y, Wan Y, Huang J, Yang J, Zhao D, Jiang Z, *Nitrogen enriched mesoporous carbon spheres obtained by facile method and its application for electrochemical capacitor*, (2007), Electrochem Commun, 9, 569-573.

[2] Conway B. E, *Electrochemical supercapacitors*. (1999), Kluwer Academic/Plenum publishers, New York, USA.

[3] Hulicova-Jurcakova D, Seredych M, Lu G Q, Bandosz T J, *Combined effect of nitrogen and oxygen containing functional groups of micropous activated carbon on its electrical performance for supercapacitors*, (2009), Adv Funct Mater, 19, 438–447.

[4] Li L, Liu E, Shen H, Yang Y, Huang Z, Xiang X, Tian Y, *Charge storage performance of doped carbons prepared from polyaniline for supercapacitors*, (2011), J Solid State Chem, 15, 175-182.

[5] Falten A, Bittencourt C, Pireaux J J, Van Lier G, Charlier J C, *Radio frequency plasma functionalization of carbon nanotubes surface O_2, NH_3 and CF_4 treatements*, (2005), J Appl Phys, 98,074308.

[6] Khare B, Wilhite P, Tran B, Teixeira E, Frequez K, Mvondo D. N, Bauschlicher C, Meyyappan M, *Functionalization of carbon nanotubes via nitrogen glow discharge*, **(**2005), J Phys Chem B, 109, 23466-23472.

[7] Ruelle B, Felten A, Ghijsen J, Drube W, Johnson R. L, Liang D, Erni Tendeloo R. V, Peeterbroeck S, Dubois P, Godfroid T, Hecq M, Bittencourt C, *Functionalization of carbon nanotubes with atomic nitrogen*, (2009), Micron, 40,85–88.

[8] Kim J-I, Park S-J, *Effect of nitrogen containing groups on enhanced capacitive behaviors of multiwalled carbon nanotubes*, (2011), J Solid State Electrochem, 184, 2184-2189.

[9] Wang B B, Cheng Q J, Chen X, Ostrikov K, *Enhancement of electron field emission of vertically aligned carbon nanotubes by nitrogen plasma treatment*, (2011), Journal of Alloys and Compounds, 509, 9329– 9334.

[10] Papakonstantinou P, Lemoine P, *Influence of nitrogen on the structure and nanomechanical properties of pulsed laser deposited tetrahedral amorphous carbon*, (2001), J Phys - Condens Mater, 13, 2971–2987.

[11] Evans J F, Kuwana T, *Introduction of functional groups on carbon electrodes via treatment with radio-frequency plasmas*, (1979), Anal Chem, 51, 358-365.

[12] Naito K, Tachikawa T, Fujitsuka M, Majima J, *Single molecule fluorescence imaging of the remote TiO_2 photocatalytic oxidation*, **(**2005), J Phys Chem B, 109, 23138-23140.
[13] Droppa Jr. R, Hammer P, Carvalho A. C. M, Dos Santos M. C, Alvarez F, *Incorporation of nitrogen in carbon nanotubes*, (2002), J Non-Cryst Solids, 299–302, 874–879.
[14] Maldonado S, Morin S, Stevenson K J, *Structure, composition, and chemical reactivity of carbon nanotubes by selective nitrogen doping*, (2006), Carbon, 44, 1429–1437.
[15] Shen W, Li Z, Liu Y, S*urface chemical functional groups modification of porous carbon*, (2008), Recent Patents Chem Eng 1, 27-40.
[16] Jones C, Sammann E, *The effect of low power plasmas on carbon fiber surfaces*, (1990), Carbon, 28, 4, 509-514.
[17] Pels J R, Kapteijn F, Moulijn J A, Zhu Q, Thomas K M, *Evolution of nitrogen functionalities of carbonaceous materials during pyrolysis*, **(**1995), Carbon, 33, 1641-1653.
[18] Wang H, Cote R, Faubert G, Guay D, Dodelet J P, *Effect of the pre-treatment of carbon black supports on the activity of Fe-based electrocatalysts for the reduction of oxygen*, (1999), J Phys Chem B, 103, 2042-2049.
[19] Toth A, Voitko K. V, Bakalinska O, Prykhodko G P, Bertoti I, Martínez-Alonso A, Tascon J M D, Gunko V M, Laszlo K, *Morphology and adsorption properties of chemically modified MWCNT probed by nitrogen, n-propane and water vapor*, **(**2012), Carbon, 50, 577-585.
[20] Bhattacharyya S, Hong J, Turban G, *Determination of the structure of amorphous nitrogenated carbon films by combined Raman and x-ray photoemission spectroscopy*, (1998), J Appl Phys, 83, 3917-3919.
[21] Biniak S, Szymanski G, Siedlewski J, Swiatkowski A, *The characterization of activated carbons with oxygen and nitrogen surface groups*, (1997), Carbon, 35, 1799-1810.
[22] Angoni K, *Remarks on the structure of carbon materials on the basis of Raman spectra*, (1993), Carbon, 31, 537–47.
[23] Cuesta A, Dhamelincourt P, Laureyns J, Martinez-Alonso A, Tascon J M D, *Raman microprobe studies of carbon materials*. (1994)**,** Carbon, 32, 1523-1532.

[24] Liu H, Zhang Y, Li R, Sun X, Désilets S, Abou-Rachid H, Jaidann M, Lussier L-S, *Structural and morphological control of aligned nitrogendoped carbon nanotubes*, (2010), Carbon, 48, 1498-1507.
[25] Reich S, Thomsen C, Maultzsch J, *Carbon nanotubes-basic concepts and physical properties*, (2004), J Chem Phys Chem, 5, 1913-1915.
[26] Antunes E F, Lobo A O, Corat E J, Trava-Airoldi V J, *Influence of diameter in the Raman spectra of aligned multi-walled carbon nanotubes*, (2007), Carbon, 45, 913–921.
[27] Ye J S, Cui H F, Liu X, Lim T M, Zhang W D and Sheu F S, *Preparation and characterization of aligned carbon nanotube-Ruthenium Oxide Nanocomposites for supercapacitors*, (2005), Small, 5, 560-565.
[28] Yao Y, Shiu K-K, *Electron-transfer properties of different carbon nanotube materials, and their use in glucose biosensors*, (2007), Anal Bioanal Chem, 387, 303–309.
[29] Liao L, Pan C, *Enhanced electrochemical capacitance of nitrogen-doped carbon nanotubes synthesized from amine flames*, (2011), Soft Nanosci Lett, 1, 16-23.
[30] Hulicova D, Yamashita J, Soneda Y, Hatori H, Kodama M, *Supercapacitors prepared from melamine-based carbon*, (2005), Chem Mater B, 17, 1241-1247.
[31] Hulicova-Jurcakova D, Seredych M, Lu G Q, Bandosz T J, *Combined effect of nitrogen and oxygen containing functional groups of micropous activated carbon on its electrical performance for supercapacitors*, (2009), Adv Funct Mater, 19, 438–447.
[32] Hulicova-Jurcakova D, Kodama M, Shiraishi S, Hatori H, Zhu Z. H, Lu G Q, *Nitrogen-enriched nonporous carbon electrodes with extraordinary supercapacitance*, **(**2009), Adv Funct Mater, 19, 1800–1809.
[33] Yan J.; Fan Z.; Wei T.; Cheng J.; Shao B.; Wang K.; Song L.; Zhang M. *J. Carbon nanotube/MnO_2 composites synthesized by microwave-assisted method for supercapacitors with high power and energy densities*, (2009), Journal *Power Sources*, *194*, 1202-1207.
[34] Frackowiak E, Metenier K, Bertagne V, Beguin F, *Supercapacitor electrodes from multiwalled carbon nanotubes*, (2000), Appl Phys Lett, 77, 2421-2423.

[35] Liu C G, Fang H T, Feng L, Min L, Cheng H M, *Single-walled carbon nanotubes modified by electrochemical treatment for application in electrochemical capacitors*, (2006), J Power Sources, 160, 758-761.
[36] Frackowiak E, Jurewicz K, Delpeux S, Beguin F, *Nanotubular materials for supercapacitors*, (2001), J Power Sources, 97-98, 822-825.

Chapter 7
Study of CNTs structural evolution during water assisted growth and transfer methodology for electrochemical applications

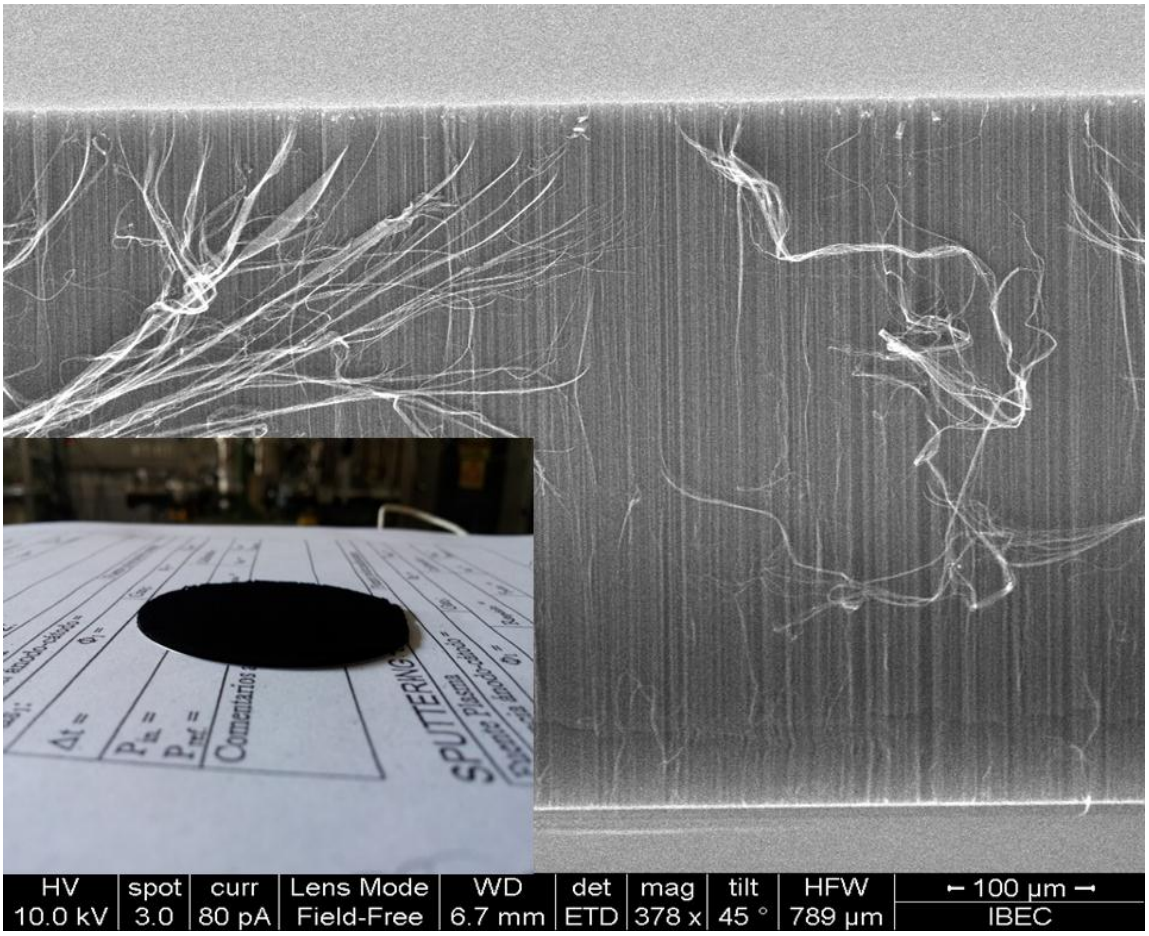

Figure 7: Image and photograph of ultralong CNTs on silicon wafer.

Chapter 7- Study of CNTs structural evolution during water assisted growth and transfer methodology for electrochemical applications

7.1. Introduction

The synthesis of ultra-long carbon nanotubes by Hata et al. [1] in millimeter scale, disclosed the possible usage of this novel material in macro scale applications such as electrical wires [2-3]. Usually, during the growth process, a thin catalyst layer (Fe, Co, Ni etc.) is deposited on the substrate and, upon heating at a higher temperature in a reducing atmosphere, granulates into nanoparticles. Each nanosized particle serves as a seed for the growth of CNTs by decomposing the carbon source gas at high temperature [4].

T. de los Arcos, et al have shown that upon heating at 850 Fe thin films on silicon wafer, iron react chemically with Silicon and converts into iron silicide (FeSi) whose catalytic efficiency is lower than pure Fe. Thus the use of a buffer layer between catalyst and Si wafer can increase the efficiency of the catalyst support layer and decrease the chemical activity between catalyst and substrate [5]. Oxide support layer underneath the catalyst thin film plays a critical role in the synthesis of CNTs. Al_2O_3 support layer have several benefits over SiO_2 layer. In general, the CNT yield for the SiO_2-supported Fe catalyst is much lower than for Fe supported on Al_2O_3. Upon annealing Fe makes oxides with the surface oxygen atoms of Al_2O_3 support. The Al_2O_3 support tends to stabilize interfacial Fe oxidation states, and prevents excessive coalescence of Fe particles. On the other hand, on SiO_2, Fe coalesces into larger islands. The reason behind this is Fe de-wets SiO_2 so that some areas become completely Fe-depleted. The resulting Fe nanoislands coarsen by cluster migration or Ostwald ripening. The coalescence is driven by a minimization of the surface free energies and the free energy of the support-metal interface [6]. Catalyst oxidation state plays an important key role in the growth process of CNTs. Eti Teblum et al. Showed that catalyst activity increased by the following order: FeO < Fe2O3 < Fe3O4 < Metallic Fe. The catalyst is active in metallic state [7].

Several studies have demonstrated the possibility to grow ultra-long forests of single-walled CNTs (SWCNTs) and multiwall CNTs

(MWCNTs) (up to several millimeters in length) by means of water-assisted chemical vapor deposition (WACVD), oxygen-assisted microwave plasma chemical vapor deposition techniques and CO_2 assisted floating-ferrocene [8, 9-11]. A small content of an oxidizer such as H_2O, O_2 and CO_2 can significantly enhance the nanotubes growth rate. The role of water is to constrain the catalyst ripening by producing large amounts of OH groups on carbon, keep catalyst particles clean from amorphous carbon and active for continuous growth [12].

$$C(s) + H_2\,O(g) \rightarrow CO(g) + H_2(g)$$

On the other hand, oxygen significantly enhances the growth rate and crystallinity of CNTs, and CO_2 is more effective in removing carbonaceous impurities as well as etching the walls of CNTs [8, 9-11]. Higher CO_2 concentrations prevent Ostwald ripening of the catalyst particles and etch the CNTs caps and walls during the growth process [11]. The properties of the CNTs depend on their geometrical characteristics such as chirality, diameter, length and existence of surface functional groups. MWCNTs consist of concentric shells of SWCNTs, each of which can have a different structure. If present, these variant structures can influence the electrical, mechanical and thermal properties of MWCNTs. In general, the diameter and number of planes of the CNTs depend on the thickness of the catalyst film. Thicker films provide larger diameters and more planes, while thinner films smaller diameters and less walls. CNTs inherent properties such as electrical, optical and light emission properties are more dominant with decreasing nanotube diameter [13]. Wide diameter SWCNTs present a metallic nature, while smaller diameter SWCNTs behave as semiconductors [14]. Thus, in order to obtain CNTs with tailored properties, a precise control of geometry and number of walls is required.

Usually, a silicon wafer is used as substrate for the growth of CNTs. The semiconducting nature of silicon and the low adhesion of CNTs to the substrate raise questions about its use as current collector in supercapacitor applications. Several methods have been adopted to transfer CNTs on conducting substrates [15-17]. Pint et al. transferred aligned SWNT to flat Cu substrates by utilizing a thin Ti/Au layer deposited on both Cu substrate and SWNT array, and then sintering these layers together under Ar at 700–750°C [16]. Honda et al. used Al current collector coated with electrically

conductive cement (phenolic glue) for the transfer of CNTs for supercapacitor applications [16]. Zhang et al. used hydrofluoric acid to peel off the CNTs from the silicon substrate and transferred them on a conductive substrate with the help of a polymer. Finally, the new substrate was heated above more than 190°C [17].

This chapter is related to the synthesis of highly dense forest of vertically aligned ultra-long CNTs with the assistance of pure water (i.e., without the addition of Ar or He as gas carriers). We observed that elongated growth time not only increases the length of CNTs but also modifies the CNTs structure. During a first growth stage the CNTs crystallinity enhances due to the removal of amorphous carbon and, in a second stage, etching of outer walls of CNTs takes place. Thus, a structural evolution from large diameter MWCNTs to SWCNTs occurs by peeling off the outer layers of MWCNTs, which can be regarded as a novel route to attain large diameter SWCNTs. Furthermore, in comparison to the aforementioned techniques, the obtained ultra-long CNTs were transferred to a conductive adhesive aluminum tape using an easy and fast methodology. Subsequently, the transferred CNTs were functionalized using a water plasma treatment that introduces defects on the side walls and oxygen functional groups [18, 19]. The electrochemical properties of the transferred CNTs on the conductive adhesive aluminum tape before and after the water plasma treatment were analyzed using cyclic voltammetry and impedance spectroscopy.

7.2. Experimental section

7.2.1. Growth process

Ultra long CNTs were grown by water assisted CVD on silicon wafer (2´´ p-type boron doped, 0.01–0.02 Ω cm range). First, a 10 nm buffer layer of alumina was deposited by magnetron sputtering. Prior to the deposition, the PEDRO reactor was purged down to a pressure of $4 \cdot 10^{-4}$ Pa and the aluminum target sputtered during 10 minutes in 20 sccm of argon to remove its thin oxide layer. Afterwards, the target was sputtered with a mixture of Ar/O_2 (17 and 3 sccm, respectively) during 100 s at a pressure of 1 Pa and 120 W of plasma power to render a 10 nm layer of alumina. Next, samples were introduced in a CVD/PECVD homemade reactor described elsewhere (chapter 2). Once the base pressure inside the reactor

was $4 \cdot 10^{-4}$ Pa, 128 sccm of Ar were introduced and a 2 nm thick layer of Fe catalyst was sputtered on the alumina deposited substrate under a pressure of 2 Pa. Then, without breaking the vacuum to avoid oxidation of the catalyst, the sample was placed under a heating element inside the reactor in order to anneal the catalyst layer and grow the CNTs. The heating element consists of a graphite resistance (2 Ω) placed above the substrate and connected to a DC power supply. The temperature on the top surface of the sample was monitored using an external optical pyrometer, and controlled with a feedback loop with the DC power supply using a proportional-integrative-derivative (PID) controller. The whole process was controlled by LabVIEW software. Annealing of catalyst thin film was done at temperatures up to 600°C with a ramp time of 750 s in a reducing atmosphere of hydrogen (100 sccm) at a pressure of 2 mbar. After a hold time of 120 s the pressure inside the reactor was lowered down to 1 mbar and C_2H_2 was introduced in the chamber (100 sccm). Then, the temperature was rapidly increased during the next 10 s up to 700°C. The water flask outlet was opened ~ 15 s after the introduction of C_2H_2. The calculated water flow was 0.04 sccm, controlled by opening ~ 0.5 mm the circular scale of a metering valve. Three samples of CNTs were grown with different growth times; sample A: 5 min, B: 30 min and C: 1h. One of the samples was transferred on adhesive aluminum tape and functionalized with water plasma.

7.2.2. Transfer of CNTs on aluminum tape

First, we sputtered ~50 nm thin nickel layer on the top of the CNTs surface using magnetron sputtering. Nickel was chosen due to its strong cohesion and affinity to the CNTs [17]. Transfer of CNTs/Ni on the aluminum tape was performed in two ways; with and without annealing under vacuum. Top surface of Si/CNTs/Ni was placed on adhesive Al tape, slightly pressed and peeled off the silicon substrate. Without the annealing process the CNTs/Ni sample transfer was not so good and empty spaces could be easily seen with naked eyes on the aluminum tape (figure 7.1. a(A)) . Homogeneous transfer of the whole sample was obtained after the annealing process (400ºC, 300 s ramp time and 3600 s hold time) under vacuum (4.10^{-4} Pa). After 3600 s heating, the sample was let to cool down under vacuum. Then, transfer on the aluminum tape was perfectly homogeneous due to the formation of nickel nanoclusters on the aligned

nanotube tips that presumably increase the adhesion between CNTs and the adhesive Al tape (figure 7.1.a (B)) [17]. Aluminum transferred CNTs (CNTs/Al) were further treated with a water plasma to increase the structural disorder and hydrophilicity. The water plasma conditions were 75 W radio frequecy power and 135 Pa water pressure [18]. (Figure 7.1 (b)) is a sequence of photographs (A) Ni sputter on the top surface of the CNTs/Si and annealed under vacuum, (B) shows the adhesive side of the aluminum tape is attached to the top surface of annealed Ni/CNTs/Si, (C) demonstrate the complete transfer of the CNTs on the adhesive conductive tape and Si wafer clearly can be seen without CNTs, (D) sample was prepared for the water plasma treatment as with the arrow sign is indicated this side was not covered from top with aluminum tape. After the plasma treatment most of sample was seperated from the tape because plasma effectively removed the adhesive by interacting from this side. In next experiment figure (D) all sides of the sample were covered as shown in with a aluminum tape. As a result we did not observed deatchement of the nanotubes from the aluminum tape.

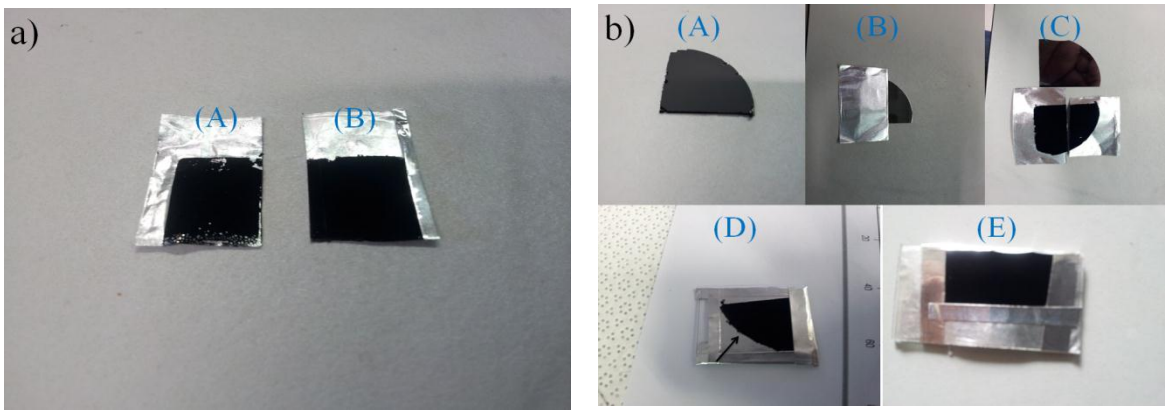

Figure 7.1: Transfer procedure of WA-CNTs from Si wafer to the sided adhesive conductive Aluminum tape and preparation of the transferred CNTs for the plasma treatment.

7.3. Results and discussion

7.3.1. Optimization of reactive sputtering of Alumina

The Al_2O_3 layer was used as a barrier to inhibit Fe-silicide formation and the agglomeration of Fe particles. For a successful growth of CNTs a

homogeneous distribution of catalyst particles on the substrate is essential. A thin layer at high temperatures such as the ones used for the annealing of the catalyst, diffusion towards the substrate happens. In order to minimize this effect a buffer layer of ten nanometers of alumina were first sputtered onto the substrate. Details about the reactor are explained in a chapter 2. Prior to the deposition, the reactor was purged down to a pressure of $4 \cdot 10^{-4}$ Pa and the aluminum target sputtered during 10 minutes in 20 sccm of argon to remove its thin oxide layer. Pulsed DC magnetron sputtering was used to deposit alumina. The power was 120 W, frequency 100 kHz, and frequency width 2016 ns. For the gas mixture used to sputter the aluminium target, three different ratios of oxygen/argon were tried. The total pressure was 1Pa and the different flow ratios were 2/18 sccm, 3/17 sccm and 4/16 sccm oxygen/argon respectively. In the first experiment aluminium was partially formed whereas in the latter case no alumina was deposited. The intermediate mixture provided a quite homogeneous layer and completely transparent.

7.3.2. Morphological characterization

Ultra long CNTs were grown by water assisted CVD on silicon wafer (2´´ p-type boron doped, 0.01–0.02 Ω cm range). First, a 10 nm buffer layer of alumina was deposited by pulsed DC magnetron sputtering as explain above. Next, samples were introduced in a CVD/PECVD. Optimized of the Fe layer thickness and annealing time of the catalyst layer prior to introduce the carbon sources was performed as follow. Fe 2 nm and 3 nm layers were sputter by RF magnetron sputtering when the base pressure inside the reactor lower down to $4 \cdot 10^{-4}$ Pa. Ar was used at flow rate of 128 sccm at a pressure of 2 pa and rf power was 50 W. Bias voltage induced in the process was -99 V. (Figure 7.2) shows SEM images of the particles formed after annealing using 4 different conditions.

(a) Fe 3 nm layer, 600 C, ramp time 750 s
(b) Fe 3 nm layer, 600 C, ramp time 300 s
(c) Fe 3 nm layer, 680 C, ramp time 750 s
(d) Fe 2 nm layer, 600 C, ramp time 750 s

As can be readily seen, (figure 7.2 (d)) shows a higher density and homogeneity of particles with a lower number of bigger ones that are

product of coalescence. Therefore, these conditions were used in the growth of the CNTs. The average diameter of the particles was calculated using the program ImageJ and the result was a mean particle diameter of 33.5 nm with a dispersion of 1.34 nm.

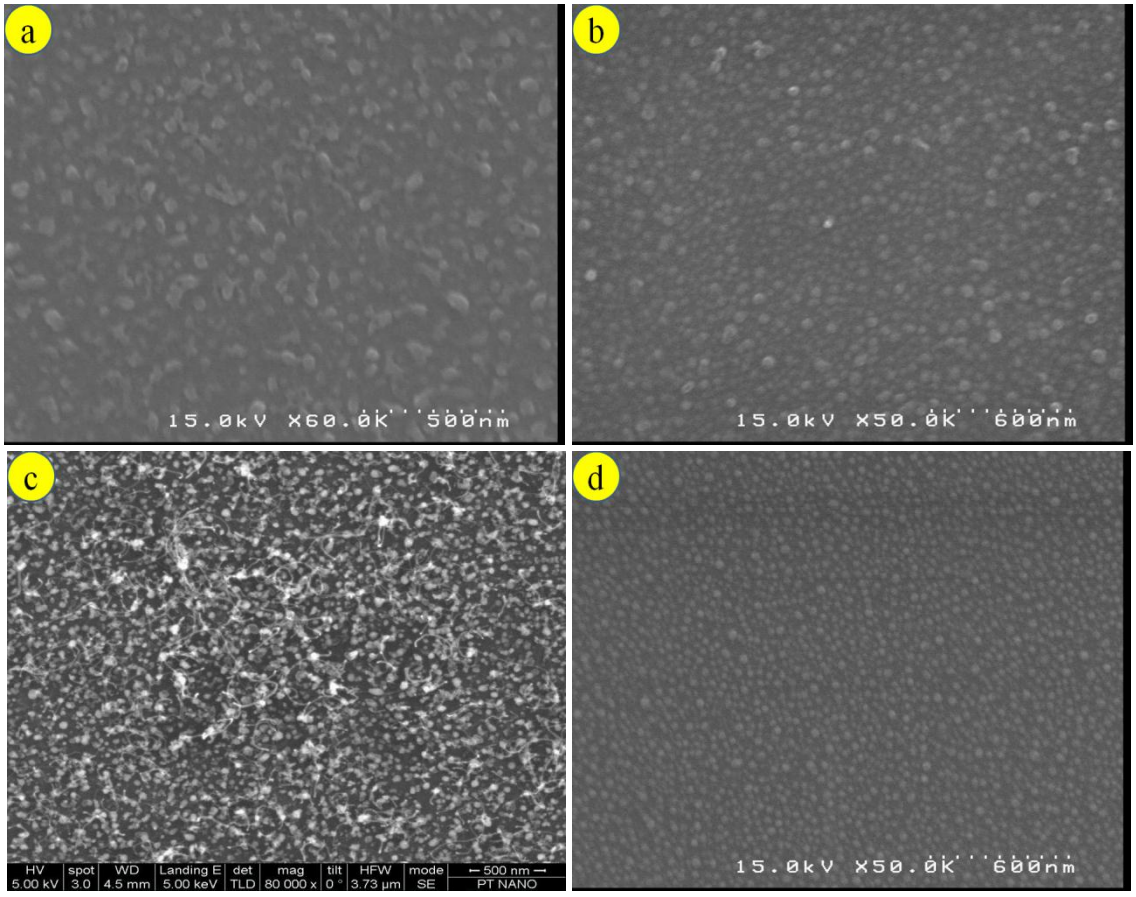

Figure 7.2: SEM images of different thickness catalyst layers annealed at different temperatures.

The effect of growth time on the morphology of CNTs was examined by SEM (Figure 7.3) and HRTEM (Figure 7.4). CNTs are highly dense, and vertically aligned on the whole silicon wafer. CNTs which are aligned by crowding effects alone tend to exhibit a greater degree of random orientation and entanglement in the tip region as compared to other areas of forest. The entangled "canopy" of a CNT forest can be removed with additional processing after growth, e.g., plasma etching, to create more alignment [20]. In our case no further treatment required to remove the "canopy" (see figure 7.3 (b,d,f)).The obtained length of samples A, B and C were ~ 75, 630 and 800 µm, respectively. Initially, the growth rate was

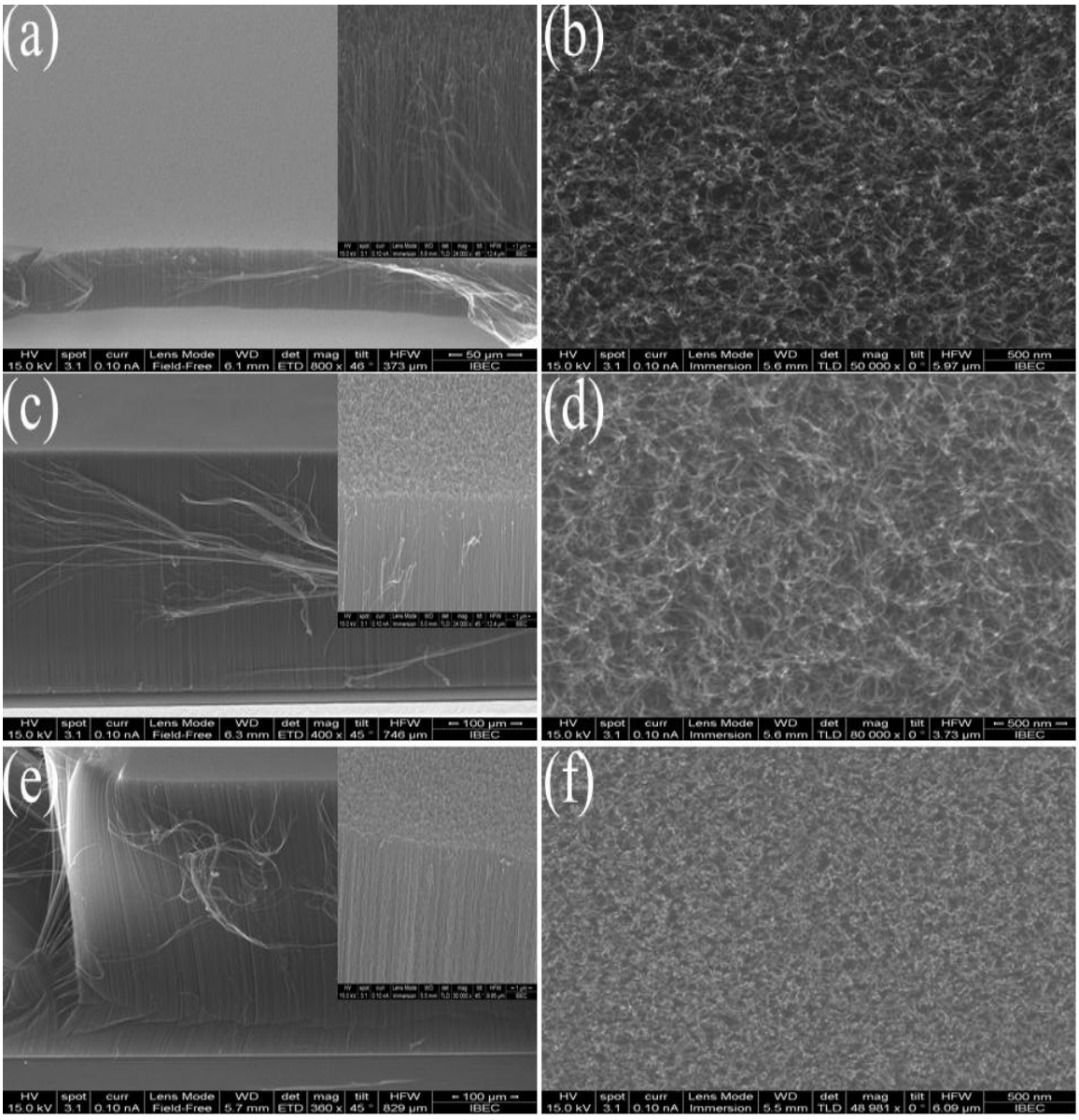

Figure 7.3: SEM images of samples A (a, b), B (c, d) and C (e,f). Side (a, c, d) and top (b, d, e) views.

slow because we introduced water vapor in the reaction chamber about 15 s after the start of the CVD process, to avoid oxidation of Fe catalyst nanoparticles. The growth rate was ~ 15 μm/min for sample A and ~ 21μm/min for sample B. We suppose that in a first stage the growth rate is slow because small amounts of amorphous carbon are deposited during the first 15 s, as confirmed by Raman analysis of sample A. Immediately after the introduction of water vapor, amorphous carbon starts to be etched from the surface of CNTs and the growth rate increases considerably. For prolonged growth times (from 30 min to 1 h) the growth rate becomes slow

(sample C) because of the evolution of the iron catalysts particles from cementite to Hägg carbide as stated by Wang et al. [21].

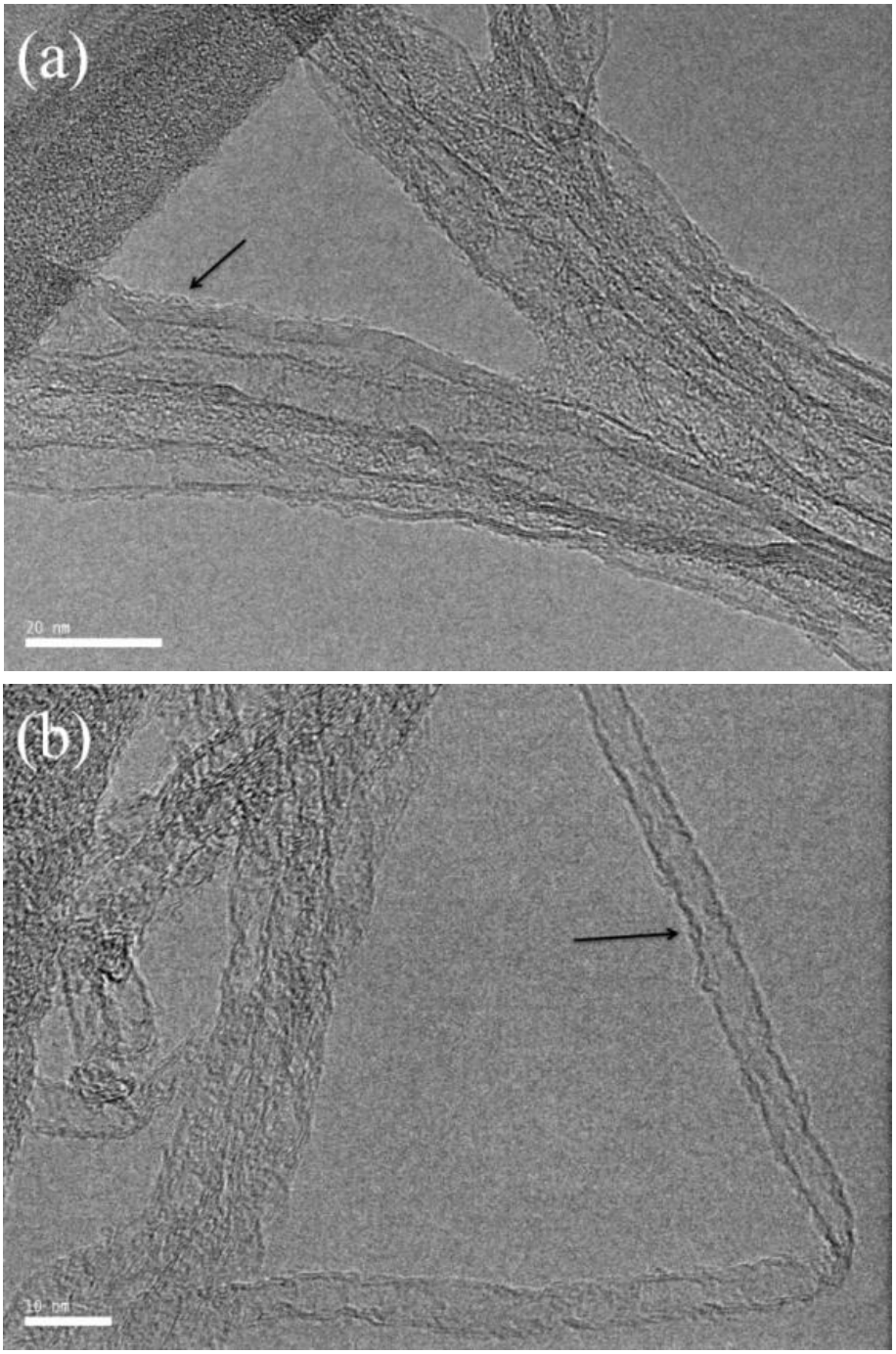

Figure 7.4: TEM images of sample A (a) and C (b). Arrow signs indicate amorphous carbon and structural defects for sample A and C, respectively.

Furthermore, Ostwald ripening also has an impact during the growth, in which shrinking and disappearing of the smaller catalyst particles takes

place. In addition, each stopping nanotube exerts a drag force on growing nanotubes due to Van der Waals forces, resulting in the slowing down of the growth rate [22]. During these processes, etching of the CNTs side walls also occurs because of the presence of excess water vapor that etches the walls of nanotubes at around 650°C [23]. Top surfaces of samples A and B present separated "spaghetti"-like structure, and the CNTs tips are well distinguishable. However, in the case of sample C, the CNTs tips have started to agglomerate together, parallel and well oriented to the substrate (Figure 7.3 (b, d, f)). HRTEM images (Figure 7.4 (a, b)) show nanotubes with more than 5 planes for sample A and mostly double-walled CNTs with a small fraction of SWCNTs and triple-walled CNTs for sample C. Presence of amorphous carbon and etched outer planes for sample A and C, respectively, are indicated by arrow signs in Figure (7.4a) and (7.4b). The etching of the outer planes of CNTs was also observed by Liu et al. when using wet argon [24].

7.3.3. Raman characterization

Radial breathing mode (RBM) is a unique Raman active mode, which usually appears for SWCNTs and even for double-wall CNTs when their inner tube diameters are in the range of 0.74-3.09 nm, in the frequency range 100-350 cm^{-1} [25]. The tangential stretching mode appears in the range 1500-1600 cm^{-1} (G band), and the position close to ~ 1580 cm^{-1} corresponds to E_{2g} symmetric first order vibrational mode in graphite-like carbon materials [26]. For small diameter nanotubes G band splits into G^+ and G^- which are related to atomic displacements along the tube axis and along the circumferential direction, respectively [27]. D band (1330-1360 cm^{-1}) is the A_{1g} double resonance Raman mode and is related to the presence of amorphous carbon, in-plane substitutional heteroatoms, vacancies, and grain boundaries [28]. In the second order Raman spectra G´ (~ 2700 cm^{-1}) is the overtone of D mode, but it does not need the presence of defects to appear since it is sensitive to the strain [29, 30].

Increasing the growth time up to 3600 s (sample C), RBM appears and the D, G and G´ peaks become broader (see Figure 7.5). The distinct appearance of RBM for sample C demonstrates that the outer layers of CNTs are being consumed during continuous growth, which leads to the formation of SWCNTs and double wall CNTs. TEM images (Figure 7.4) prove that there are very small number of walls (two and three), and

therefore, the appearance of RBM is possible [25]. The decrease in the intensity of the G´ peak for sample C indicates a reduction in the mass fraction of CNTs due to etching effects on the side walls, and increase in the disorder. In second order Raman spectra the intensity must decrease with increasing number of impurities, which is apparent in the Raman spectra of (figure 7.5) [36].

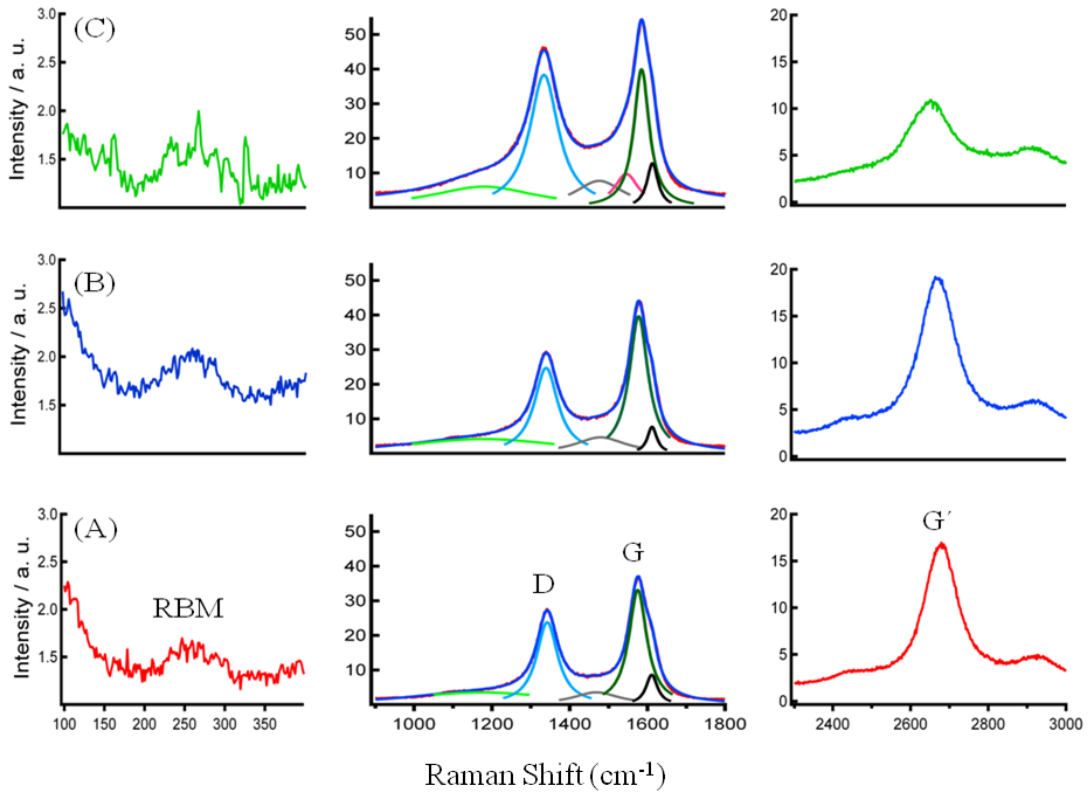

Figure 7.5: Raman spectra of samples A, B and C in three different frequency regions. Graphs in the middle column show the peaks obtained from the fitting process.

The peak fitting process required some other bands to obtain a suitable adjustment; I band (~ 1200 cm^{-1}) related to impurities in the graphite lattice [31], D´´ band (~ 1470 cm^{-1}) related to staking or interstitial defects in the graphene layers [34] and D´ (~ 1610 cm^{-1}), which is a double resonance Raman feature induced by disorder, defects along the tube axis or ion intercalation between the graphitic walls [28]. Sample C shows one more peak around 1558 cm^{-1} wavelength assigned to G^{-}. The appearance of this band implies that the diameter of the CNTs decreases from large numbers of graphene walls to just a few walls or even single wall. Due to

the large diameter of MWCNTs, peak splitting is very narrow and smeared out [27]. The intensity of D´ first decreases from sample A to B possibly because of the removal of amorphous carbon with time. Then, it increases again for sample C achieving twice the intensity value of sample A due to etching of the side walls. Full width half maximum (FWHM) of D band was 1342.3, 1339.4 and 1334.4 for samples A, B and C, respectively. The decrease in the FWHM evidences the peeling of the outer layers with time, and proves the decrease in diameter of the CNTs. D´´ band intensity also increases with increasing growth time suggesting that the turbostratic effect takes place in the adjacent layers of CNTs [33]. Furthermore, the increase in the intensity and area of D´´ peak with growth time agrees with the decrease in the number of planes [34].

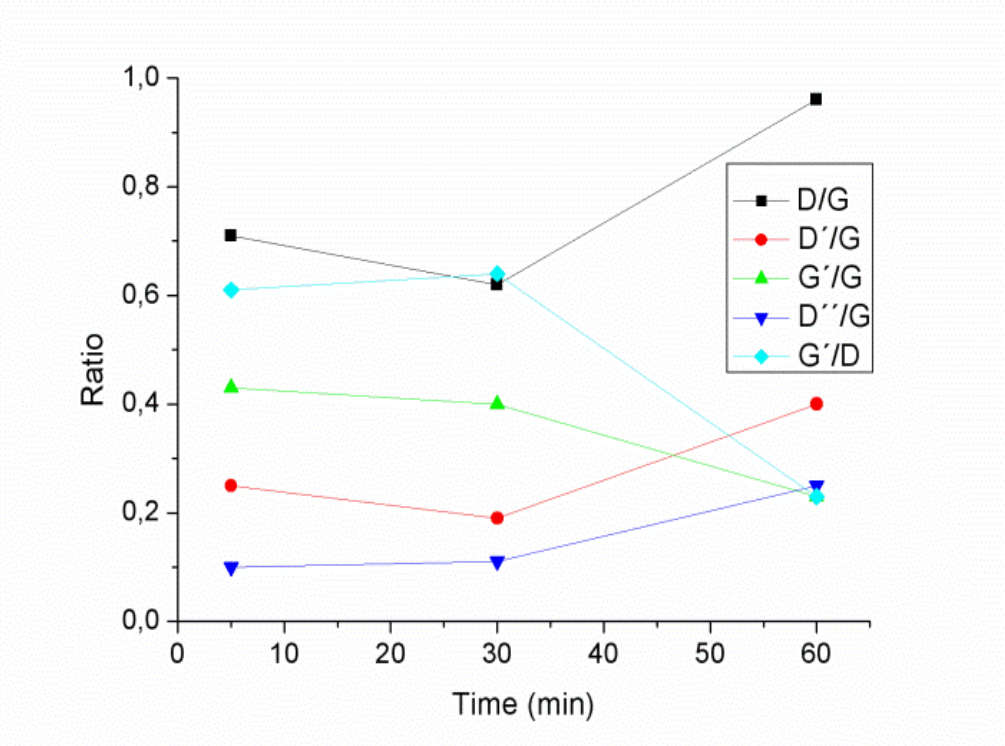

Figure 7.6: Comparison of various Raman intensities properties.

Structural changes were further confirmed by analyzing several Raman ratios (i.e., I_D/I_G, $I_{D'}/I_G$, $I_{D''}/I_G$, $I_{G'}/I_D$ and $I_{G'}/I_G$) (Figure 7.6). I_D/I_G and $I_{D'}/I_G$ ratios provide information about structural defects and impurities. The I_D/I_G decreases from 0.71 to 0.62 for sample A to sample B, respectively, and corresponds to less amount of amorphous carbon in sample B. For sample C the ratio increased up to 0.95 and indicates a large

number of structural defects. Similar trend is observed for $I_{D'}/I_G$ ratio. Change in the diameter with time can be evaluated using the $I_{G'}/I_G$ ratio. The decrease in this ratio from 0.43 to 0.23 for sample A to C, respectively, is an evidence of the decrease in the number of CNTs walls with increasing growth time [29]. $I_{G'}/I_D$ first increases from 0.61 to 0.64 for sample A to B, and is an indication of the increased purity. However, it decreases down to 0.23 (sample C), and thus, presents almost two times more structural defects than sample B [32]. Additionally, the increase in the (FHWM) of G´ from sample A to C (A: 99.69, B:105.02, C:127.11) and downshift of G´ frequency from sample A to C agrees with the decrease in CNTs diameter with time [29, 35].

7.3.4. X-ray photoelectron spectroscopy (XPS) characterization

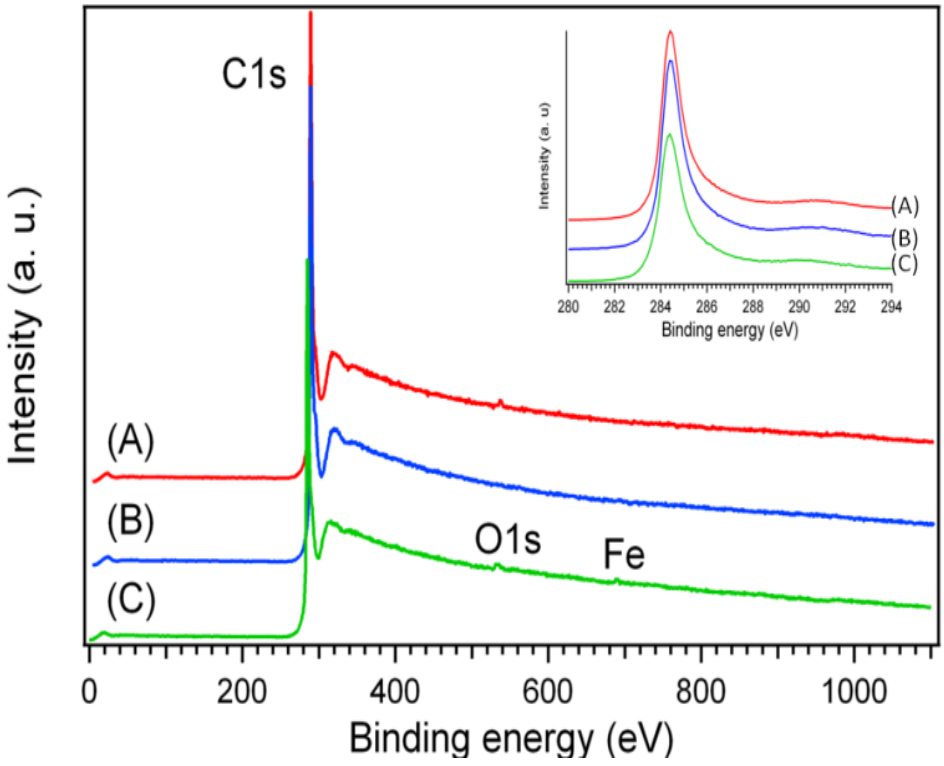

Figure 7.7: XPS survey scan of samples A, B and C. Inset shows high resolution spectra of C1s.

(Figure 7.7) shows XPS survey scans of the three samples. Appearance of Fe peak in sample C indicates the peeling of the top layers around the catalyst as well as the side walls. In addition, detection of this

peak suggests a tip growth mechanism of the CNTs. Samples show different C1s and O1s ratios; for sample A and C the O1s ratios are 0.76 and 0.89%, respectively, while for sample B O1s is 0%, which indicates that the surface of the sample does not present active edges or defect sites. Thus, sample B is cleaner and without reactive sites on the CNTs that would react with moisture from ambient air. In agreement with the aforementioned characterization results, sample C shows an increase in the O1s ratio that confirms enhancement of structural defects with elongated growth time. The C1s position does not change for samples A and B (284.33 eV), whereas for sample C there is a 0.04 eV up shift in the binding energy, and the calculated broadening of the C1s peak could be assigned to lattice disorder [33].

7.3.5. X-ray diffraction (XRD)

XRD pattern of samples A, B and C is shown in (Figure 7.8). The diffraction peaks at 24.9°, 42.4° and 77.6° can be assigned to hexagonal graphitic structure; (002), (100) and (110) planes, respectively [36]. The (002) peak presents an interlayer spacing of 3.4 Å in the different shells of CNTs, and (100) peak corresponds to the reflection of carbon atoms [37]. The peak at 68.9° corresponds to Si. For sample A the (002) peak is very broad, the intensity of the (100) peak is very small and the (110) peak does not appear, which implies that the CNTs are covered with amorphous carbon [36] (see TEM images). In the case of sample B the (002) and (110) peaks are clearly observed, and the relative intensities of all the peaks considerably increases with respect to sample A, which accounts for an improved crystallinity [36] of the CNTs as already proven by Raman spectroscopy. The distinguished appearance of (002) is due to the removal of amorphous carbon and misalignment of the nanotubes [38]. The (002) peak in sample C decreases again. It is assumed that, as explained above (morphological characterization, Figure 7.3), prolonged peeling of the outer planes of CNTs and Oswald ripening makes them align, and as a consequence the intensity of (002) peak decreases a lot [38].

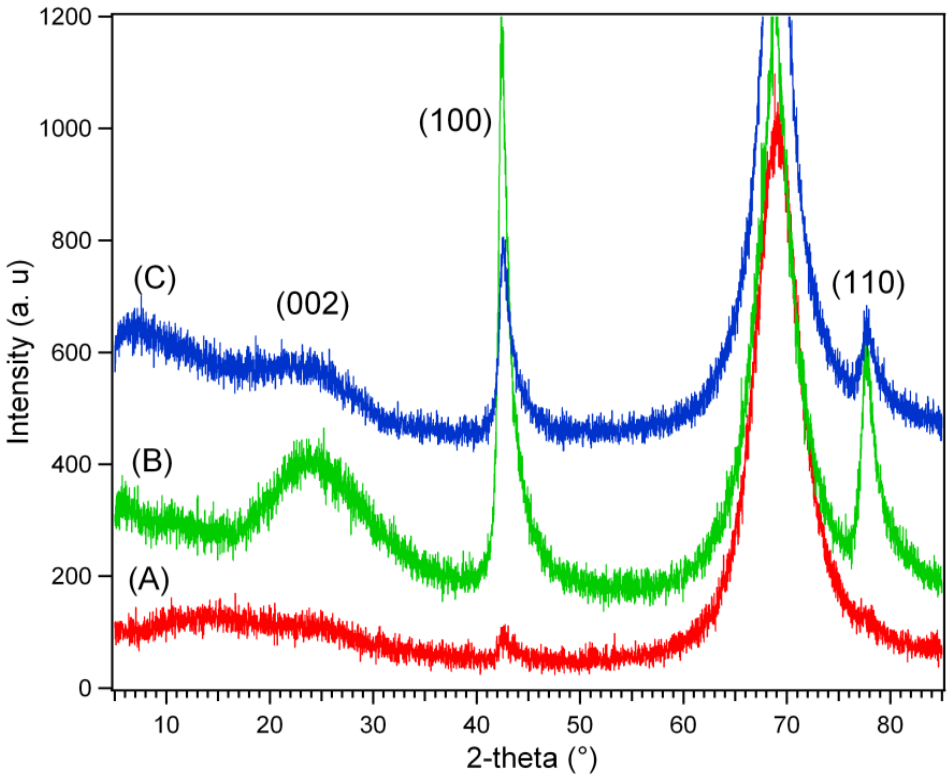

Figure 7.8: XRD spectra of samples A, B and C

7.3.6. Characterization of transferred CNTs

(Figure 7.9) demonstrates that after the transfer on the adhesive aluminum tape and with or without water plasma treatment, nanotubes are still vertically aligned and are completely and strongly attached to the adhesive tape without any exfoliation. The top surface of the transferred nanotubes is dense, curly and with large outer diameters (see inset of Figure 7.9 (a) and (b)). After the water plasma treatment (inset of Figure 7.9(b)) there are bright spots on the surface that correspond to charge accumulation on the defect sites of CNTs. Elements concentration was determined by energy dispersive x-ray spectroscopy (EDS) data. In the case of untreated CNTs carbon and oxygen concentration was 98.1% and 1.90%, respectively. After the plasma treatment, other peaks related to sulphur and nickel appeared in the EDS spectra, which are probably related to the adhesive tape and the sputtered layer of nickel. In this sample, the concentration of carbon, oxygen, sulphur and nickel was 96.56, 2.61, 0.11 and 0.72%, respectively.

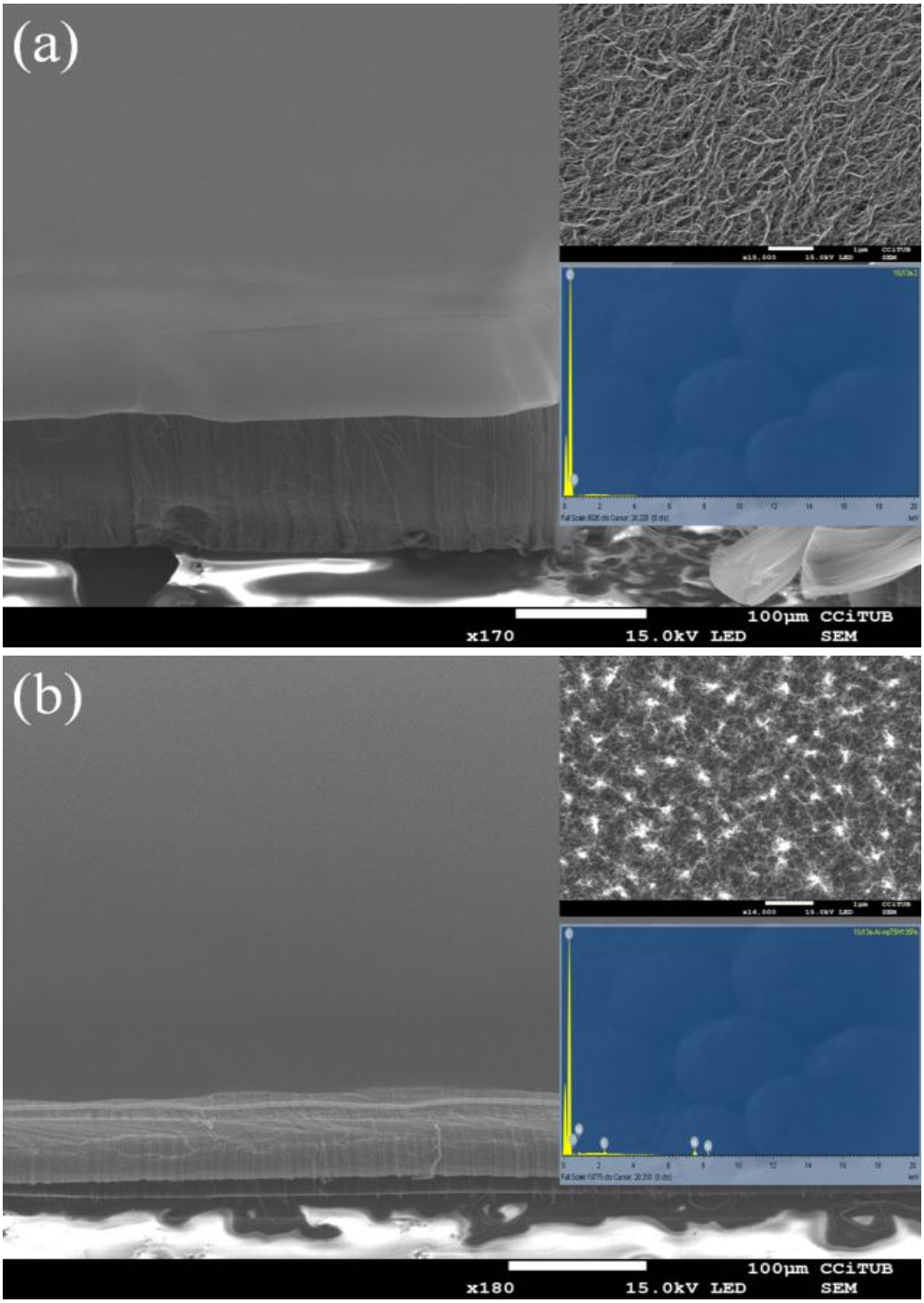

Figure 7.9: SEM images of transferred CNTs on the adhesive tape and EDS spectra of untreated and water plasma treated CNTs.

(Figure 7.10) shows Raman spectra of the CNTs transferred on adhesive aluminum tape (CNTs/Al) and water plasma treated CNTs/Al. I_D/I_G increases from 0.38 to 1.66 from untreated to water plasma treated CNTs/Al, and correspond to an increase in structural defects. FWHM of D

band decreases from 70.5 to 54 for untreated to water plasma treated CNTs, and suggests a decrease in the diameter of the CNTs due to plasma etching [40].

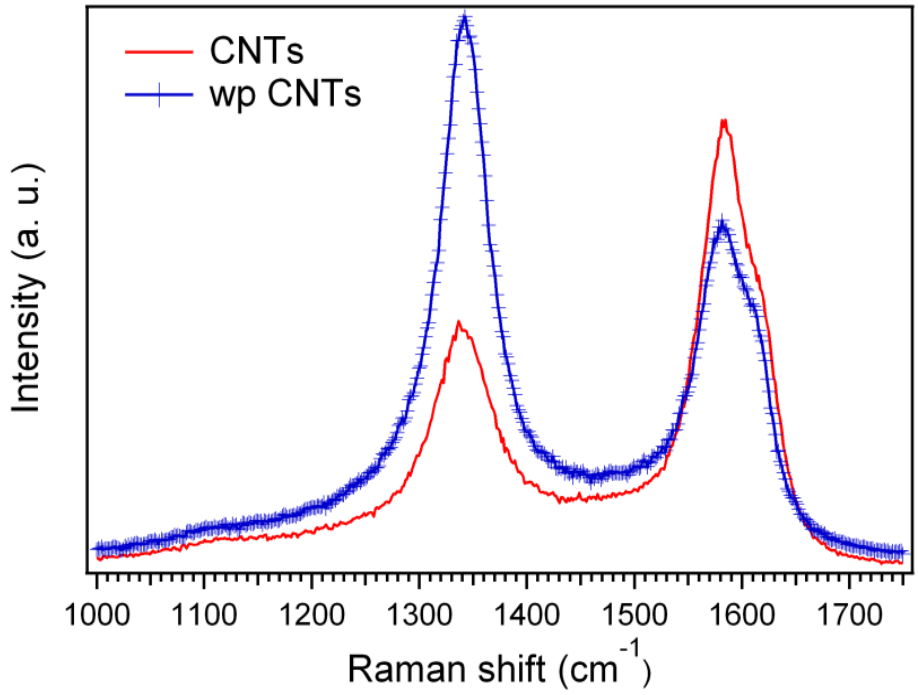

Figure 7.10: Raman spectra of transferred CNTs on Al tape and water plasma treated CNTs/Al.

7.3.7. Electrochemical Characterization of transferred CNTs

Electrochemical characterization was performed by using untreated CNTs/Al and water plasma (75 W, 135 Pa) treated CNTs/Al as the working electrode. Prior to the electrochemical measurements the working electrode was dipped in the electrolyte (1.0 M Na_2SO_4) for 24 h to improve the wetting of CNTs. Cyclic voltammetry was performed in the voltage range of 0-1 V. (Figure 7.11 (a)) shows a comparison between untreated and water plasma treated CNTs/Al cyclic voltammograms at a scan rate of 10 mVs^{-1}. The voltammogram of the untreated sample has a typical quasi-rectangular shape without redox peaks around 0.25 V, which accounts for a totally capacitive charge storage mechanism. Whereas the cyclic voltammogram of the water plasma treated sample displays deviation in shape and appearance of redox peaks, which is probably due to the contribution of pseudocapacitive effects [31, 40]. This pseudocapacitance is related to the introduction of oxygen surface functional groups as can be

seen from EDS measurements (figure 7.9) [39]. (Figure 7.11(b)) shows cyclic voltammograms of this sample at different scan rates. At higher scan rates the redox peaks vanish and correspond to mostly double layer capacitive behavior, which decrease with increasing scan rate. This decrease at higher scan rates is related to the voltage signals that are not reaching deep inside the pores of CNTs [41]. The specific capacitance of

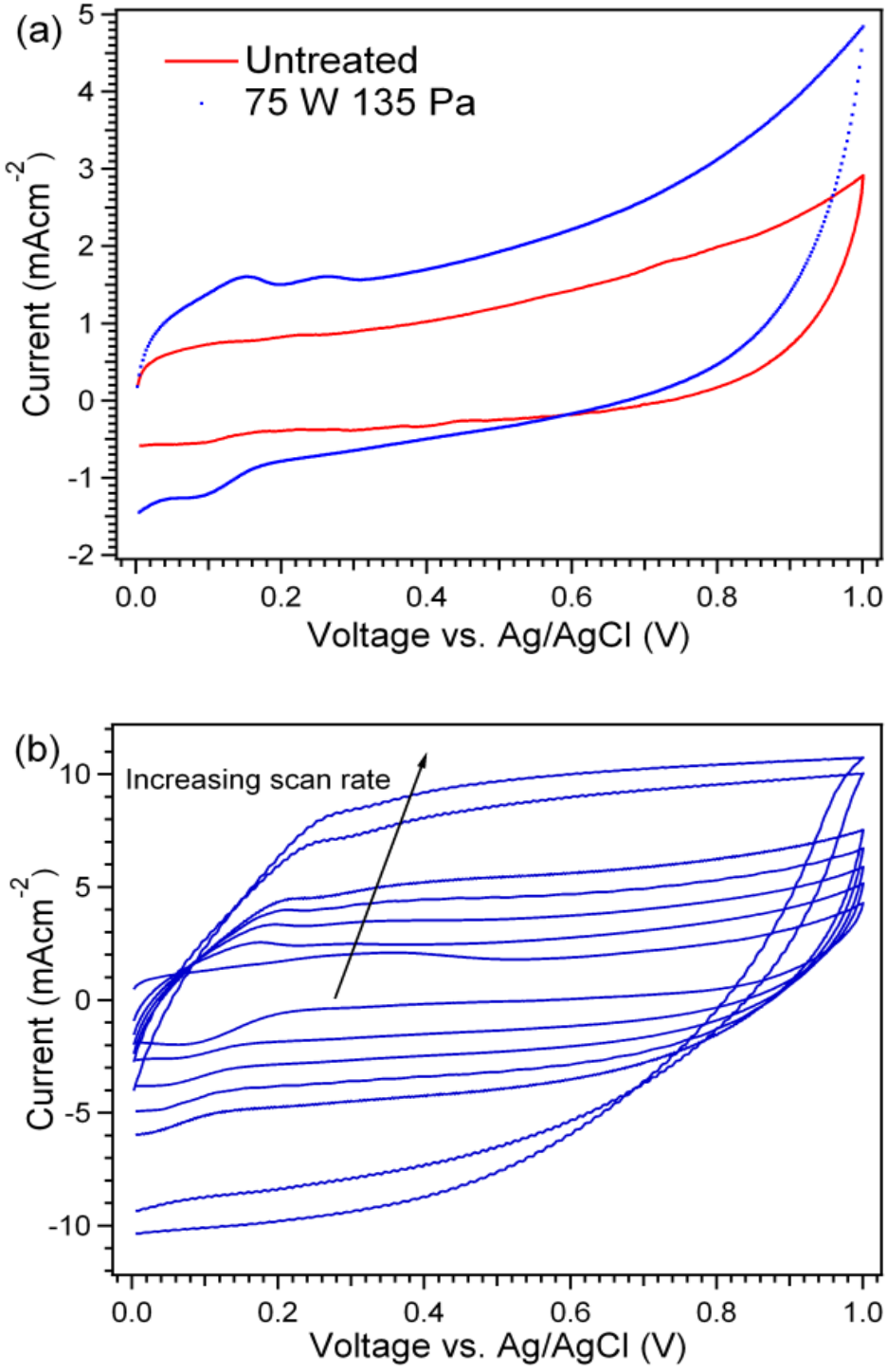

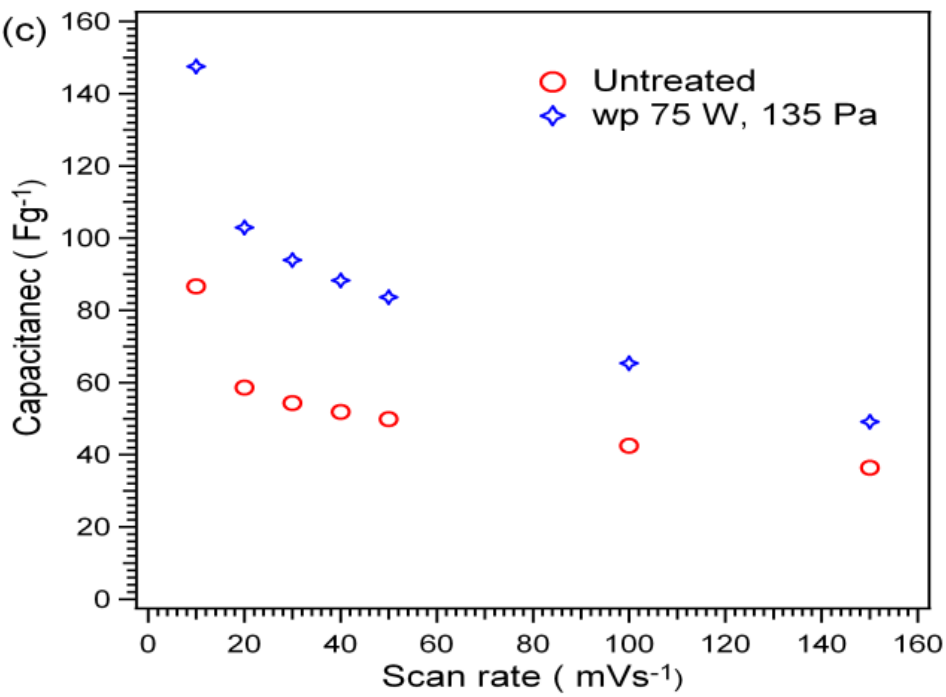

Figure 7.11: CV comparison of untreated CNTs/Al and wp treated CNTs/Al, (b) CVs of wp CNTs/Al at various scan rates 10, 20, 30, 40, 50, 100, 150 mVs^{-1}, (c) specific capacitance comparison of untreated and water plasma treated CNTs/Al at different scan rates.

CNTs was calculated by using (equation 2.12). The capacitance increases from 87 Fg^{-1} to 148 Fg^{-1} for untreated to water plasma treated CNTs/Al, respectively, at 10 mVs^{-1} scan rate (Figure 7.11 (c)). Clearly, water plasma treated CNTs show higher capacitance values in all scan rates than untreated ones. The hump at 0.05 V during the anodic scan was already observed by Beguin in 0.5 M Na_2SO_4 and was associated to the electro oxidation of hydrogen being trapped in the pores of the activated carbon at negative potentials [42].

The cycling stability of CNTs was investigated applying galvanostatic charge/discharge cycles, using a constant current density of 5.26 mA cm^{-2} in a potential window from 0 to 0.9 V during 4000 cycles. The specific capacitance was calculated from the discharge curve using (equation 2.13). Both untreated and water plasma treated CNTs display an increase in the capacitance due to the electrochemical oxidation and increased wetting of the nanotubes with time. For untreated CNTs the capacitance increases from 26 Fg^{-1} to 30 Fg^{-1} after 4000 charge/discharge cycles, whereas for water plasma treated CNTs the capacitance increases

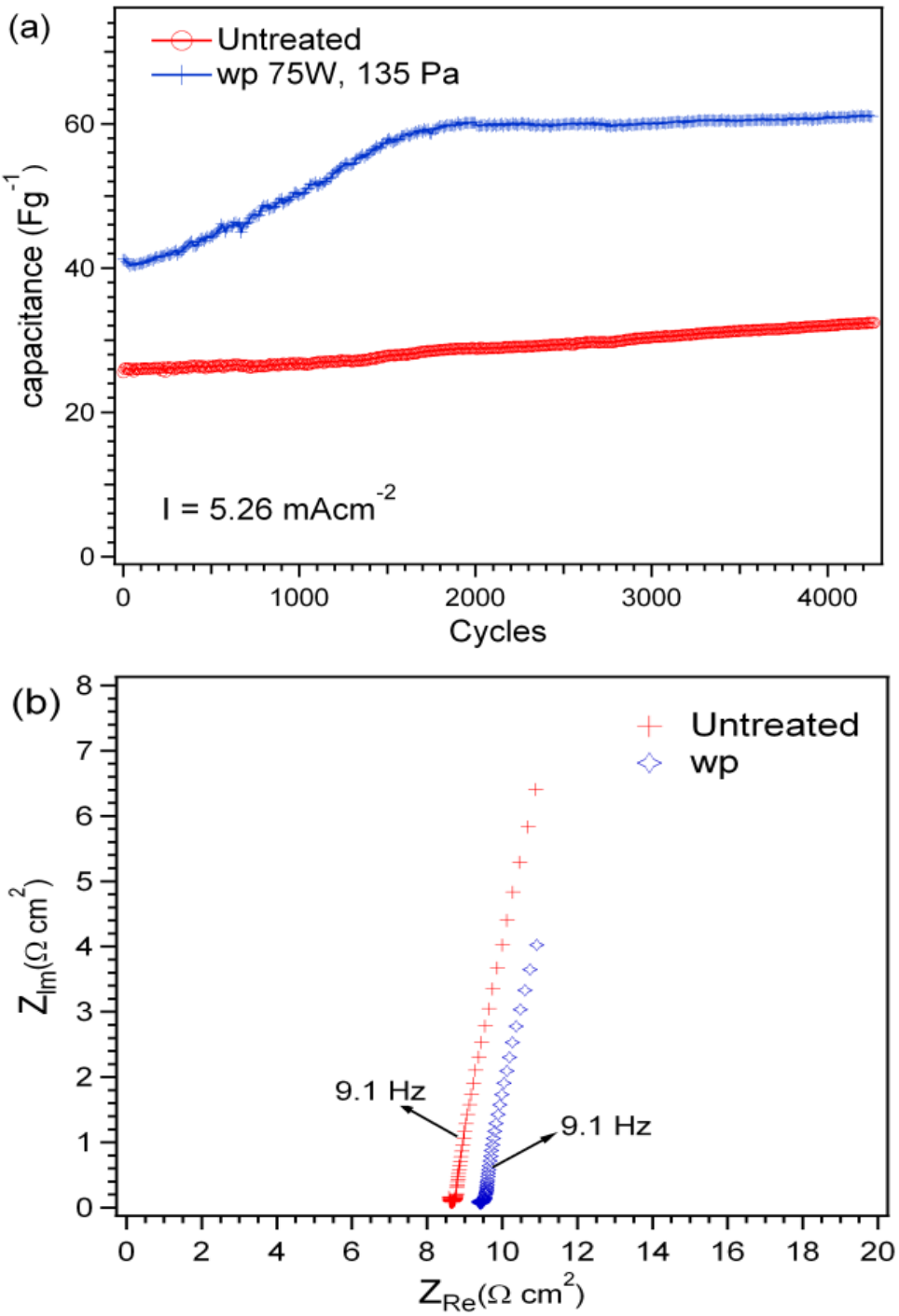

Figure 7.12: (a) Galvanostatic charge discharges cyclic stability in the 0.0-0.9 V potential range, (b) Nyquist plot of untreated and water plasma treated CNTs/Al.

from 41 Fg^{-1} to 60 Fg^{-1} after 2000 cycles. Afterwards, it almost remains constant at 60 Fg^{-1} up to 4000 cycles without any decay (figure 7.12 (a)). It is assumed that this increase in capacitance with the number of cycles is

related to a slow wetting process of the CNTs due to their ultra-long axial dimension and the increased hydrophilicity that results from the water plasma treatment.

Electrochemical impedance was performed to study the electrode kinetics behavior of untreated and water plasma treated CNTs/Al. The equivalent series resistance (ESR) of the electrode is a contribution of several factors in the measurements such as electrolyte resistance R_s, faradic charge resistance R_f, electrode resistance and the contact resistance between electrode and current collector. It can be determined from the Nyquist plot (Figure 7.12 (b)) and was found to be 8.7 ohm cm^2 for untreated CNTs/Al and 9.3 ohm cm^2 for water plasma treated CNTs/Al. This little increase in the ESR is related to the proliferation of structural disorder and surface oxygen functional groups after the water plasma treatment as observed in Raman and EDS measurements. The Nyquist plots of the samples present almost straight lines parallel to the imaginary axis in the low frequency regions and indicate that the CNTs are polarized. The reason behind the slightly high ESR value (8.7 ohm cm^2) is related to the solution resistance and working electrode surface area. Increasing the concentration of the electrolyte and the surface area of the working electrode would decrease the ESR.

7.4. Conclusions

The structural evolution of CNTs during water assisted growth has been demonstrated. Water vapor removes amorphous carbon and increases the crystallinity of carbon nanotubes during the first 30 min. After 30 min, growth rate becomes slower, the etching rate of the growing nanotubes outer planes increases extremely, and the nanotubes structure changes from curly to aligned, resulting in vertically aligned nanotubes with few walls (one to three) and large diameters. Transfer of ultralong CNTs on conductive adhesive aluminum tape was carried out using a novel methodology that lowers the series resistance of the electrode. Water plasma treatment increases the structural disorder and oxygen ratio in the transferred CNTs and their specific capacitance increases considerably. Furthermore, charge/discharge cycling stability measurements show stable capacitance values up to 4000 cycles.

7.5. References

[1] Hata K, Futaba D N, Mizuno K, Namai T, Yumura M, Iijima S, *Water-assisted highly efficient synthesis of impurity-free single-walled carbon nanotubes*, (2004), Science, 306, 1362-1364.
[2] Song L, Toth G, Vajtai R, Endo M, Ajayan P M. *Fabrication and characterization of single-walled carbon nanotube fiber for electronics applications*, (2012), Carbon, 50, 5521-5524.
[3] *Kurzepa L, Lekawa-Raus A, Patmore J, Koziol K. Replacing Copper Wires with Carbon Nanotube Wires in Electrical Transformers*, (2013), Adv. Funct. Mater.,1-6.
[4] Amade R, Jover E, Caglar B, Mutlu T, Bertran E. *Optimization of MnO_2/vertically aligned carbon nanotube composite for supercapacitor application*, (2011), J Power Sources, 196, 5779-5783.
[5] T. de los Arcos, Z.M. Wu, P. Oelhafen. *Is aluminum a suitable buffer layer for carbon nanotube growth?* (2003), Chemical Physics Letters., 380, 419–423.
[6] Mattevi C, Wirth C T, Hofmann S, Blume R, Cantoro M, Ducati C, Cepek C, Knop-Gericke A, Milne S, Castellarin-Cudia C, Dolafi S, Goldoni A, Schloegl R, and Robertson J. *In-situ X-ray Photoelectron Spectroscopy Study of Catalyst-Support Interactions and Growth of Carbon Nanotube Forests, (2008)*, J. Phys. Chem. C, 112, 12207–12213.
[7] Teblum E, Gofer Y, Pint C L, and Nessim G D. *Role of Catalyst Oxidation State in the Growth of Vertically Aligned Carbon Nanotubes*, (2012), J. Phys. Chem. C, 116, 24522−24528.
[8] Hata K, Futaba D N, Mizuno K, Namai T, Yumura M, Iijima S, *Water-Assisted Highly Efficient Synthesis of Impurity-Free Single-Walled Carbon Nanotubes*, (2004), Science, 306, 1362-1364.
[9] Zhang G, Mann D, Zhang L, Javey A, Li Y, Yenilmez E, Wang Q, McVittie J P, Gibbons J, Dai H. *Ultra-high-yield growth of vertical single-walled carbon nanotubes: Hidden roles of hydrogen and oxygen*, (2005), PNAS,102, 45, 16141-16145.
[10] Kim Y, Song W, Lee S Y, Shrestha S, Jeon C, Choi W C, Kim M, Park C Y. *Growth of Millimeter-Scale Vertically Aligned Carbon Nanotubes by Microwave Plasma Chemical Vapor Deposition*, (2010), Japanese Journal of Applied Physics, 49, 085101 (1-4).

[11] Yang X, Yuan L, Peterson V K, yin Y, Minett A I, Harris A T. *Open-Ended Aligned Carbon Nanotube Arrays Produced Using CO2-Assisted Floating-Ferrocene Chemical Vapor Deposition*, (2011), J. Phys. Chem. C, 115, 14093–14097.
[12] Xie K, Muhler M, and Xia W. *Influence of Water on the Initial Growth Rate of Carbon Nanotubes from Ethylene over a Cobalt-Based Catalyst*, (2013), Ind. Eng. Chem. Res, *52* (39); 14081–14088, **DOI:** 10.1021/ie401829e.
[13] Liu K, Sun Y, Chen L, Feng C, Feng X, Jiang K, Zhao Y, Fan S. *Controlled Growth of Super-Aligned Carbon Nanotube Arrays for Spinning Continuous Unidirectional Sheets with Tunable Physical Properties*, (2008), Nano Lett, 8, 2, 700-705.
[14] Han Z H, Ostrikov K. Uniform, *Dense Arrays of Vertically Aligned, Large-Diameter Single-Walled Carbon Nanotubes*, (2012), J. Am. Chem. Soc, 134, 6018−6024.
[15] Pint C L, Nicholas N W, Xu S, Sun Z, Tour J M, Schmidt H K, Gordon R G, Hauge R H. *Three dimensional solid-state supercapacitors from aligned single-walled carbon nanotube array templates*, (2011), Carbon, 49, 4890–4897.
[16] Honda Y, Haramot T, Takeshig M, Shiozaki H, Kitamura T, Ishikawa M. *Aligned MWCNT Sheet Electrodes Prepared by Transfer Methodology Providing High-Power Capacitor Performance*, (2007), Electrochemical and Solid-State Letters,104A 106-110.
[17] Chen M X, Song X H, Gan Z Y, Liu S. *Low temperature thermocompression bonding between aligned carbon nanotubes and metallized substrate*, (2011), Nanotechnology, 22, 345704-345709.
[18] Hussain S, Amade R, Jover E, Bertran E. *Functionalization of carbon nanotubes by water plasma*. (2012), Nanotechnology, 23, 385604.
[19] Hussain S, Amade R, Jover E, Bertran E. *Water plasma functionalized CNTs/MnO_2 composites for supercapacitors.* The ScientificWorld Journal Volume 2013, Article ID 832581, 8 pages.
[20] J J Nguyen, T L Bougher, P P S S Abadi, A Sharma. *Postgrowth microwave treatment to align carbon nanotubes*, (2013), Journal of Micro and Nano-Manufacturing, 1, 014501-5.
[21] Wang X, Feng Y, Emrah Unalan H, Zhong G, Li P, Yu H, Ibitayo Akinwande A, Milne W I, *The mechanism of the sudden termination of carbon nanotube supergrowth*, (2011), Carbon, 49, 214-221.

[22] Amama P B, Pint C L, McJilton L, Kim S M, Stach E A, Murray P T, Hauge R H, Maruyama B. *Role of water in super growth of single-walled carbon nanotube carpets*, (2009), Nano Lett, 9, 1, 44-49.
[23] Yao Y, Moon K S, Mcnamara A, Wong C P. *Water vapor treatment for decreasing the adhesion between vertically aligned carbon nanotubes and the growth substrate*, (2013), Chem. Vap. Deposition, 19, 224–227.
[24] Liu H, Zhang Y, Li R, Sun X, Wang F, Ding Z, Merel P, Desilets S. *Aligned synthesis of multi-walled carbon nanotubes with high purity by aerosol assisted chemical vapor deposition: Effect of water vapor*. (2010) Applied Surface Science,256, 4692–4696.
[25] Kim D Y, Yang C M, Park Y S, Kim K K, Jeong S Y, Han J H, Lee Y H. *Characterization of thin multi-walled carbon nanotubes synthesized by catalytic chemical vapor deposition*, (2005), Chemical Physics Letters, 413, 135–141.
[26] Dresselhaus MS, Dresselhaus G, Saito R, Jorio A. *Raman spectroscopy of carbon nanotubes*, (2005), Phys Rep, 409, 47-99.
[27] Jurio A, Pimenta MA, Filho AGS, Saito R, Dresselhaus G, Dresselhaus MS. *Characterizing carbon nanotube samples with resonance Raman scattering*, (2003), New J Phys, 5, 139, 1-17.
[28] Oswald S, Havel M, Gogotsi Y. *Monitoring oxidation of multiwalled carbon nanotubes by Raman spectroscopy*, (2007), J Raman Spectroscopic, 2007, 38, 728-736.
[29] E. F. Antunes, A. O. Lobo, E. J Corat and V. J. Trava-Airoldi. *Influence of diameter in Raman spectra of aligned multi-walled carbon nanotubes*, (2007), Carbon, 45, 913-921.
[30] Utegulov Z N, Mast D B, He P, Shi D, Gilland R F. *Functionalization of single-walled carbon nanotubes using isotropic plasma treatment: Resonant Raman spectroscopy study*, (2005), Journal of Applied Physics, 97, 104324, 1-4.
[31] Hussain S, Amade R, Jover E, Bertran E. *Nitrogen plasma functionalization of carbon nanotubes for supercapacitor applications*, (2013), J Mater Sci, 48 7620–7628.
[32] Dileo R A, Landi B J, Raffaelle R P. *Purity assessment of multiwalled carbon nanotubes by Raman spectroscopy*, (2007), Journal of Applied Physics, 101, 064307, 1-5.

[33] Maldonado S, Morin S, J. Stevenson K. *Structure, composition, and chemical reactivity of carbon nanotubes by selective nitrogen doping*, (2006), Carbon, 44, 1429-1437.
[34] Gupta A, Chen G, Joshi P, Tadigadapa S, Eklund P C. *Raman scattering from high-frequency phonons in supported n-graphene layer films*, (2006), Nano Lett, 6, 12, 2667-2673.
[35] Singh D K, Iyer P K, Gir P K. *Diameter dependence of interwall separation and strain in multiwalled carbon nanotubes probed by X-ray diffraction and Raman scattering studies*,(2010) Diamond & Related Materials,19, 1281–1288.
[36] Li W, Liang C, Zhou W, Qiu J, Zhou Z, Sun G, Xin Q, *Preparation and Characterization of Multiwalled Carbon Nanotube-Supported Platinum for Cathode Catalysts of Direct Methanol Fuel Cells,* (2003), J. Phys. Chem. B, 107, 6292-6299.
[37] Endo M, Takeuchi K, Hiraoka T, Furuta T, Kasai T, Sun X, Kinag C H, Dresselhaus M S. *Stacking nature of grapheme layers in carbon nanotubes and nanofibers*, (1997), J. Phys. Chem. Solids, 58, 11, 1707-1712.
[38] Cao A, Xu C, Liang J, Wu D, Wei B, *X-ray diffraction characterization on the alignment degree of carbon nanotubes,* (2001), Chemical physics letters, 344, 13-17.
[39] Hussain S, Amade R, Jover E, Bertran E. *Nitrogen plasma functionalization of carbon nanotubes for supercapacitor applications,* (2013), J Mater Sci, 48, 7620–7628.
[40] Frackowiak E, Metenier K, Bertagna V, Beguin F. *Supercapacitor electrodes from multiwalled carbon nanotubes*, (2000), Applied Physics letters, 77, 15, 2421-2423.
[41] Prabaharan S R S, Vimala R, Zainal Z. *Nanostructured mesoporous carbon as electrodes for supercapacitors*, (2006), Journal of power sources, 161, 730-736.
[42] Demarconnay L, Raymundo-Piñero E, Béguin F. *A symmetric carbon/carbon supercapacitor operating at 1.6 V by using a neutral aqueous solution*, (2010), Electrochemistry Communications, 12, 1275–1278.

Chapter 8
Growth of CNTs on conductive substrates (carbon paper, copper)

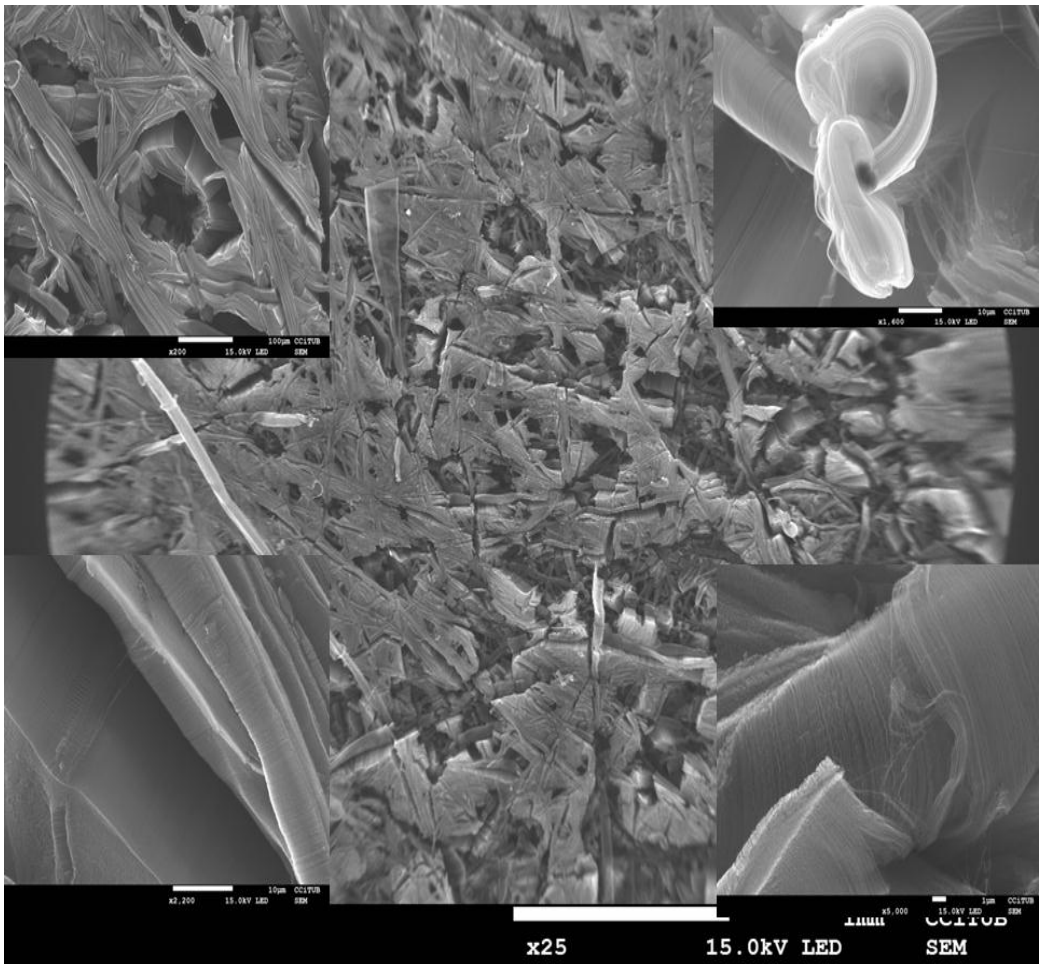

Figure 8: Images of water assisted grown CNTs on carbon paper.

Chapter 8- Growth of CNTs on conductive substrates (carbon paper, copper)

8.1. Introduction

Chemical vapor deposition (CVD) is a most attractive technique for the growth of CNTs being easier, low cost for industrial application. Generally, a metal catalyst (Fe, Co or Ni) is deposited on a semiconducting or insulating substrate and serves as seeds for the CNTs growth. The nucleation of the catalyst on these kinds of substrate (semiconducting or insulating) impose restrictions to the growth of CNTs on a conductive substrate. Additionally contact resistance is higher between MWCNTs and nonmetallic substrates. The contact resistance depends mostly on the alignment of Fermi energy levels of CNTs and the substrate. To overcome these problems it is important to grow MWCNTs directly on a conductive substrate since the MWCNTs are predominantly metallic [1]. Carbon microfibers (carbon paper) have highly porous and electrically conductive characteristics, which can be a good candidate for various kinds of application where a direct contact of CNTs is required with the conductive substrate. Two problems in CNT growth on graphite substrates are that transition metals are easily diffused into the carbon substrates and that the different phases of carbon materials are able to form on the graphite substrates because the growth conditions are similar to the diamond or diamond-like carbon growth [2, 4]. Copper is the preferred substrate because of its high electrical and thermal conductivity, as well as low economical cost. Direct growth of CNTs on copper substrate is beneficial for their use as binder free current collector for Li-ion batteries, supercapacitors and thermal interface materials. SWCNTs could behave as a semiconductor or metal depending on their chiral angle. The density of the nanotubes on the conductive substrate is lower because the high surface energy of the metal support hinders the catalyst film dewetting and nanoparticle formation. The metal catalyst tends to diffuse into the substrate and catalyst particles sinter and can be easily lifted off from the metal substrate during growth [5]. There are very few studies related to the growth of CNTs on copper substrate using various intermediate layers between catalyst film and copper in order to avoid the diffusion of catalyst particles into the substrate. G Li et al. used e-Beam Lithography to deposit

intermediate layers of Ti and Ni–Cr between the Cu substrates and the alumina buffer layer to reduce surface cracking and defects of the copper substrates, and promote vertically aligned CNT growth [6]. G. Atthipalli et al. sputtered Ni and Inconel thin films on copper substrate and Fe nanoparticles were supplied from ferrocene [7]. I Lahiri et al. sputtered Ti as diffusion barrier on copper and Ni as catalyst for the growth of CNTs [8]. T Hiraoka made a detailed study of SWCNTs and double wall carbon nanotubes growth on metallic substrate using nickel based alloy [9]. J. Garcıa-Cespedes et al. employed TiN on bulk copper substrate as a diffusion barrier in ferrocene injection CVD for the growth of CNTs [10]. J Zhu et al. synthesized CNTs on a copper foil by catalytic chemical vapor deposition (CVD) from ethanol [11]. All these above mentioned studies are performed by chemical vapor deposition. Some sort of alignment achieved by CVD is due to crowding effects. CNTs forests that align by crowding effects alone tend to exhibit a greater degree of random orientation and entanglement in the tip region as compared to other areas of the forest [12]. Fei-Lung Lu et al. adopted substrate-shielded microwave PECVD technique to synthesize CNTs on copper sputtered Fe-Si thin film. They concluded that without shielding only few randomly oriented CNTs were found [13].

Alumina (Al_2O_3) is proven to be an excellent buffer layer. During the annealing process under reducing atmosphere, surface roughness of Al_2O_3 increases, which prevents aggregation of catalyst particles. The increase in roughness is related to the etching effect of H_2 at high temperature [14]. In addition, Al_2O_3 layer increases the adhesion force between catalyst particle and substrate, and promotes the diffusion of reactant gas to the catalyst clusters [6]. The growth of CNTs on copper substrate is related to its catalytic properties. The native oxide layer on copper surface restricts the adhesion of another deposited film with the metal. Copper substrate easily oxidizes and cracks during CVD of CNTs [11, 15]. To the best of our knowledge, there is no study related to the improvement of adhesion of alumina on copper for the growth of CNTs by radio frequency plasma enhanced chemical vapour deposition, and their electrochemical properties as supercapacitors.

Previous chapters are related to the growth of CNTs on Si substrate for supercapacitor application [chapter 4, 5, 6, 7]. In this work MWCNTs were grown on carbon paper by means of water assisted CVD and as well

as by means of rf-PECVD on copper substrate. Hydrogen plasma was performed to remove oxide layer from the copper substrate. Alumina was sputtered as a diffusion barrier. The role of different metallic intermediate layers between copper and alumina has been studied to improve the adhesion and growth of carbon nanotubes. Post synthesis treatment with nitrogen plasma to introduce nitrogen functionalities was carried out on the grown nanotubes to improve their supercapacitive properties.

8.2. Water assisted growth of CNTs on conductive substrates

CNTs were grown on two different kinds of conductive substrate (copper foil and carbon paper). Prior to the deposition of the diffusion barrier on copper substrate it was first immersed in acetic acid to remove the oxide layer [15].Experimental details about the diffusion barrier are listed in (table 8.1).

Table 8.1: experimental details of CNTs grown of metal substrate by WACVD.

Sample	Ni (nm)	Ti (nm)	Al_2O_3 (nm)	Fe (nm)	Annealing (s), 600°C , Hold time(s)	WACVD (s),700°C
A (Cu)	-	-	30	2	750, 150	900
B (Cu)	-	75	30	2	750, 150	900
C (Cu)	150	75	30	2	750, 150	900
D-(carbon paper)	-	-	30	2	750, 150	900

(Figure 8.1) shows SEM images of CNTs grown under different conditions on copper substrate and carbon paper. (Figure 8.1 (a)) shows CNTs grown on a sample with just alumina layer as diffusion barrier. As can be clearly seen, aligned and long nanotubes are grown on copper foil, but they are detached from substrate. A possible reason could be the presence of remaining oxide layer on copper even after cleaning with acetic acid, which restricts the adhesion of Al_2O_3 onto the copper substrate. Sample B (figure 8.1 (b)) shows the same problem as sample A (see figure 8.1 (a)). In the case of sample C the adhesion of nanotubes improved by introducing Ni intermediate layer as can be seen from figure 1(c). In (figure

8.1 (d)) CNTs are grown on a carbon paper and are densely packed in all direction of carbon fibers.

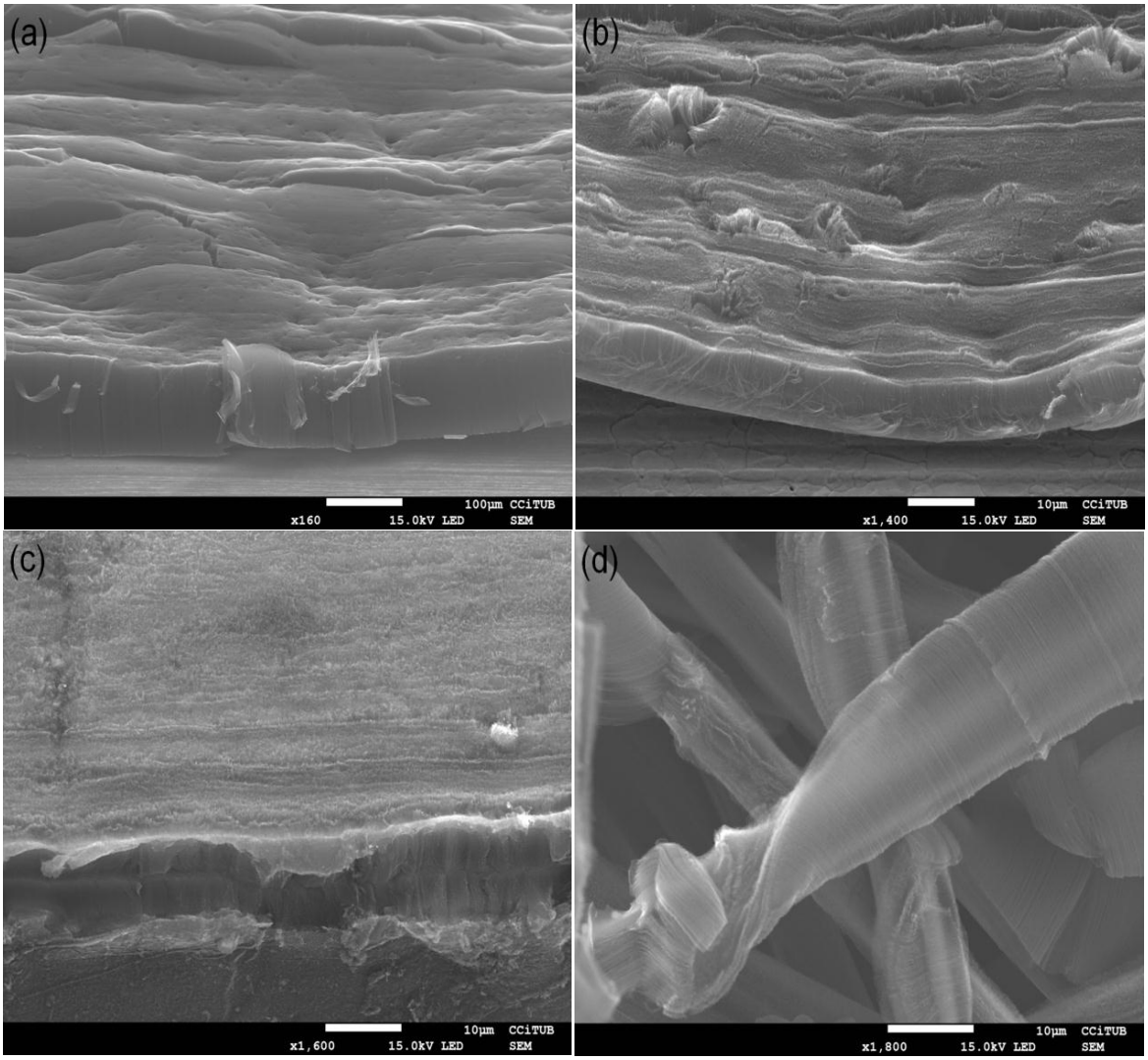

Figure 8.1: SEM images of (a) sample A, (b) sample (B), (c) sample (d) (see table 8.1).

8.3. Growth of CNTs on copper substrate by rf-PECVD

8.3.1. Experimental details

Copper foil (Cu 000720/31, thickness 0.25 mm, purity 99.9%) was bought from good fellow company. The foil was cut into 4 × 4 cm^2 pieces, cleaned in ultrasonic bath with acetone and isopropanol for 10 minutes each. Afterwards, the sample was introduced in to the home made reactor. This reactor enables the sputtering of different kinds of thin films without

taking out the substrate. Thus, the sample remains under high vacuum while the target material is replaced. It should be noted that all experiments were performed with a background pressure below 4×10^{-4} Pa to ensure clean deposition conditions. First, pulsed DC hydrogen plasma was used to reduce the copper substrate. The conditions were; 20 sccm H_2 flow, 20 Pa pressure, 100 W DC power, 100 kHz frequency, 2016 ns pulse width during 10 min. In order to optimize the adhesion of alumina on copper substrate four different intermediate layers were investigated (see table 1). Pulsed DC magnetron sputtering was used for the sputtering process of Al_2O_3, Ni and Ti. The parameters used were; 120 W plasma power, 100 kHz frequency, 2016 ns pulse width, and a working pressure of 1 Pa.

Table 8.2: sputtering parameters.

	Ni		**Ti**		**Al_2O_3**		
	Ar (sccm)	Thickness (nm)	Ar (sccm)	Thickness (nm)	Ar (sccm)	O_2 (sccm)	Thickness(nm)
A	-	-	-	-	17	3	30
B	20	300	-	-	17	3	30
C	-	-	20	50	17	3	30
D	20	300	20	50	17	3	30

Afterwards, samples were introduced in a CVD/PECVD homemade reactor. This reactor facilitates the sputtering and growth process of carbon nanotubes. Once the base pressure inside the reactor was $4\cdot10^{-4}$ Pa, 128 sccm of Ar were introduced and a 3 nm thick layer of Fe catalyst was sputtered on the sample. Then, without breaking the vacuum to avoid oxidation of the catalyst, the sample was placed under a heating element inside the reactor in order to anneal the catalyst layer and grow the CNTs. The heating element consists of a graphite resistance (2 Ω) placed above the substrate and connected to a DC power supply. The temperature on the top surface of the sample was monitored using an external optical pyrometer, and controlled with a feedback loop with the DC power supply using a proportional-integrative-derivative (PID) controller. The whole process was controlled by LabVIEW software. Annealing of catalyst thin film was done at temperatures up to 680°C with a ramp time of 750 s in a reducing atmosphere of hydrogen (100 sccm) at a pressure of 2 mbar. After a hold time of 120 s, H_2 is replaced by NH_3 gas during 30 s and the

pressure inside the reactor is lowered down to 0.8 mbar. Afterwards, rf plasma is ignited, C_2H_2 introduced in the chamber (100 sccm) and the pressure increased to 1mbar (see table 8.3).

Table 8.3. Summary of CNTs growth conditions.

Parameter	Value
Catalyst layer thickness	3 nm
Annealing time	870 s
PECVD process temperature	680ºC
PECVD process plasma power	50 W
PECVD process time	1800 s

Nitrogen plasma was performed to sample D to introduce nitrogen based functionalities on the surface of CNTs for supercapacitor applications. The plasma parameters were 100 sccm N_2 flow, 10 Pa pressure, 75 W RF power and 120 s treatment time.

8.3.2. Results and discussion

Plasma reduction of copper oxide is mainly performed by atomic hydrogen produced in plasma that leads to a chemical reduction of corrosion products. Reduction of copper oxide to copper is achieved in hydrogen plasma via the reaction of the hydrogen radicals with the metal oxide; further more plasma will roughen the surface [16].

$$CuO + 2H^{\cdot} \rightarrow Cu + H_2O \qquad (8.1)$$

The evolution in the copper surface due to hydrogen plasma treatment, which is removal rate of oxide, was determined by optical emission spectroscopy (OES). The out coming light from the discharge was collected through a quartz optical fiber and led to a spectrophotometer (Stellarnet EPP2000C), which operated centered in the UV–VIS range (185–850 nm). The time dependence of OH radical integral spectral intensity in the spectral range of 305–330 nm can provide important information about the number of plasma treatment steps needed for successful removal of oxides [17]. (Figure 8.2) shows OES spectra of hydrogen plasma treatment of copper substrate. The intensity of OH (316 nm) radical decreases from 1180 to 288 (a.u.) after 10 min of hydrogen

plasma treatment of copper surface, which corresponds to about 24 %. This provides an evidence of the removal of the oxide layer from the copper surface.

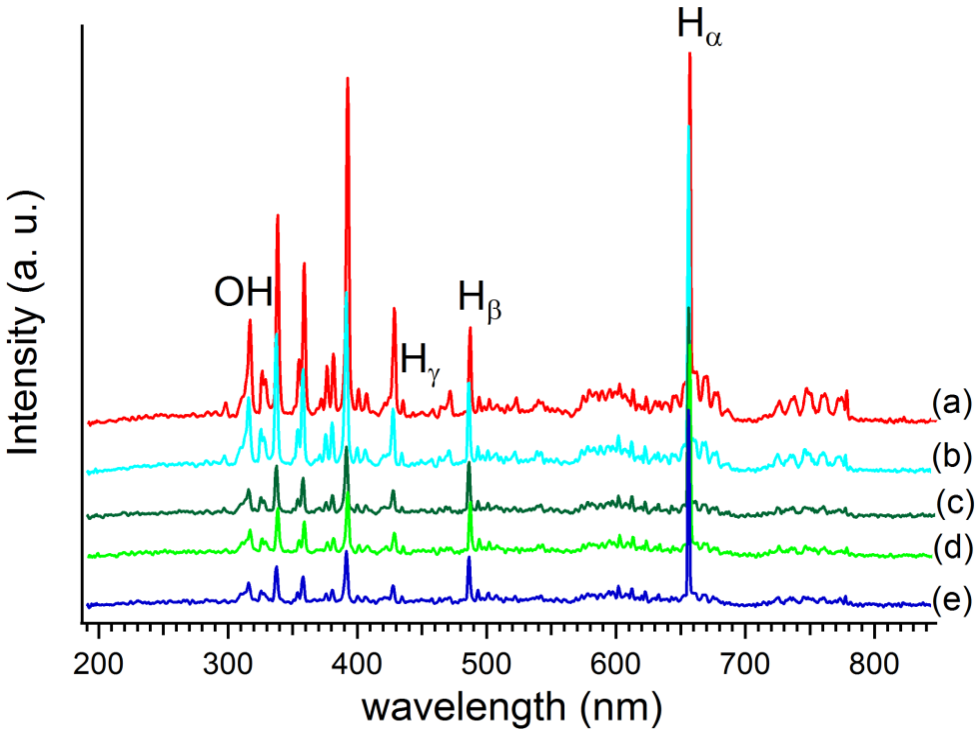

Figure 8.2: Optical emission spectroscopy of hydrogen plasma during reduction of copper at different treatment times; (a) 1 min, (b) 3 min, (c) 5 min, (d) 9 min and (e) 10 min.

Morphological characterization of the samples was performed using scanning electron microscopy (Jeol J-7100). The catalytic growth of CNTs on copper can be significantly improved if the adhesion of the buffer layer Al_2O_3 is strong. However, adhesion loss arises during the annealing process due to differences in the thermal expansion properties of Al_2O_3 and copper. Al_2O_3 adhesion to copper can be control by using suitable intermediate layers. The first layer on the copper substrate must have good adhesion to copper and a thermal expansion coefficient lower than that of copper ($\alpha = 17 \times 10^{-6} K^{-1}$). Nickel has a thermal expansion coefficient ($\alpha = 13 \times 10^{-6} K^{-1}$) lower than copper and, in addition, it has good compatibility with copper, which is shown by its high solubility in copper in the solid state [18]. Poor adhesion to copper surface was observed when only Al_2O_3 used as a buffer layer. As a result the catalyst activity decreases

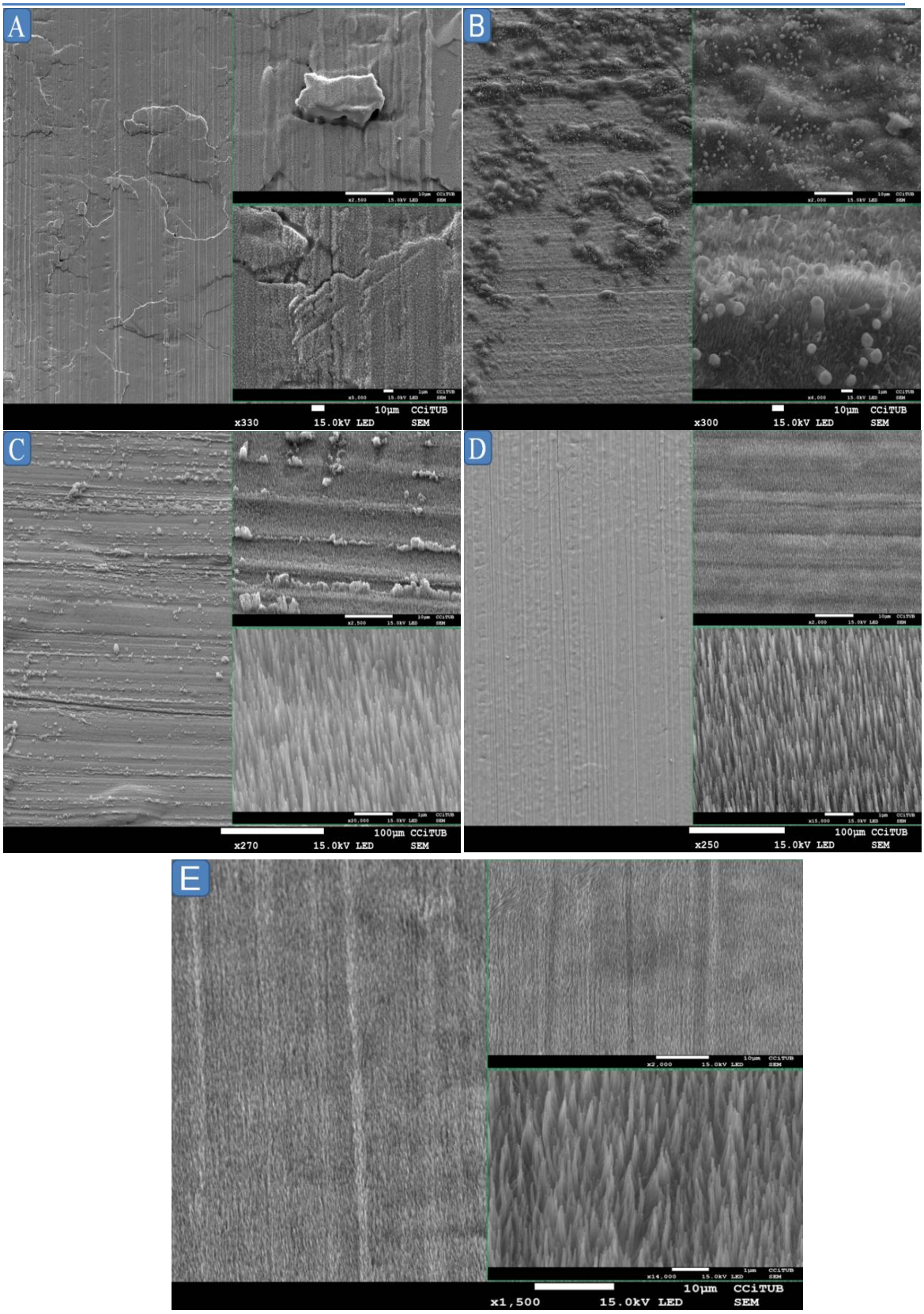

Figure 8.3: SEM images of samples (A (A), B (B), C (C), D (D) and nitrogen plasma treated sample D (E)).

and the growth rate is very slow (figure 8.3 (A)). As can be seen inset figure 8.3 (A) the nanotubes barely start to grow even after 30 min growth time. (Figure 8.3 (B)) show CNTs grown when Ni was used as an intermediate layer between Al_2O_3 and copper. An improvement in the growth of CNTs can be observed with the addition of Ni film. Big diameter CNTs are probably catalyzed by nickel particles (see inset figure 8.3 (B)).

It has been shown that reactive metals, which form stable oxides, normally show good adhesion to other oxides. Ti has thermal expansion coefficient very close to Al_2O_3 [18]. In sample C, Titanium (Ti) was sputtered on copper as an intermediate layer below the Al_2O_3. For this sample the growth rate of CNTs increases (Figure 8.3 (C)). Lower inset in figure 8.3 (C) shows dense and vertically aligned nanotubes. The main concern in this sample is that the catalyst becomes deactivated very fast as can be seen from (Figure 8.3 (C)); a lot of amorphous carbon is deposited on the surface of CNTs. In sample D two intermediate layers (Nickel and Titanium) were combined between copper and Al_2O_3. As explained above, both nickel and titanium improve the adhesion to Al_2O_3 and growth of CNTs. (Figure 8.3 (D)) shows CNTs grown when the configuration ($Cu/Ni/Ti/Al_2O_3$) was employed. Under these conditions the CNTs growth all over the copper substrate is homogeneous and without cracking. The nanotubes are vertically aligned, highly dense and long in comparison to other samples. (Figure 8.3 (E)) corresponds to nitrogen plasma treated sample D. The main purpose of the nitrogen plasma was to remove the amorphous carbon, which is a byproduct of the PECVD process, and to decorate the surface of nanotubes with nitrogen based functional groups [19]. The nanotubes remain vertically aligned without decreasing their length. The only morphological difference between untreated and nitrogen plasma treated CNTs is that plasma treated tips of nanotubes tend to agglomerate (see bottom inset figures 8.3 (D, E).

The quality of the CNTs was examined by Raman spectroscopy by using micro-Raman spectroscopy (HORIVA LabRam HR800, Japan). A green laser of wavelength 532 nm, 0.5 mW power and a 50LWD objective were used during the measurements. (Figure 8.4) shows Raman spectra of sample D (untreated and nitrogen plasma treated CNTs). Analysis of the ratio between the D and G band intensities (I_D/I_G) gives us information about structural disorder. The peak fitting of Raman spectra was performed using four peaks: G band ~ 1593 cm^{-1}, D band ~ 1357 cm^{-1}, I band ~1210

cm^{-1} and D´´ band ~ 1500 cm^{-1}. I_D/I_G ratio increases from 1.120 to 1.133 from after the nitrogen plasma. This very little increase in ratio indicates soft etching of amorphous carbon. The increase in the intensities of Raman bands after the plasma treated is clearly a sign of the removal of the amorphous carbon. I band is attributed to impurities in the graphite lattice, and incorporation of nitrogen in CNTs [19, 20]. D´´ appears near 1500 cm^{-1} wavenumber and is related to stacking defects in graphene layer [21].

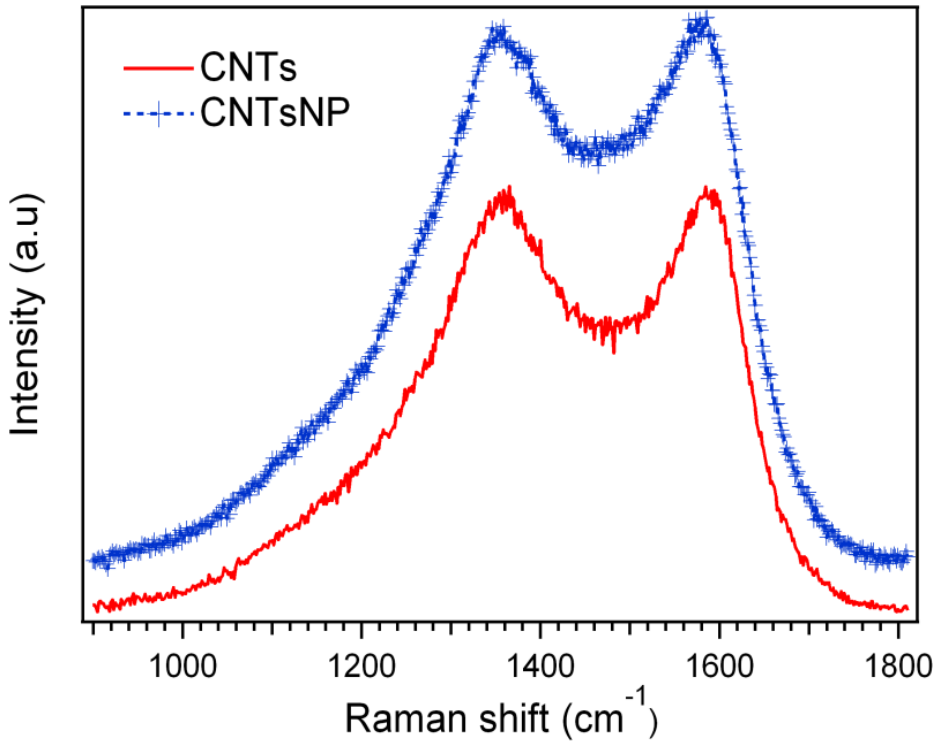

Figure 8.4: Raman spectra of sample D before and after nitrogen plasma treatment.

The capacitors were fabricated in a MBRAUN Unilab dry glove box by sandwiching an organic-electrolyte soaked separator (Whatmann glassy-fiber GF/A) between two carbon nanotube electrodes (sample D). The area of each electrode was 0.56 cm^2. The 1.0-molar liquid electrolyte solution consisted of lithium perchlorate ($LiClO_4$) (99%, Fluka BioChemica) dissolved in ethylene carbonate (EC) and diethyl carbonate (DEC) (both 99%, anh. from Sigma-Aldrich) mixed in 1:1 volumetric proportions. Cyclic voltammetry was used to record the electrochemical cell current against its voltage at a fixed scan rate. The specific capacitance of the

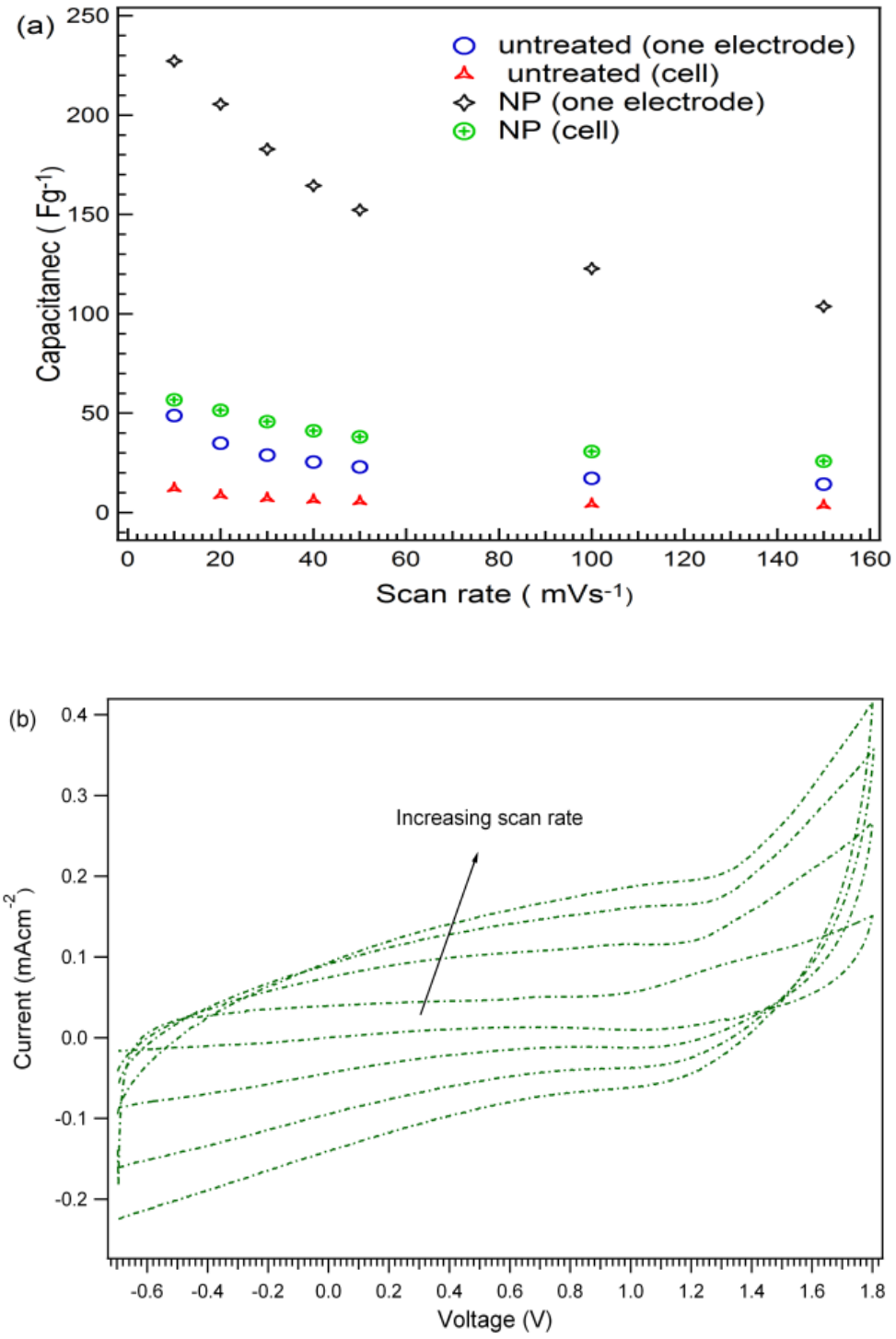

Figure 8.5: (a) comparison between the specific capacitance of untreated and plasma treated samples, (b) cyclic voltammograms at 10, 50, 100 and 150 mVs^{-1}.

samples was calculated from the cyclic voltammograms using equation (8.2).

$$C_s = \frac{q_a + |q_c|}{2m\Delta V} \quad (8.2)$$

Where C_s is the specific capacitance in Fg^{-1}, m is the mass of the active material in g, ΔV is the voltage window in V, q_a and q_c are the anodic and cathodic charge in C, respectively.
The relationship between the specific capacitance measured with two electrodes and 3-electrode technique is [22].

$$C_{spec-3E} = 4 \times C_{spec-2E} \quad (8.3)$$

Where $C_{spec\text{-}3E}$ is the specific capacitance obtained in a three-electrode cell configuration. The measurements were performed in a voltage window range of 2.5 V, from -0.7 to 1.5 V.

(Figure 8.5 (a)) shows a comparison of the specific capacitance between untreated and nitrogen plasma CNTs for two and three electrodes cell at different scan rates. Using equation 8.3 the calculated specific capacitances for untreated CNTs at a scan rate of 10 mVs^{-1} was ~ 49 Fg^{-1}. As can be seen in figure 8.5 (a) even at a high scan rate of 150 mVs^{-1} the capacitance is ~ 15 Fg^{-1}. For nitrogen plasma treated CNTs the capacitance increases up to 227 Fg^{-1} at a scan rate of 10 mVs^{-1}. This increase is related to the introduction of nitrogen base functionalities such as pyridinic and pyrrolic, which can significantly enhance the specific capacitance of the nanotubes as altready described in our previous article [19].

At lower scan rates, such as 10 mVs^{-1}, the shape of the cyclic voltammograms is almost rectangular without any hump during the scan (figure 8.5(b)), which describes a pure capacitive behavior of the electrodes. The shape of CVs at higher scan rates is slightly deviated and distorted, possibly due to the contribution of pseudocapacitance to the total capacitance of the cell and as also, to the solution and electrode resistance [22]. The pseudocapacitance contribution to the untreated sample is possible because of surface oxygen groups, which readily react with the PECVD grown sample when taken out of the reaction chamber [23, 24]. In the case of nitrogen plasma treated sample, nitrogen functionalities also contribute to enhance the total capacitance due to the pseudocapacitive effect.

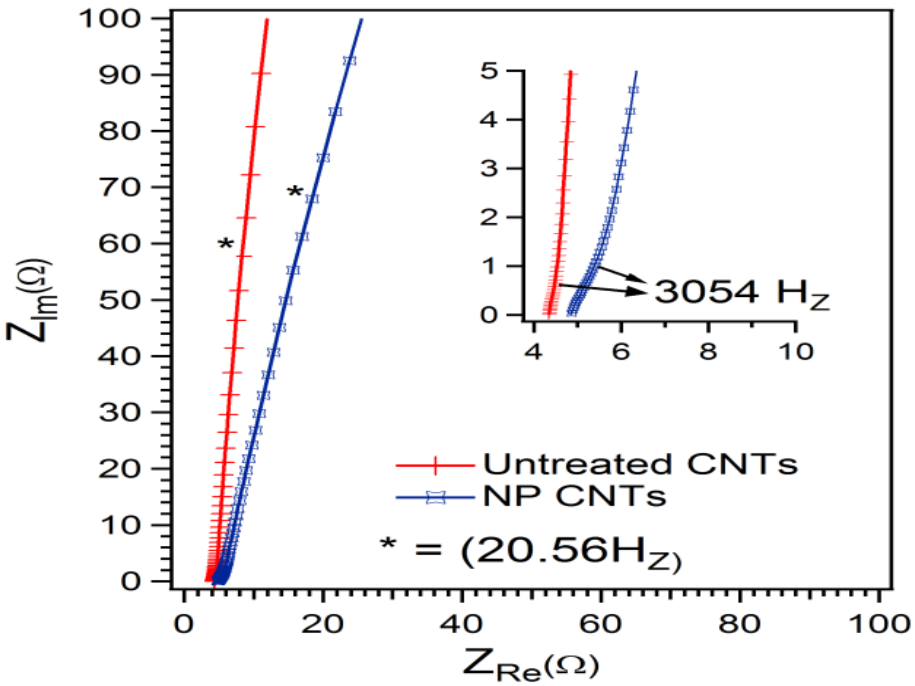

Figuer 8.6: Nyquest plot for untreated and nitrogen plasma treated CNTs.

Electrochemical impedance spectroscopy (EIS) has been known as a valuable tool for probing the features of capacitance and resistance of supercapacitor materials. The impedance measurements were carried out at a dc bias of 0 V with a 10 mV amplitude of a sinusoidal signal over a frequency range between 100 kHz and 0.01 Hz. (Figure 8.6) show the Nyquist plot of two electrode supercapacitor cell (untreated and treated sample D). The equivalent circuit of a supercapacitor based on porous electrodes and electrolyte presents a complex combination of capacitance (C) and resistance (R) components. The interfacial impedance of a supercapacitor is associated with a double-layer capacitance C_{dl}, a pseudocapacitance C_p, a Faradaic charge-transfer resistance R_f and the sum of the electrolyte resistance, the electrode resistance, and the contact resistance between the electrode and the current collector R_s. The presence of a semicircle in MWCNTs supercapacitors is attributed to the Faradic reaction of oxygen containing functional groups at the electrode surface [27].

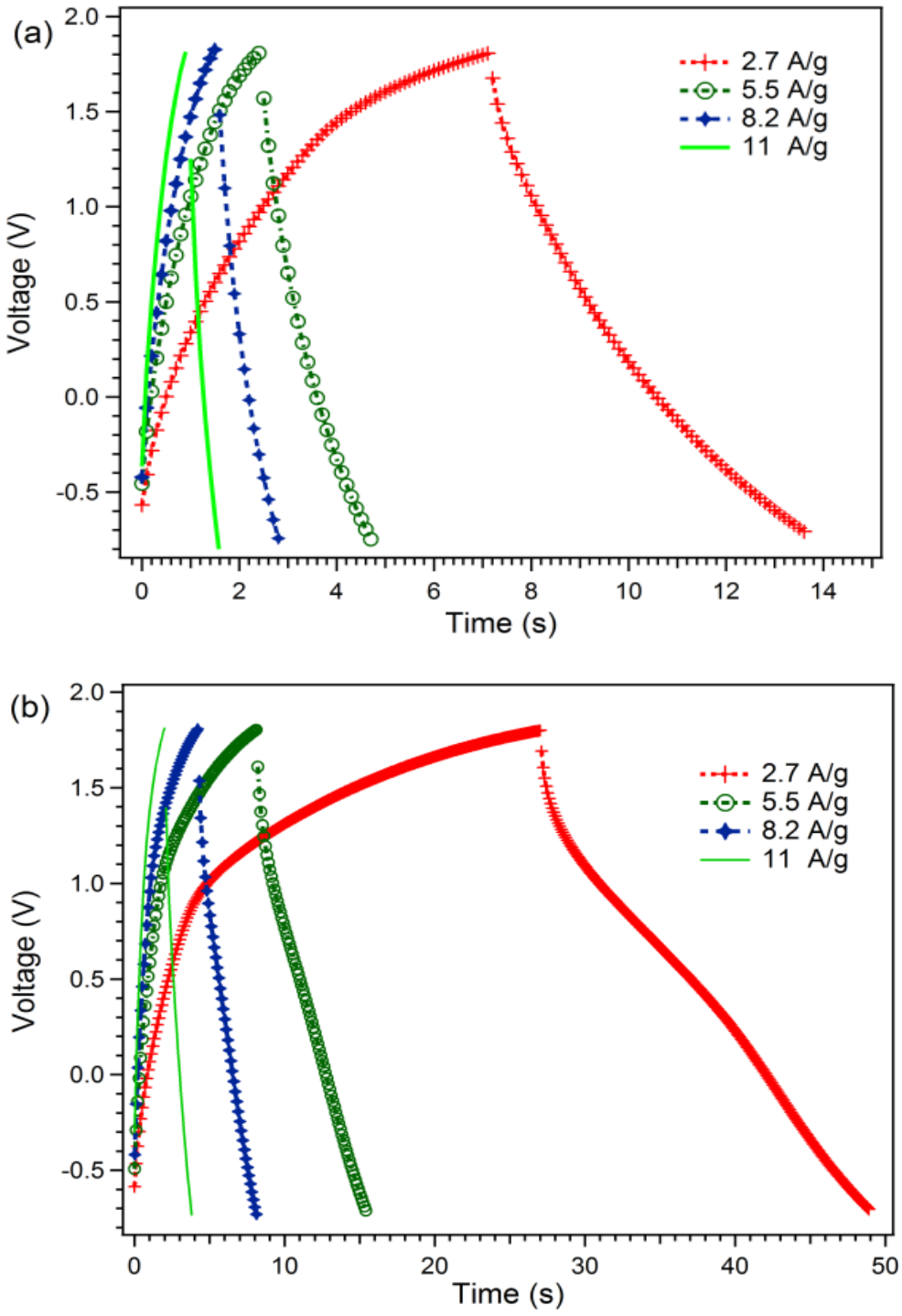

Figure 8.7: Galvanostatic charge/discharge curves (a) untreated CNTs, (b) nitrogen plasma treated CNTs.

The Nyquist plots consist of (a) a high-frequency intercept on the real Z_{Re} axis, (b) a semicircle in the high-to-medium-frequency region, and (c) a straight line at the very low-frequency region. The equivalent series resistance (ESR) i.e., contacts resistance, solution resistances, and charge

transfer resistance of the electrode material is about 4.2 Ω. The small increase in the ERS after the nitrogen plasma treatment could be related to an increase of the surface area due to a higher porosity of the CNTs. Highly porous medium provides less conduction paths. In addition, difference between the semicircles of untreated and nitrogen plasma treated samples show that the intrinsic resistance is smaller for the untreated sample (see inset figure 8.6) [26]. At frequencies below 3054 H_z the straight line is parallel to imaginary axis and explains an exactly polarized system (inset figure 8.6) [27]. Both samples show an almost straight-line behavior at low frequencies.

Galvanostatic charge/discharge curves were measured applying various current densities from 2.7 to 11 Ag^{-1} for untreated and nitrogen plasma treated CNTs (figure 8.7 (a, b)). The smaller ohmic drop at lower current densities indicates a lower ESR. The charge curve for untreated CNTs at low current density shows two regions: from -0.7 to 1.4 V, which is mainly due to double layer capacitance contribution, and above 1.4 V, where the curve deviation indicates the prevalence of the pseudocapacitive effect related to faradaic charge transfer. In the case of the nitrogen-plasma treated sample the double-layer capacitance predominates in the region from -0.7 to 1 V [27], and above 1 V contribution of pseudocapacitance increases due to the presence of nitrogen functional groups.

Cycling stability of the electrodes was tested applying up to 1200 galvanostatic charge/discharge cycles at a current density of 5.5 Ag^{-1} (Figure 8.8). The specific capacitance was calculated from the discharge curve using equation 8.44.

$$C_S = \left(\frac{I}{(\Delta V / \Delta t) \cdot m} \right) \tag{8.4}$$

Where C_s is the specific capacitance in Fg^{-1}, ΔV is the voltage difference during the discharge curve in V, I is the current in A and Δt the discharge time in s.

Both samples show almost constant capacitance from the first to the last cycle. The capacitance increases from 4 to 22 Fg^{-1} after the nitrogen plasma treatment. The capacitance of the untreated sample is almost constant up to 1200 cycles, whereas the capacitance of nitrogen plasma treated CNTs decreases slightly. This decrease in capacitance is possibly

due to the presence of oxygen functional groups, which form at the surface defects created during the plasma treatment when exposing the sample to ambient air. Oxygen functionalities which preferentially form at the edges of the graphite like microcrystallites increase the barrier for electrons to transfer from one microcrystalline element to the next [28].

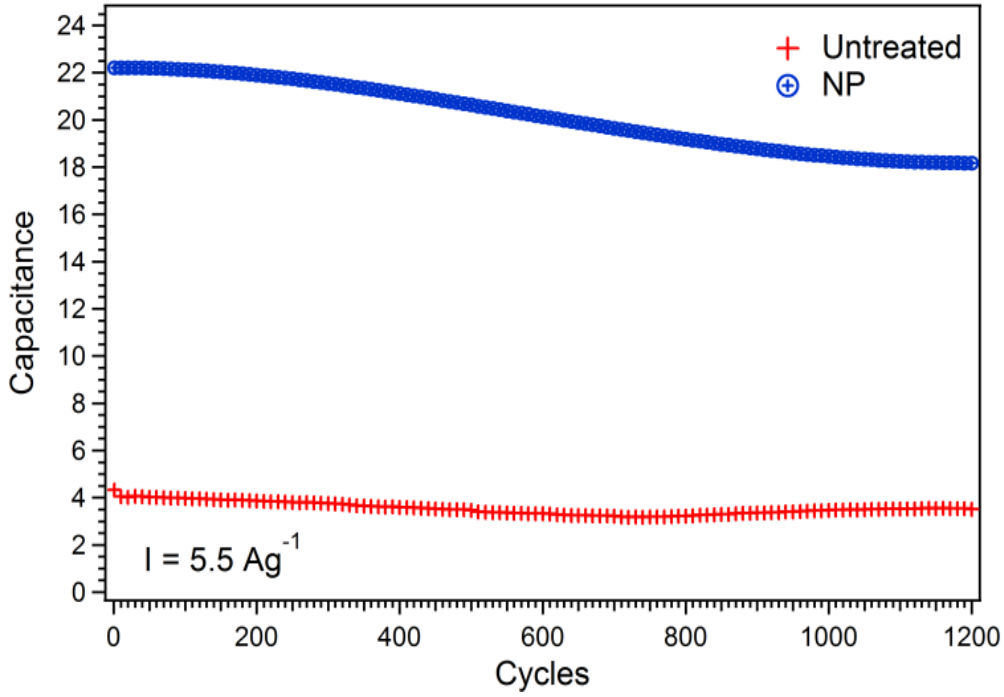

Figure 8.8: Charge/discharge cyclic stability

8.4. Conclusions

CNTs were grown on carbon paper and copper foil successfully. The catalyst activity, growth rate and density of the CNTs significantly improved by the reduction process of copper substrate through hydrogen plasma as well as using intermediate layers of Ti and Ni between copper and alumina. Structural disorder of the CNTs increases after the nitrogen plasma treatment. After the nitrogen plasma treatment contribution of pseudocapacitance increases the total capacitance of the CNTs. CNTs show almost stable cyclability up to 1200 cycles at a current density of 5.5 Ag^{-1} in a voltage window of 2.5 V.

8.5. References

[1] N Zhao, J Kang, *Direct growth of carbon nanotubes on metal supports by chemical vapor deposition*, (2011). ISBN 978-953-307-497-9.

[2] S Zhu, C H Su, S L Lehoczky, I Muntele D Ila, *Carbon nanotube growth on carbon fibers*,
(2003), Diamond and Related Materials, 12, 1825–1828.

[3] F L Lu, J M Ting, *Very rapid growth of aligned carbon nanotubes on metallic substrates*, (2013), Acta Materialia, 61, 2148–2153.

[4] L H Chen, J F AuBuchon, I C Chen, C Daraio, X R Ye, A Gapin, and S Jin, *Growth of aligned carbon nanotubes on carbon microfibers by dc plasma-enhanced chemical vapor deposition*, (2006), Applied Physics Letters, 88, 033103.

[5] H Sugime, S Esconjauregui, J Yang, L D Arsie, R A Oliver, *Low temperature growth of ultra-high mass density carbon nanotube forests on conductive supports*, (2013), Applied Physics Letters, 103, 073116.

[6] G Li, S Chakrabarti, M Shulz, V Shanov. *Growth of aligned multiwalled carbon nanotubes on bulk copper substrates by chemical vapor deposition*, (2009), J. Mater. Res, 24, 9, 2813-2820.

[7] G Atthipalli, Y Tang, A Star, J L Gray, *Electrochemical characterization of carbon nanotube forests grown on copper foil using transition metal catalysts*,(2011), Thin Solid Films, 520 1651–1655.

[8] I Lahiri, S W Oh, J Y Hwang, S Chao, Y K Sun, R Banarjee, W Choi, *High capacity and excellent stability of Lithium ion battery anode using interface-controlled binder-free multiwall carbon nanotubes grown on copper*, (2010), ACS Nano, 4, 6, 3440-3446.

[9] T Hiraoka, T Yamada, K Hata, D N Futaba, H Kurachi, S Uemura, M Yumura, S Iijima,
Synthesis of Single- and Double-Walled Carbon Nanotube Forests on Conducting Metal Foils, (2006), J. AM. CHEM. SOC., 128, 13338-13339.

[10] J G Cespedes, S Thomason, K B K Teo, I A Kinloch, W I Milne, E Pascual, E Bertran,
Efficient diffusion barrier layers for the catalytic growth of carbon nanotubes on copper substrates, (2009), Carbon, 47, 613-621.

[11] J Zhu, J Jia, F L Kwong, D K L Ng, *Synthesis of bamboo-like carbon nanotubes on a copper foil by catalytic vapor deposition from ethanol*, (2012), Carbon, 50, 2504-2512.

[12] J. J. Nguyen, T. L. Bougher, P S S Abadi, A. Sharma, S. Graham, B. A. Cola, *Postgrowth Microwave Treatment to Align Carbon Nanotubes,* (2013), Journal of Micro and Nano-Manufacturing, 1, 014501, 1-6.
[13] F L Lu, K H Liao, J M Ting, *Growth of Carbon Nanotubes on Metallic Substrates Using a Substrate-Shielded Microwave Plasma-Enhanced Chemical Vapor Deposition*, (2012), Journal of The Electrochemical Society, 159 (2) K50-K54.
[14] S Chakrabarti, H Kume, L Pan, T Nagasaka, Y Nakayama, *Number of walls controlled synthesis of millimeter-long vertically aligned brushlike carbon nanotubes*, (2007), J. Phys. Chem. C, 111, 1929-1934.
[15] K L Chaves, D W Hess, *A novel method of etching copper oxide using acetic acid*, (2001), Journal of The Electrochemical Society, 148, 11, G640-G643.
[16] J D Getty, *How Plasma-Enhanced Surface Modification Improves the Production of Microelectronics and Optoelectronics*. © 2002 *Chip Scale Review*.
[17] Z. Rašková, F. Krčma, M. Klíma, J. Kousal, *Czech. (2002),* J. Phys., 52 Suppl. D, 927.
[18] R Jarvinen, T Mantyla, P Kettunen, *Improved adhesion between a sputtered alumina coating and a copper substrate*, (1984), Thin Solid Films, 114, 311-317.
[19] S Hussain, R Amade, E Jover, E Bertran, *Nitrogen plasma functionalization of carbon nanotubes for supercapacitor applications*. (2013), Journal of Materials Science, 48 7620–7628.
[20] Maldonado S, Morin S, Stevenson K J, *Structure, composition, and chemical reactivity of carbon nanotubes by selective nitrogen doping,* (2006), Carbon, 44, 1429–1437.
[21] Shen W, Li Z, Liu Y, *Surface Chemical Functional Groups Modification of Porous Carbon,* (2008), *Recent Patents Chem. Eng,* 1, 27-40.
[22] D Qu, H Shi, *Studies of activated carbons used in double-layer capacitors,* (1998), Journal of Power Sources, 74, 99–107.
[23] S Hussain, R Amade, E Jover, E. Bertran, *Functionalization of carbon nanotubes by water plasma,* (2012), Nanotechnology, 23 1–8.
[24] S Hussain, R Amade, E Jover, E Bertran, *Water Plasma Functionalized CNTs/MnO_2*

Composites for Supercapacitors, (2013), The scientific world journal 2013 Volume 2013, Article ID 832581, 8 page. http://dx.doi.org/10.1155/2013/832581.

[25] C G Liu, M Liu, F Li, H M Cheng, *Frequency response characteristic of single-walled carbon nanotubes as supercapacitor electrode material*, (2008), Applied physics letters, 92 143108.

[26] L Li, E Liu, H Shen, Y Yang, Z Huang, X Xiang, Y Tian, *Charge storage performance of doped carbons prepared from polyaniline for supercapacitors*, (2011), J Solid State Electrochem, 15 175-182.

[27] Conway BE Electrochemical supercapacitors. Kluwer Academic/Plenum publishers, New York (1999). ISBN 0-306-45736-9

[28] A G Pandolfo, A F Hollenkamp, Carbon properties and their role in supercapacitors, (2006), Journal of Power Sources, 157, 11–27.

Chapter 9
Growth and functionalization of VACNTS on Quartz filter for environmental applications

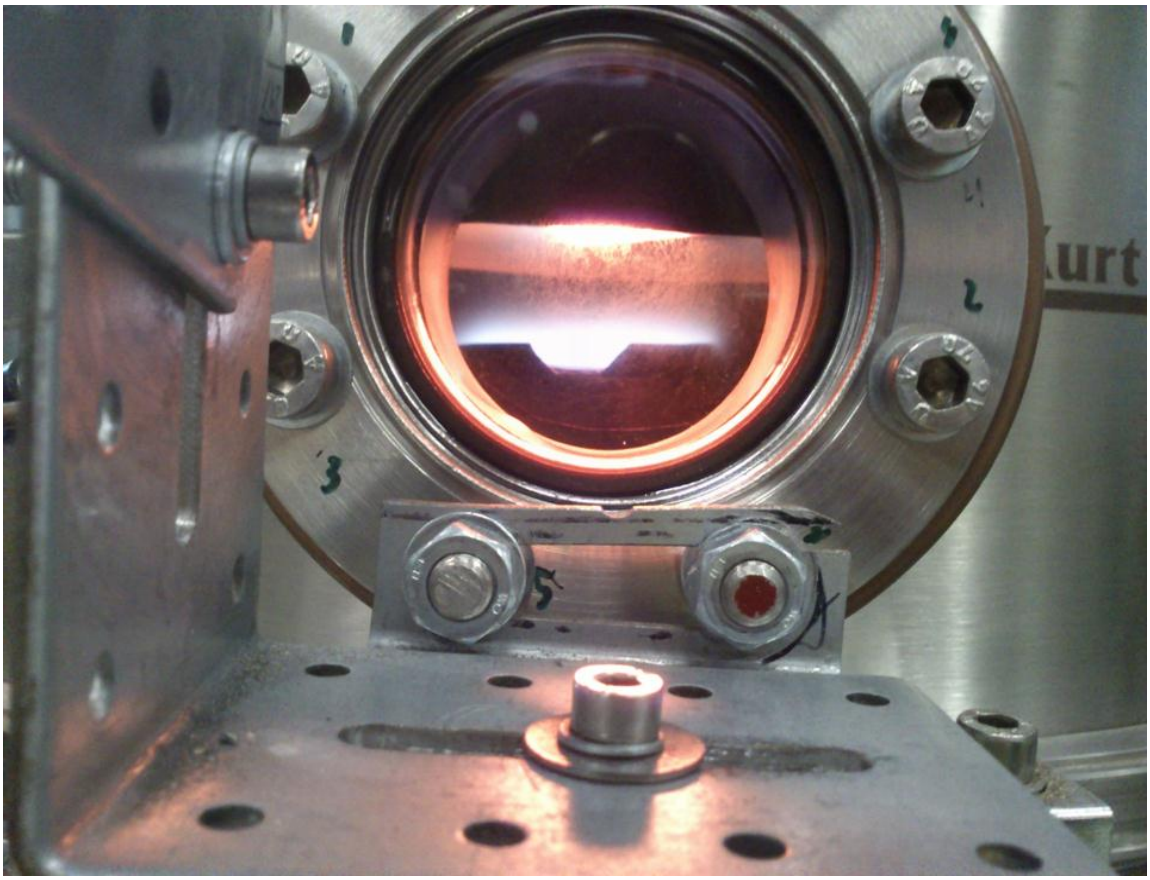

Chapter 9- Growth and functionalization of VACNTS on Quartz filter for environmental applications

9.1. Introduction

A large number of households and industrials products contain volatile organic compounds (VOCs). VOCs can easily evaporate at room temperature and are extremely harmful for the health of human being. Among various types of VOCs, chlorinated compounds are used frequently in a wide range of industrial products and chemical processes, polluting the environment and ground water resources. Therefore, it is desirable to control the chlorinated VOCs emission in air by utilizing various kinds of adsorption / removal processes.

Usually, carbon based adsorbents are used for the removal of contaminants due to their high surface area. The surface area of CNTs is in the range of 150-3000 m^2/g [1], which is comparable to other carbon based adsorbents. CNTs have been shown to be an efficient adsorbent for the elimination of dibenzo-p-dioxin from contaminant water [2]. Also, they can adsorb a variety of gases and have been proven to be superior to activated carbon for the removal of dioxin [3] 1-2 dichlorobenzene from water in a wide range of pH (3-10) [4]. Recently, X Ma et al. [5] have shown the adsorption/desorption of chlorinated compounds by pristine and thermally treated multi-walled carbon nanotubes (MWCNTs). Several features provide CNTs with superior adsorption properties than activated carbon; well defined structure, interstitial region between the nanotubes in the bundles, grooves, the curved surface outside of the nanotube bundles, defect sites and, if the caps of nanotubes are open, the inner surface of tube. Several investigations can be found in the literature, which have shown that CNTs are more effective adsorbents for organic molecules compared to activated carbon [6, 7].

The characteristics of CNTs suggest that they have strong interaction with organic molecules through non-covalent forces, hydrogen bonds, π–π interactions, for instance in polycyclic aromatic hydrocarbons (PAHs) [8], electrostatic forces and van der Waals forces. Three main interactions are responsible for the adsorptions of organic compounds by CNTs; hydrophobic effect, π-electron donor−acceptor (π-EDA) bonds and

hydrogen bonds [9-11]. Multilayer adsorption may also occur when organic chemicals are adsorbed on the surface of CNTs [12]. In addition, it has been shown that CNTs display faster desorption for a wide range of non-polar compounds [13, 14].

Generally, amorphous carbon and catalyst particles are also present on the surface of the as grown CNTs, which can significantly decrease the adsorption and desorption efficiency of the CNTs by blocking their pores [15]. The removal of amorphous carbon is usually achieved by heating the CNTs at 300-500ºC and the catalyst particles can be eliminated by acid treatment [16]. This treatment results in the destruction of the structure and introduction of carboxylic groups in CNTs. Furthermore, it is rather difficult to control and very harsh for the graphitic walls of CNTs [16-18]. Our previous studies show that the CNTs surface can be cleaned and crafted with different functional groups by controlling the plasma treatment conditions (rf plasma power, gas composition and pressure) [19, 20].

In the present chapter, vertically-aligned multiwall carbon nanotubes (VAMWCNTs) were grown on quartz filters, which at the best of our knowledge, has not been previously reported in the literature. A water plasma treatment was performed on the as grown CNTs to remove the amorphous carbon, increase the defect sites and to preferentially introduce different kinds of oxygen functional groups [19]. The introduction of oxygen groups on the surface of CNTs through a water plasma treatment allows us to increase the interactions with VOCs. Surface functional groups such as carboxyl groups facilitate the formation of stronger π–π bonds between CNTs and aromatic molecules [21]. The hydroxyl groups can form hydrogen bonds with electronegative atoms, typically F, O, N and Cl. Moreover, hydrogen atoms attached to a carbon atom can also participate in hydrogen bonding when the carbon atom is bounded to electronegative atoms, like in the case of chloroform ($CHCl_3$).

The adsorption/desorption properties of chlorinated VOCs on quartz filter (QF), carbon nanotubes grown on QF (CNTsQF) and water plasma treated CNTsQF (WP-CNTsQF) have been investigated in detail.

9.2. Experimental section

9.2.1. Synthesis and functionalization of VA-MWCNTs on Quartz Filters

VAMWCNTs were grown on quartz filters by using radio-frequency plasma-enhanced chemical vapour deposition (rf-PECVD). A summary of the growth conditions is given in (Table 9.1). High-purity quartz (SiO_2) microfiber filters (Whatman^{tm}, UK) were used as substrates for the growth of CNTs. These quartz filters have 47 mm of diameter, 450 μm thickness and they are formed by long fibers having a diameter below 1.5 μm. Briefly, a thin layer of 3 nm Fe catalyst was deposited by rf-magnetron sputtering on a quartz filter and annealed at 680ºC during 120 s (ramp time: 750 s) in hydrogen atmosphere to obtain Fe nanoislands. Then, the precursor gas (NH_3, 80 Pa, 100 sccm) and the carbon source (C_2H_2, 100 Pa, 50 sccm) are allowed to enter the reaction chamber and the PECVD reaction takes place with the formation of CNTs.

Table 9.1: Summary of the VACNTs growth conditions.

Parameter	Value
Catalyst layer thickness	3 nm
Annealing time	870 s
PECVD process temperature	700ºC, 730ºC,
PECVD process plasma power	50 W
PECVD process time	900 s, 1800 s

In a first attempt, the sample was heated using a PID Xantrex heater (XDC 60-100) controlled by a pyrometer. However, due to the fibrous nature of the quartz filter the radiation emitted by the heating element was scattered in all directions. As a consequence, the temperature measured by the pyrometer corresponded to that of the heating element and not of the substrate. In order to correct this, the power supplied to the heater while annealing a silicon wafer under the same conditions, was applied to our quartz filters.

In a further step some of the samples were treated with water plasma to remove amorphous carbon and introduce oxygen groups on the CNTs surface. The CNTs were treated with10 W rf power and 135 Pa water pressure for 120 s, which is only specific to the removal of amorphous

carbon and the introduction of different oxygen containing functional groups, without destroying the nanotubes [19].

9.2.2. Volatile Organic Compounds (VOCs)

The adsorption/desorption properties of CNTs were studied using three chlorinated VOCs; trichloroethylene, chloroform and 1,2-dichlorobenzene. The chemicals were from high purity (99.9 %, Sigma-Aldrich) and were used undiluted.

9.2.3. Adsorption study setup

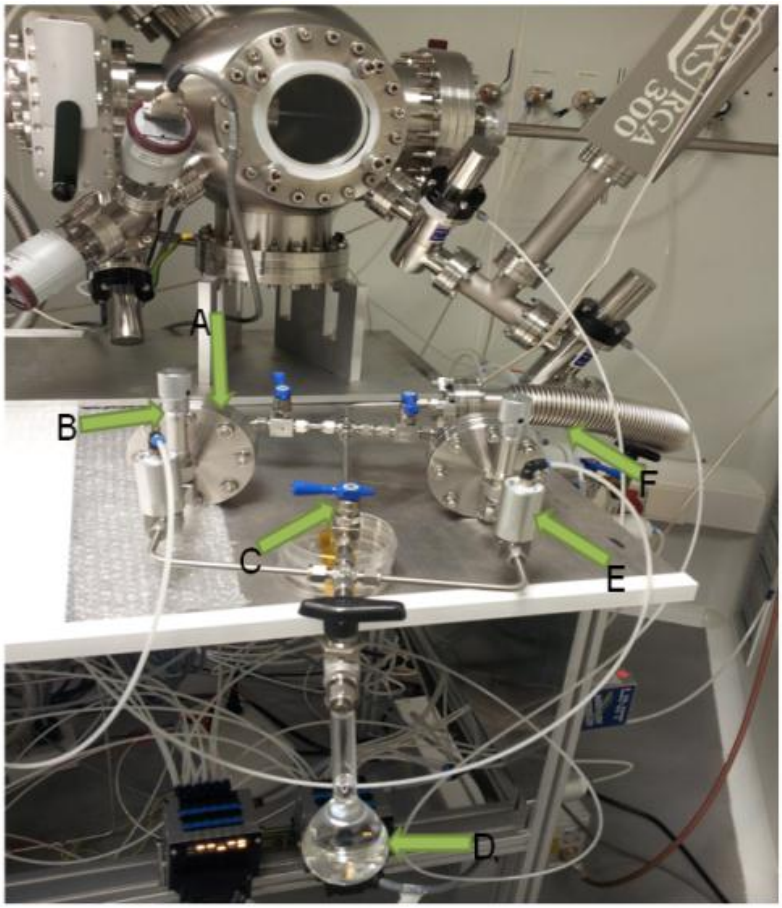

Figure 9.1: Experimental set-up to measure adsorption of VOCs. A) filter holder, B) flow valve, C) manual valve, D) flask containing VOC, E) pneumatic valve, F) RGA input.

A system was devised to study the adsorption of volatile organic compounds by CNTs-based filters (see figure 9.1). The system has three

channels made of a stainless steel tube with an internal diameter of 4 mm and an external diameter of 6.32 mm. A flask containing the chlorinated compound to be studied is placed at the start of the central channel, and is connected to a three-way valve. Both left and right channels have a filter holder at the end, where the carbon nanotubes filter is placed. The filter is held by an aluminum filter holder, designed especially for the size of the filters. The whole system is connected to a turbo-molecular pump, which allows operation under high vacuum conditions (10^{-5} Pa) and all experiments were carried out at room temperature.

A filter without carbon nanotubes is placed in the right channel and is taken as a reference. In the left channel different types of carbon nanotube filters are placed and systematically analyzed (untreated CNTs and wp-treated CNTs). In order to perform the measurements, a LabVIEW program controls the opening of the pneumatic valves present at the entrance of each channel during a period of 50 ms, letting the chlorinated compound flow through the filter under study. Immediately after opening the valves, the RGA detects a fast increase of the partial pressures of the species followed by a slower decrease related to adsorption and desorption processes. The partial pressure of the compounds can be related to the concentration of the chemical species in the gas phase. Therefore, we can get an idea about the kinetics of the adsorption/desorption processes that occur at the surface of the different CNTs-based filters by representing the partial pressure versus time in a semi-logarithmic scale.

Since the adsorption process was too fast to be analyzed with our setup, we studied the desorption curves of the different compounds. The measurements could be fitted with a double exponential (equation (9.1)), which indicates the presence of two desorption processes. Depending on the interactions between VOC and filter, only one of the two mechanisms was observed. In those cases, a simple exponential equation was used.

$$P(t) = P_R + P_1 \exp[-(t - t_0)/\tau_1] + P_0 \exp[-(t - \tau_0)/\tau_2] \quad (1)$$

where P_1 and P_2 are partial pressures in Pa, P_R is the residual pressure in Pa, t is the time in s, t_0 the initial time of desorption process in s, τ_1 and τ_2 are the characteristic times in s.

9.3. Results *and discussion*

9.3.1. *Morphological characterization*

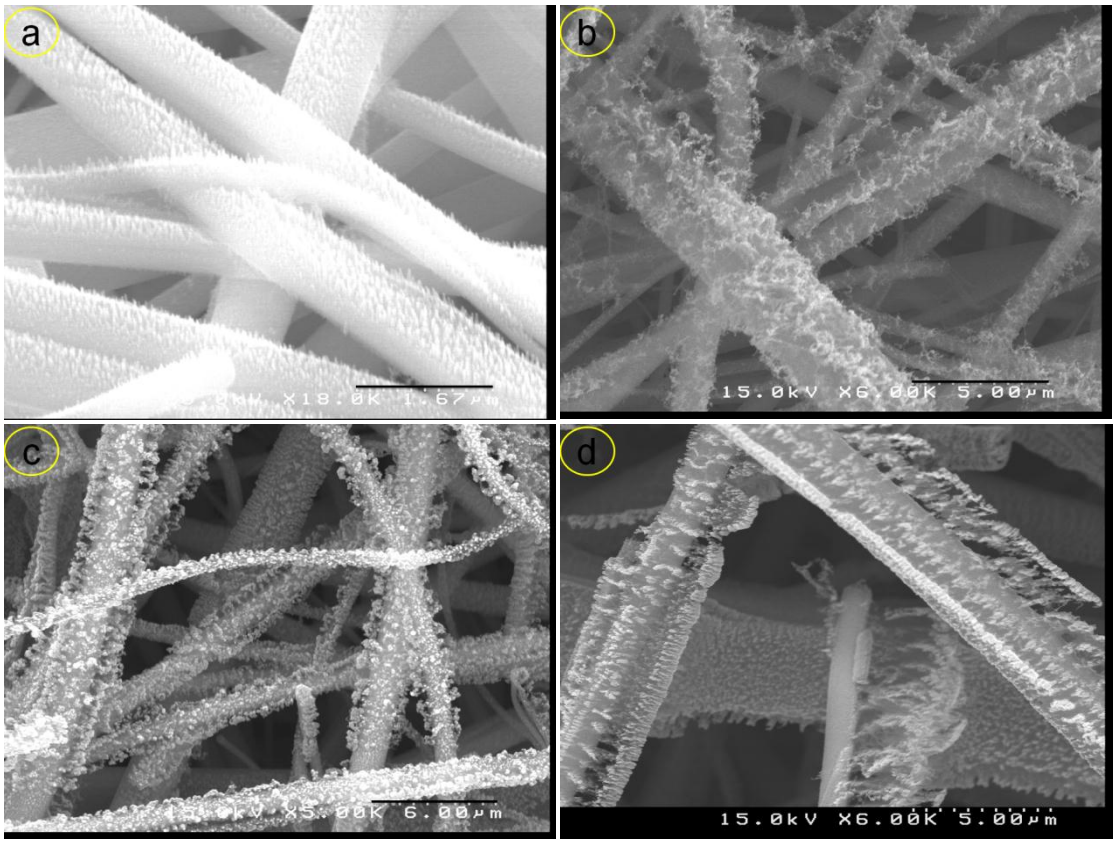

Figure 9.2: SEM images of CNTs grown on quartz filter (a) at 700ºC for 15 min and (b) at 730ºC for 30 min. (c) WP-treated CNTsQF at 10 W plasma power and 135 Pa pressure.

In order to increase the VOCs adsorption capacity of the quartz filters, a large surface area is needed, which can be achieved by growing long CNTs with high surface density on top of them. 'Figure 9.2(a)' shows CNTs grown without controlling the power manually to anneal the quartz filter, as it can be seen CNTs barely start to grow. 'Figure 9.2(b)' shows CNTs grown on QF at an annealing temperature of 680ºC, a growth temperature of 700ºC and growth time of 15 min. Under these conditions the CNTs were not vertically aligned and their density was also not very high. 'Figure 9.2(c)' shows a SEM image of CNTs grown at a higher growth temperature (730ºC) and longer deposition time (30 min). The density of CNTs increases significantly with respect to those grown at 700ºC and they are vertically aligned in all directions of the quartz fibers. 'Figure 9.2(d)' shows WP-treated CNTsQF at an rf power of 10 W and 135 Pa water pressure. Most of the amorphous carbon is removed while

keeping the alignment and a difference in texture can be appreciated in comparison to untreated CNTs. ‘Figure 9.3(a, b)’ shows a TEM image of untreated MWCNTs CNTs attached to the quartz fiber that clearly displays their “bamboo”-like structure, as well as the amorphous carbon on the surface and Fe catalyst particles on the tips of CNTs.

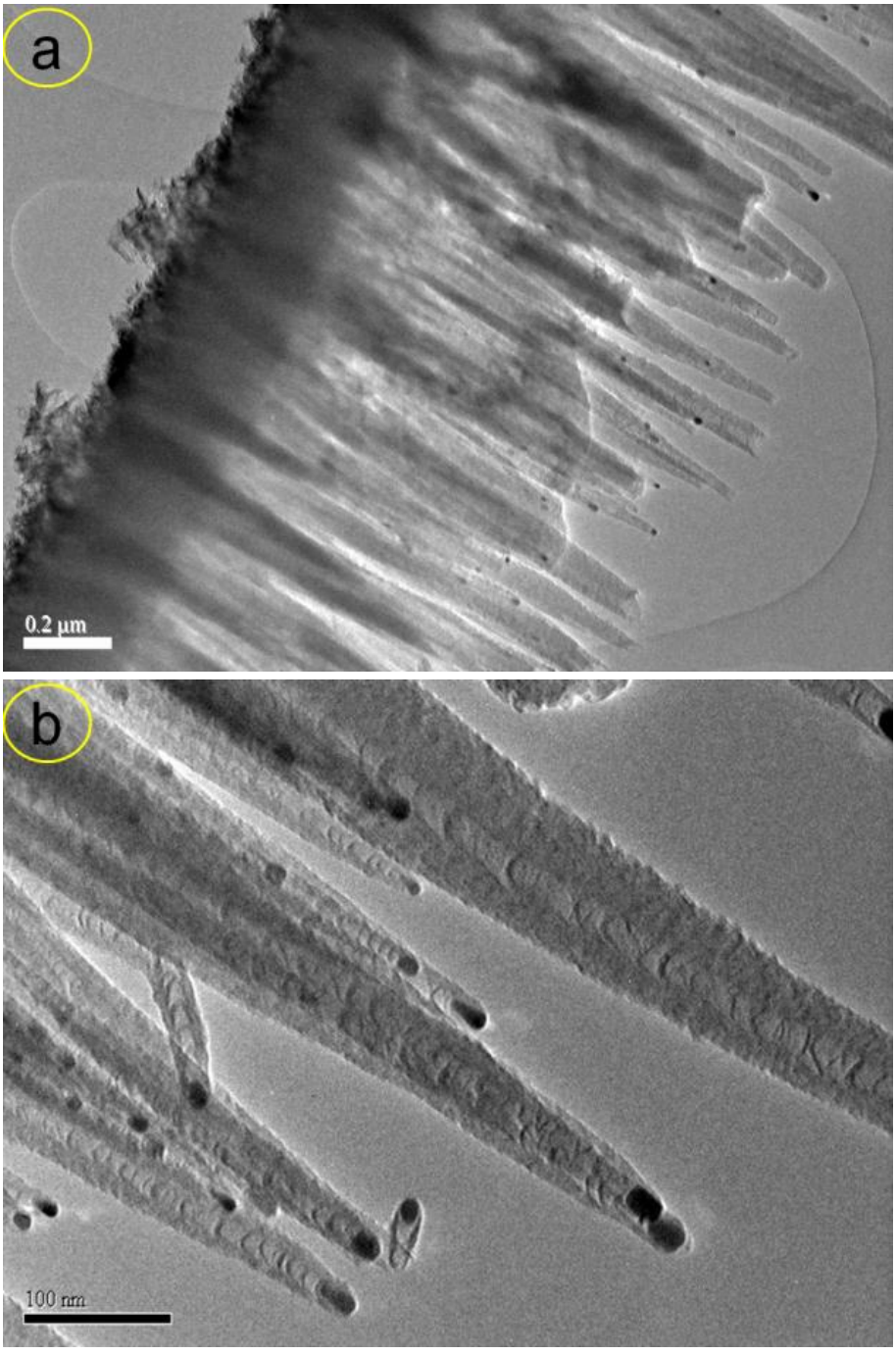

Figure 9.3: HRTEM image of untreated CNTs on quartz filter.

9.3.2. Raman characterization

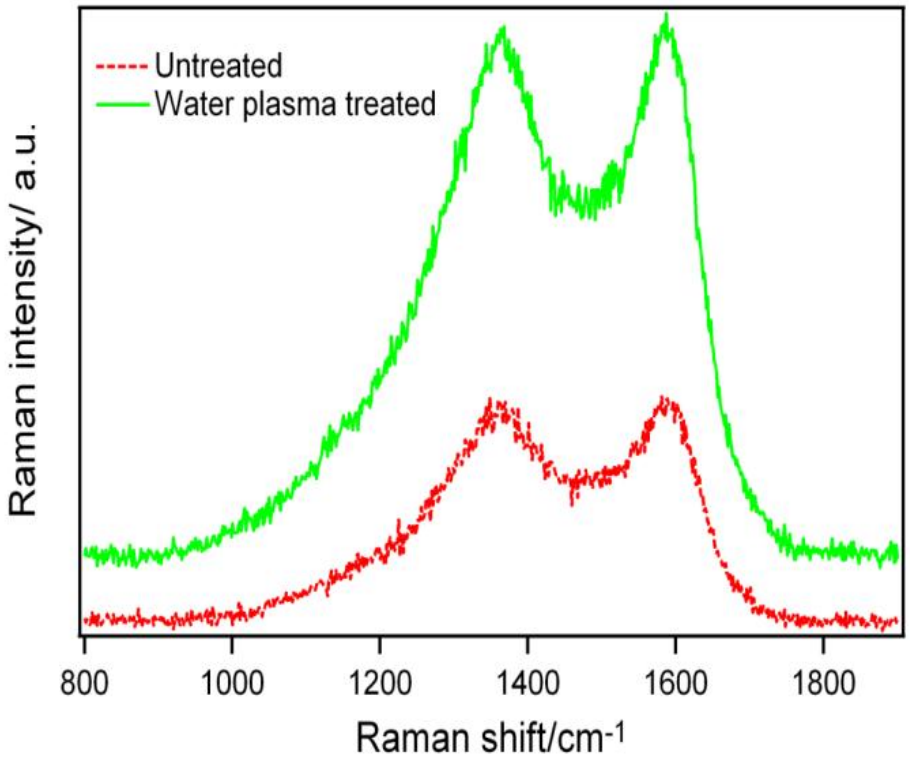

Figure 9.4: Raman spectra of untreated CNTsQF and WP-CNTsQF.

'Figure 9.4' shows Raman spectra of CNTsQF and WP-CNTsQF. The fitting process was improved by the introduction of I band at ~1210 cm^{-1} and $D^{''}$ band at the frequency of ~1520 cm^{-1} [22]. D band position was 1360 cm^{-1} with full width half maximum (FWHM) of 83 cm^{-1} for untreated CNTsQF. After the water plasma treatment a very small shift in the D band position and FWHM for water plasma treated CNTsQF was observed, because the treatment is mainly specific to the removal of amorphous carbon, i.e very little etching of CNTs walls, and to the introduction of functional groups in CNTs [23]. The I_D/I_G ratio was 1.1 for untreated CNTsQF and increases up to 1.3 for water plasma treated MWCNTsQF, which suggests a higher disorder in the structure of treated CNTs. After the water plasma treatment I and $D^{//}$ bands become more prominent. The enlargement of the $D^{//}$ band is in agreement with the expected attachment of polar groups on the CNTs surfaces [24, 25]. The area of the $D^{//}$ peak increases from 170 to 547 and the $I_{D^{''}}/I_G$ ratio from 0.46 to 0.62, for untreated CNTsQF to WP-CNTsQF, respectively.

9.3.3. Adsorption/desorption studies

CNTs are normally grown in the form of bundles and behave as heterogeneous sorbents. They provide four sites for the adsorption of contaminants, namely; interstitial channels, external groove sites between the bundles, external surfaces and, if the tips are open, i.e. without catalyst particles that remain on the top of each individual nanotube, internal surfaces of CNTs [22]. Since the presence of amorphous carbon reduces the adsorption/desorption efficiency of CNTs [26], it is desirable to remove it while preserving the structure of the CNTs. Here, a water plasma treatment was used to eliminate amorphous carbon. In addition, the treatment introduces oxygen functional groups and defect sites on the CNTs surface that can significantly enhance the adsorption efficiency of contaminants [27-29].

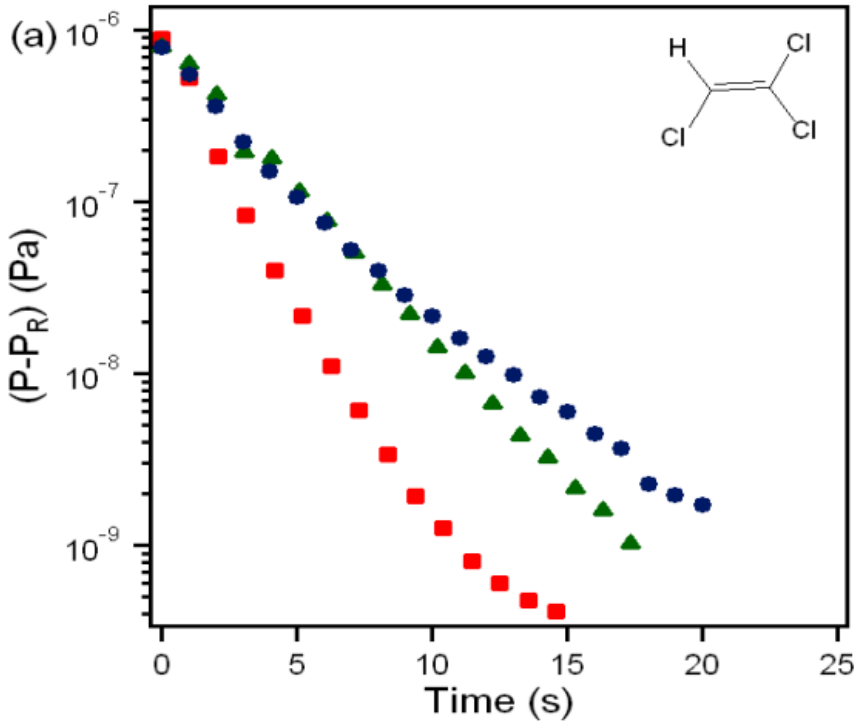

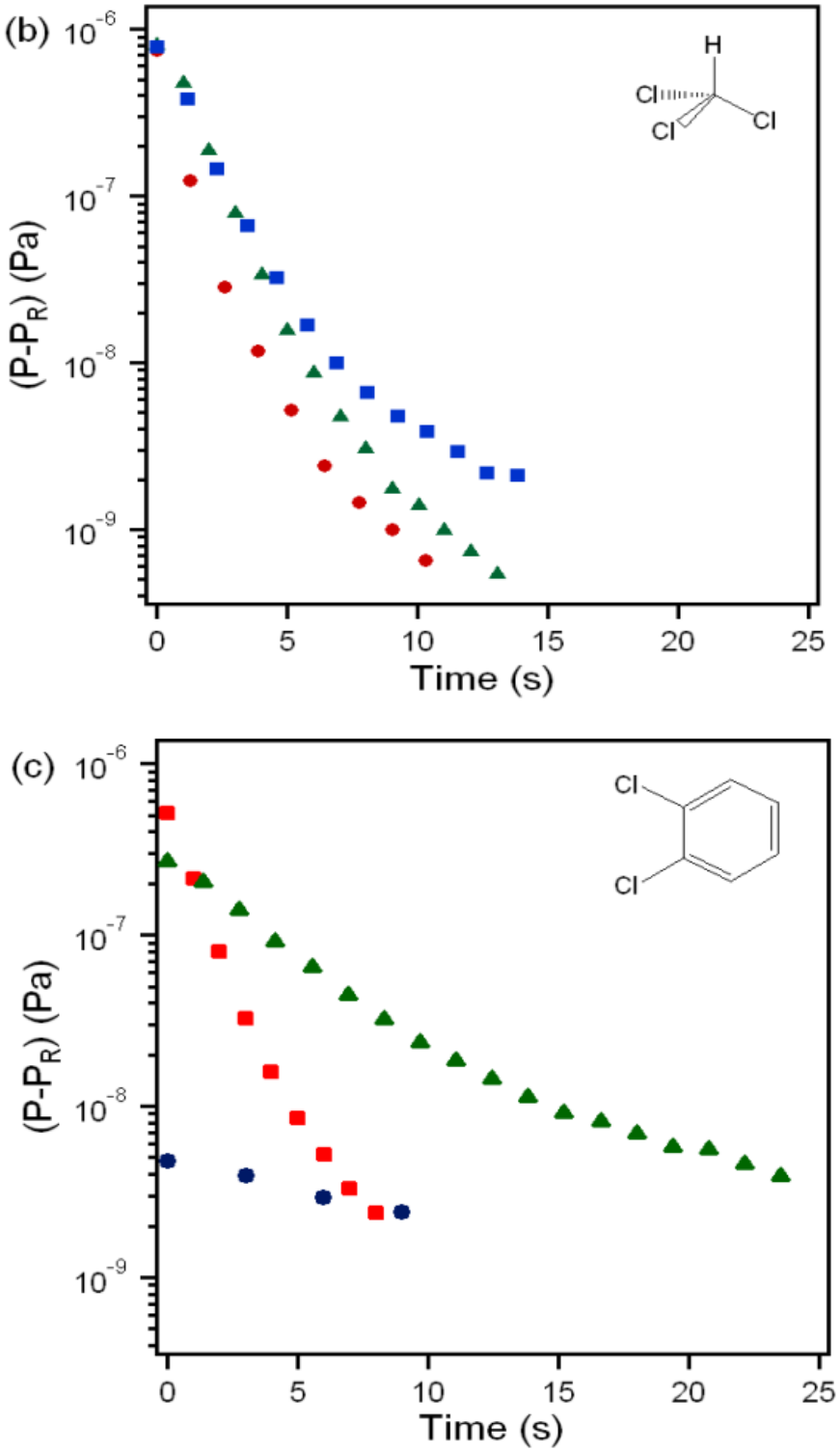

Figure 9.5: Comparative desorption study. Desorption process of (a) trichloroethylene, (b) chloroform and (c) 1,2-dichlorobenzene. Squares: QF, triangles: CNTsQF and circles: WPCNTsQF.

The three chlorinated compounds are non-polar solvents with a low solubility in water (i.e., hydrophobic). In particular, the water solubility values are 0.11, 0.815 and 1.4 %, which follow the same trend as the molecular dipole moment; 0.8, 1.01 and 2.5 D for trichloroethylene, chloroform and 1,2-dichlorobenzene, respectively.

For all the studied VOCs characteristic desorption times increased from bare QF to CNTsQF and wp-CNTsQF. The latter being the one with the longest characteristic desorption times (see table 9.2). In the case of trichloroethylene it was found that carbon nanotubes increase the time constant of the slow desorption mechanism (τ_2) (table 9.2, figure 9.5 (a)), which is assumed to be mainly related to π-π interactions between CNTs and the C=C bond present in C_2HCl_3 [5, 8]. Due to the removal of amorphous carbon after the water plasma treatment, and the corresponding surface area enhancement that provides more space for solute adsorption, the desorption time of the wp-CNTsQF sample increased with respect to that of untreated CNTs (figure 9.5(a), table 2). Moreover, the introduction of oxygen groups on the CNTs surface enhanced the πEDA interactions with the VOC.

Owing to the lack of π electrons in chloroform, the main interactions with CNTs are πEDA and hydrogen bonding. The water solubility and dipole moment are slightly higher than for trichloroethylene and hence, the interactions are stronger and characteristic times longer (table 2, figure 9.5(b)). However, the total desorption time is shorter than for trichloroethylene, probably due to steric effects that avoid the adsorption of more molecules.

In comparison to the other studied VOCs, 1,2-dichlorobenzene contains an aromatic ring and combines a high polarity index with a high solubility in water. Thus, the main interactions with CNTs are supposed to be polar-π interaction, πstacking and hydrogen bonding. Plasma-treated CNTs without amorphous carbon and with oxygen functional groups attached on their surface increase the aromatic-aromatic interactions between 1,2-dichlorobenzene and aromatic rings present in the CNTs structure [29]. Due to the large difference in the characteristic time between bare QF and carbon nanotubes-based filters, we can assume that possibly a multilayer condensation occurs (πstacking interactions), which significantly increases their adsorption (figure 9.5(c)).

Table 9.2: Characteristic desorption times of different VOCs on quartz filter, CNTsQF and plasma treated CNTsQF.

VOC	Filter τ_1(s) / τ_2(s)		
	QF	CNTs	wp-CNTsQF
trichloroethylene	0.85 / 1.74	- / 2.38	- / 2.70
chloroform	0.65 / 2.28	0.99 / 2.32	1.28 / 2.70
1,2-dichlorobenzene	1.10 / -	3.25 / 13.76	- / 15.29 *

* due to the small number of points, this value has a large error associated with it. However, the value fits well with the one obtained for desorption of 1, 2-dichlorobenzene on CNTsQF, and therefore, it is regarded as reliable.

From the above results it was not possible to determine the difference between the mechanisms that govern the two characteristic desorption times (τ_1 and τ_2). Future experiments should be carried out in order to explain the observed behavior.

9.4. Conclusions

Vertically-aligned multiwall carbon nanotubes have been successfully deposited on quartz fiber filters for environmental applications. A water plasma treatment of the grown nanotubes introduces oxygen functional groups on their surface without modification of their alignment. The presence of inner cavities and functional groups on the CNTs surface contribute to improve their capability to remove or selectively detect organic pollutants. It has been proven that the adsorption/desorption capacity of chlorinated VOCs by CNTsQF and wp-CNTsQF is higher than that of bare QFs. In addition, the presented results show that CNTsQF and wp-CNTsQF affinity for the adsorption/desorption of chlorinated VOCs increases with compound solubility in water and polarity. Finally, molecules with aromatic rings present stronger interactions with CNTs (π–stacking) and thus, significantly longer desorption times and time constants.

9.5. References

[1] Agnihotri S, Root MJ and Abadi MR, *Adsorption equilibrium of organic vapors on single-walled carbon nanotubes*, (2005), Carbon, 43, 2379-2388.

[2] Fugestsu B, Satoh S, Iles A, Tanaka K, Nishi N and Watari F, *Encapsulation of multi-walled carbon nanotubes (MWCNTs) in Ba^{2+} alginate to form coated micro-beads and their applications to the pre-concentration/elimination of dibenzo-p-dioxin, dibenzofuran, and biphenyl from contaminated water*, (2004), Analyst, 129, 565-566.

[3] Long RQ and Yang RT, *Carbon nanotubes as superior sorbent for dioxin removal*, (2001), J Am Chem Soc, 123, 2058-9.

[4] Peng X, Li Y, Luan Z, Di Z, Wang H, Tian B and Jia Z, *Adsorption of 1,2-dichlorobenzene from water to carbon nanotubes*, (2003), Chem. Phys.Lett, 376, 154–158.

[5] Ma X, Anand D, Zhang X and Talapatra S. *Adsorption and desorption of chlorinated compounds from pristine and thermally treated multiwalled carbon nanotubes*, (2011), J. Phys. Chem. C, 115, 4552-4557.

[6] Su F and Lu C, *Adsorption kinetics, thermodynamics and desorption of natural dissolved organic matter by multiwalled carbon nanotubes*, (2007), J Environ Sci Health A Tox Hazard Subst Environ Eng, 42, 1543-52.

[7] Sheng G, Li J, Shao D, Hu J, Chen C, Chen Y and Wang X, *Adsorption of copper(II) on multiwalled carbon nanotubes in the absence and presence of humic or fulvic acids*, (2010), J Hazard Mater, 178, 333-40.

[8] Kah M, Zhang X, Jonker MT and Hofmann T, *Measuring and modeling adsorption of PAHs to carbon nanotubes over a six order of magnitude wide concentration range*, (2011), Environ Sci Technol, 45, 6011-7.

[9] Yang K, Wu W, Jing Q and Zhu L, *Aqueous adsorption of aniline, phenol, and their substitutes by multi-walled carbon nanotubes*, (2008), Environ Sci Technol, 42, 7931-6.

[10] Lin D and Xingt B, *Adsorption of phenolic compounds by carbon nanotubes: role of aromaticity and substitution of hydroxyl groups*, (2008), Environ Sci Technol, 42, 7254-9.

[11] Yang K, Wu W, Jing Q, Jiang W and Xing B, *Competitive adsorption of naphthalene with 2,4-dichlorophenol and 4-chloroaniline on multiwalled carbon nanotubes*, (2010), Environ Sci Technol, 44, 3021-7.

[12]. Gotovac S, Hattori Y, Noguchi D, Miyamoto J, Kanamaru M, Utsumi S, Kanoh H and Kaneko K, *Phenanthrene adsorption from solution on single wall carbon nanotubes*, (2006), J Phys Chem B, 110, 16219-24.
[13] Agnihotri S, Mota JP, Rostam-Abadi M and Rood MJ, *Theoretical and experimental investigation of morphology and temperature effects on adsorption of organic vapors in single-walled carbon nanotubes*, (2006), J Phys Chem B, 110, 7640-7.
[14] Hussain CM, Saridara C and Mitra S, *Microtrapping characteristics of single and multi-walled carbon nanotubes*, (2008), J Chromatogr A, 1185, 161-6.
[15] Gotovac S, Song L, Kanoh H and Kaneko K, *Assembly structure control of single wall carbon nanotubes with liquid phase naphthalene adsorption*, (2007), Colloids and Surfaces A: Physicochem. Eng. Aspects, 300, 117–121.
[16] Chen J, Hamon MA, Hu H, Chen Y, Rao AM, Eklund PC and Haddon RC, *Solution properties of single-walled carbon nanotubes*, (1998), Science, 282, 95-8.
[17] Datsyuk V, Kalyva M, Papagelis K, Partgenios J, Tasis D, Siokou A, Kallitsis I and Galiotis C, *Chemical oxidation of multiwalled carbon nanotubes*, (2008), Carbon, 46, 833-40.
[18] Chakrapani N, Curran S, Wei B and Ajayan PM, *Spectral fingerprinting of structural defects in plasma treated carbon nanotubes*, (2003), J. Mater. Res, 18, 10, 2515-2521.
[19]. Hussain S, Amade R, Jover E and Bertran E, *Functionalization of carbon nanotubes by water plasma*, (2012), Nanotechnology, 23, 385604.
[20] Hussain S, Amade R, Jover E and Bertran E, *Nitrogen plasma functionalization of carbon nanotubes for supercapacitor applications*, (2013), J. Mater. Sci. 48, 7620-7628.
[21] Li P, Zong Y, Zhang Y, Yang M, Zhang R, Li S and Wei F, *In situ fabrication of depth-type hierarchical CNT/quartz fiber filters for high efficiency filtration of sub-micron aerosols and high water repellency*, (2013), Nanoscale, 5, 3367-72.
[22] Oswald S, Havel M and Gogotsi Y, *Monitoring oxidation of multiwalled carbon nanotubes by Raman spectroscopy*, (2007), J. Raman Spectrosc, 38, 728-36.

[23] Cuesta A, Dhamelincourt P, Laureyns J, Martinez-Alonso A and Tascon JMD, *Raman microprobe studies on carbon materials*, (1994), Carbon, 32, 1523-1532.
[24]. Reich S, Thomsen C and Maultzsch J, *Carbon Nanotubes: Basic Concepts and Physical Properties.* Weinheim: Wiley–VCH. 2004; 224.
[25] Ramos SC, Vasconcelo C, Antunes EF, Lobo AO, Trava-Airoldi VJ and Corat EJ, *Wettibility controlon vertically aligned multiwalled-carbon nanotube surfaces with oxygen pulsed DC plasma and CO_2 laser treatments,* (2010), Diam.Relat. Mat, 19, 752–755.
[26] Yang K and Xing B, *Desorption of polycyclic aromatic hydrocarbons from carbon nanomaterials in water*, (2007), Environ Pollut, 145, 529-37.
[27] Chakrapani N, Zhang YM, Nayak SK, Moore JA, Carroll DA, Choi YY and Ajayan PM, *Chemisorption of acetone on carbon nanotubes*, (2003), J. Phys. Chem. B, 107, 9308-9311.
[28] Zhou LG and Shi SQ, *Adsorption of foreign atoms on stone-walls defects in carbon nanotubes,* (2003), Carbon, 41, 579–625.
[29] Pan B and Xing B, *Adsorption mechanisms of organic chemicals on carbon nanotubes*, (2008), Environ Sci Technol, 42, 9005-13.

PART IV- CONCLUSIONS

Conclusions

1) CNTs were successfully grown on different types of substrates (Si wafer, copper, MEAs, carbon paper, and graphite) by means of hot wire radio frequency plasma chemical vapor deposition. SEM and HRTEM observations tell the nanotubes were vertically aligned and posses the bamboo like multiwall structure.

2) Water plasma treatment was performed to remove amorphous carbon and to functionalize the surface of CNTs with different oxygen groups. Box-Wilson experimental design was adopted to optimize two important parameters (rf-power and water pressure). We are able to introduce the desired oxygen functional groups on the surface of CNTs. Moreover, we also found the strong water plasma conditions that can completely destroy the CNTs.

3) MWCNTs were decorated with various nitrogen based functional groups (pyridinic, pyrrolic and quaternary). To achieve the desired functionalities, we optimized two experimental parameters (rf-power and nitrogen pressure) by following Box-Wilson experimental design.

4) Raman and HRTEM characterizations show that water plasma is more effective over nitrogen plasma to remove the amorphous carbon. As well as peeling of the outer planes of MWCNTs by water plasma in much faster than nitrogen plasma. We can successfully renovate the CNTs with oxygen or nitrogen functional groups, depending on the desired application.

5) Cyclic voltammetry measurements show water plasma treatment significantly increased the active surface area of CNTs, and nitrogen plasma is more effective to improve the charge transfer. Both nitrogen and water plasma raise the capacitance of CNTs notably in comparison to untreated CNTs.

6) Manganese dioxide was deposited by galvanostatic method on the untreated CNTs, water plasma treated and nitrogen plasma treated

nanotubes. Electrochemical measurements of the nanocomposite MnO_2/CNTs show voltage window plays an important role on the morphology of the MnO_2. The MnO_2 structure could change from nanoflower as deposited to needle like or to a layer coating on the surface of CNTs during the cycling measurements. The CNTs treated with 75 W plasma power and 10 Pa nitrogen pressure, and further functionalized with MnO_2, exhibit highest specific capacitance of 955 Fg^{-1} at 10 mVs^{-1}. This value is almost 87% of the theoretical value for MnO_2.

7) Ultra long CNTs were synthesized by sputtering alumina as a buffer layer between Fe (catalyst) and Si substrate during the water assisted growth of CNTs. Annealing of thin catalyst film was done at 600°C and growth of CNTs at a relatively low temperature (700°C).

8) Water vapor enhances the crystallinity of growing nanotubes and their length increases with growing time. However, the presence of water vapor gradually changes their structure from multiwall to thinner one or, even, single wall carbon nanotubes.

9) The electrochemical properties of the obtained ultralong CNTs forests were analyzed by transferring them on adhesive conductive aluminum tape using a novel methodology.

10) A water plasma treatment was performed in order to introduce oxygen functional groups on the transferred CNTs (CNTs/Al). The specific capacitance of CNTs/Al increases from 87 to 148 Fg^{-1} for untreated and water plasma treated CNTs/Al, respectively.

11) For a successful growth of CNTs a homogeneous distribution of catalyst particles on the substrate is essential. A thin layer at high temperatures such as the ones used for the annealing of the catalyst (Fe, Ni), diffusion towards the substrate happens. In order to minimize this effect a buffer layer of 10 nm of alumina were first sputtered onto the substrate.

12) In addition, we found a strong adhesion of CNTs through the alumina buffer layer to the substrate, which shows the key role of alumina during the growth process of CNTs on copper substrate.

13) We found a multilayered setup ($Cu/Ni/Ti/Al_2O_3$) prior to deposit catalyst could boost the growth rate and quality of CNTs.

14) CNTs were tested for supercapacitor application, as grown on copper substrate and after a nitrogen plasma treatement. Two CNTs electrode cell configuration was used with $LiClO_4$ as electrolyte in a voltage window of 2.5 V. The specific capacitance increases from 49 to 227 Fg^{-1} for untreated to nitrogen plasma treated CNTs at scan rate of 10 mVs^{-1}. CNTs shown almost stable cyclability up to 1200 cycles at a current density of 5.5 Ag^{-1} in a voltage window of 2.5 V.

15) Vertically-aligned CNTs were synthesized on the quartz fiber filters for environmental applications. Three chlorinated VOCs; trichloroethylene, chloroform and 1,2-dichlorobenzene were used to stuy the adsorption/desorption properties of CNTs/QF. The ability to detect or remove organic pollutants increased after the water plasma functionalization and also by removing the catalyst from the top of CNTs to provide the inner cavities for use. We found molecules with aromatic rings present stronger interactions with CNTs (π–stacking).

Although a number of important conclusions have been reached in the course of this thesis, several phenomena reported here need further investigation. As a general conclusion and looking at future work, we can suggest the next research points:

1) Optimization of growth parameters of hollow cylindrical shape multiwall carbon nanotubes. Investigation of the difference in supercapacitor properties of hollow cylindrical shaped, permiting internal electronic transport, and bamboo-like shaped MWCNTs.

2) Deposition of MnO_2 and other metal oxides on untreated hollow cylindrical shape MWCNTs and plasma treated MWCNTs by anodic

deposition method or other techniques for supercapacitor applications.

3) Deposition of metal oxides on the aluminum transferred ultralong CNTs.

4) The use of CNTs grown directly on the copper substrate as an anode material for Li-ion batteries.

5) Improve the adsorption/desorption properties of CNTs based quartz filters by growing ultralong CNTs with high specific surface.

Appendix: List of deposited CNTs

	sample	Substrate			Annealing				RF-PECVD (50 W)						
		Type	RF magnetron		H_2 parameters		General parameters		Gas replacement H_2 to NH_3			C_2H_2 parameters			
			Fe (nm)	Bias (V)	sccm	Pa	˚C	R, H (s)	(sccm), (Pa)	(s)	(V)	(sccm)	Pa	G (t)	R
1	08G10a	Si	3	-106	100	200	680	750, 120	100, 80	30	-416	50	100	900	ok
2	09G10a	Si	3	-106	100	200	680	750, 120	100, 80	30	P		-	-	NG
3	15G10a	Si	3	-97	100	200	680	750, 120	100, 80	30	-443	50	100	900	G
4	19G10a	Si	3	-105	100	200	680	750, 120	100, 80	30	-406	50	100	900	G
5	20G10a	Si	3	-96	100	200	680	750, 120	100, 80	30	-480	50	100	900	NG
6	20G10b	Si	3	-93	100	200	680	750, 120	100, 80	30	-425	50	100	900	NG
7	22G10a	Si	3	-102	100	200	680	750, 120	100, 80	30	P	-	-	-	NG
8	22G10b	Si	3	-98	100	200	680	750, 120	100, 80	30	P	-	-	-	NG
9	27G10a	Si	3	-97	100	200	680	750, 120	100, 80	30	P	-	-	-	NG
10	28G10a	Si	3	-94	100	200	680	750, 120	100, 80	30	P	-	-	-	NG
11	05H10a	Si	3	-97	100	200	680	750, 120	100, 80	30	-420	50	100	900	G
12	06H10a	Si	3	-99	100	200	680	750, 120	100, 80	30	-398	50	100	900	G
13	09H10a	Si	3	-99	100	200	680	750, 120	100, 80	30	P	-	-	-	NG
14	10H10a	Si	3	-97	100	200	680	750, 120	100, 80	30	-400	50	100	900	G
15	01I10a	Si	3	-94	100	200	680	750, 120	100, 80	30	-420	50	100	900	G
16	02I10a	Si	3	-96	100	200	680	750, 120	100, 80	30	-398	50	100	900	NG
17	08I10a	Si	3	-94	100	200	680	750, 120	100, 80	30	-443	50	100	900	NG
18	09I10a	Si	3	-95	100	200	680	750, 120	100, 80	30	-400	50	100	900	NG
19	06J10a	Si	3	-94	100	200	680	750, 120	100, 80	30	-413	50	100	900	G
20	06J10b	Si/Pt/Fe-Ni(CNM)			100	200	700	750, 120	100, 80	30	-442	50	100	900	ok
21	11J10b	MEAs (Ni/30 nm)			100	200	600	800, 30	100, 80	30	-390	50	100	900	ok
22	19J10a	MEAs (Ni/30 nm)			100	200	600	800, 30	100, 80	30	-400	50	100	900	ok
23	19J10c	Si	3	-96	100	200	600	750, 120	100, 80				-	-	-
24	20J10a	Si	3	-95	100	200	680	750, 120	100, 80	30	-396	50	100	900	ok
25	21J10b	Si	3	-96	100	200	680	750, 120	100, 80	30	-400	50	100	900	ok
26	25J10a	Si	3	-91	100	200	680	750, 120	100, 80	30	Problem with plasma			-	-
27	25J10b	Si	3	-100	100	200	680	750, 120	100, 80	30	Problem with plasma			-	-
28	29J10a	Si	3	-94	100	200	680	750, 120	100, 80	30	-416	50	100	900	NG
29	02K10b	QF	3	-94	100	200	680	750, 120	100, 80	30	-409	50	100	900	NG
30	03K10a	QF	3	-96	100	200	680	750, 120	100, 80	30	-402	50	100	900	NG
31	03K10b	Si	3	-96	100	200	680	750, 120	100, 80	30	-432	50	100	900	ok
32	04K10a	Si	3	-94	100	200	680	750, 120	100, 80	30	-423	50	100	900	G
33	05K10a	QF	3	-95	100	200	680	750, 120	100, 80	30	-450	50	100	900	NG
34	10K10a	MEAs (Ni/30 nm)			100	200	650	120, 1	100, 80	-	-545	Problem with pressuer			-
35	10K10b	MEAs (Ni/30 nm)			100	200	650	120, 1	25, 80	30	-434	50	100	900	ok
36	17K10a	MEAs (Ni/30 nm)			100	200	600	120, 10	10, 80	10	-400	C_2H_2 did not work			
37	18K10a	MEAs (Ni/30 nm)			100	200	600	120, 10	12, 80	10	-434	60	100	600	ok
38	24K10a	Si	3	-96	100	200	680	750, 120	CH_4 did not work		-	-	-	-	-
39	28K10a	Gl	Calibration of Si			-	-	-	-	-	-	-	-	-	
40	28K10b	Gl	Calibration of Fe			-	-	-	-	-	-	-	-	-	-
41	28K10c	Gl	Calibration of Ni			-	-	-	-	-	-	-	-	-	
42	31L10a	Si	3	-96	100	200	680	750, 120	100, 80	30	-454	50	100	900	ok
43	13A11a	Si	3	-95	100	200	680	750, 120	100, 80	30	-479	50	100	900	ok
44	14A11a	Si	3	-95	100	200	680	750, 120	100, 80	30	-543	CH_4 10	100	900	NG
45	18A11a	Si/NP		-	100	200	680	120, 120	100, 80	30	-440	50	100	900	ok
46	01B11a	MEAs (Ni/30 nm)			100	200	650	120,1	10,80	30	-528	CH_4 10	100	1800	NG
47	01C11a	Si	3	-94	100	200	680	750, 120	100, 80	30	-439	50	100	900	ok
48	02C11a	Si	3	-94	100	200	680	750, 120	100, 80	30	-454	50	100	900	ok
49	11C11a	MEAs (Ni/30 nm)			100	200	650	120, 1	----	30	-440	CH_4 did not work		-	-
50	11C11b	MEAs (30 nm)			100	200	Heating problems			-	-	-	-	-	-
51	22C11a	Si	3	-95	100	200	680	750, 120	100, 80	30	-424	50	100	900	ok
52	29C11a	Si	3	-92	100	200	680	750, 120	100, 80	30	-442	50	100	900	ok
53	01D11a	Si	3	-93	100	200	680	750, 120	100, 80	30	-440	50	100	900	G
54	27D11a	Si	3	-93	100	200	680	750, 120	100, 80	30	-444	50	100	900	G
55	28D11a	Si	3	-93	100	200	680	750, 120	100, 80	30	-442	50	100	900	G
56	13E11a	Si	3	-93	100	200	680	750, 120	100, 80	30	-424	50	100	900	ok
57	30E11a	Si	3	-95	100	200	680	750, 120	100, 80	30	-442	50	100	900	ok
58	06F11a	Si	3	-98	100	200	680	750, 120	100, 80	30	-427	50	100	900	NG
59	14F11a	Si	3	-94	100	200	680	750, 120	100, 80	30	-427	50	100	900	NG
60	16F11a	Si	3	-95	100	200	680	750, 120	100, 80	30	-403	50	100	900	NG
61	20F11a	Si	3	-94	100	200	680	750, 120	100, 80	30	-403	50	100	900	NG
62	04G11a	Si	3	-86	100	200	680	750, 120	100, 80	30	-414	50	100	900	NG
63	06G11a	Si	3	-92	100	200	680	750, 120	100, 80	30	-400	50	100	900	NG
64	08G11a	Si	3	-93	100	200	680	750, 120	100, 80	30	Problem wit plasma			-	NG
65	18G11a	Si	3	-94	100	200	680	750, 120	100, 80	30	-427	50	100	900	OK

	sample	Substrate			Annealing				RF/PECVD (50 W)						
		Type	RF magnetron		H_2 parameters		General parameters		Gas replacement H_2 to NH_3			C_2H_2 parameters			
			Fe (nm)	Bias (V)	sccm	Pa	˚C	R, H (s)	(sccm), (Pa)	(s)	(V)	(sccm)	Pa	G (t)	R
66	19G11a	Si	3	-95	100	200	680	750, 120	100, 80	30	-425	50	100	900	G
67	20G11a	Si	3	-92	100	200	680	750, 120	100, 80	30	-437	50	100	900	G
68	21G11a	Si	3	-95	100	200	680	750, 120	100, 80	30	-407	50	100	900	G
69	25G11a	Si	3	-93	100	200	680	750, 120	100, 80	30	-421	50	100	900	G
70	13I11a	Si	3	-95	100	200	680	750, 120	100, 80	30	-427	50	100	900	G
71	13I11c	Si	3	-95	100	200	680	750, 120	100, 80	30	-419	50	100	900	G
72	14I11a	Si	3	-95	100	200	680	750, 120	100, 80	30	-419	50	100	900	NG
73	14I11b	Si	3	-95	100	200	680	750, 120	100, 80	30	-415	50	100	900	G
74	20I11a	Si	3	-96	100	200	680	750, 120	100, 80	30	-416	50	100	900	G
75	11J11a	Si	3	-96	100	200	680	750, 120	100, 80	30	-342	50	100	900	NG
76	13J11a	Si	3	-94	100	200	680	750, 120	100, 80	30	-427	50	100	900	G
77	17I11a	Si	3	-96	100	200	680	750, 120	100, 80	30	-424	50	100	900	G
78	03K11a	Si	3	-94	100	200	680	750, 120	100, 80	30	-424	50	100	900	G
79	12L11a	Gl	Calibration of Ni												
80	20A11a	Gl	Calibration of Fe												
81	06B12a	Si	3	-93	100	200	680	750, 120	100, 80	30	-456	50	100	900	G
82	07B12a	Si	3	-93	100	200	680	750, 120	100, 80	30	-445	50	100	900	G
83	08B12a	QF	3	-93	100	200	680	750, 120	100, 80	30	-455	50	100	900	G
84	06B12a	QF	3	-88	100	200	680	750, 120	100, 80	30	-423	50	100	900	G
85	17B12a	Gl	Calibration of Ni												
86	20B12a	QF	3	-96	100	200	680	750, 120	100, 80	30	-448	50	100	900	G
87	27B12b	QF	3	-95	100	200	680	750, 120	100, 80	30	-452	50	100	2700	G
88	13C12a	QF	3	-95	100	200	680	750, 120	100, 80	30	-420	50	100	1800	G
89	16C12a	Si	3	-93	100	200	680	750, 120	100, 80	30	-422	50	100	900	G
90	21C12a	QF	3	-95	100	200	680	750, 120	100, 80	30	-443	50	100	900	G
91	22C12a	Si	3	-94	100	200	680	750, 120	100, 80	30	-432	50	100	900	G
92	28C12a	Si	3	-95	100	200	680	750, 120	100, 80	30	-404	50	100	900	G
93	27D12a	Si	3	-95	100	200	680	750, 120	100, 80	30	-404	50	100	900	G
94	09E12a	Si	3	-92	100	200	680	750, 120	100, 80	30	-404	50	100	900	G
95	15E12b	Gl	Calibration of Fe			-	-	-	-	-	-	-	-	-	-
96	16E12a	Si	3	-107	100	200	680	750, 120	100, 80	30	-436	50	100	900	G
97	16E12b	QF	3	-107	100	200	680	750, 120	100, 80	30	-443	50	100	2700	G
98	31E12a	Si	3	-108	100	200	680	750, 120	100, 80	30	-408	50	100	900	G
99	01F12a	Gl	Fe calibration		-	-	-	-	-	-	-	-	-	-	-
100	02F12a	Si	3	-108	100	200	680	750, 120	100, 80	30	-408	50	100	900	NG
101	23F12a	Si	3	-107	100	200	680	750, 120	100, 80	30	-434	50	100	900	ok
102	04G12b	Si	3	-108	100	200	680	750, 120	100, 80	30	-434	50	100	900	G
103	05G12b	QF	3	-108	100	200	680	750, 120	100, 80	30	-440	50	100	2700	G
104	12G12a	QF	3	-107	100	200	680	750, 120	100, 80	30	-440	50	100	1800	G
105	19G12a	QF	3	-108	100	200	680	750, 120	100, 80	30	-437	50	100	1800	G
106	25G12a	QF	3	-105	100	200	680	750, 120	100, 80	30	-437	50	100	1800	G
107	27G12a	Si	3	-105	100	200	Problem with heating			-	-	-	-	-	-
108	04J12a	QF	3	-110	100	200	680	750, 120	100, 80	30	-414	50	100	1800	G
109	06J12a	QF	3	-109	100	200	680	750, 120	100, 80	30	-414	50	100	1800	G
110	11J12a	QF	3	-107	100	200	680	750, 120	100, 80	30	-434	50	100	1800	G
111	27J12a	Si	3	-144	100	200	680	750, 120	100, 80	30	-575	50	100	900	ok
112	29J12b	Si	HF treatment for 40 min , Alumina deposition 10 nm and after wards deposition of Fe 3nm									50	prob		
113	03K12a	Si	HF treatment for 40 min , Alumina deposition 10 nm and after wards deposition of Fe 3nm									50	100	900	NG
114	23K12b	Si	3	-104	100	200	680	750, 120	100, 80	30	-409	50	100	900	G
115	23K12c	Si	3	-104	100	200	680	750, 120	100, 80	30	-434	50	100	900	G
116	29K12a	Si	3	-106	100	200	680	750, 120	100, 80	30	-415	50	100	900	G
117	07L12a	Si	3	-106	100	200	680	750, 120	100, 80	30	-433	50	100	900	G
118	12L12a	Cu	Acetic acid treatment 90 min, Al_2O_3 (20nm)						100, 80	30	-406	50	100	900	ok
119	12L12b	CP	3	-108	100	200	680	750, 120	100, 80	30	-418	50	100	900	G
120	14A13a	CP	3	-107	100	200	680	750, 120	100, 80	30	-460	50	100	1200	G
121	22A13a	Si	3	-105	100	200	680	750, 120	100, 80	30	problem with plasma				-
122	24A13a	Si	3	-106	100	200	680	750, 120	100, 80	30	-427	50	100	900	G
123	28A13a	Si	Ni 3	-126	100	200	680	750, 120	100, 80	30	-436	50	100	900	NG
124	29A13a	Si	Al_2O_3 6nm, Ni 4			200	680	750, 120	100, 80	30	-418	50	100	900	NG
125	30A13a	Si	Al_2O_3 6nm, Ni 4			200	680	750, 120	100, 80	30	-432	50	100	900	ok
126	31A13a	Si	Fe sputtering problem			-	-	-	-	-	-	-	-	-	-
127	04B13	Gl	Calibration of Ni and Fe			-	-	-	-	-	-	-	-	-	-
128	04B13a	Si	3	-99	100	200	680	750, 120	100, 80	30	-419	50	100	900	G
129	05B13b	Si	3	-99	100	200	820	900, 120	100, 80	30	-414	50	100	900	NG
130	09B13a	Si	3	-98	100	200	680	750, 120	100, 80	30	-432	50	100	900	G

	sample	Substrate			Annealing				RF/PECVD (50 W)						
		Type	RF magnetron		H_2 parameters		General parameters		Gas replacement H_2 to NH_3			C_2H_2 parameters			
			Fe (nm)	Bias (V)	sccm	Pa	˚C	R, H (s)	(sccm), (Pa)	(s)	(V)	(sccm)	Pa	G (t)	R
131	13B13a	Si	3	-98	Problem with reactor			-	-	-	-	-	-	-	-
132	14B13a	Si	3	-97	100	200	680	750, 120	100, 80	30	-416	50	100	900	G
133	23B13a	Si	3	-96	100	200	680	750, 120	100, 80	30	-428	50	100	900	G
134	15E13a	Si	3	-97	100	200	680	750, 120	100, 80	30	-413	50	100	900	G
135	18F13a	Si	3	-99	100	200	680	750, 120	100, 80	30	Problem with plasma				
136	20F13a	Gl	Calibration of Fe			-	-	-	-	-	-	-	-	-	-
137	27F13a	Si	3	-103	100	200	680	750, 120	100, 80	30	-463	50	100	900	G
138	28F13a	Si	3	-104	100	200	680	750, 120	100, 80	30	-460	50	100	900	G
139	28F13b	Si	3	-103	100	200	680	750, 120	100, 80	30	-455	50	100	900	G
140	01G13a	Si	3	-106	100	200	680	750, 120	100, 80	30	-418	50	100	900	G
141	18J13	Gl	Fe calibration												
142	27F13a	Si	3	-103	100	200	680	750, 120	100, 80	30	-463	50	100	900	G
143	28F13a	Si	3	-104	100	200	680	750, 120	100, 80	30	-460	50	100	900	G
144	28F13b	Si	3	-103	100	200	680	750, 120	100, 80	30	-45	50	100	900	G
145	27F13a	Si	3	-103	100	200	680	750, 120	100, 80	30	-463	50	100	900	G
146	01G13a	Si	3	-106	100	200	680	750, 120	100, 80	30	-418	50	100	900	G
147	18G13	Gl	Fe calibration		-	-	-	-	-	-	-	-	-	-	-
148	18G13a	Si	3	-107	100	200	680	750, 120	100, 80	30	-464	50	100	900	Ok
149	01H13a	Gl	Fe calibration		-	-	-	-	-	-	-	-	-	-	-
150	11I13a	Si	3	-98	100	200	680	750, 120	100, 80	30	-434	50	100	900	ok
151	17I13a	Si	3	-97	100	200	680	750, 120	100, 80	30	-400	50	100	900	G
152	15A14a	Si	3	-97	100	200	680	750, 120	100, 80	30	-405	50	100	900	G
153	16A14a	Si	3	-100	100	200	680	750, 120	100, 80	30	-400	50	100	1100	G
154	24D14a	Si	3	-100	100	200	680	750, 120	100, 80	30	-380	50	100	900	ok
155	28D14a	Si	3	-100	100	200	680	750, 120	100, 80	30	-399	50	100	360	G

(Si = Silicon wafer), (QF = Quartz filter), (Gl = Glass), (CP = Carbon paper), (V = Bias voltage), (R, H (s) = Ramp time, Hold time), (G (s) = Growth time, ((s) = time, (R = results)), (G = Good sample, Ok = Nanotubes grow on some parts of sample, NG = not good sample)

	sample	Substrate			Annealing				WA-CVD (50 W)						
		Type	RF magnetron		H_2 parameters		General parameters		replacement H_2 to H_2		C_2H_2 parameters				
			Al_2O_3 (nm)	Fe (nm)	sccm	Pa	˚C	R, H (s)	(Pa)	(s)	sccm	(Pa)	WF	G (s)	R
1	11H11a	Si	-	3	100	200	750	1200, 1	100	30	25	100	A	600	NG
2	14H11a	Si	-	3	100	200	750	1200, 1	80	30	50	100	A	600	NG
3		Gl	Calibration of Al_2O_3												
4	12I11a	Si	10	5	100	200	750	1200, 1	80	-	50	100	A	600	NG
5	16I11a	Si	10	5	100	200	750	1200, 1	80	30	50	100	A	600	NG
6	19I11a	Si	10	5	100	200	700	1200, 1	80	30	50	100	A	600	NG
7	20I11a	Si	10	5	100	200	750	1200, 1	80	30	50	100	A	600	NG
8	23I11a	Si	10	5	100	200	700	1200, 1	80	30	50	100	A	600	NG
9	26I11a	Si	10	5	100	200	700	1200, 1	80	30	50	100	A	600	NG
10	27I11a	Si	10	5	100	200	700	1200, 1	80	30	50	100	A	600	NG
11	29I11a	Si	10	5	100	200	Resistance problem			-	-	-	-	-	-
12	07J11a	Si	10	3	100	200	650	1200, 1	80	30	50	100	A	600	NG
13	13J11b	Si	10	5	100	200	600	750, 120	80	30	50	100, 700˚C	A	600	NG
14	14J11a	Si	10	5	100	200	600	750, 120	100	30	50	100, 700˚C	A	600	ok
15	20J11a	Si	10	5	100	200	600	750, 120	100	30	50	100, 700˚C	A	600	ok
16	26J11b	Si	10	5	100	200	600	750, 120	100	30	50	100, 650˚C	A	600	NG
17	27J11a	Si	10	5	100	200	600	750, 120	100	30	50	100, 750˚C	A	600	NG
18	04K11a	Si	20	5	100	200	600	750, 120	100	30	50	100, 750˚C	A	600	NG
19	08K11a	Si	10	5	100	200	600	750, 120	100	30	50	100, 700˚C	A	600	NG
20	17K11a	Si	10	5	100	200	600	750, 120	100	30	50	100, 700˚C	A	600	NG
21	23K11a	Si	Al 10	5	100	200	600	750, 120	100	30	50	100, 700˚C	A	600	NG
22	24K11a	Gl	Calibration of Al, Pulsed DC magnetron sputtering												
23	25K11	Gl	Calibration of Al_2O_3 Pulsed DC magnetron sputtering												
24	25K11a	Si	10	5	100	200	600	750, 120	100	30	50	100, 700˚C	A	600	NG
25	27K11a	Si	10	5	100	200	600	750, 120	100	30	50	100, 700˚C	A	600	NG
26	29K11a	Si	10	5	100	200	600	750, 120	100	30	50	100, 700˚C	A	600	NG
27	30K11a	Gl	Al target cleaning 5 min		Calibration of Al_2O_3 Pulsed DC magnetron sputtering							-	-	-	-
28	01L11a	Gl	Al target cleaning 5 min		Calibration of Al_2O_3 Pulsed DC magnetron sputtering							-	-	-	-
29	13L11a	Si	10	3	100	200	600	750, 120	100	30	50	100, 700˚C	A	600	G
30	18L11a	Si	10	3	100	200	600	750, 120	100	30	50	100, 700˚C	A	600	G
31	26L11a	Si	10	3	100	200	600	750, 120	100	30	50	100, 700˚C	A	600	G
32	31L11a	Si	10	3	100	200	600	750, 120	100	30	50	100, 600˚C	A	600	NG
33	20B12a	Si	10	3	100	200	600	750, 120	100	30	50	100, 680˚C	A	600	NG
34	22B12a	Si	10	3	Problem with reactor										
35	12C12a	Si	10	3	100	200	600	750, 120	100	30	50	100, 700˚C	A	600	G
36	23C12a	Si	10	3	100	200	600	750, 120	100	30	50	100, 700˚C	A	600	NG
37	19D12a	Si	10	>1	100	200	600	750, 120	100	30	50	100, 700˚C	A	600	NG
38	07E12a	Si	10	>1	100	200	600	750, 120	100	30	50	100, 700˚C	A	600	NG
39	11E12a	Si	10	>1	100	200	600	750, 120	100	30	50	100, 700˚C	A	600	NG
40	18E12a	Si	10	0.5	100	200	600	750, 120	80	30	50	100, 700˚C	A	360	NG
41	26E12a	QF	10	3	100	200	600	750, 120	80	30	50	100, 700˚C	A	1200	NG
42	03F12a	Si	11	0.5	100	200	600	750, 120	80	30	50	100, 700˚C	A	600	NG
43	14F12a	Si	11	0.6	100	200	600	750, 120	80	30	50	100, 700˚C	A	900	NG
44	25F12a	Si	11	1	100	200	600	750, 120	80	30	50	100, 700˚C	A	900	G
45	26F12a	QF	11	2	100	200	600	750, 120	80	30	50	100, 700˚C	A	900	NG
46	30F12a	QF	20	2	100	200	600	750, 120	80	30	50	100, 700˚C	A	900	OK
47	21I12a	QF	20	2	100	200	600	750, 120	100	30	50	100, 700˚C	A	900	G
48	22J12a	QF	10	3	100	200	600	750, 120	100	30	50	100, 700˚C	A	900	NG
49	15L12a	CP	15	3	100	200	600	750, 120	100	30	50	100, 700˚C	A	900	G
50	25A13a	Si	10	2	100	200	600	750, 120	80	30	50	100, 700˚C	A	900	G
51	28A13b	QF	10	2	100	200	600	750, 120	80	30	50	100, 700˚C	A	900	G
52	30A13b	QF	10	Problem with sputtering			-	-	-	-	-	-	-	-	-
53	05B13b	QF	11	3	100	200	600	750, 120	100	30	50	100, 700˚C	A	900	ok
54	07B13a	QF	11	3	100	200	600	750, 120	100	30	50	100, 700˚C	A	900	NG
55	07B13b	Si	10	2	100	200	600	750, 120	100	30	50	100, 700˚C	A	900	NG
56	08B13a	Si	10	2	100	200	600	750, 120	100	30	50	100, 700˚C	B	900	G
57	19B13b	Si	20	2	100	200	600	750, 120	100	30	50	100, 700˚C	A	900	NG
58	20B13a	Si	20	2	100	200	600	750, 120	100	30	50	100, 700˚C	B	3600	G
59	19D13a	Si	20	2	100	200	600	750, 120	100	30	50	100, 700˚C	B	1800	NG
60	23D13a	Si	20	2	Problem with reactor			-	-	-	-	-	-	-	-
61	01E13a	Si	40	2	100	200	600	750, 120	100	30	50	100, 700˚C	B	1800	G
62	07E13a	Si	40	2	100	200	600	750, 120	100	30	50	100, 700˚C	B	300	G
63	08E13a	Si	20	2	100	200	600	750, 120	100	30	50	100, 700˚C	B	600	G

		Substrate	sputtering				Annealing				WA-CVD, and RF (50 W)				
64	13E13a	Si	40	2	100	200	600	750, 120	100	30	50	100, 700˚C	B	600	G
65	17E13a	Si	40	2	100	200	600	750, 120	100	30	50	100, 700˚C	B	900	G
66	29F13a	Si	20	2	100	200	600	750, 120	100	30	50	100, 700˚C	B	3600	G
67	13I13b	Si	20	2	100	200	600	750, 120	100	30	50	100, 700˚C	B	1800	G
68	01J13a	Si	20	2	100	200	600	750, 120	100	30	50	100, 700˚C	B-rf	900	ok
69	02J13b	Si	40	2	100	200	600	750, 120	100	30	50	100, 700˚C	B	1800	G
70	18J13a	Si	30	2	100	200	600	750, 120	100	30	50	100, 700˚C	B	1800	G
71	22J13a	Si	30	2	100	200	600	750, 120	100	30	50	100, 700˚C	B	600	NG
72	22J13b	Si	20	0.52	100	200	600	750, 120	100	30	50	100, 700˚C	B	600	G
73	02L13a	Si	20	0.5	100	200	600	750, 120	100	30	50	100, 700˚C	B	900	G
74	02L13b	Gra	20	2	100	200	600	750, 120	100	30	50	100, 700˚C	B	900	G
75	09L13a	CP	20	2	100	200	600	750, 120	100	30	50	100, 700˚C	B	900	G

(Si = Silicon wafer), (QF = Quartz filter), (Gl = Glass), (CP = Carbon paper), (V = Bias voltage), (R, H (s) = Ramp time, Hold time), (G (s) = Growth time, ((s) = time, (R = results)) (WF = water flow), (A= 0.5 mm main scale open micrometer, B= 0.5 mm main circular scale open micrometer), (V = Bias voltage), (R, H(s)= Ramp time, Hold time), (G (s)= Growth time), ((s)= time), (R = results), (G = Good sample, Ok = Nanotubes grow on some parts of sample, NG = not good sample)

	sample	Type	pt	Pulsed DC			RF	H_2 parameters		General parameters		replacement H_2 to H_2 for WA, to NH_3 for rf plasma		C_2H_2 parameters				
				Ni (nm)	Ti (nm)	Al_2O_3 (nm)	Fe (nm)	(sccm)	Pa	˚C	R, H (s)	(Pa)	(s)	(sccm)	(Pa)	WF	G (s)	R
1	23J13b	Cu	1	-	-	30	2	100	200	600	750, 120	100	30	50	100,700˚C	A	900	G
2	26J13b	Cu	1	-	50	30	2	100	200	600	750, 120	100	30	50	100,700˚C	A	900	G
3	22K13a	Cu	1	300	50	30	2	100	200	600	750, 120	100	30	50	100,700˚C	A	900	G
4	25K13a	Cu	1	-	50	30	2	100	200	600	750, 120	100	30	50	100,700˚C	A	900	ok
5	29K13b	Cu	1	300	50	30	2	100	200	600	750, 120	100	30	50	100,700˚C	A	900	G
6	06L13a	Cu	1	150	50	20	3	100	200	680	750, 120	100	30	50	100 (-417V)	-	900	G
7	08L13a	Cu	1	150	75	20	Ni4	100	200	680	750, 120	100	30	50	100 (-419V)	-	900	G
8	12L13a	Cu	1	-	50	-	Ni20	100	200	680	300,120	100	30	50	100 (-427V)	-	900	NG
9	15L13a	Cu	1	150	-	20	3	100	200	680	750, 120	100	30	50	100 (-418V)	-	900	G
10	20L13a	Cu	2	-	75	20	3	100	200	680	Problem with annealing			-	-	-	-	-
11	27L13a	Cu	2	150	-	30	3	100	200	680	750, 120	100	30	50	100 (-408V)	-	1200	G
12	28L13a	Cu	2	150	75	30	3	100	200	680	750, 120	100	30	50	100 (-410V)	-	1200	G
13	29L13a	Cu	2	-	50	-	Ni5	100	200	680	750, 120	100	30	50	100 (-405V)	-	1200	NG
14	29L13b	Cu	2	-	50	- Ni5	3	100	200	680	750, 120	100	30	50	100 (-405V)	-	1200	NG
15	30L13a	Cu	2	Al 60	-	30	3	100	200	680	750, 120	100	30	50	100 (-402V)	-	1800	G
16	03A14a	Cu	2	Al 60	-	30	Ni5	100	200	680	750, 120	100	30	50	100 (-406V)	-	900	G
17	04A14a	Cu	2	300	50	Al 60, 3	3	100	200	680	750, 120	100	30	50	100 (-400V)	-	1200	G
18	06A14a	Cu	2	-	-	30	3	100	200	680	750, 120	100	30	50	100 (-388V)	-	1800	G
19	08A14a	Cu	2	300	50	30	3	100	200	680	750, 120	100	30	50	100 (-370V)	-	1800	G
20	10B14a	Cu	2	-	50	30	3	100	200	680	750, 120	100	30	50	100 (-373V)	-	1800	G
21	14B14a	Cu	2	300	50	30	3	100	200	680	750, 120	100	30	50	100 (-372V)	-	1800	G
22	14B14a	Cu	2	300	50	30	3	100	200	680	Problem with reactor							

(pt= pretreatment), (1=acetic acid bath 10 min), (2= acetone and isopropanol ultrasound bath10 min each and H_2 plasma treatment 10 min), (WF = water flow), (A= 0.5 mm main scale open micrometer, B= 0.5 mm main circular scale open micrometer), (V = Bias voltage), (R, H(s)= Ramp time, Hold time), (G (s)= Growth time), ((s)= time), (R = results), (G = Good sample, Ok = Nanotubes grow on some parts of sample, NG = not good sample)

Publications

PUBLICATIONS

1. Functionalization of carbon nanotubes by water plasma.
   Nanotechnology. **2012**, 23 – 385604.
   Shahzad Hussain, Roger Amade, Eric Jover, Enric Bertran

2. Nitrogen plasma functionalization of carbon nanotubes for supercapacitor applications.
   Journal of Materials Science. **2013** 48, pp. 7620 – 7628
   Shahzad Hussain, Roger Amade, Eric Jover, Enric Bertran

3. Water plasma functionalized CNTs/MnO_2 composites for supercapacitors.
   The Scientific World Journal. Volume 2013 (**2013**),
   Article ID 832581, 8 pages
   http://dx.doi.org/10.1155/2013/832581
   Shahzad Hussain, Roger Amade, Eric Jover, Enric Bertran.

4. Growth and functionalization of carbon nanotubes on quartz filter for environmental applications.
   Journal of Environmental Engineering & Ecological Science
   2014 3: 2 (5 March 2014) http://dx.doi.org/10.7243/2050-1323-3-2
   Roger Amade, Shahzad Hussain, Ismael R. Ocana and Enric Bertran.

5. 3D network of magnetic CoNi alloy nanoparticles electrodeposited on vertically aligned MWCNT showing exceptional coercive field.
   Journal of Materials Letters **2014** 124 8-14.
   J. Vilana, R. Amade, S. Hussain, E. Bertran, E. Gómez, E. Vallés.

6. Study of CNTs structural evolution during water assisted growth and transfer methodology for electrochemical applications.
   Journal of materials Chemistry and Physics (under minor review **June 2014**)
   Shahzad Hussain, Roger Amade and Enric Bertan.

7. RF-PECVD growth and nitrogen plasma functionalization of CNTs on copper foil for electrochemical applications.

Journal of Diamond and related materials **(Submitted June 2014)**
Shahzad Hussain, Roger Amade, Harold Moreno and Enric Bertran

8. Vertically-aligned carbon nantoubes coated with manganese dioxide as improved cathode material for microbial fuel cells.
   Journal of Materials Science **(submitted June 2014)**
   Roger Amade, Maria Vila-Costa; Shahzad Hussain; Emilio O. Casamyor; Enric Bertran.

9. Growth and functionalization of CNTs on stainless steel for supercapacitor applications
   H. A. Moreno, S. Hussain, R. Amade, E. Bertran.
   Manuscript **June 2014**

CONFERENCES

1: Title: Carbon nanotubes grown on stainless steel for supercapacitor applications.
Conference: Programa de la sisena jornada institut de nanociencia I Nanotecnologia in^{2}ub// Universitat de Barcelona Spain June 5 (2014).
Contribution: Poster
Shahzad Hussain, Harold Moreno, Roger Amade and Enric Bertran.

2: Title: Growth and functionalization of MWCNTs on quartz filter for environmental applications.
Conference: DIAMOND 2013, International Conference on Diamond and Carbon Materials 2013, Carbon Nanotubes, September 2-5, 2013, Riva Del Garda (Italy).
Contribution: Poster
Shahzad Hussain, Roger Amade, Ismael R. Ocaña and Enric Bertran.

3: Tilte: Functionalization of CNTs by water plasma for energy applications.
Conference: 2nd International Conference on Materials for

Energy EnMat II, May 2013, Karlsruhe, Germany,
Contribution: Poster
Shahzad Hussain, Roger Amade, Enric Bertran.

4: Title: Functionalization of vertically aligned carbon nanotubes with nitrogen plasma and deposition of MnO2 for supercapacitor applications.
Conference: 2nd International Conference on Materials for Energy EnMat II, May 2013, Karlsruhe, Germany,
Contribution: Oral presentation
Hussain, S.; Amade, R.; Bertran

5: Title: Functionalization of vertically aligned carbon nanotubes by nitrogen plasma.
Conference: DIAMOND'12, International Conference on Diamond and Carbon Materials 2012, Carbon Nanotubes, September 3rd, 2012, Granada (Spain).
Contribution: Poster
Hussain, S.; Amade, R.; Jover, E.; Bertran, E."DIAMOND'12 Abstracts book, P1-19.

6: Title: Functionalization and Characterization of CNTs by Plasma techniques.
Conference: Poster contribution at Garmisch-Partenkisrchen (Germany) Sep 4-8 (2011).
Contribution: Poster
Amade, R; Hussain, S; Bertran, E;

7: Title: Vertically aligned CNTs/MnO_2 nanocomposite for supercapacitor application using aqueous and ionic liquid electrolytes.
Conference: EMRS, Spring meeting, May 9-13, 2011, Nice (France)
Contribution: Poster
Amade R, Jover E, Hussain S, Ibáñez A, Mesquida N, Dinarès I, Bertran E.

8: Title: Functionalization and characterization of CNT's by means of Water Plasma.

Conference: IMAGINENANO, Nanospain2011, April 11-14, 2011. Bilbao (Spain)
Contribution: Poster
Hussain, S.; Jover, E.; Amade, R.; Bertran,E.

Resumen en español

La nanociencia y nanotecnología han experimentado un enorme crecimiento en pocos años. Las nanotecnologías son el diseño, caracterización, producción y aplicación de estructuras, dispositivos y sistemas de control de forma y tamaño a escala nanométrica. El concepto de nanotecnología fue introducido por primera vez por el premio Nobel Richard Feynman el 29 de diciembre de 1959 en la reunión anual de la Sociedad Americana de Física en el Instituto de Tecnología de California (Caltech). En su clásica conferencia titulada: "Hay mucho espacio en el fondo", Feynman dijo: "A mi modo de ver, los principios de la Física no se pronuncian en contra de la posibilidad de maniobrar las cosas átomo por átomo". Más tarde, Norio Taniguchi de la Universidad de Ciencias de Tokio definió por primera vez la nanotecnología como: (1) la creación de materiales útiles, dispositivos y sistemas a través del control de la materia a escala nanométrica (10^{-9} m) y (2) la explotación de nuevas propiedades y fenómenos desarrollados en esa escala. Hasta el momento, un número cada vez mayor de aplicaciones se han demostrado. Particularmente, los nanotubos de carbono son uno de los nanomateriales con las propuestas más novedosas y prometedoras para aplicaciones en mecánica y estructuras superficiales, almacenamiento de energía, medio ambiente, biomedicina, electroquímica o fotónica. Los nanotubos de carbono (CNT) tienen características únicas que les permiten actuar como electrodos en dispositivos de almacenamiento de carga, sensores y trampas para contaminantes, entre otros.

Uno de los objetivos principales de esta tesis es la síntesis i optimización de nanotubos de carbono para supercondensadores. En aplicaciones que requieren cierta cantidad de energía en forma de pulsos, los condensadores tradicionales utilizados en los circuitos electrónicos no son adecuados porque no pueden almacenar suficiente energía por unidad de volumen y masa. Sin embargo, dadas las características de los nanotubos de carbono, tales como una estrecha distribución de tamaño, gran superficie específica, baja resistividad y alta estabilidad química, estos son considerados un material prometedor y adecuado para electrodos en supercondensadores.

Por otro lado, el desarrollo de nuevos sistemas basados en nanotubos de carbono, que podrían superar algunas de las limitaciones actuales en la

captura de contaminantes emergentes en fluidos, tales como partículas nanométricas, que además son difíciles de detectar, y contaminantes orgánicos a muy bajas concentraciones, es un objetivo adicional de la presente tesis.

El contenido se divide en cuatro partes.

La primera parte contiene una introducción básica acerca de la nanociencia y la nanotecnología. El carbono existe en tres formas: grafito, carbono amorfo y diamante. Dependiendo de cómo están dispuestos los átomos de carbono, sus propiedades varían. Por ejemplo, la forma más común de carbono, el grafito, es suave, negro, y estable. En el grafito, los átomos de carbono se encuentran en las esquinas de hexágonos regulares y fusionados, dispuestos en capas paralelas, y su densidad es de 2,26 g/cm^3. Sin embargo, el diamante es duro y transparente debido a su patrón regular y repetitivo donde cada átomo de carbono está unido a otros cuatro átomos de carbono y su densidad de 3,51 g/cm^3 es mayor que la del grafito. Otra configuración del carbono: la forma tipo polímero se encuentra cuando el carbono se diluye con hidrógeno, y presenta baja dureza, alta transparencia y eléctricamente se comporta como un aislante eléctrico. El fulereno es una forma más del carbono y es único en la gran familia de materiales con base carbono y tiene aplicaciones como puntos cuánticos de dimensión cero. Los nanotubos de carbono, que tienen medio fulereno en cada extremo, han despertado un gran interés en la comunidad científica debido a sus propiedades eléctricas, térmicas y mecánicas. Los nanotubos multicapa (MWCNTs) y de pared simple (SWCNTs) fueron descubiertos en 1991 y 1993, respectivamente, por Ijima. Un nanotubo de carbono de pared simple se puede describir como una hoja de grafeno enrollada en forma cilíndrica de modo que la estructura tiene una simetría axial. Las excelentes propiedades de los nanotubos de carbono hacen que sea un candidato ideal para dispositivos electrónicos, sensores químicos/electroquímicos y biosensores, electrones de emisión de campo, baterías de ion litio, fuentes de luz blanca, almacenamiento de hidrógeno, tubos de rayos catódicos (CRT), descargas electroestáticas (ESD) y en aplicaciones de apantallamiento eléctrico. Los supercondensadores almacenan y descargan energía muy rápidamente, se utilizan en diversas aplicaciones y se están considerando muchas otras para el futuro. Los supercondensadores complementan una fuente de energía primaria, como puede ser un motor de

combustión interna, pila o batería, que no puede ofrecer rápidas ráfagas de energía.

La segunda parte describe una comparación entre las diversas tecnologías para la síntesis de nanotubos de carbono (CNTs) y detalles sobre las técnicas utilizadas para su caracterización.

En la tercera parte se presentan los resultados de la tesis. El primer capítulo de esta sección está relacionado con el crecimiento de nanotubos de carbono verticalmente alineados sobre una oblea de silicio mediante deposición química de vapor asistida por plasma de radio-frecuencia (rf-PECVD). Los CNTs fueron funcionalizados mediante un tratamiento con plasma de agua, que introduce diferentes grupos funcionales de oxígeno. Utilizando el diseño experimental de Box-Wilson se ha obtenido una mejor comprensión del mecanismo de funcionalización. Modificando los principales parámetros del plasma de agua (energía del plasma y presión del vapor de agua), hemos sido capaces de controlar el proceso de funcionalización. Nanotubos de carbono no funcionalizados y funcionalizados fueron caracterizados mediante diferentes técnicas y se observó que la energía del plasma es el parámetro principal en el proceso de funcionalización, mientras que presiones elevadas de agua tienen un efecto negativo en la funcionalización. Esto podría atribuirse a la formación de una capa de agua sobre la superficie de los nanotubos que los protege del ataque del plasma. La caracterización morfológica sugiere que después del tratamiento con plasma las superficies de los CNTs se vuelven ásperas y aumenta el número de defectos. Además, se observó una eliminación de la mayoría de partículas de catalizador en las puntas de los nanotubos. Análisis mediante espectroscopía Raman muestra que el número de defectos aumenta y la cristalinidad de los CNTs disminuye después del tratamiento con plasma. Los resultados de la espectroscopía de fotoelectrones emitidos por rayos X (XPS) demuestran que cambiando los parámetros del tratamiento por plasma (potencia del plasma y presión del agua), es posible decorar los CNTs con los grupos funcionales deseados, como carboxílico o hidroxilo. Además, este tratamiento de oxidación también aumenta la hidrofilicidad de los nanotubos de carbono, que los hace más adecuados para aplicaciones biomédicas. Las propiedades electroquímicas de los nanotubos pueden ser ajustadas mediante los parámetros de control del plasma de agua. En particular, las condiciones óptimas para eliminar carbono amorfo y mejorar el almacenamiento de

carga fueron 10 W de potencia de plasma y 135 Pa de presión de vapor de agua. Utilizando estas condiciones se obtuvo una capacidad específica de 68 Fg^{-1}.

En el segundo capítulo de resultados se estudia con detalle el tratamiento de los nanotubos de carbono con plasma de agua para funcionalizar y purificar su superficie, así como para mejorar sus propiedades electroquímicas. Un aumento adicional de su capacidad de almacenamiento de carga se consigue mediante la electrodeposición anódica de dióxido de manganeso recubriendo la superficie de los nanotubos (sin y con tratamiento de plasma) para formar electrodos nanocompuestos de MnO_2/CNTs. Las imágenes de microscopía electrónica de barrido (SEM) confirman la eliminación del carbono amorfo y revelan la formación de MnO_2 con una estructura de "nanoflor" depositado sobre los CNTs. Los resultados de espectroscopia Raman y XPS indican que el ciclado electroquímico en el rango de potencial entre 0-1V convierte MnO_2 en Mn_3O_4, lo cual conlleva un importante cambio en la morfología del óxido de metal observada mediante SEM. Por otro lado, una ventana de potencial entre 0,1-0,8 V no cambia el estado de oxidación del MnO_2 y sólo induce un ligero cambio morfológico de "nanoflor" a una estructura de capas. Unos valores de capacidad específica elevados se alcanzaron utilizando condiciones óptimas de plasma de agua; baja potencia de plasma rf y altas presiones de agua. En concreto, se obtuvo una capacidad específica de 750 Fg^{-1} utilizando wpCNTs/MnO_2 (10W, 135 Pa) como electrodo nanocompuesto.

En el tercer capítulo de la sección de resultados se analiza la funcionalización de los CNTs mediante plasma de nitrógeno para aplicaciones en supercondensadores. Tanto el cambio estructural como la concentración de nitrógeno en los nanotubos aumentan después del tratamiento con plasma de nitrógeno. El efecto de la energía del plasma y la presión de nitrógeno en la capacidad de almacenamiento de carga de los nanotubos se ha investigado detalladamente. Grupos funcionales de nitrógeno tales como nitrógeno cuaternario en los planos basales y nitrógeno pirrólico en la superficie se introdujeron de manera significativa en los MWCNTs. Los resultados de espectroscopia Raman muestran que el desorden estructural aumenta al aumentar la concentración de nitrógeno. Presiones medias/elevadas en el plasma (150-260 Pa) son adecuadas para la introducción de nitrógeno pirrólico, mientras que presiones bajas de plasma

(10 Pa) lo son para la introducción de funcionalidades tipo piridínico. La diferencia de potencial entre los picos anódico y catódico del par redox Fe^{3+} / Fe^{2+} disminuye de 102 mV a 75,7 mV después del tratamiento con plasma de nitrógeno, lo cual representa un aumento en la reversibilidad del proceso de transferencia de electrones entre los nanotubos y el electrolito. Un aumento en la capacitancia específica de los nanotubos de carbono está relacionado con un aumento en el desorden estructural y la introducción de grupos funcionales tanto piridínicos como pirrólicos. La capacitancia específica en solución acuosa a una velocidad de barrido de 10 mVs^{-1} aumentó de 22 a 55 Fg^{-1} después de aplicar un plasma de nitrógeno a 75 W y 260 Pa. Frackowiak et al. obtuvieron una capacidad específica de 137 Fg^{-1} (en solución 6 M de KOH) utilizando MWCNTs purificados con ácido nítrico al 69% y a 80°C. Sin embargo, estos nanotubos de carbono presentan aplicaciones limitadas debido a procesos de auto-descarga. Tratamientos electroquímicos aumentan la capacitancia de los nanotubos de carbono hasta 56 Fg^{-1} en una solución acuosa 6 M de KOH, y nanotubos de carbono tratados térmicamente presentan una capacitancia específica de hasta 80 Fg^{-1} en una solución electrolítica 1 M de H_2SO_4. En comparación con estos estudios, el presente trabajo tiene la ventaja de utilizar un tratamiento relativamente rápido, y un electrolito respetuoso con el medio ambiente y más seguro; una solución acuosa 0,1 M de Na_2SO_4. Por otro lado, una elevada capacidad específica (955 Fg^{-1}) se obtuvo a una velocidad de barrido de 10 mVs^{-1} para un electrodo nanocompuesto de NPCNTs/MnO_2 (75 W, 10 Pa).

El cuarto capítulo de resultados presenta el crecimiento de bosques altamente densos y largos de nanotubos de carbono (CNT) mediante CVD asistido por agua (WACVD). El recocido de la capa fina de catalizador se realizó a 600°C y el crecimiento de los nanotubos de carbono a una temperatura relativamente baja (700°C). Una pequeña cantidad de agua destilada (0,04 sccm) se introdujo sin la ayuda de un gas portador como pudiera ser Ar o He durante el crecimiento. Inicialmente, el vapor de agua aumenta la cristalinidad y longitud de los nanotubos con el tiempo de crecimiento. Sin embargo, la presencia del vapor de agua cambia gradualmente la estructura multicapa de los nanotubos a nanotubos con pocas paredes o incluso de pared simple. Después de un cierto tiempo, la velocidad de crecimiento se vuelve lenta y el desorden estructural empieza a aumentar. Para analizar las propiedades electroquímicas de los bosques

ultra-largos de CNTs obtenidos se tuvieron que transferir a una cinta adhesiva de aluminio conductor utilizando una novedosa metodología. Además, se realizó un tratamiento de plasma de agua con el fin de introducir grupos funcionales de oxígeno en los nanotubos de carbono (CNT transferidos/Al). La capacidad específica de los CNT/Al aumenta de 87 a 148 Fg^{-1} después del tratamiento con plasma de agua. Por otra parte, las medidas de estabilidad cíclica de carga/descarga muestran valores de capacitancia estables hasta los 4000 ciclos.

El quinto capítulo describe principalmente una forma eficaz de mejorar la adherencia, la velocidad de crecimiento y la densidad de los nanotubos de carbono sobre un sustrato de cobre usando rf-PECVD. La adhesión de una capa previa de alúmina sobre el substrato de cobre es un factor crítico para un buen crecimiento de los nanotubos de carbono. Con la finalidad de reducir el óxido de cobre en la superficie y mejorar la adhesión, se realizó un plasma de hidrógeno sobre el sustrato de cobre. El efecto de dos capas intermedias (Ti, Ni), individuales o en combinación, entre la alúmina y el substrato de cobre en el crecimiento de los nanotubos de carbono, se ha investigado y optimizado. Además, un tratamiento con plasma de nitrógeno se llevó a cabo para funcionalizar los nanotubos de carbono obtenidos. Las medidas electroquímicas se realizaron utilizando nanotubos de carbono crecidos sobre el sustrato de cobre como electrodos y $LiClO_4$ como electrolito. Como consecuencia del tratamiento con plasma de nitrógeno la contribución de la pseudocapacitancia a la capacitancia total de los CNTs aumentó. La capacitancia específica de los electrodos obtenidos se incrementó de 49 hasta 227 Fg^{-1}, utilizando una velocidad de barrido de 10 mVs^{-1}, después de tratarlos con plasma de nitrógeno. Los supercondensadores hechos de nanotubos de carbono crecidos sobre electrodos de cobre y con un electrolito orgánico presentan una ciclabilidad que se mantiene casi estable durante 1200 ciclos a una densidad de corriente de 5,5 Ag^{-1} y en una ventana de tensión de 2,5 V.

El último capítulo de la parte de resultados está relacionado con el uso de nanotubos de carbono para aplicaciones ambientales. La contaminación del aire se ha convertido en un problema importante en todo el mundo debido a sus efectos adversos sobre la salud. Entre los diferentes contaminantes del aire, los compuestos orgánicos volátiles (VOC) son líquidos o sólidos con una alta presión de vapor a temperatura ambiente, que son extremadamente peligrosos para la salud humana. La eliminación de estos compuestos se

puede lograr utilizando nanomateriales con propiedades óptimas tales como los nanotubos de carbono. Nanotubos multicapa verticalmente alineados (CNT) se crecieron con éxito sobre filtros de cuarzo mediante rf-PECVD. Además, se realizó un tratamiento de plasma con el fin de modificar las propiedades superficiales de los nanotubos de carbono. Los procesos de adsorción/desorción de tres compuestos clorados (tricloroetileno, 1, 2-diclorobenceno y cloroformo) en los nanotubos de carbono se estudiaron usando mediciones de espectrometría de masas con un analizador de gas residual. La capacidad de adsorción de los nanotubos de carbono aumentó después de la funcionalización de su superficie con el tratamiento de plasma de agua. Además, se encontró que la presencia de anillos aromáticos, solubilidad en agua y la polaridad de los compuestos orgánicos volátiles juegan un papel importante en la cinética de adsorción/desorción sobre la superficie de los nanotubos de carbono. La presencia de anillos aromáticos en compuestos orgánicos volátiles resulta en interacciones de tipo apilamiento-π con un aumento significativo de su adsorción. Por otra parte, se encontró que las interacciones superficiales en los CNTs aumentan con la solubilidad en agua y la polaridad de los VOCs.

La cuarta parte de la tesis se dedica a presentar las conclusiones del trabajo, y también se listan los detalles experimentales de las muestras realizadas.